EXPERIMENTAL INVESTIGATION OF TRANSIENT LIQUID PHASE BONDING OF IN 718 SUPERALLOY AND ENHANCEMENT OF BOND QUALITY

UTTAM KUMAR TARAI

Department of Mechanical
Engineering Indian Institute of
Technology Guwahati Guwahati
781039, Assam, India

2023

Experimental Investigation of Transient Liquid Phase Bonding of IN 718 Superalloy and Enhancement of Bond Quality

Thesis submitted to

Indian Institute of Technology Guwahati For the award of the degree

Doctor of Philosophy

By

Uttam Kumar Tarai

Under the supervision of

Prof. Sukhomay Pal & Prof. P S Robi

Department of Mechanical Engineering Indian Institute of Technology Guwahati Guwahati 781039, Assam, India

January 2023

Department of Mechanical Engineering

Indian Institute of Technology Guwahati

Guwahati-781039,

INDIA

CERTIFICATE

It is certified that the work contained in the thesis entitled "**Experimental Investigation of Transient Liquid Phase Bonding of IN 718 Superalloy and Enhancement of Bond Quality**" submitted by **Mr. Uttam Kumar Tarai** (Reg. No. 146103037) to the Indian Institute of Technology Guwahati for the award of degree of Doctor of Philosophy has been carried out under our supervision in the Department of Mechanical Engineering, Indian Institute of Technology Guwahati. This work has not been submitted elsewhere for the award of any other degree or diploma.

The thesis, in our opinion, has reached the standard fulfilling the requirements for the award of degree of Doctor of Philosophy in accordance with the regulations of the institute.

Dr. Sukhomay Pal & Dr. P. S. Robi

Professor,

Department of Mechanical Engineering

Indian Institute of Technology Guwahati

Guwahati-781039

India

Declaration

I declare that, the present work contained in this thesis is original and has been done by me under the guidance of my supervisors. The work has not been submitted to any other institute for any degree or diploma. I have followed the guidelines, principles, academic morality, and ethical code of conduct provided by the institute in the present thesis. Whenever I have used materials from other sources, I have adequately cited and referred in the text of the thesis. Further, I realize that any violation of the above will be cause of disciplinary action by the institute and can induce disciplinary action from the sources which have thus not properly cited.

Date: 9thth June 2023 (**Uttam Kumar Tarai)**

(Roll. No.: 146103037)

Acknowledgements

First and foremost, I would like to thank God for keeping me healthy, giving me strength and encouragement throughout all the challenging moments of completing this dissertation. I am truly grateful for His unconditional and endless love, mercy, and grace. I wish to express my deep gratitude to all those who have helped me in various ways directly and indirectly during the tenure of my PhD work at IIT Guwahati. In each step of the PhD work was supported by many people and each one have played important role. I am grateful to all of them.

I express my sincere gratitude and appreciation to my supervisors, **Dr. Sukhomay Pal**, and **Dr. P. S. Robi**, Professor, Department of Mechanical Engineering, IIT Guwahati, for their valuable advices, expert guidance, patience, encouragement, and for all the support they has given me from the day one and throughout the PhD work. Without their support, advice, and motivation, it would have just been an impossible task for me to carry over this research work. Regardless of their workload, they always found time to discuss with me for the PhD work and also given so many suggestions for betterment of my personal life. I really feel privileged for having the opportunity to work under them and as my PhD supervisors.

I would like to thank my doctoral committee chairman **Dr. S. Senthilvelan,** Professor, Department of Mechanical Engineering for his valuable suggestion and encouragement during the PhD work. Also, I would like to extend my appreciation to my doctoral committee members **Dr. Pankaj Biswas,** Professor in the Department of Mechanical Engineering and **Dr. B. P. Mandal,** Professor in the Department of Chemical Engineering for their constructive criticisms and helpful suggestions which make thesis improvement. I sincerely appreciate **Prof. K. S. R. Krishna Murthy**, **Prof. S. K. Dwivedy**, **Prof. A. K. Dass**, and **Prof. P. Mahanta**, the present and former Head of the department, for extending all necessary facilities of the department. Thanks to all the faculty members of the department for not only their technical suggestions at times but also their friendly interactions that create an enjoyable working environment in the department.

I wish to express my sincere thanks to Mr. S. Sharma, Mr. S. Ahmed, Mr. R. Saikia,

Mr. J. Basumatary, Mr. N. Bora and Mr. P. Pal for their assistant whenever needed during experimentation. Also thanks to CIF HOC, staff and TA for their helping hand for the analysis of the specimens. I am very much thanks to workshop superintendent Mr. N. K. Das, and staff Mr. C. Banikya, Mr. D. Khaklary, Mr. M. Medhi, Mr. M. Sharma, Mr. M. Baishya, Mr. N. Saikia, Mr. U. Gohain, for their helping hand for the experimentation.

I would like to express my sincere thanks and gratitude to my lab-mates Vivekananda, Dipankar, Ankan, Sunil, Debtanay, Sujit, Amritava, Saptarshi, and Biswajyoti for their cooperation and support during my Ph.D. work. We've all been there for one another and have taught ourselves and each other during the experimentation and analysis. Sincere thanks to my seniors and friends Dr.Purnendu Mandal, Dr. Mrutyunjay Maharana, Durga, Jayashree and Sibabrata, for their help, support and advice in different occasions of my PhD work.

I shall always be grateful to my parents **Mrs. Kuluri Tarai and Mr. Binod Tarai** for their great encouragement, guidance, love, affection, motivation, sacrifice and warm blessings. I am extremely thankful to my family members; Urmila Behera, Bhagabata Behera, Urbasi Behera, Bishnu Behera, Upendra Tarai, Lilybala Dalei, Urpama Behera, Bikash Behera, for their support, prayers and sacrifice. I am very thankful to my wife Mrs. Anita Behera and daughter Dhanaly for their unconditional and endless love, prayers, understanding, support and sacrifice.

I may have missed out a few names in the above list; my sincere apologies are due for any such inadvertent oversight.

I dedicate this Thesis to

My Family, Wife, and Daughter

I love you all dearly

Abstract

The present research work started with an objective to understand the fundamental kinetics of transient liquid phase (TLP) bonding of nickel-base superalloys; Inconel 718 (IN 718) and deliver methodologies for the improvement of bond properties. The role of process parameters in joining IN 718 with the TLP bonding process is explored with an aim to improve the mechanical properties of the bond. From the experimental investigation, it was ascertained that the bonding temperature, time, and interlayer type and size are the most important process parameter of the TLP bonding process. The higher bonding temperature, time, and optimal interlayer thickness improve the mechanical properties of the TLP bonded IN 718 joint. Higher bonding temperature reduces the isothermal solidification (IS) time. Inadequate bonding time leads to the formation of centreline eutectics in the TLP joint due to athermal solidification of the residual liquid remaining in the bond area. The IS time of the TLP bonding process depends upon factors like temperature, the diffusivity of the melting point depressants (MPD), and the width of the interlayer material. To obtain good bond properties, complete isothermal solidification is necessary. In order to determine IS time, the kinetics of TLP bonding should be known to the industries. To study the kinetics of the TLP bonding and to reduce the experimental time and cost, the interrupted differential scanning spectroscopy (DSC) method was used in the current investigation. The DSC method successfully described the kinetics of the TLP bonding. From the enthalpy of solidification of the DSC curve, the IS time of a material was obtained. And the results of the investigations are in good agreement with the experimental results of the other author.

The presence of centerline eutectic and boride precipitates in the microstructure of the TLP bonded IN 718 joint affects the mechanical properties of the joint. The number of eutectics and borides present in the bond zone should be minimized to enhance the mechanical properties of the bond. This can be achieved to a great extent by prolonged isothermal holding. However, it can induce adverse effects by modifying the microstructure of the base material. Therefore, the homogenization stage of the TLP bonding is essential in removing these deleterious phases. The concentration gradient, borides, and the second phase eutectics formed in the isothermal solidified zone can be reduced by the employment of the homogenization stage of the TLP bonding. Homogenization can dissolve the second phase precipitates from the bond zone and achieve a uniform microstructure. Therefore, homogenization of the bond was carried out as per the TTT diagram of the IN 718. Which resulted in improved mechanical properties of the

bond and uniform microstructure. Sometimes, complete homogenization requires higher time to dissolve all the phases to improve the mechanical properties of the bond. Therefore, post-bond heat treatment (PBHT) processes can be implemented to improve the mechanical properties without inducing any harmful effect of prolonged heating. With the application of the PBHT process, the room temperature tensile strength, room temperature fatigue life, and elevated temperature tensile strength of the TLP bonded IN 718 joint has improved significantly. The strength of the TLP bond could be compared to that of the heat-treated base material. The formation of γ″ and γ′ precipitates in the IN 718 joint during PBHT, enhanced the mechanical properties of the joint.

TLP bonding is a diffusion-controlled process, therefore, complete isothermal solidification requires higher bonding time. In the case of incomplete isothermal solidification, the remnant liquid solidifies athermally and forms an inhomogeneous microstructure. The thermal mismatch between the bond zone and base material and the inhomogeneous microstructure induces residual stress in the TLP bonding. Residual stress plays a significant role in designing and manufacturing commercial aero-engine components made of IN 718 for their excellent fatigue strength**.** Thus, a quantitative analysis of the residual stresses is an important aspect of TLP bonding. In this study, the evolution of the surface residual stresses in the TLP bonded samples were investigated using a non-destructive X-ray diffraction measurement $\sin^2\psi$ technique. The quantitative analysis of residual liquid showed there is a compressive stress present in the TLP bonded IN 718 sample.

Interlayer plays important role in the TLP bonding. Designing a suitable interlayer material can reduce the isothermal solidification time. The interlayer material must contain the main alloying elements of the base material and at least one MPD element in order to uphold higher strength. Therefore, in this current study, a Ni-Cr-B-Si-Fe base filler alloy powder has been synthesized by mechanical alloying (MA) technique in a high-energy ball mill to join IN 718 by TLP bonding. The MA process produced a nano-crystalline, and a non-equilibrium solid solution of face-centered cubic structured Ni (Cr, Fe, Si, B) interlayer material. IN 718 superalloys were joined by the TLP bonding process using the newly developed interlayer material successfully.

Keywords: Transient liquid phase bonding, Inconel 718, Post-bond heat treatment, Isothermal solidification, High- temperature property, Mechanical alloying, Homogenization stage

List of Acronyms

ABS	As bonded sample
Al	Aluminium
ASTM	American Society for Testing and Materials
ARIN 718	As received Inconel 718
ASZ	Athermal solidified zone
AWS	American welding society
BCT	Body-centered tetragonal
B	Boron
BMZ	Base metal zone
BM	Base metal
C	Carbon
Cr	Chromium
DAZ	Diffusion affected zone
DSC	Differential scanning calorimetry
EDS	Energy-dispersive X-ray spectroscopy
EBW	Electron beam welding
EDM	Electro discharge machining
Exp.	Experiment no.
FESEM	Field emission scanning electron microscope
FETEM	Field emission transmission electron microscope
FEL	Fatigue endurance limit regime
Fe	Iron
FFT	Fast Fourier transform
GB	Grain boundaries
HAZ	Heat affected zone
HCF	High cycle fatigue

HTREM	High-resolution transmission electron microscopy
HT	Heat treatment
IN	Inconel
IN 718	Inconel 718
IS	Isothermal solidification
ISZ	Isothermal solidified zone
LBW	Laser beam welding
LPSA	Laser particle size analyser
MC	Metal carbide
Mo	Molybdenum
MPD	Melting point depressant
MWHP	modified Williamson-Hall plot
Ni	Nickel
Nb	Niobium
OM	optical microscope
PAW	Plasma arc welding
PBHT	Post bond heat treatment
P	Phosphorous
PBHTed	Post bond heat treated
SAED	Selective area electron diffraction
S	Sulphur
TB	Twin boundaries
TCP	Topologically close pack
TEM	Transmission electron microscope
TIG	Tungsten inert gas
Ti	Titanium
TLP	Transient liquid phase
TG-TLP	Temperature gradient transient liquid phase
TLPD	Transient liquid phase diffusion

TTT	Time Temperature and Transformation
UTM	Universal testing machine
UTS	Ultimate tensile strength
WG-TLP	Wide gap transient liquid phase bonding
XRD	X-ray diffraction

Nomenclature

W_o	Initial thickness
$C_{L\alpha}$	Initial composition
$C\alpha$	Solid composition at interface
FWHM	full width at half maximum
LMP	Larson– Miller parameters
d	Inter-planar spacing
TB	Bonding temperature
tB	Bonding time
γ	Ni-austenite matrix
γ'	Gamma prime
γ"	Gamma double prime
MC	Metal-carbide
b	Basquin exponent
γ_{ML}	Surface energy between base metal and liquid
γ_{SL}	Surface energy between solidifying metal and liquid
γ_{SM}	Surface energy between solidifying metal
φ	Wetting angle
°C	Degree centigrade
min	Minutes
L	Liquid
δ	Delta phase
$V_{f,i}$	Volume fraction of a phase
N_t	Number of cycles
A_i	Integral area of that phase
σ	Nominal stress amplitude
σ_f	Fatigue strength coefficient
α	Surface concentration

D_s	Diffusivity
x	Distance
t	Time
W_{loss}	Coating weight loss
t_0	Total heat up time
W_t	Width of base metal dissolved at time
W_0	Equilibrium dissolution width, and K is a constant
ρ	Densities ratio of liquid and solid
h	Half initial liquid width
Mt	Total amount of element entered the base metal
C_F	Solute content in filler material
W_{max}	Maximum liquid width
$S(t)$	Position variable with time
$C(x,t)$	Concentration at point x and time t
D	Crystallite size
m	Mass of the liquid solidified
ΔH_0	Enthalpy of solidification
ΔH_t	Enthalpy of solidification after isothermal holding
M	Mass of the original eutectic interlayer foil
V_0	Initial volume of the interlayer
w_0	Initial width and area of the interlayer material
A_0	Initial area of interlayer material
A_b	Actual area of base material wetted
$2w_t$	Interlayer full width
C	Slope of the curve
T_m	Melting temperature
R	Stress ratio of
θ_B	Bragg angle of reflection
$\Delta\theta_B$	Peak FWHM

λ	X-rays wavelength
n	Order of reflections
a	Lattice constant
B	A constant
C_{hkl}	Dislocation contrast factor of the plane
(hkl)	Miller indices of plane
C_{44}, C_{11} ,C_{12}	Elastic constants
$\langle \eta_{rms} \rangle$	Lattice strain root mean square
f_{GB}	Fraction of grain boundaries
d_{eGB}	Effective grain boundary thickness
D_{aad}	Average atomic diameter
$\emptyset$	Heating rate
T_p	Peak transformation temperature
E_a	Activation energy
K_0	Constant
R	Universal gas constant
θ	Angle between the reflected beam and the reflecting planes
d_0	Stress free inter-planar spacing
$d_{\phi\psi}$	Inter-planar spacing at a given $\psi\phi$
Ψ	Angle between the plane *S3* and *L3*
E	Young's modulus of the plane
v	Poisons ratio of the lattice plane
L	Average length
P	Applied load
L1, *L2* and *L3*	Orthogonal directions relative to the laboratory frame of reference
S1, *S2* and *S3*	Orthogonal directions relative to the r substrate reference

List of Figures

List of Tables

Contents

Chapter 1

Introduction

1.1 Overview of Ni-base Superalloy

Gas turbine engines are extensively used in aircrafts and land-based power generators with different shapes and sizes. The parts of the gas turbine engines are subjected to severe operating conditions for prolonged time intervals at elevated temperatures. As the parts are exposed to the most severe working environments, where high-temperature oxidation resistance, tensile strength, ductility, and creep strength are required to withstand the loadings imposed on it. Specifically, to meet the needs of the hot components in aero-engines, nickel-base superalloys are mostly used as raw material for the fabrication of gas turbine components. Due to their excellent mechanical strength, corrosion and oxidation resistance at elevated temperatures **[1-3]** given primarily by the precipitation strengthening by γ′ and γ" precipitates, and carbides. Unlike other nickel-based superalloys, Inconel 718 (IN 718) has a high resistance to strain age cracking during welding or post-weld heat treatment **[4]**. IN 718 is a γ" precipitation-hardened nickel-based superalloy **[5]**. The superalloy has been the workhorse in the jet gas turbine field for the past 60 years and accounts for a significant portion of superalloy production and usage **[6]**. IN 718 has found use in high-temperature applications, such as turbine disks, blades, cases, tubes, fasteners, stators, seals, shafts, space shuttle rocket engines, and compressors due to its excellent corrosion resistance and mechanical strength at high temperatures (up to 650˚C) **[7-9]**. In order to meet the ever increasing demand for superior engine efficiency, both advanced processing techniques and alloy designs are the most important factors. However, to increase the turbine efficiency, the geometrical complexity of the engines has to be increased. Previously, the parts are fabricated by various casting processes as a single component. Fabrication of a single cast component has generally poorer properties and inhomogeneous microstructure **[10]**. Therefore, it is often necessary to fabricate engine components in smaller parts and joined together by an appropriate bonding technique. The fabrication techniques used to produce the components affect the life of the IN 718 components.

Introduction

Moreover, as the aero-engine components undergoes through high creep and fatigue loading at severe operating conditions, the degradation of engine components is often observed. Economic necessity requires refurbishment and repairing of the parts rather than complete replacement of expensive service-damaged components. Numerous procedures for joining turbine components have been developed in the past; these include fusion welding (tungsten inert gas (TIG) welding, plasma arc welding (PAW), electron beam welding (EBW), and laser beam welding (LBW)) **[8-9]**, conventional brazing **[11]**, and solid-state diffusion bonding [12]. However, considering the welding aspects, IN 718 has disadvantages mainly: (i) poor weld penetration (ii) micro-fissuring in the heat-affected zone (HAZ), and (iii) poor ductility and impact resistance at the weld fusion zone **[13, 14]**. The difficulty of obtaining good penetration with root pass during welding of IN 718 is attributable to the poor fluidity of the molten IN 718 superalloy. The root penetration can be improved by anyone or combinations of the following factors: (a) proper shielding gas like helium, (b) preparing U-groove weld geometry, (c) higher root gap, and (d) high heat inputs. However, these factors have their own limitations. Using helium as a shielding gas increases the manufacturing cost. Preparation of U-groove weld geometry for IN 718 is difficult and expensive. High heat input results in burn-through problems. The second disadvantage during fusion welding (like TIG, PAW, and LBW) of IN 718 is the formation of micro-fissures, which are fine cracks, usually around 1 or 2 grains in length, that form in the HAZ of the weld adjacent to the fusion zone. These cracks are intergranular and seem to form along the boundaries of the partially melted grains close to the fusion zone. The HAZ cracking has been primarily attributed to the constitutional liquation of NbC, and the formation of a low melting laves eutectic in the inter-dendritic regions. These eutectics solidify at a much lower temperature than the solidus temperature of the bulk alloy **[15-18]**. Though the micro-fissures can be decreased to a great extent by solution heat treatment and low heat inputs, they cannot be completely eliminated **[19-21]**. Fusion welding (like TIG, PAW, and LBW) has its constraint in welding high-strength superalloys, particularly those containing higher gamma primer formers (Al+Ti) since they are highly susceptible to hot cracking in the weld metal and HAZ, and strain-age cracking in HAZ **[22-26]**. Poor weldability of most high-strength precipitation-hardened superalloys requires pre and post-heating or the use of more compliant weld filler materials

with lower strength than the parent metals, restricting the repairs to low stress areas such as the blade tips. Lack of accessibility (TIG and PAW) also limits the use of fusion welding.

For newer generation airfoils, which have much thinner gauge sections and more sophisticated cooling systems, welding becomes impractical due to heavy distortion and the possibility of blocking cooling holes. Another fusion welding process frequently used to join superalloy is electron beam welding. But the main disadvantage of the process is that it is very costly and requires a vacuum chamber for processing. To avoid liquation cracking, the brazing process is applied to join the superalloy. The eutectic formed during brazing deteriorates the high-temperature properties of the bond. So researchers tried to join the material by solid-state joining processes, like solid-state diffusion bonding and inertia friction welding. High pressure requirement during the solid-state joining process creates residual stress in the bond area. Which creates cracking in the bond area. The poor impact and ductility properties of the IN 718 weldments are due to the presence of Lave phases in the inter-dendritic region of the weld metals. The Lave phase is considered to be the main factor for the embrittlement of weldments. This can be overcome to a great extent by high-temperature post-weld solution treatment **[27]**. However, the full dissolution of the Lave phase is not achieved yet. The facts mentioned above are considered as serious drawbacks of IN 718 components joined by conventional fusion welding techniques, especially for use in critical applications **[28]**.

In order to overcome these problems, the transient liquid phase (TLP) bonding **[29]** process was introduced by a few researchers. Taking the advantage of solid-state diffusion bonding and brazing this new viable alternate technique for joining difficult-to-weld superalloys was developed. In TLP bonding process an interlayer containing a melting point depressant element such as boron (B), silicon (Si), or phosphorous (P), is kept between the substrate and heated to above the melting temperature of the interlayer and held for sufficient time. Subsequent to the melting of the interlayer, dissolution of the base material occurs, which results in the widening of the liquid zone. The solid and liquid phase attains equilibrium at the interface and inter-diffusion of the alloying elements between the liquid interlayer and base material results in an increase in the liquidus point of the liquid phase at the interface and as a result, isothermal solidification begins. As isothermal solidification

progresses, the width of the liquid reduces and the solid-liquid interface moves toward the center of the joint. If the assembly is held for sufficient time, complete isothermal solidification of the liquid occurs, and further holding at elevated temperature results in homogenization of the joint with the base metal. However, if the holding time is not sufficient, the residual liquid present at the joint transforms into eutectic-type brittle phases, which may reduce the mechanical properties of the bond **[30]**. The main advantage of the process is that the joint obtained a uniform microstructure and which is similar to the base material. The mechanical properties of the bond are nearly equal to that of the base material. And the melting temperature of the bond is higher than the bonding temperature. An important factor in the consideration of TLP bonding for commercial applications is the bonding time required to complete the isothermal solidification, which is essential to inhibit the formation of deleterious brittle eutectic phases.

1.2 Motivation

Several studies have been carried out in the past on the joining of wrought and cast IN 718 via transient liquid phase bonding. Previous studies have shown that the amount of eutectic formation in the bond area, is highly influenced by process parameters (bonding temperature, time, pressure, and interlayer) and metallurgical factors. These eutectics have a detrimental effect on the mechanical and microstructural properties of the bond. Eutectic formation can be avoided by selecting proper interlayer material (with suitable composition) and holding the bond at a higher temperature for a sufficient amount of time. It may take hours to a few days **[31-33]**. Currently, TLP bonding research involves investigation on the influence of process parameters on the microstructural and mechanical properties evaluation of the bond. There is limited information on proper interlayer selection procedures, ways to reduce the isothermal solidification time, and methods to improve the bond quality.

It is prudent to apply proven effective joining techniques in safety demanding industries, like the aerospace industry. The lack of a database on TLP bonding of IN 718 motivated this research to investigate and gain more understanding of the process. The present study investigates the influence of process parameters such as bonding temperature, holding time, and interlayer types on the isothermal solidification time of TLP bonding of IN 718, and to determine the kinetics of the TLP bonding of IN 718 to reduce the isothermal

solidification time. Also, implementation of various post-bond heat treatment techniques to improve the room temperature and high-temperature properties of the TLP bonding. There is also a need to develop a suitable interlayer to join the material.

1.3 Research Objectives

Based on the research gap found in the published research work, the objectives of the present work are summarized as follows:

- Study the kinetics of the TLP bonding for the determination of isothermal solidification time.
- Improvement of mechanical and metallurgical properties of the TLP bond by designing a post-bond heat treatment technique.
- Study the effect of the homogenization stage of TLP bonding on the microstructure and mechanical properties of the joint.
- Investigation of high-temperature tensile properties and high cycle fatigue properties of TLP bonded IN 718 joint.
- Study the surface residual stress profile of TLP bonded IN 718 joint.
- Design and synthesize an interlayer material for TLP bonding of Inconel 718.

1.4 Contribution of the Thesis

The important contributions of this research work are summarized as follows:

- A detailed experimental investigation is carried out to evaluate the influence of process parameters on the bond properties of the TLP bonded IN 718 joint.
- The influence of the homogenization stage on the microstructure and mechanical properties of the TLP bond is investigated.
- The kinetics of the TLP bonded sample is determined by the differential scanning calorimetry (DSC) technique.
- Post-bond heat treatment is designed to improve the room temperature and elevated temperature bond quality of the TLP bonded samples.
- The Fatigue life of the TLP bonded sample is determined.
- The effect of residual stress in the TLP bonded sample is studied.

- A new Ni-Cr-Fe-B-Si base interlayer material is developed for TLP bonding of IN 718.

1.5 Outlines of the Thesis

The contents of the thesis focus on the TLP bonding of IN 718 superalloy. It covers the effects of process parameters on the mechanical and microstructural properties of the TLP bonded IN 718 joint. The kinetics of the TLP bonded IN 718 joint is studied by DSC. The presence of residual stress in the TLP bonded sample is analyzed and the fatigue life of the TLP bonded IN 718 joint is determined. A new interlayer is developed and compared with the commercially available interlayer. The principal aim of the work is to improve the mechanical properties and microstructure of the TLP bond and predict the kinetics of the TLP bonding of IN 718.

The contents of the thesis are divided into five chapters and they are as follows:

Chapter 1 provides a general introduction and brief background of Ni-base superalloy.

Chapter 2 has been devoted to giving a brief literature review on the various techniques used to join IN 718 superalloy. And the evolution of the TLP bonding technique to overcome the limitation of fusion welding and brazing processes. It also described briefly the effect of process parameters on the mechanical and microstructural properties of TLP-bonded joints and research work in the area of TLP bonding of IN 718.

Chapter 3 elaborates on the procedures, methods, or techniques implemented for conducting the TLP bonding experiments. This chapter also outlines different techniques used for analyzing and testing experimental specimens.

Chapter 4 presents the results and discussion of the experiments. It describes the effect of process parameters like temperature, time, pressure, and thickness on bond quality. It also highlights the influence of TLP bonding on the fatigue life of the joint.

Chapter 5 displays the concise conclusions of the research work with relevant future scope of work.

Finally, the thesis is ended with a list of references.

Chapter 2
Literature Review

2.1 Introduction

The nickel-based superalloys have been extensively used to fabricate hot section components of aero-engines as these components are subjected to severe fatigue, creep, and oxidation service conditions. The joining of Ni-based superalloys draw significant attention among researchers in the field of superalloy joining across the globe to improve the efficiency of the aero-engines. Out of various joining techniques, TLP bonding is a comparatively new bonding technique that was developed from diffusion bonding and brazing to fabricate components with high strength in difficult-to-weld superalloys for critical applications. This bonding technique has gained immense exposure with the advantages of joining difficult to weld superalloys and being free from defects that are inevitable in brazing and fusion welding processes. This technique has been explored to join various materials like GTD-111 **[34-36]**, IN 718 **[37, 38]**, IN 600 **[39]**, IN 617 **[40]**, Waspaloy **[41],** IN **625 [42, 43]**, and IN 738 **[44-46].** Not only similar materials, but dissimilar materials have also been successfuly joined using TLP bonding **[47-51]**.

An extensive literature survey of the available published literature is carried out with the intention to find out the research gaps and sorting out the objectives with different approaches to enhance the mechanical and metallurgical properties of the TLP bond. This chapter is sub-divided into different sections and subsections to highlight the major findings of the reviewed literature. The literature review has been divided into nine different sections.

- Section 2.2 explores the Ni-base superalloys and their microstructure.
- Section 2.3 discusses various joining methods implemented for joining Ni-base superalloys and their limitations.
- Section 2.4 highlights the historical background of the development of TLP bonding
- Section 2.5 describes the TLP bonding process, mechanism, and kinetics of the TLP bonding.

- Section 2.6 reviews the critical process parameters and their combined effects on the TLP bonding.
- Section 2.7 describes different variant of the TLP bonding process.
- Section 2.8 discusses various analytical and numerical modelling techniques used in TLP bonding process.
- Section 2.9 finally presents the major research gap realized from the reviewed literature, followed by the objectives of the thesis in the Section 2.10.

2.2 Ni-Base Superalloys

Ni-based superalloy was developed with an aim to increase the thermal efficiency of aero-engines by increasing the service temperature **[52]**. The high mechanical strength, and corrosion and oxidation resistance at elevated temperatures allow these alloys to be used extensively in gas turbines, nuclear power plant components, and petrochemical components **[53]**. Moreover, the Ni-based superalloys mostly exhibit consistent microstructure stability at higher temperatures. From room temperatures to the melting point, Ni is stable in face-centered-cubic (FCC) crystal structure. Therefore, no phase transformation occurs for Ni at high temperatures, and hence there are no complications of significant expansion and contraction at higher temperatures. However, except IN 718, almost all other Ni-base superalloys are susceptible to post-weld strain-age cracking. The sluggish aging response of IN 718 superalloys prevents it from strain-age cracking problems. The advantage of the sluggish aging response of IN 718 was first recognized by a metallurgist at General Electric-Evandale **[54]**. The lack of strain-age cracking in IN 718 superalloys enhances the weldability of the age-hardenable nickel-based superalloys. Due to the high weldability of IN 718, it is widely used in aerospace industries compared to other Ni-based superalloys **[55]**. IN 718 is extensively used in aircraft gas turbines components (e.g. blades, vanes, shafts, exhaust systems, disks, casings, combustion chamber, burners, cans, stack gas re-heaters, etc.) **[56]**, space vehicles (e.g. rocket engine parts and aerodynamically heated skins) **[57]**, chemical and petrochemical industries **[58]**, nuclear power plants, and heat exchangers **[59]**.

2.2.1 Microstructural phases in IN 718

Generally, IN 718 contains up to eight different alloying elements, viz., nickel (Ni), chromium (Cr), iron (Fe), titanium (Ti), aluminum (Al), tantalum (Ta), niobium (Nb), molybdenum (Mo), and minor amounts of carbon (C), zirconium (Zr), silicon (Si), and boron (B) **[60]**. IN 718 has different phases which can be identified by characteristic morphology or temperature of formation if the thermal history of the alloy is known **[61]**. The phases normally found in the γ matrix of IN 718 are disk-shaped γ" (Ni_3Nb), spheroidal γ' (Ni_3Al, Ti), needle/plate-like δ phase, discrete metal-carbide (MC) particles, and round, island-like Laves phase **[62-64]**, which are shown in **Fig. 2.1**. The major strengthening phases are the γ" and γ' phases, which strengthen the alloy by producing coherency strains in the γ matrix **[65]**. The alloy is known to have exceptionally high strength from cryogenic to intermediate temperatures, considering the relatively low volume fraction of the strengthening precipitates and their sluggish precipitation kinetics **[66, 67]**. The details of various phases are described in the following sub-sections.

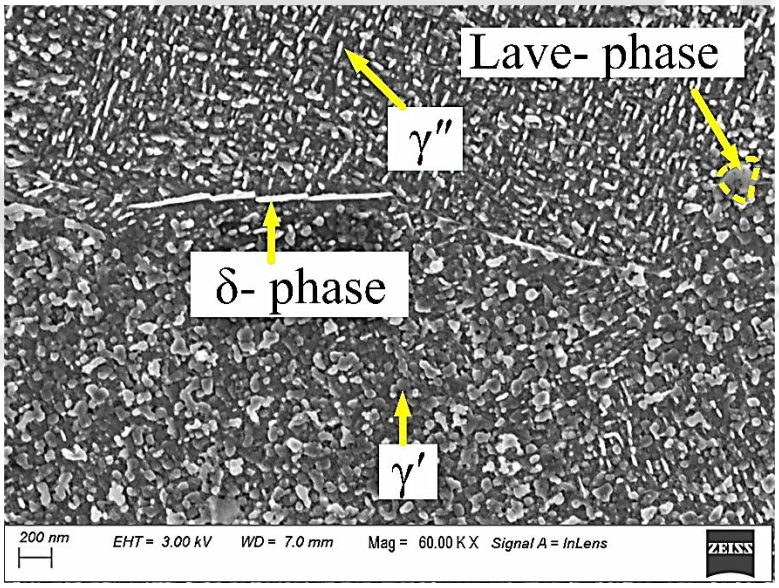

Fig. 2.1 Various phases in IN 718 superalloy

2.2.2 Gamma matrix (γ)

IN 718 is made of FCC nickel-based austenitic matrix phase called as gamma (γ), which contains alloying elements, such as Ni, Cr, Fe, and Mo **[68]**. The γ matrix is a base on which the other phases are formed.

2.2.3 Gamma double prime (γ") phase

The metastable γ" phase is the principal strengthening phase in IN 718 since its body-centered tetragonal (BCT) crystal lattice structure offers a higher coherency strain than γ' **[69]**. The γ" is a DO2 ordered Ni_3Nb phase with a lattice parameter ratio c/a =2.04 and it strengthens the alloy due to strains that arise from the tetragonal distortion of its lattice, which is a mismatch with the FCC γ matrix **[70, 71]**. The precipitation of the γ" phase bestows a fully strengthened microstructure and acceptable ductility. During isothermal aging, γ" is precipitated at a temperature range of approximately 704 °C – 899 °C with a peak at 760 °C for the shortest time of 7 minutes **[72,73]**. Upon ingot solidification, γ" is precipitated in the alloy within the cooling temperature range of 815 °C – 704 °C **[74]**. IN 718 is stable at 600 °C during long thermal exposure, but deterioration of its creep and tensile strengths can occur at higher temperatures due to **[75]**:

- Rapid coarsening of the γ" phase at the range of 640 – 760 °C and possible loss of coherency
- Coarsening and partial dissolution of γ" and γ' above 760 °C decreases the volume fraction of these precipitates
- The accompanied transformation of metastable γ" and γ' to stable δ above 843 °C

2.2.4 Gamma prime (γ') phase

The γ' phase (Ni_3 (Al, Ti)) is the secondary strengthening phase in IN 718 **[76]**. The γ' is an L12 ordered intermetallic compound with an FCC crystal structure. It also produces a coherency strain with the matrix and is richer in Al than γ". Upon ingot solidification, the precipitation of γ' occurs below 704 °C and during isothermal aging from 593 °C – 704 °C **[77]**. It has been suggested that the solvus temperature for γ' in IN 718 is between 843– 871 °C **[78]**. Its shape is related to the matrix-lattice mismatch. Hagel and Beattie **[79]** observed

that the γ' phase appears as a sphere at a 0.2 % lattice mismatch, becomes cubes at lattice mismatch around 0.5 %-1.0 %, and then is in plate form at mismatch above approximately 1.25 %.

2.2.5 Delta (δ) phase

The equilibrium δ phase is a stable, Ni_3Nb, intermetallic with an orthorhombic (DOa ordered) crystal structure **[80]**. The δ phase is sometimes considered undesirable because it is incoherent with the γ matrix and therefore, is not an effective strengthener **[81]**. The approximate range of temperatures in which the δ phase precipitates is 843 °C - 982 °C **[82]** in the form of platelets and its precipitation precedes the γ" and γ' phases at temperatures below 900 °C **[83]**. The δ phase precipitates on grain boundaries (inter-granularly), twin boundaries and intra-granularly in association with stacking faults located within pre-existing γ" or Laves phase particles **[84]**. The maximum precipitation rate of the δ phase is achieved at 900 °C **[83]**. In the absence of other grain boundary particles, such as carbides, the alternative nucleation of the δ phase in a uniform manner effectively controls and refines grain size, which affects material strength and ductility **[85]**. The presence of globular δ phase at grain boundary inhibits long-range grain boundary sliding. The dissolution temperature range of the δ phase is 925 °C -1010 °C.

2.2.6 Laves phase

The brittle, topologically close pack (TCP) Laves phase can be represented as A_2B, where "A" atoms are primarily Ni, Fe, and Cr, and the "B" atoms are typically Nb, Mo, and Ti, i.e. $(Fe,Ni,Cr)_2$ (Nb, Mo, Ti) **[86]**. This phase forms as a result of the segregation of "B" atoms into the liquid region (inter-dendritic) in between solidified material (dendrite) during cast solidification **[87]**. Therefore, the Laves phase, like carbides, is a terminal solidification product formed on the grain boundary of IN 718 **[88]**. This phase is detrimental to fatigue properties as well as the weldability of IN 718 **[89, 90]**. The Laves phase and Nb-rich MC carbides precipitate within a cooling temperature range of about 1260 °C – 1093 °C during solidification **[91]**. The amount of the Laves phase in cast IN 718 can be used as an indicator of the degree of alloying elements homogeneity in IN 718 **[92]**.

2.2.7 Carbides

Refractory and reactive elements like Nb and Ti, combine with carbon and nitrogen (N) to form MC or carbo-nitride phase particles **[93]**. The carbides exhibit an FCC crystal structure and are promoted by the strong tendency of the forming elements to segregate into the liquid phase during solidification, which causes carbide distribution typically along the inter-dendritic and solidification grain boundary regions i.e. localized areas that solidify last **[94, 95]**. The MC carbides and/or carbonitride can also be precipitated at grain boundaries during processing **[94]**. Their morphology is usually cubic, irregular or "Chinese script" shape. "Chinese script" morphology could suggest that the formation of MC carbide occurred by eutectic-type transformation during the later stage of solidification. The MC and titanium nitride (TiN) phases are considered stable at low temperatures. Their temperature stability is useful for grain refinement during processing and globular carbides prevent grain boundary sliding, which is beneficial for good rupture life and ductility. In IN 718, titanium carbide (TiC) has a higher stability temperature than NbC **[92, 94]**.

2.3 Joining Techniques for Nickel-Base Superalloys

The IN 718 superalloys are subjected to severe operating conditions during their service periods. With prolonged service periods, the parts experience severe functional degradation **[96]**. As specialized methods are used for the fabrication of these materials, the manufacture of components made of IN 718 is usually very expensive. Therefore, the complete replacement of damaged components may not be economical. Repairing and refurbishing the defective components are therefore desirable to replace them entirely **[97]**. As a result, a lot of effort has been placed into developing suitable and reliable techniques for joining and repairing Ni-base superalloy components. Conventionally, fusion welding and diffusion brazing are commonly used for joining and repairing IN 718 structural parts, which are discussed below.

2.3.1 Fusion welding of Ni-base superalloys

In fusion welding, two materials are joined through controlled melting by localized heating and subsequent cooling of the melted liquid. Arc, gas, and high-energy beam welding are the most common fusion welding processes that are used to join Ni-based superalloy **[60]**.

Among these welding processes, gas welding generates the maximum heat input and least power density. High heat input causes workpiece damage, whereas low heat input and high energy beam welding improve penetration and overall weld quality. The joint that requires multiple passes in arc welding processes, can be joined by a single pass in electron beam welding (EBW) with a high speed and a narrow heat-affected zone **[98, 99]**. However, the initial equipment cost of EBW is very high and requires a vacuum chamber and X-ray shielding. Fusion welding is generally used to join superalloy materials, however, its utility in Ni-based superalloys containing large amounts of Ti and Al is limited. The material containing a high amount of Ti and Al is susceptible to HAZ cracking during joining and subsequent heat treatment. Also, the rapid heating and cooling during fusion welding produce thermally-induced stresses and liquation of the grain boundaries, which result in inter-granular micro fissuring **[100]**. During post-weld heat treatment due to the combination of weld residual stresses and aging contraction, the cracks present in the weld may further increase. The Ni-base superalloy with a high volume of γ′ has weldability problems.

2.3.2 Brazing of Ni-base superalloys

In the aerospace industry, brazing techniques are extensively used to join Ni-base superalloys. In this joining method, a filler material is heated above 425˚C to join two metal surfaces. At the brazing temperature, the filler material melts and the resultant liquid reacts with the substrates and upon cooling solid bond is formed. The holding time in the conventional brazing technique is very less, therefore the extent of solid-state inter-diffusion is limited. In some brazing processes, like diffusion brazing, the sample is held for a longer time period so that a significant amount of diffusion of elements can take place. High-temperature brazing is generally used for the manufacture of Ni-base superalloy components. In this technique, an interlayer material is kept between the parts to be bonded and the assembly is heated to a temperature above the liquidus temperature of the interlayer material but less than the liquidus temperature of the base metal. The interlayer material used are usually in the form of paste, powder, foil, wire, or slugs **[101]**. The interlayer material commonly contains at least one melting point depressant (MPD) element like Si, B, and P to lower the melting temperature of the filler material. Elements like C, Al, and Ti are intentionally exempted from interlayer material in order to reduce the formation of undesired

stable eutectic phases in the joints. Various heating methods like induction heating, resistance heating, and oxy-fuel gas heating can be implemented to melt the filler material. To avoid contaminants from the atmosphere, it is necessary to conduct the brazing in a controlled atmosphere. The surface quality of the parts to be joined plays a very crucial role in the fabrication of a good quality joint. The presence of any residual oils, grease, or oxide contaminants may hinder the wetting of the base material by the liquid interlayer. Also, the presence of oxides at the solid/liquid interface can potentially act as a diffusion barrier. The surfaces to be joined should have adequate surface roughness so that the liquid filler wet the surface properly. Good flowability and low viscosity are also essential properties to improve the quality of the brazing joints **[102]**.

Although brazing has several advantages, such as complex and multi-component assemblies can be fabricated economically, it can join parts whose size and thickness varies widely, close tolerance joint can be achieved, and joints can be made rapidly and inexpensively. However, the mechanical and physical properties of the joint produced by the brazing technique, are inferior to that of the base metal properties due to the presence of the intermetallic eutectic compound at the brazed joint.

2.4 Transient Liquid Phase (TLP) Bonding

The TLP bonding was developed to overcome the limitation of the brazing and fusion welding processes *i.e.* formation of brittle eutectic phase in the brazement and hot cracking, respectively. TLP bonding is a joining technique that incorporates the advantageous features of solid-state diffusion bonding and liquid phase joining. It can be used to manufacture parts made of difficult-to-join heat-resistant alloys with a higher strength. In this technique an interlayer material containing at least one MPD element like P, Si, and B is used to join the alloys. When the assembly is heated to bonding temperature (*i.e*. below the melting temperature of base material but above the melting temperature of the interlayer material), the interlayer melts and inter-diffusion of elements takes place between the base material and the liquid interlayer. Inter-diffusion of elements results in the compositional change of the liquid and solid interfaces until equilibrium is achieved between these phases. Further inter-diffusion of the elements raises the melting point of the liquid at the interface, and isothermal solidification (IS) begins. Complete IS can be attained if the bond is held at the bonding

temperature for a sufficient time period before cooling the bond to the ambient temperature. Moreover, the assembly may need to hold at an elevated temperature, which should be below the bonding temperature, to homogenize the microstructure and composition of the bond zone. In TLP bonding, there is no plastic deformation involved in the joint, although some pressure is applied to confirm that intimate contact is achieved at the bonding interfaces **[103]**.

In contrast to brazing, as the TLP bonded joint has a similar microstructure and mechanical properties to that of the base material, the TLP bonding is more applicable for joining parts designed for service at high temperatures. TLP bonding can also be used to join similar and dissimilar alloys of different thicknesses and complex shapes and mass production of the components can significantly reduce production costs **[104, 105]**. As IS occurs in TLP bonding through solid-state diffusion, to accomplish complete IS, a longer bonding time may be required, which restricts the commercial application of this process. Eutectic-type phases are formed at the bond area due to incomplete IS. These eutectic phases are brittle in nature. These particles act as the sites of crack initiation and easy path for crack propagation. Due to the diffusion of the MPD into the base material, second-phase particles precipitate near the bond interface which may also have detrimental effects on the mechanical properties of the joint. Poor bonding atmosphere, inadequate or improper surface preparation may result in poor bond properties similar to the case of brazing.

2.4.1 Historical development of TLP bonding

A comprehensive description of the development of diffusion-induced joining processes has been provided by MacDonald and Eagar **[106]**. History describes that back in 2500 BC King Tutankhamen's gold dagger was fabricated using a transient interlayer technology **[107]**. In ancient times, Etruscan art used to join gold beads to gold articles using similar technology, they called it as granulation. The granulation process has been cited for centuries like Mappae Clavicula in the eighth century **[106, 107]** and Theophilus in the twelfth century **[108]**. An Italian goldsmith Benvenuto Cellini **[109]**, used to join small gold balls onto a gold article using a copper oxide paint interlayer. He used to heat the assembly using a reducing flame and holds it at that temperature for some time so that a homogenized diffusion bonded joint is produced through the eutectic reaction between the copper and gold. The trace of copper oxide after the bond is invisible. With the advancement of technologies in modern

era, the use of the granulation technique was disappeared till it was reinvented by Littledale and Wilm and Treskow **[107, 109]**. In the modern granulation technique, the surface of the component to be bonded is covered with a mixture of fish glue and metallic oxide. On heating the assembly, the fish glue reduces the oxide and through an in-situ reaction between the base material and the metallic component a liquid produced between the surfaces. As a result of this reaction, a bond is obtained through the diffusion of elements. During ancient times, isomorphous and azeotropic system were applied to produce a transient liquid interlayer; however, binary eutectic alloy systems are used in modern applications to produce the liquid interlayer **[106, 110]**. In recent research **[111]**, efforts were mainly focused on the joining of high-temperature materials such as nickel-based superalloys, titanium and single crystal, and small scale joining applications such as microelectronics and medical implant devices instead of decorative jewelry. People have been using a different naming convention for the transient liquid phase bonding process. Lynch et al. **[106]** used a nickel-copper interlayer to join titanium and referred to this technique as 'eutectic brazing'.Owczarski et al. **[112]** joined 304 stainless steel to Zircaloy 2 through in-situ reaction and termed this process as 'eutectic bonding'. Bernstein and Bartholomew **[113]**, made bonds on electrical components using the ternary Ag-In-Sn system and called the bond as 'solid-liquid inter-diffusion bonding'. In this technique, the bond was produced at a lower temperature and hold at a high temperature to produce a joint with homogenized components. Liquid interface diffusion was developed to bond honeycomb sandwich structures using Cu-Ni interlayers **[114]**.

During the 1970s TLP bonding was introduced in the aerospace industries by Hoppin and Berry of General Electric Aircraft Engine Group to join René 80 superalloy through an activated diffusion bonding technique using a Ni-based eutectic interlayer **[115]**. Wells and Mikus **[116]**, joined titanium structural parts using an electrolytically deposited copper interlayer material. They used a resistance heating system to melt the interlayer. Niemann and Garrett **[117]** of MacDonnell Douglas joined aluminum-boron composites by a eutectic bonding technique. They successfully joined aluminum-boron composites using Cu interlayer. A group at Pratt and Whitney in the year 1974 coined and copyrighted the term 'transient liquid phase' (TLP) bonding. Duvall et al. **[118]**, bonded Udimet 700 through TLP bonding using a Ni-Co interlayer and later observed that in most of the superalloys the bond properties are similar to the base material properties. There are a few more variations of the TLP bonding

method that have their own names, viz.; transient insert metal bonding' which was developed by Nakao et al. **[119]**, later they modified the process by using powder interlayer and named it wide-gap TLP bonding, and temperature gradient transient liquid phase' (TG-TLP) bonding, where a temperature difference is imposed between two surfaces to reduce the time of the IS stage. Therefore, it is very confusing to have a single nomenclature of this process and all of its variants. The American Welding Society (AWS) named this process 'diffusion brazing' **[120]**; however, the most widely recognized name is 'TLP bonding'.

2.5 Process Description

The TLP bonding has been described extensively by several researchers. Duvall et al. **[118]** described the solidification mechanism of the TLP bonding process by dividing the whole process into five steps. The stages are: (i) heating to the bonding temperature and subsequent melting of the interlayer, (ii) dissolution of the base metal by the liquid interlayer, (iii) isothermal solidification, (iv) completion of isothermal solidification, and (v) homogenization to dissolve eutectic phase at joint center. Zhou et al. **[105]** reduced the description stated by Duvall et al. **[118]** to three distinct stages such as (i) base metal dissolution, (ii) isothermal solidification, and (iii) homogenization. Tuah-Poku et al. **[121]** divided the base metal dissolution stage into two stages: (i) dissolution of the interlayer, and (ii) homogenization of the liquid by base metal dissolution.

To account for the heating time from room temperature to time just before liquation of the interlayer, MacDonald and Eagar **[106]** included an initial stage called it as stage 0. This is in response to the loss of solute in the interlayer during heating of the bond described by Niemann and Garrett **[117]** during TLP bonding of Al-B using a Cu interlayer. They observed that if the heating rate is very slow, insufficient liquid forms at the bond interface due to diffusion of solute into the base metal. According to MacDonald and Eagar **[106]**, TLP bonding process is divided into five stages such as; (i) heating stage, (ii) dissolution of base material, (iii) widening of liquid interlayer, (iv) isothermal solidification, and (v) homogenization. Finally, Zhou et al. **[105]** reclassified TLP bonding into four distinct stages, they consider stage 0 of MacDonald and Eagar as stage 1, combined stage 1 and stage 2 into one stage i.e.; dissolution and widening stage, which is further subdivided into stage 2-I (heating from melting point to bonding temperature) and stage 2-II (isothermal dissolution at

the bonding temperature). Stages 3 and 4 are remained same as IS and homogenization, respectively. In this thesis, the classification prescribed by Zhou et al. **[105]** is followed.

2.5.1 Initial conditions

Initially, a thin interlayer containing an MPD solute is placed between the surfaces of the metal to be joined and pressure is applied to bring intimate contact between the faying surfaces. The interlayer can be added in the form of a thin foil, a powder, a coating, or a paste. The liquefaction of the interlayer can be attained by either with an in-situ reaction of interlayer with the base material or a eutectic reaction at the eutectic temperature. MacDonald et al. **[106]** classified the different variants of the interlayer on the basis of liquefaction mechanism: the type-I interlayer, which uses a pure metal as interlayer material and the in-situ reaction of the metal with the base material forms liquid at the interface; whereas in the type-II interlayer, with composition is near to the eutectic point at the bonding temperature is considered **[106, 123]**. For eutectic system as shown in **Fig. 2.2**, the bulk constituents of the interlayer can be altered to melt at the eutectic temperature. This can reduce the overall bonding time of TLP bonding by decreasing the volume of the solute to be diffused from the liquid interlayer. The interlayer has a great effect on the process kinetics of different stages in the TLP bonding. Therefore, the initial thickness (W_o) and the initial composition $C_{L\alpha}$, given as the compositional fraction of B, where element B is the MPD solute, are two major concerns during the selection of the interlayer material. **Figure 2.2** displays the initial composition profile of solute across the TLP bond assembly in the special type-II case of a eutectic interlayer. The type-I case of a pure interlayer will be discussed in Section 2.5.2. The TLP bonding process has been broken down into four distinct stages **[106, 121,122]**. These four stages are (1) heating (2) dissolution and widening (3) isothermal solidification and (4) homogenization. Each of these stages has been examined in detail in the following sub-sections.

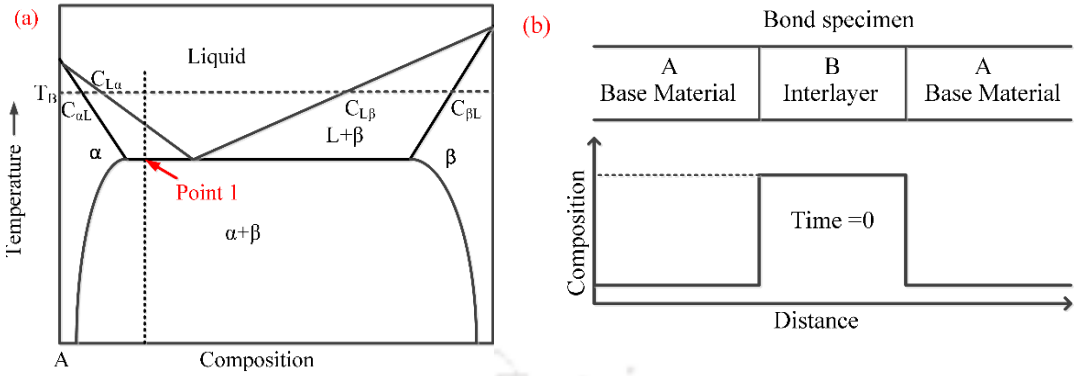

Fig. 2.2 (a) Schematic of eutectic type interlayer and (b) and compositional profile of TLP bond

2.5.2 Type-I interlayer

In the case of type-I (pure) interlayer, due to diffusion of elements eutectic composition is achieved in some areas, which initiates the melting of the base material and the interlayer interface **[123]**. The liquid will grow from each interface through the dissolution of both the base metal and the interlayer. Dissolution is completed when the entire interlayer has been consumed by the liquid phase. In this type of interlayer, the time required for complete dissolution depends upon the initial width of the interlayer, solute diffusivity, and initial composition of the interlayer. Therefore, for a thick interlayer, the time required for complete dissolution is longer. In the case of type-II interlayer, the dissolution process is instantaneous and the time required for dissolution is less compared to the type-I interlayer. Tuah-Poku et al. **[121]** observed the dissolution process in TLP bonding of Ag (bond made at 820 °C using 80 μm Cu interlayer) and found that the dissolution stage (i.e. stage 2-I) was completed in a fraction of seconds, whereas the widening stage (i.e. stage 2-II) required times in the order of minutes. After 20 minutes of the widening stage, the width of the liquid was increased from 79 μm to 420 μm.

2.5.3 Heating stage

During the heating stage, the entire assembly is heated from room temperature to just below the eutectic temperature of the interlayer material, shown in point 1 in the **Fig. 2.2 (a)**. The heating can be performed in an inert atmosphere or vacuum to protect the bond from oxidation at elevated temperatures. In this stage, some solid-state inter-diffusion occurs

between the base material and interlayer. The volume of the inter-diffusion depends upon the surface roughness, and holding pressure exerted normally to the interface. The pressure and surface roughness ensure more contact between the faying surfaces. The extent of inter-diffusion depends upon the heating rate, eutectic temperature, and diffusivity of the elements. However, in most cases, the magnitude of mass transfer during the heating stage is very small **[106,121, 123]**. The typical diagram of the heating stage is presented in **Fig. 2.3**. If the heating rate is very slow, diffusion of the solute (MPD) from the interlayer into the base material is increased, which decreases the solute concentration at the interface and as a result less liquid is available to wet the material **[106]**. Li et al. **[124]** joined alumina metal matrix composites using a copper interlayer. They investigated the effect of heating rate on bond quality and found that decreasing the heating rate from 5 to 1 K/s resulted in a need to increase the interlayer thickness from 0.6 to 2 μm to achieve acceptable bonds quality. Hence, it is important to control the heating rate during the heating stage of TLP bonding.

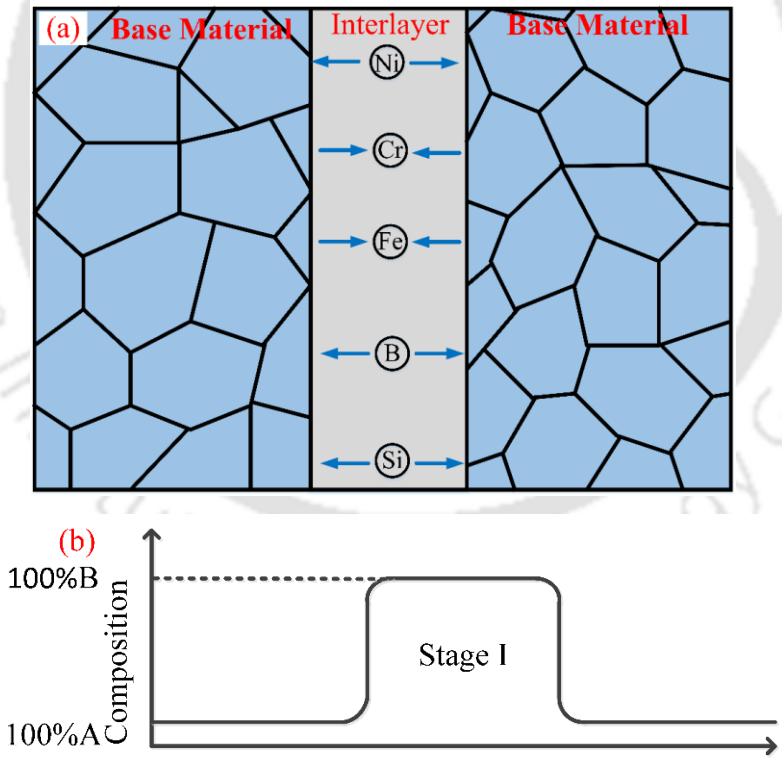

Fig. 2.3 (a) Schematic diagram of heating stage of TLP bonding and (b) compositional profile

2.5.4 Dissolution and widening stage

When the assembly is further heated and the temperature pasts the eutectic temperature, the interlayer melts and wets the base material at the interface. Referring to the binary phase diagram schematic in **Fig. 2.2**, shows that the composition of the liquid just above point 1 is eutectic composition and the composition of the solid at the solid/liquid interface is at the limit of solid solubility. Due to the inter-diffusion of the elements, the composition of the solid at the solid/liquid interface increases and achieves eutectic composition. As a result, the base material dissolves and causes the widening of the liquid zone. **Figure 2.4 (b)** shows that when the temperature is increased above point 1, the equilibrium composition of both the solid and the liquid at the interface move along the liquidus and solidus phase boundaries, respectively.

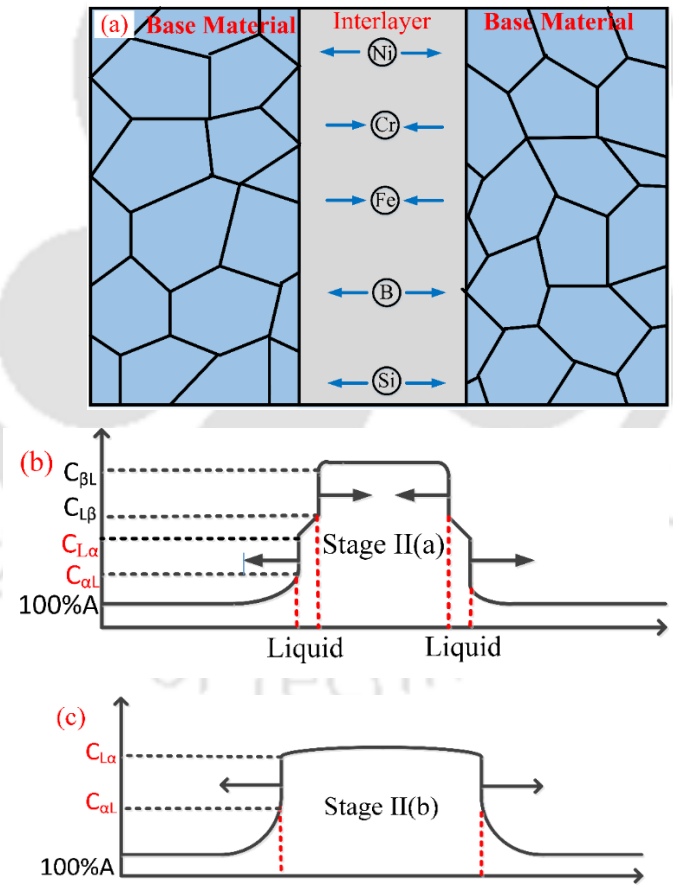

Fig. 2.4 (a) Schematic diagram of dissolution and widening stage of TLP bonding, (b) dissolution of base material (c) fully widened liquid

To retain equilibrium at the liquid/solid interface, the base metal is dissolved by the liquid resulting in a widening of the liquid zone due to the conservation of solute mass. Since the diffusion of MPD in the liquid-phase is quite fast, the MPD solute quickly moves across the liquid to the solid/liquid interface, where the base metal is rapidly dissolved. The maximum width of the liquid is achieved at bonding temperature, where the liquid composition is $C_{L\alpha}$, as shown in **Fig. 2.4 (c)**. The kinetics of dissolution depends on the diffusivity of MPD in the base material and heating rate such that the widening of the liquid is continued sometime after the bonding temperature is reached and until a steady state is achieved following the equilibrium phase diagram schematic as shown in **Fig. 2.4 [106]**.

2.5.5 Isothermal solidification stage

After achieving maximum width during the dissolution and widening stage, MPD solute diffuse across the solid/liquid interface into the base material and the IS stage initiates. This diffusion process is similar to the two-phase diffusion couple. During isothermal holding to maintain the equilibrium phase diagram, the liquid and solid composition at the interface must be constant i.e. CLα and CαL, respectively **[105, 106, 123]**. Since the diffusion of solute in the liquid phase is very fast, the composition of the liquid is assumed to be uniform across the liquid **[105, 125]**. Ensuring mass balance at each liquid / solid interface, the interface progresses toward bond centerline. The interfacial motion is shown schematically in **Fig. 2.5 (a-b)**. In isothermal solidification, the mechanism of movement of the interface is epitaxial growth of the solid phase into the liquid. The complete IS stage is achieved when the two interfaces meet at the bond centerline and there is no residual liquid at the interface. The compositional profile after completion of IS is shown in **Fig. 2.5 (c)**. The velocity of the interfacial motion depends on the diffusivity of the solute in the base material, the miscibility gap between CαL and CLα, the initial width of the liquid zone, and the concentration gradient of the solute in the base material.

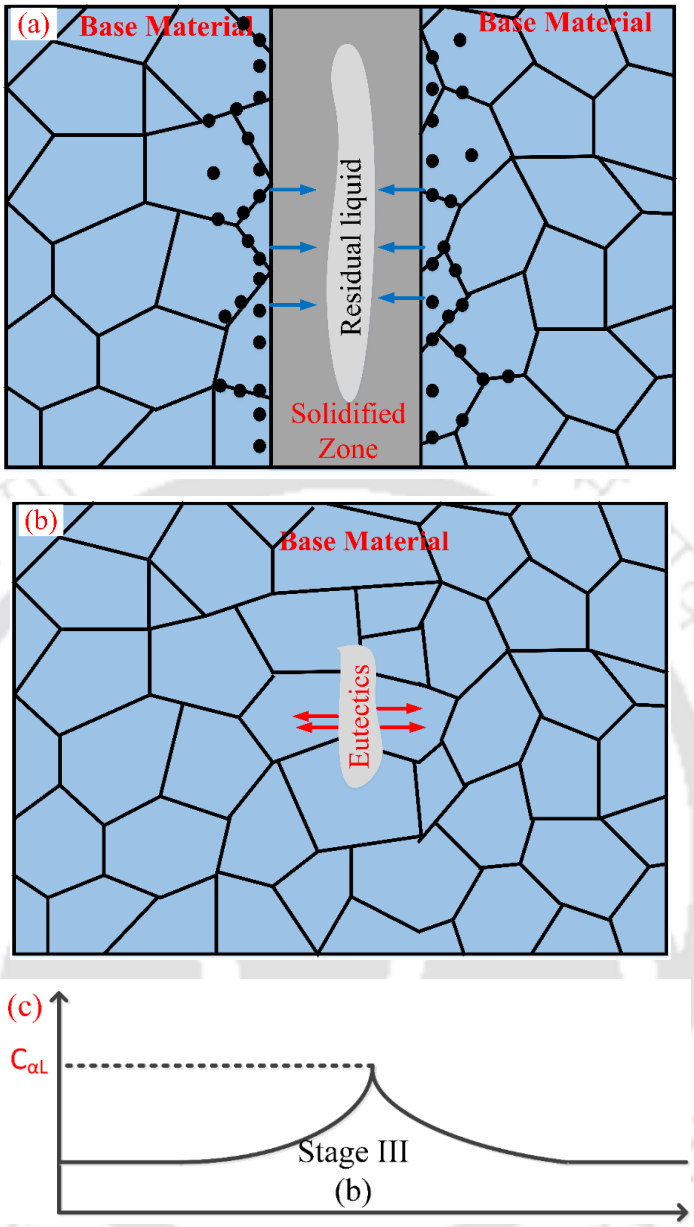

Fig. 2.5 (a) Schematic diagram of IS stage, (b) residual liquid forms to eutectic compound and (c) compositional profile of IS zone

2.5.6 Homogenization stage

After completion of isothermal solidification, there will be a peak of solute at the solidus composition (CαL) along the joint centerline, shown by the profile in **Fig. 2.6 (a-b)**. To reduce the peak height, the bond is held at an elevated temperature so that the magnitude is reduced by diffusion. This homogenization of the joint continues until an acceptable level

of solute remains. The acceptable level depends on the material and the application. However, it should be below the concentration at which harmful phases will precipitate in the solid-state during cooling. Precipitates may degrade the mechanical properties of the bond **[126]**.

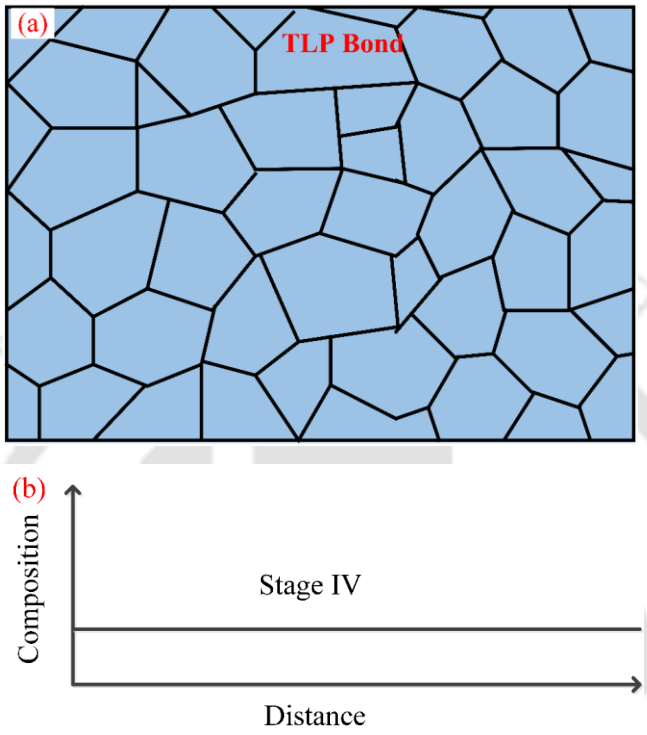

Fig. 2.6 (a) Schematic diagram of homogenization stage and (b) compositional profile

2.5.7 Critical stages in TLP bonding

The two most important stages in TLP bonding are IS and homogenization stages. The bond quality depends upon these two stages **[127]**, coincidently longer time period is required for the completion of these stages. If the solubility of MPD in the base material is low, a longer solidification time is required. Therefore, it is essential that the solidification stage should not be terminated before complete isothermal solidification. Cooling before the required time will lead to the rejection of solute from the residual liquid and the formation of segregated phases, which may degrade the properties of the bond. On the other hand, in some systems where the solubility is high, a longer homogenization stage is required for good bond quality. An inhomogeneous microstructure is formed if the homogenization stage is terminated before the completion of IS. Since the IS and homogenization stages depend on the diffusion of the solute

in the solid base metal, they are orders of magnitude longer than the heating or dissolution stages. Thus, it is appropriate that most of the attention given to the parameters that focuses on the time required for the completion of these stages.

2.5.8 Mechanism of isothermal solidification

Previous studies reported that the IS process in TLP bonding is epitaxial in nature **[125, 1128]**. In epitaxial solidification, nucleation of the solid phase starts from the existing solid surface and grows toward the liquid layer. The solidifying grains are derived from the grains of the base material **[128]** and the crystallographic orientation of the new grains is aligned with the base material grains. The heterogeneous growth of the grains during epitaxial solidification is governed by a balance of surface energy between base metal and liquid (γ_{ML}), solidifying metal and liquid (γ_{SL}), and solidifying metal (γ_{SM}) and base metal. In TLP bonding, the composition of the liquid is similar to the composition of base material, therefore a balance of the surface energies (**Equation 2.1**) can be simplified by the assumption of γ_{ML} = γ_{SL} and γ_{SM} = 0 **[128]**. From this, the wetting angle is found as φ = 0, and there is a negligible barrier to solidification at the solid/liquid interface.

$$\gamma_{ML} = \gamma_{SM} + \gamma_{SL} \times cos\varphi \qquad (2.1)$$

Pouranvari et al. **[129]** studied the microstructure–strength relationship in TLP bonding of IN 718 superalloy using BNi-2 amorphous interlayer. Bonding was carried out in a furnace at 1273, 1323 and 1373 K under a vacuum of approximately 10^{-5} Torr. Bonding time was varied from 1 to 60 minutes. With increasing bonding time and temperature, the size of ASZ decreased. Higher bonding time and temperature results in diffusion of more MPD elements into the base material. To explore the effect of bonding temperature (TB) and time (tB) on the progress of IS, a TLP bonding parameter was defined in the form of LMP = TB[C+ ln (tB)] based on the Larson– Miller parameters (LMP). A linear relationship between the LMP and IS zone size was observed in this investigation. With increasing LMP the shear strength of the bond increased. It was reported that solid solution strengthening mechanism plays important role in determining the hardness of the bond. Pouranvari et al. **[130]** also investigated solidification and solid state precipitation phase transformations during TLP bonding of IN 718 using Ni–4.5Si–3.2B ternary filler alloy. The bonding was performed in a

10^{-5} torr vacuum furnace at 1100 °C for 10 min. Optical micrographs showed a microstructural gradient in the bonding area. Three distinct zones were observed in the bond area, namely: Diffusion affected zone (DAZ), Athermal solidification zone (ASZ), Isothermal solidification zone (ISZ). It was reported that due to interdiffusion of the MPD and Cr, Fe, Nb, Mo, and Al IS occurred in the ISZ. And ASZ was formed due to cooling of the remaining liquid present in the bond-affected area. The solidification sequence of the unsolidified liquid in the joint centerline was found to be (1) proeutectic γ, followed by (2) γ/Ni_3B eutectic reaction, followed by (3) ternary eutectic of γ/Ni_3B/Ni_6Si_2B. The diffusion of boron from the interlayer into the BMZ induced Mo–Nb-Cr–rich boride precipitation, this resulted in local depletion of Nb Mo, and Cr, composition in the adjacent matrix that reduced corrosion resistance and the aging response of the alloy.

2.6 Critical Parameters in Optimizing the TLP Bonding

As previously discussed, the required time for the completion of IS and homogenization in TLP bonding processes is usually high due to the slow nature of solid-state diffusion. The time required for the completion of bonding is the most critical aspect of the TLP bonding process. The bond microstructure is another critical aspect of the TLP bonding process, it must be properly maintained in order to achieve desired physical and mechanical properties. In order to obtain good bond quality, some critical process parameters and material characteristics are optimized to attain the best combination of joining time and microstructure. In this section, these critical parameters of the TLP bonding are discussed.

2.6.1 Bonding temperature

The bonding temperature is one of the most essential process parameters in TLP bonding. The TLP bonding is a diffusion controlled process **[106, 123]** and the diffusivity of the solute in the base material plays a critical role in determining the time of completion of the isothermal solidification. Since the diffusivity of the solute increases asymptotically with temperature according to the Arrhenius equation, the diffusion rate of solute into the base material will increase with temperature. This could lead to the conclusion that raising the bonding temperature will enhance the rate of IS and reduce the time required for the completion of the joint **[131]**. However, by increasing the bonding temperature, the

concentration gradient at the solid/liquid interface decreases as can be seen in the typical binary phase diagram in **Fig. 2.2 (a)**. The lesser concentration gradient at the interface decreases the diffusion rate hence it increases the IS time **[106]**. Also, increasing bonding temperature increases the bond width of the joint by forming more eutectic liquid during the dissolution and widening stage of the TLP bonding. This results in the dissolution of the bond interface and more widening of the bond area **[105, 106]**. Widening of the bond area decreases the strength of the bond. Therefore, an optimum bonding temperature minimizes the bonding time by balancing the diffusion coefficient value **[131]**, changing the equilibrium phase diagram concentration values **[106]** and bond width **[105]** to have higher bond quality.

Cooke et al. **[132]** investigated the effect of bonding temperature on microstructural development of TLP diffusion (TLPD) bonded Al-6061 (comprising 15 vol. % Al_2O_3 powder) joint. A 5 μm thick electrodeposited Ni-coating comprising 18 vol. % nano-sized Al_2O_3 powder was used as the interlayer. The assembly was heated to a bonding temperature ranging from 570 °C to 620 °C at a heating rate of 65 °C/min and held for 10 min. The diffusion of Ni into the Al-6061 alloy and IS at the joint interface followed by eutectic compound formation was attributed to the bond formation in this study. Maximum hardness value was observed at the bond centerline and decreased with increasing distance from the bond centerline. With increasing bonding temperature increase in shear strength was observed. This was attributed to presence of nano sized ceramic particles in the bond area.

Lee et al. **[133]** investigated the effect of temperature on bonding phenomenon and the mechanism involved in the TLP bonding of directionally solidified Ni-based superalloy GTD-111. A thin foil of Ni-19.3 Cr -7.19Si-1.2B (MBF-50) alloy was used as the filler metal. At 1403 K, a linear correlation between the reduced eutectic width and the square root of holding time was found. It was reported that the bonding mechanism is solid state diffusion of the MPD. However, at 1453 K the bonding mechanism was due to liquefaction at the grain boundary. And the IS was controlled by the diffusion of Ti not by the B or Si.

2.6.2 Bonding time

TLP bonding process is a diffusion controlled process where the rate of diffusion determines the bonding time. The solid-state diffusion of the elements from the interlayer into

the base material follows Fick's second law of diffusion. Increasing TLP bonding time increases the volume of inter-diffusion of elements between the interlayer and the base material. Which decreases the fraction of eutectic phases formed at the bond zone after IS **[134]**. A large bonding time is beneficial for the formation of bonds with homogeneous microstructure and high strength **[135]**. Atieh et al. **[136]** found that at higher holding time, finer and smaller intermetallics were formed at the joint centerline, which enhanced the mechanical properties of the bond. Increasing bonding time leads to the completion of isothermal solidification, and reduced volume of brittle eutectic phase in the bond area which is the main reason for the enhancement of bond strength **[137]**. However, Jin et al. **[138]** observed that, when the bonding time crossed the isothermal completion time, the shear strength of the interface decreased and this was attributed to the formation and segregation of brittle intermetallics within the joint. Therefore, an optimum bonding time is necessary for high bond quality.

Sayyedain et al. **[139]** investigated the influence of bonding time on the bonding strength and microstructure of the TLP diffusion bond of Al_2O_3p/Al nanocomposite using an electroplated Cu interlayer. Complete IS of the melt was not achieved with bonding time of 20 and 40 min. At a constant bonding temperature of 580 °C, when the bonding time increased from 20 to 60 minutes, complete IS was achieved. The maximum bond strength obtained was about 85 % of the strength of the base material which was observed for the bond made at 580 °C and held for 60 minutes. The improvement in bond strength was primarily caused by a reduction in the number of brittle eutectic phases in the bond area caused by an increase in bonding time.

Kenevisi et al. **[140]** studied the influence of bonding time on the properties of TLP bonded Ti–6Al–4V and Al7075 joint made at 500 °C using 50 μm thick Sn–10Zn–3.5Bi film as interlayer. The bonding time was varied up to 60 min. It was reported that a metallurgical bond at the interface was produced due to the interdiffusion of Cu, Ag, Sn, Al, and Ti in the bond zone. The interdiffusion of elements at the interface causes the precipitation of various second-phase particles in the bond area. With the increasing bonding time, the interdiffusion of atoms in the interface increased, and as a result, the shear strength and hardness of the bond

were increased. A maximum strength of 30 MPa was achieved after increasing the bonding time to 60 minutes.

Li et al. **[141]** examined the effect of bonding time on the chemical homogeneity of TLP-bonded Ni-based single crystal using a Ni-based interlayer. TLP bonding was carried out at 1473 K to 1523 K for 0.5 to 24 h in a vacuum chamber. The microstructure obtained was mainly consisting of γ′ and some white bulky phases. On increasing the holding time, the amount of precipitates decreases and disappears. At higher temperatures and longer holding times, the γ′ in the bond interlayer was almost identical to that of the base material. Also, the crystallographic orientation of the bonded regions was same as the base material.

Maity et al. **[142]** investigated the TLP bonding of an aluminum metal matrix composite (6061-15 wt. % SiCp) using a mixed Cu-Ni powder interlayer at 560 °C, 0.2 MPa, and holding time varied up to 6 h. It was observed that the bond region mainly consisted of two zones, namely, the ISZ, and the central bond zone. The ISZ contained $CuAl_2$ and Al_9Ni_2 in the matrix of a-solid solution along with the reinforcement particles (SiC). The central bond zone was highly heterogeneous at the lower bonding time. With increasing bonding time, the structural heterogeneity gradually diminished and high joint efficiency was obtained.

2.6.3 Interlayer alloy composition

The selection of proper interlayer material to use in the TLP bonding process relies on number of parameters. The interlayer should have adequate fluidity to wet the base material and flow over the bond surfaces **[143]**. The major alloying elements present in the interlayer should match with the main alloying elements of the base material. The MPD elements present in the interlayer should be compatible with the base material and form a solid solution in the base material. Again, the selection of the best filler alloy is determined by the solubility and compatibility of the MPD.

Zhai et al. **[144]** designed an interlayer to join DD6 (5.4Al, 6.14Ta, 8.44W, 1.98Mo, 9.01Co, 4.34Cr, 0.98Nb, 3.02Re, 0.12Hf, remaining Ni (wt. %)) single crystal alloys. Considering the eutectic temperature, chemical composition of the DD6 single crystal, and the differential electronegativity value of elements, which influence the stability of the borides, the composition range of the interlayer alloy was designed as: $1.5 \leq Al \leq 3.0$, $3.0 \leq$

Co ≤ 4.5, 2.5 ≤ W ≤ 4.0, 0.5 ≤ Mo ≤ 1.0, 1.0 ≤ Cr ≤ 2.0, 3.0 ≤ B ≤ 3.6 and remaining Ni (wt %). At a bonding temperature of 1200˚C, holding time of 8h, and pressure of 0.3 MPa, the structure of a typical join made with the interlayer alloys, when the chemical composition of alloys was 2.2 ~ 3Al, 3.7 ~ 4.5Co, 3.2 ~ 4W, 0.7 ~ 1 Mo, 1.5 ~ 2Cr, 3.2B, remain Ni (wt %), was composed of weld center zone, ISZ, and DAZ. Borides were formed at the DAZ. The join produced of very good quality.

2.6.4 Initial thickness, type and composition of the interlayer material

The suitability of an interlayer material for use in TLP bonding relies on some key factors. The melting temperature of the interlayer material must be lower than the melting temperature of the base material. The interlayer must have the proper fluidity at the bonding temperature to ensure proper wetting and flow of the liquid across base material surfaces **[145]**. The initial interlayer thickness is selected in such a way that it produces only sufficient liquid to wet the faying surfaces. Like the previous parameters, the thickness of the interlayer should be adjusted to an optimal value. A very thick interlayer produces more liquid, hence higher IS time is required for complete removal of the liquid. A too-thin interlayer may not be able to wet the surfaces properly **[106, 145]**. Therefore, a critical interlayer thickness is required for the TLP bonding **[106]**. Zakipour et al. **[146]** studied the effect of interlayer thickness on the microstructure and mechanical properties of SS 316, and Ti-6Al-4V bonds. The results showed that increasing the interlayer thickness led to the extension of the diffusion zone which increased the final joint width. This decreased the shear strength of the joint. As mentioned in the section 2.5, the type of interlayer plays a great role to decide the bonding quality. Type-II interlayer can join material at a lower bonding temperature and time than the Type-I interlayer. Type-II interlayer forms eutectics with the base material, which reduces the bonding temperature and time. The composition of the interlayer also plays an important role, the amount of MPD elements in the interlayer decides the solidification time. The difference in a concentration gradient of MPD elements decreases the isothermal rate between the interlayer and the substrate **[105, 106]**. The composition of interlayer elements decides the melting temperature of the interlayer and hence the solubility of MPD elements changes with different compositions. The volume of precipitates formed in the DAZ changes with the

solubility of MPD in the substrates. The segregation of precipitates controls the solidification of the TLP bond.

Yuan et al. **[148]** studied bonding behavior during TLP bonding of a duplex stainless steel using two different Ni-B-Based filler materials. MBF-30 (Ni-4.5Si-3.2B) and MBF-50 (Ni-7.5Si-1.4B-18.5Cr) were used as the interlayer material. Using MBF-30, the bond prepared at 1060 °C for 60 seconds showed incomplete isothermal solidification. Three distinct zones were observed such as DAZ, ISZ and ASZ. On increasing the holding time to 300 seconds, complete IS was observed. The join was free from remaining melt. However, bond made using MBF-50, made at 1175 °C for 300 seconds, showed residual liquid. The decreased of isothermal rate was due to decrease of concentration gradient in B between the interlayer and the substrate, and the reduced solubility of B at high temperature.

2.6.5 Bonding pressure

In TLP bonding, pressure is commonly applied to the bond assembly to align the substrate and encourage intimate contact between the workpiece **[149]**. The applied pressure increases the area of contact between the base material and the interlayer, which encourages the diffusion process. However, too much pressure may result in a squeeze out of the liquid **[47]**. Luozzo et al. **[150]** conducted TLP bonding process to join two carbon steel tubes using 3.8-B, 96.2-Fe (in wt. %) interlayer. TLP bonding was carried out at temperatures of 1250 °C for different time intervals and under pressures of 4, 3, and 2 MPa. From microstructural analysis, it was found that the bonding process was completed in 7.0 min when a pressure of 4 MPa was applied. Whereas at less pressure, more holding time was required for complete thermal solidification. They also developed a model using finite element method to simulate diffusion-controlled, two-phase, moving-interface problems. The total process time estimated from the actual initial conditions resulted several times greater than the experimental value because of the pressure effect. Ghaderi et al. **[47]** found that application of higher bonding pressure resulted in the widening of the bonding zone and the reduction of the amount of eutectic phases in the bond zone.

2.6.6 Combine effect of the process parameters

Atieh et al. **[136]** studied the effect of bonding temperature, time, and pressure on the microstructure evolution and mechanical properties of the TLP-bonded Ti-6Al-4V and Mg-AZ31 alloys, bonded by using pure Ni interlayer. The investigation was carried out at a temperature range from 500 to 540 °C, bonding time from 1 to 60 min, and bonding pressure from 0 to 0.8 MPa. A heterogeneous bond was obtained at different temperatures. The different sizes of phases and intermetallic were observed in the bond zone. Increasing bonding temperature increased the bond width due to the formation of more eutectic liquid which resulted in the dissolution of Mg-AZ31 interface. The shear strength of the joint was increased up to 520 °C then started to decrease. The width of the bond zone was increased on increasing holding time up to 20 min then started to decrease. At higher holding time, the intermetallics formed were finer, smaller in size, and agglomerated at the joint centerline when compared with a bond made at 5 min. Increasing bonding pressure increased the surface-to-surface contact and enhanced the diffusion of Ni into Mg-AZ31 and Ti-6Al-4V alloys, hence resulting in higher joint width.

Jalilvand et al. **[151]** investigated the effect of process variables on the microstructure and mechanical properties of TLP bonded IN-738LC superalloy using AMS 4776 (Cr- 14.0, Si-4.5, Fe-4.5, B-3.1 and balance is Ni) filler metal. They observed that at 50 μm gap-width, the samples which were bonded at 1100 °C for 15 min, non-equilibrium centerline eutectic micro constituents consisting of γ solid solution, nickel-rich boride, and chromium-rich boride were formed. Boron-rich intermetallics were observed in the DAZ. Increasing the bonding time to 45 min led to the completion of the IS. It was also observed that increasing interlayer thickness, requires more time to complete IS. The centerline eutectic was observed with the increase in the interlayer thickness. At constant temperature with increasing bonding time and homogenization, increased the shear strength of the bond zone. The hardness of the joint was lower than DAZ and ASZ.

Lin et al. **[152]** joined TiAl (Ti-48Al-2Cr-2Nb (at. %)) by the TLP bonding process using Ni/Ti interlayer material and studied the effects of process parameters on bond microstructure and IS. The base material and interlayer assembly was held at 970 °C -1150 °C for 5 – 240 minutes to obtain the bond. With increasing in bonding time and temperature,

the total reaction layer thickness of the TLP bond was increased, due to more dissolution of BM. With the increase in bonding temperature, the IS rate was increased. At 1150 °C, the IS rate was increased, and as a result, the continuous α2 layer disappeared and a bond with a uniform microstructure was obtained. Decreasing Ni content in the interlayer dissolves less TiAl substrate into liquid interlayer material and as a result, the IS rate was reduced. The interlayer thickness and composition of the interlayer material play an important role during isothermal solidification.

Jalilvand et al. **[46]** investigated the effect of bonding parameters on the microstructural developments of TLP bonded IN-738LC superalloy using AMS 4777 filler alloy. The bonding process was carried out at 1050 °C under vacuum atmosphere for various holding times of 15 to 75 min. The microstructural studies showed continuous centerline eutectic phases of Ni-rich boride, Cr-rich boride and Ni-rich silicide. At 75 min bonding time complete IS was observed. Homogenization of isothermally solidified joints at 1120 °C for 300 min resulted in the elimination of intermetallic phases formed at DAZ and the formation of significant γ′ precipitates in the joint region.

Jalilian et al. **[153]** investigated the influences of the interlayer thickness, bonding temperature and holding times on TLP bonding of IN 617 using Ni–11 % P filler metal. Interlayer thickness of 25.4 and 38.1 μm, bonding temperature of 1065 and 1150 °C, and holding time of 5 min to 24 h were taken as process parameters. For the 25.4 μm thick interlayer at 1065 °C IS was completed after 18 h, while for 38.1 μm interlayer even after 24 h it was not completed. It was also seen that, by increasing the bonding temperature and the holding time, the elimination rate of the liquid phase was increased, thereby increased the thickness of the diffusion layer. The behavior was independent of the thickness of the interlayer. For short holding times, the hardness of bond zone was higher than the base material. At higher holding times uniform hardness was observed in the bond affected area.

2.7 Variants of TLP Bonding

2.7.1 Wide gap TLP bonding (WG-TLP)

In some situations, like repairing cracks in Ni-base turbine parts, a large joint gap can be practically necessary to repair the parts. In this variant of TLP bonding the interlayer thickness is usually greater than 100 μm **[154]**. The interlayer uses in the wide gap TLP

bonding is generally in the form of powder compacts containing the MPD and some additive that is designed not to melt at the bonding temperature. To reduce the bonding time, a composite interlayer can be used **[155]**. The composite interlayer contains a layer of higher melting point constituents and a layer of lower melting point constituents. The higher melting point layer composition is similar to the base material composition and it does not melt entirely, but only participates in the dissolution of the base material **[155]**. The additive present in the interlayer reduces the amount of liquid and increases the interfacial area between the solid and liquid phases and hence effectively increases the diffusion rate **[156]**. This is shown schematically in **Fig. 2.7**. According to Gale and Butts, the composite ratio should be maintained properly so that excess liquid is not formed and dissolved the additives completely **[157]**. Similarly, the insufficient liquid formation leads to joints with excessively porous. Huang et al. **[153]**, studied the WG-TLP bonding of Al-based composites dissimilar using interlayer material such as Al-Si, Al-Cu, and Al-Si-SiC powders mixture. They found that the SiC particles were segregated along the joint areas with some porous microstructure at the joint. This leads to a reduction in the joint shear strength. They also observed that the shear strength of the joint increased with increasing bonding time. Wu et al. **[159]** also studied WG-TLP bonding of Ni-base superalloy to stainless steel. They found that some portion of the additive particles dissolved in the liquid; however, the un-melted particles provided sites for solidification. They also reported that with increasing bonding temperature the strength of the bond improved. The high bonding temperature allows the liquid to fill the space between the un-melted additive particles, which otherwise could lead to a porous joint.

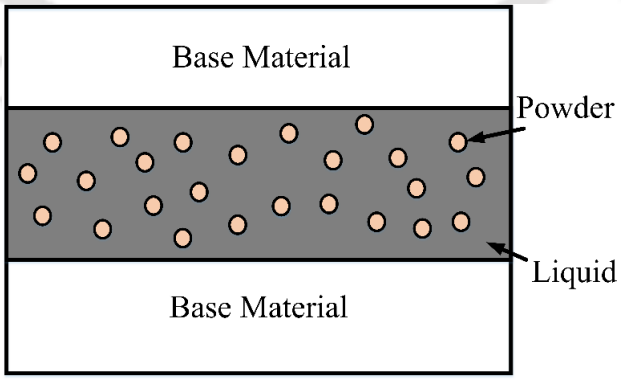

Fig. 2.7 Schematic diagram of wide gap TLP bonding

2.7.2 Partial transient liquid phase (PTLP) bonding

The PTLP bonding is mainly employed to join ceramics **[127]**. This technique is an overlap of both wide gap and active TLP bonding. In PTLP bonding three-layered interlayers are used, the interlayers consist of a thick refractory core layer and two low melting point reactive metals on either side of the refractory layer. Upon heating the assembly to the bonding temperature, liquid layers are formed on either side of the refractory layer by melting of the thin layers. This liquid wets the ceramic surfaces and concomitantly diffuses into the solid refractory core. The liquid solidifies isothermally and homogenization of the entire bond region leads to a refractory bond. As ceramics are chemically inert, active elements like Al, Cr, Hf, Nb, Ni, Si, Ta, Ti, V, or Zr are required for getting a good bond in PTLP bonding. The bond quality of the PTLP bonding depends on the thickness of the reactive layer, bonding temperature and bonding time.

Lan et al. **[160]** applied PTLP bonding to silicon nitride/nickel-based superalloy (DZ483) joints using Ti/Cu/Ni interlayers. Bonding was carried out in a vacuum furnace under various bonding temperature for 60 min. The heating and cooling rates were 8 °C/ min and 4 °C/ min, respectively. Bond carried out at 1273 K for 60 min. was well bonded and free form discontinuities. EDS line scan result showed diffusion trace of N, Si, Ti and Cu in the reaction zone. Variation of bonding temperature did not affect the width of the bond zone. Three point bending test was carried out to determine the mechanical strength of the bond. It was observed that with increasing joining temperature flexural strength of the joint increased initially and then decreased. When the joining temperature was 1323 K, the maximum strength value of 170 MPa was obtained. It was also found that the microstructure of the bond region determined the bond strength.

Chen et al. **[161]** joined Zr–Sn–Nb alloy and 304 stainless steel by means of PTLP bonding using Ni interlayer and without any interlayer in a vacuum furnace. The bonding was carried out at a temperature of 1000 °C, holding time for 30 minutes, a fixed load of 1 kPa and a heating and cooling rate of 10 °C. From the microstructure and EDS analysis, it was observed that Fe, Ni, and Cr from the SS304 and Zr from Zr–Sn–Nb dissolved into the reaction zone. In the direct bonded joint, a reaction layer with a thickness of 55 μm is formed between the Zr–Sn–Nb and SS304 substrates. While the thickness of the reaction layer with the Ni

interlayer reaches to 135 μm, which is distinctly larger than that without the Ni interlayer. Cracks were observed in the directly bonded reaction layer, due to a mismatch of thermal coefficient between the Zr–Sn–Nb and SS304 substrates during the cooling process. While, with the Ni interlayer, cracks were not detected. Using the Ni interlayer, the thickness of the reaction layer increased and the wider reaction layer enhanced the relaxation effect for residual stresses. The bonding strength of the joint obtained by the Ni interlayer was higher compared to the bond without the interlayer due to crack free reaction layer.

Atabaki et al. **[162]** joined magnesium alloy (AZ91D) to aluminum metal matrix composite (Al/Mg2Si) via PTLP diffusion bonding using an Al-based interlayer. They studied the effect of heating rates on the microstructure, shear strength, and microhardness of the joint. Decreasing the heating rate from 20 to 2 °C/min, the Mg composition in the bond area reduced, and complete coalescence of the mating surfaces was observed. The joints fabricated at the lower heating rate showed the highest shear strength, attaining 92.5 % of the parent materials strength. The hardness of the join was controlled by the intermetallic formation in the bond layer. It was observed that with increasing the heating rate, better homogenization in hardness was achieved because of interdiffusion of the main elements.

Atabaki et al. **[163]** applied PTLP diffusion bonding to join stainless steel 321 to zirconium alloy (Zr–2.5Nb) using two zirconium based interlayers and one active titanium-based interlayer. The samples were bonded in a vacuum furnace at various temperatures under 0.5 MPa dynamic pressure of contact. The result showed that the increase in the bonding temperature caused a significant reduction in the radius of the wetting, spread factor, spread ratio, and contact angle. However, by increasing the bonding temperature the height of the interlayer was decreased on the surface of the substrates. Bonds made at 850 °C for 15 min for all the interlayers give suitable wetting behavior. At higher temperatures brittle intermetallic compounds were formed at the interface of the joints, which reduced the mechanical properties of the joint. The titanium-based interlayer operates as a barrier for the diffusion of Fe and Cr and prevents the formation of brittle intermetallic compounds like Zr_3Fe_2, Zr_2Ni, and Zr_3Fe.

Park et al. **[164]** joined Si_3N_4 to Inconel 718 using multi-layer filler material (Ti-Cu-Ni) via PTLP bonding. The bonding temperature was varied from 850 ℃ to 1000 ℃ and the

holding time was from 10 to 100 min. The heating rate and cooling rate were 8 ℃/min and 2 ℃/min, respectively. During heating, the reactive Ti diffused into Ni and Cu and formed a liquid. The liquid phase wetted and reacted with the surface of the Si_3N_4 and Inconel 718. It was observed that the joint strength seems to depend significantly on bonding temperature and holding time. As the holding time was increased to 100 min., the joints showed high interfacial reliability. Compared to the previous joint made by Cu as an interlayer, a strong bond was obtained when Ti-Cu-Ni was used as an interlayer element.

2.7.3 Temperature gradient TLP bonding

In temperature gradient TLP bonding, a temperature gradient is imposed across the liquid interface. The schematic diagram with a compositional profile of temperature gradient TLP bonding is shown in **Fig. 2.8**. Shirzadi and Wallach **[165]** were the first to impose a temperature gradient in TLP bonding of Al-6082, they observed that the IS kinetics of the TLP bond was improved due to the temperature gradient. They proposed that by simply imposing a temperature gradient across the bond, a compositional gradient is induced in the liquid **[158]**. The interface which is subjected to a higher temperature will have low concentration and the surface exposed to low temperature will have high concentration to maintain equilibrium. As diffusion solute in the liquid is relatively fast, solute transport across the liquid occurs rapidly. The solute moves from low temperature (high concentration) to high temperature (low concentration) quickly. The decrease of solute concentration at the low temperature locally increases the equilibrium solidification temperature of the interface and which initiates the solidification of the bond from the low-temperature interface. This enhances solidification kinetics in TLP bonding and results in the improvement of the microstructure and mechanical properties of the join **[166]**.

Ghaznavi et al. **[147]** studied the effect of solidification mechanism on microstructure and mechanical properties of TLP bonded Al2024-T6 alloy. They found that on imposing temperature gradient, the solidification mechanism changes from planar to dendritic. That improves the bond microstructure and mechanical properties. Bigvand et al. **[168]** imposed small scale temperature gradient in TLP bonding and found asymmetric diffusional solidification. Also, they observed that a transition from bi-directional to unidirectional

solidification, under a constant temperature gradient. With this changes in solidification mechanism the bond strength improved.

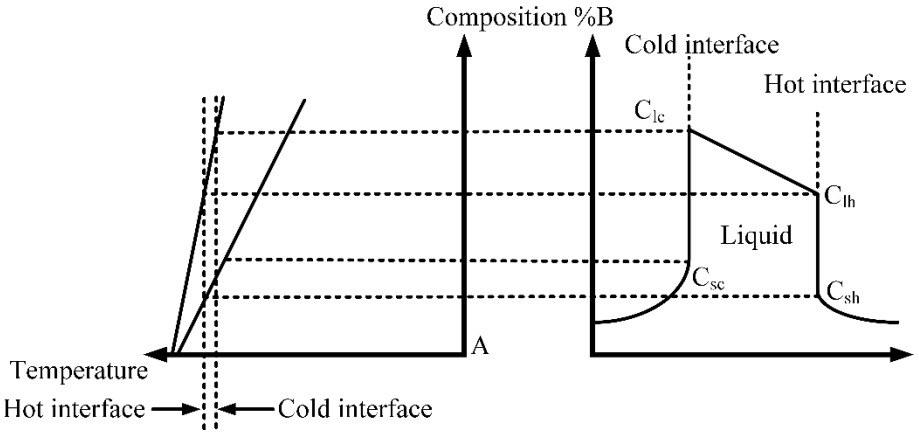

Fig. 2.8 Composition profile of temperature gradient TLP bonding

2.8 Basis of Modeling in TLP bonding Process

As stated before, the IS stage is considered as the most significant stage in the TLP bonding process, which determines the completion time of the bond. The dissolution stage is also an important stage, during this stage, the base material dissolves and the widening of the liquid layer occurs, that lead to more time to complete the isothermal solidification. These two stages mainly determine the morphology of a TLP bond. Similar to other solidification processes, the diffusion-driven IS process can also be considered a moving boundary problem. In this type of problem, Fick's second law of diffusion can be followed during the modeling.

2.8.1 Analytical modeling

Several analytical models have been proposed to describe the kinetics of the TLP bonding process. These are analytical descriptions based on Fick's law using mass balance arguments and are generally limited to the dissolution and IS stages of TLP bonding **[105, 106]**. Wells et al. **[169]** used thin-film diffusion equations to model the TLP bonding for joining Ti with Cu. The concentration profile, *C(x, t)* was given as,

$$C(x,t) = \frac{\alpha}{2\sqrt{\pi C}} exp\left(\frac{-x^2}{4D_s t}\right) \tag{2.2}$$

where, α is the surface concentration (g/cm^3), D_s is the diffusivity (cm^2/sec), x is the distance from the centerline (cm), and t is the time (sec). It was used to predict the solidification time. But the actual time was 15 times longer than the predicted time. A thick film diffusion equation was also used but could not predict accurately. Seeing the complexity of the process, researchers divided the process into four stages and each stage was modeled. Niemann et al. **[117]** calculated the Cu loss during the heating stage of TLP bonding (during the joining of Al-B composite material). They developed a relation

$$W_{loss} = 8.25\, C_{\alpha s} \left(D_s t\right)^2 \tag{2.3}$$

where, W_{loss} is the coating loss. The result can be compared with the experimental value by using an effective diffusion coefficient.

$$D_{eff} = \int_0^{t_0} \frac{D(t)dt}{t_0} \tag{2.4}$$

Where t_0 is the total heat up time. Putting effective diffusion coefficient value overestimates the time. No analytical solution has been reported regarding the dissolution of base material during the heating cycle from eutectic temperature to bonding temperature since the solute concentration at the interface varies with temperature. Nakao et al. **[119]** examined isothermal dissolution during TLP bonding based on Nernst-Brunner theory and developed a dissolution parameter P

$$P = Kt = h \ln\left[\frac{W_0\left(W_t + \rho h\right)}{\rho h\left(W_0 - W_t\right)}\right] \tag{2.5}$$

Where W_t is the width of base metal dissolved at time t, W_0 equilibrium dissolution width, ρ is the densities ratio of liquid and solid, h is the half initial liquid width, and K is a constant. Considering the uniform distribution of solute in liquid during the IS stage, the diffusion of solute in the liquid is ignored. Therefore, IS stage can be analytically modeled as a single-phase diffusion-controlled moving interface problem. Tuah-Poku **[169]** proposed a method for estimating the completion time of IS stage. The problem was assumed to be a semi-infinite base material with an interface solute concentration of CαL. An error function solution was used to define the distribution solute in the base metal.

$$C(y,t) = C_{\alpha L} + C_{\alpha L}\left(\frac{y}{(4D_s)^{1/2}}\right) \tag{2.6}$$

Where $C\alpha L$ is the solute concentration in the solid at the interface. The total amount *Mt* that has entered the base metal at time *t* can be calculated from the relation:

$$M_t = 2C_{\alpha L}\left(\frac{D_s t}{\pi}\right)^{1/2} \tag{2.7}$$

Ignoring the fraction of solute diffused during heating and dissolution, the total amount of solute diffused into base material during IS is equal to the original solute content in the filler material, i.e.

$$C_F W_0 = 4C_{\alpha L}\left(\frac{D_s t}{\pi}\right)^{1/2} \tag{2.8}$$

Where C_F is solute content in filler material, W_0 is the initial width of the filler material. The completion time for IS can be calculated using the relation:

$$t_s = \frac{\pi}{16D_s}\left(\frac{C_F W_0}{C_{\alpha L}}\right)^2 \tag{2.9}$$

Blanc and Mevrel, **[170]** used an similar derivation technique to obtain a formulation which accounts for boron consumption as a result of boride formation during TLP bonding of nickel base super alloy as base material. The time for completion of the IS during TLP bonding can be calculated using the relation:

$$t_s = \frac{(W_{\max})^2}{16K^2 D_s} \tag{2.10}$$

Where $W_{max}$the maximum liquid width is calculated using mass balance method.

2.8.2 Numerical modelling

The analytical modeling of IS can only predict solidification behavior under some ideal and limited conditions. For example, in all of the models discussed in the previous section, the base metal is considered to be a semi-infinite solid with no concentration gradient

in the liquid. And most of these research studies have modeled symmetric TLP bonding processes. Therefore, significant efforts have been put in over the last two decades to develop numerical models which consider more realistic conditions. In early attempts, some scholars tried to solve the diffusion equations by imposing a precondition like the interface has to move on the specified locations of the nodes **[105, 106]**. Since the movement of the interface and the distribution of solute in phases are mutually dependent on each other, this kind of approach is not physically feasible. The prescribed displacement violates the conservation of mass principle in the TLP bonding process.

Zhou et al. **[105]** reviewed the modeling of TLP bonding. Most of the researchers considered two aspects. The first aspect is one-dimensional modeling only. The second aspect is the solution of a two-phase moving interface problem in a simple binary alloy system. To calculate solute diffusion in solid and liquid phases, researchers employed, an explicit finite difference method. And to determine solid/liquid interface movement in TLP bonding, a stepwise 'mechanical' mass balance method was used. Though this method determined the exact location of the liquid/solid interface location, it required extremely long calculation times when the whole TLP bonding process was modeled. These problems were overcome by developing a fully implicit finite difference model that simulated the TLP bonding process in a continuous manner. Many research has been carried out on TLP modelling of two component system **[171]**. Sinclair et al. **[172]** implemented an explicit version of Fick's law and used it to investigate the solidification of ternary systems. A fixed grid discretization model was developed to predict the IS time.

Campbell et al. **[173]** simulated TLP bonding of Ni-10.3 at. % Al alloy and a Ni-10 at. % B filler material using the finite-difference diffusion code, DICTRA. The model correctly predicted the liquid width as a function of isothermal holding time. The experimentally measured Al composition profiles in the matrix were in good agreement with the predictions; however, the agreement in the liquid region was not good. Illingworth et al. **[174]** developed a numerical model to predict the bonding time using a variable grid meshing by introducing a wholesale coordinate transformation. TLP process was assumed as a one dimensional planar geometry, as shown in **Fig. 2.9**. The variable $S(t)$ is introduced to describe the position of the

solid/liquid interface (which varies as a function of time). The moving boundary problem was expressed as:

$$\frac{\partial C(x,t)}{\partial t} = \frac{\partial}{\partial x}\left(D_A\left(C(x,t)\right) \times \frac{\partial C(x,t)}{\partial x} \right), \quad 0 < x < s(t) \tag{2.11}$$

$$\frac{\partial C(x,t)}{\partial t} = \frac{\partial}{\partial x}\left(D_B\left(C(x,t)\right) \times \frac{\partial C(x,t)}{\partial x} \right), \quad s(t) < x < L \tag{2.12}$$

$$D_A\left(C(x,t)\right)\frac{\partial C(x,t)}{\partial x}\bigg|_{x=s(t)^-} - D_B\left(C(x,t)\right)\frac{\partial C(x,t)}{\partial x}\bigg|_{x=s(t)^+} = \left[C_A - C_B\right]\frac{\partial s(t)}{\partial t}, \; x = s(t) \tag{2.13}$$

A good agreement was observed between the experimental data and the numerical values.

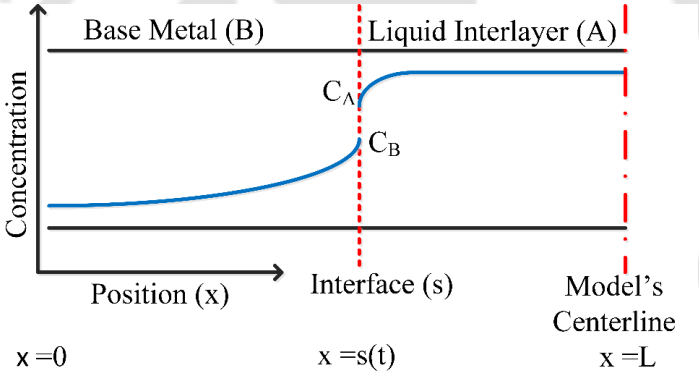

Fig. 2.9. Schematic diagram showing the concentration profile across half of a TLP bond at one instant in time **[174]**

Li et al. **[175]** used a fixed-grid source-based method to model TLP bonding. The governing equation and boundary conditions were solved using the volume-controlled finite-difference method. Under the assumption of constant Molar volume, the current fixed-grid source-based model predictions were in good agreement with those predicted by Illingworth et al. **[174]**. Ghoneim et al. **[176]** developed a new 2-D moving-mesh, implicit finite element simulation model, without the symmetry assumption to study asymmetric diffusional solidification behavior during TLP bonding of dissimilar alloys. Good correlations between the model predictions and the experimental results were observed. In the case of dissimilar material joining, with an increase in bonding temperature, the IS time was increased.

Abdelfatah et al. **[177]** studied the effects of process parameters on microstructure of a TLP joint in a precipitation-hardened nickel-based superalloy, IN 738. A deviation from the parabolic relationship between displacement of the liquid/solid interface and holding time was observed experimentally. An increased in IS time with temperature was observed due to increase in width of the diffusion zone. The deviation was duly rationalized by the application of an implicit, numerical finite-difference model to solve the Fick's diffusion equation. Shirzadi et al. **[178]**, Assadi et al. **[166]** and Jabbareh et al. **[179]** modelled the TLP bonding imposing temperature gradient in the molten interlayer for a Al and Cu system and validated with experimental results. It was reported that the predictions were of good agreement with the experimental values. It was also observed that imposing temperature gradient in the liquid interlayer shortens the solidification time to a great extent. The temperature gradient created non-planar morphology in the bond interface, which led to increase in shear strength of the bond.

2.9 Major Gaps from the Literature

The information drawn from the published literature produce several research gaps and possibilities remain for further investigation. The gaps found from the literature are summarized as follows.

- The effects of individual process parameters such as temperature, time, pressure, interlayer thickness have been investigated comprehensively, however their interactive effects has not been studied properly. Also, the effect of different form of interlayer, such as powder and foil, has not been reported.
- Commercially available BNi-2 interlayer was only used during investigations of TLP bonding of IN 718. However, the application of other interlayer materials has not been reported in the existing literature.
- After IS, the homogenization stage is very important. However, a limited work has been reported on homogenization of the bond.
- Inconel 718 usually used in high temperature applications. But, the high temperature properties of TLP bonded IN 718 superalloy has not been reported.
- Little research data has been found on the kinetics of TLP bonding of IN 718

- Analytical models have been developed to predict the completion time of IS, however, the prediction accuracy of these models for polycrystalline materials is inferior.

2.10 Objectives of the Present Work

Based on the research gap found in the published research work, the objectives of the present work are summarized as follows:

- **Design and develop an interlayer material for TLP bonding of Inconel 718**
  - A suitable interlayer material will be design and developed by considering phase diagrams of MPD elements and major constituent of the base material. The diffusivity, solubility and electronegativity of the elements will also be considered. The effect of interlayer thickness and interlayer form (*i.e.*, powder and foil) on the bond quality will be studied.
  - The newly developed interlayer material will be compared with the commercially available interlayer materials for TLP bonding of IN 718.
- **Simulate the interface kinetics of TLP bonding using DSC method in a solid/liquid diffusion couple and compare with various experimental results**
  - An interrupted DSC technique will be implemented to determine the complete isothermal solidification time for TLP bonding of IN 718 superalloy.
- **Improvement of mechanical and metallurgical properties of the bond using suitable post bond heat treatment technique**
  - A post bond heat treatment method will be designed considering the Time Temperature and Transformation (TTT) of the IN 718 to improve the bond quality.
  - The bond properties like microstructure, microhardness, and tensile strength of the as bonded and PBHT samples will be compared.
- **Study the high temperature tensile properties of TLP bonded IN 718 bond**
  - The tensile properties of the bonded samples will be studied at 650 °C.

The methodology adapted to complete the stated objectives, observations and summary of the present work are discussed in detail in the subsequent chapters of the thesis.

Chapter 3

Experimental Procedure

3.1 Introduction

This chapter extensively elaborates on the procedures and methods, or techniques implemented for conducting the TLP bonding experiments. Apart from the experimental procedures, this chapter also outlines different techniques used for analyzing and testing TLP bonded specimens. The experimental procedures consisting of synthesis and characterization of the interlayer materials, TLP bonding procedures, characterization of the joint, etc. are presented. The entire sample preparation, microstructural analysis, and mechanical testing are discussed in detail. Also, the pre and post-bond heat treatment of the bonded samples are discussed in detail. The prepared specimens are taken for different mechanical testing and macro-microstructural analysis.

3.2 Material Preparation for TLP Bonding

The IN 718 base metal was procured from a commercial firm in the form of 10 mm diameter rods. Cylinders with a nominal height of 70 mm were cut from the IN 718 rods using a wire-cut EDM. The faying surface of each base metal cylinder was ground flat. The samples were ground using silicon carbide polishing disc with grit sizes of 220, 350, 400, 600 and 1000 in order. This operation was carried out to ensure a uniform, flat surface with consistent roughness. Subsequent to the grinding operation, each base metal sample was cleaned ultrasonically in acetone for 10 min to remove any impurities or debris (e.g., SiC particles) remaining and ensure a clean faying surface. The chemical composition of the IN 718 superalloy is presented in **Table 3.1.**

3.3 Interlayer Materials

In this research work, two types of interlayer materials were used for carrying out the TLP bonding experiments. Interlayer-1 was a 40 µm thick and 10 µm width commercially available amorphous BNi-2 foil interlayer, which was obtained from a commercial firm. The interlayer-2 used was a nano-sized Ni-Cr-Fe-B-Si-based powder interlayer synthesized at IIT

Guwahati by mechanical alloying (MA) process. Two nano-sized interlayer materials with different chemical composition were synthesized in the laboratory. However, only the best alloy powder (having low melting point) was used for the TLP bonding of IN 718 alloy. The elemental composition of the two interlayer material used for the TLP bonding is presented in **Table 3.1**. The detailed methodology followed during the preparation of powder interlayer material (i.e. interlayer-2) was described in section 3.3.1.

Table 3.1 Composition of base material and interlayer (wt. %)

Elements / Materials	Ni	Fe	Cr	Nb	Mo	Al	Ti	Ta	B	Si	S	Cu	Mn
IN718	55.7	17.7	16	5.1	2.0	0.5	0.9	0.5	-	0.2	0.2	0.8	0.2
Interlayer-1	82.3	3.0	7	-	-	-	-	-	3.2	4.5	-	-	-
Interlayer-2	80.8	1.5	10	-	-	-	-	-	3.2	4.5	-	-	-

3.3.1 Synthesis and characterization of powder interlayer material

A nano-size powder interlayer materials were synthesized by MA processes using powders of Ni, Cr, Fe, B, and Si obtained from LOBA CHEMIE. **Table 3.2** shows the details regarding the elemental powders, the purity of elements and the weight percentage of powders used for the preparation of the interlayer materials for the current study. The powder mixture was ball milled using a planetary ball mill (Make: Insmart Systems, Model: PBM07) for mechanical alloying. The various milling parameters are presented **Table 3.3**.

The powder samples collected after milling for various time periods were characterized using laser particle size analyzer (LPSA), Field Emission Scanning Electron Microscope (FESEM) fitted with Energy Dispersive X-ray analysis system, Field Emission Transmission Electron Microscope (FETEM), X-ray Diffractometer (XRD) and Differential Scanning calorimetry (DSC). The FESEM was used to study the surface morphology and composition of the powder evolved during milling. XRD was used to determine the extent of mechanical alloying identification, composition analysis and crystal structure of phased formed during the milling process. FETEM was used to study the lattice parameters and crystal structure analysis. DSC was carried out to determine the melting point of the alloy.

Table 3.2 Weight percentages and purity of the elements powders

Interlayer materials	Weight percentage of the elements				
	Ni (98 % pure)	Cr (98 % pure)	Si (98 % pure)	B (98 % pure)	Fe (98 % pure)
Interlayer-I	80.8	10	4.5	3.2	1.5

Table 3.3 Details of milling of the powder mixture

Make / model of the equipment	:	Insmart Systems / PBM07
Vial	:	Hardened steel
Milling balls	:	7.9 mm diameter hardened steel balls
Milling condition	:	dry
Total powder charge	:	100 grams
Ball to powder weight ratio	:	10:1
Milling speed	:	300 rpm with 15 minute relaxation after every 45 minute of milling
Total milling duration	:	60 hours
Sampling time	:	after 2, 5, 10, 20, 35, 50 and 60 hours of milling
Sampling weight	:	2 grams

3.4 Experimentation

The work piece material used for the investigation were cylindrical rods of wrought IN718 nickel-based superalloy having 10 mm diameter and 70 mm length. The samples were machined in the form of half tensile testing sample as shown in **Fig. 3.1**. The contacting surface (end face) of the base material samples was polished using 220, 320, 400, 600, and 800 grit size SiC polishing papers. Interlayer -1 and Interlayer-2 were separately used for the TLP bonding of IN 718 alloy. Prior to the bonding, the interlayer materials and base material were cleaned ultrasonically to remove any impurities present on the bonding surfaces. The nano-sized interlayer alloy powder (interlayer-2) was mixed with ethanol and made in the form of a paste. This paste is uniformly spread on the bonding surface of the samples. The

Interlayer-1 (amorphous foil of BNi-2) foil strip was cut into 6 mm dia. discs. Nine experiments were conducted by varying bonding time, temperature, interlayer thickness, and bonding pressure; the detailed process parameters settings are shown in **Table 3.4.** Three bonded samples were prepared for each experimental condition. The TLP bonding was carried out in an induction-heating machine (Make: Ambrell Inc. maximum power 10 kW) attached with a cooling unit (make- Werner Finley Pvt. Ltd.) to draw the heat generated in the coil during TLP bonding. The induction coil was used for the heating is a circular copper coil of 30 mm inner diameter and 35 mm outer diameter. An in-house designed and fabricated (shown in **Fig. 3.2**) set-up was used to hold the sample perfectly aligned during the application of bonding pressure. The fixture consists of a stage to hold the sample, a loading unit to apply the load, and a pyrometer to measure the bonding temperature. Dead weights were used to apply load to the bonding sample through a loading shaft.

The samples were placed in the sample holder of the set-up, and the interlayer was sandwiched between the two ends of the samples. The required bonding pressure was applied axially using dead weights. The constant bonding temperature was maintained by adjusting the coil current. Bonding temperatures of 1050 ºC, 1100 ºC, and 1150 ºC were maintained by passing currents of 341A, 365A and 386A, respectively. An infrared pyrometer was used to measure the temperature of the bond zone. The bonding was performed in an open atmosphere.

Fig. 3.1 Photograph of the half tensile testing workpiece material

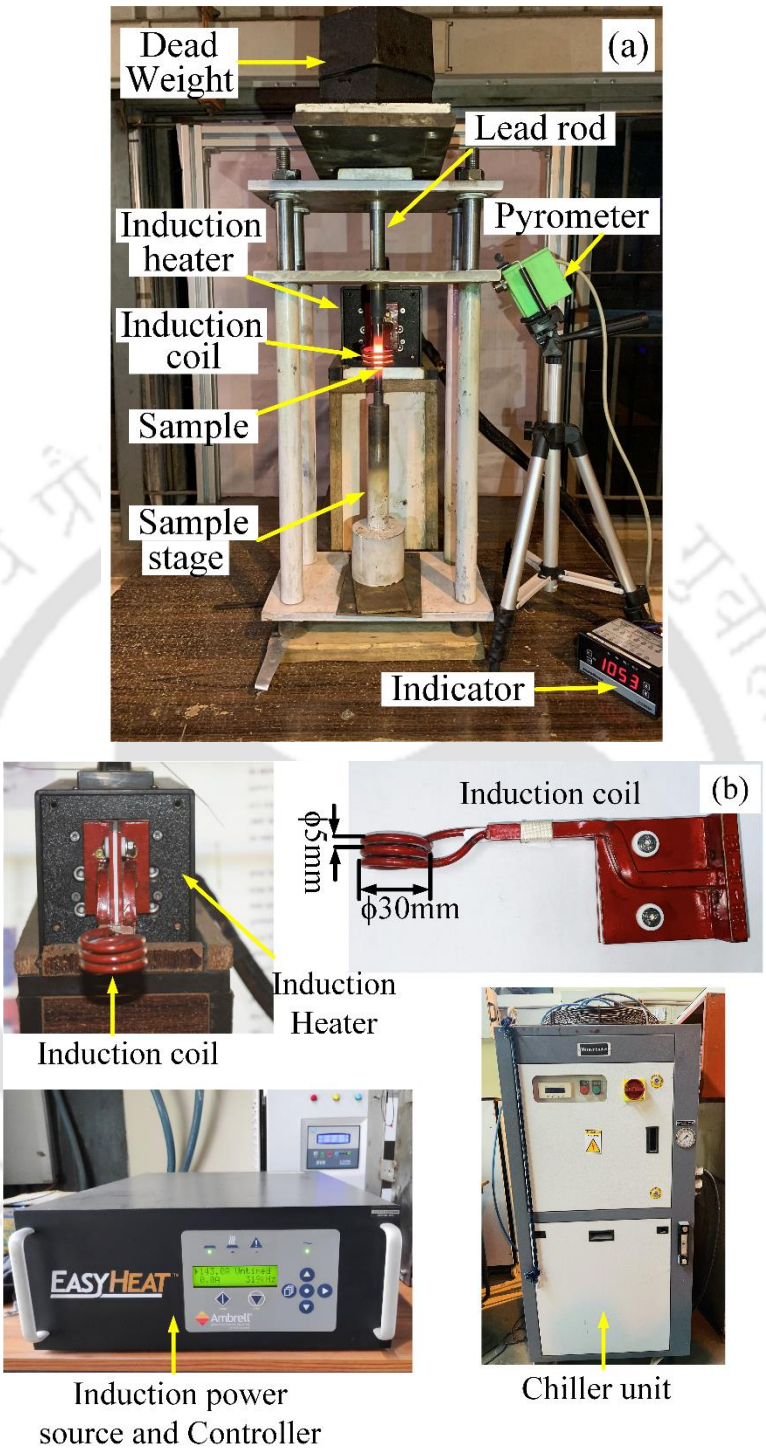

Fig. 3.2 Experimental set-up, (a) fixture and (b) different parts of set-up

Table 3.4 Experimental process parameters settings

Exp. No.	Temperature (˚C)	Time (mins.)	Interlayer thickness (μm)	Load (Kg)
E.1	1050	60	80	12.5
E.2	1050	90	120	15.7
E.3	1050	120	160	19.6
E.4	1100	60	120	19.6
E.5	1100	90	160	12.5
E.6	1100	120	80	15.7
E.7	1150	60	160	15.7
E.8	1150	90	80	19.6
E.9	1150	120	120	12.5

3.5 Macro/Microstructure by Optical Microscope (OM)

The bonded samples were sliced perpendicular to the plane of the bond using wire-cut EDM and the sliced surface was polished to mirror finish using standard metallographic specimen preparation procedures. The samples were then etched using glyceregia etchant solution. Subsequently, investigation of the microstructure and grain size of the TLP bonded joints were carried out using an optical microscope (OM) (Make: Carl Zeiss; Model: Axiotech- 100HD). **Figure 3.3** shows the photographs of the OM system used in this investigation.

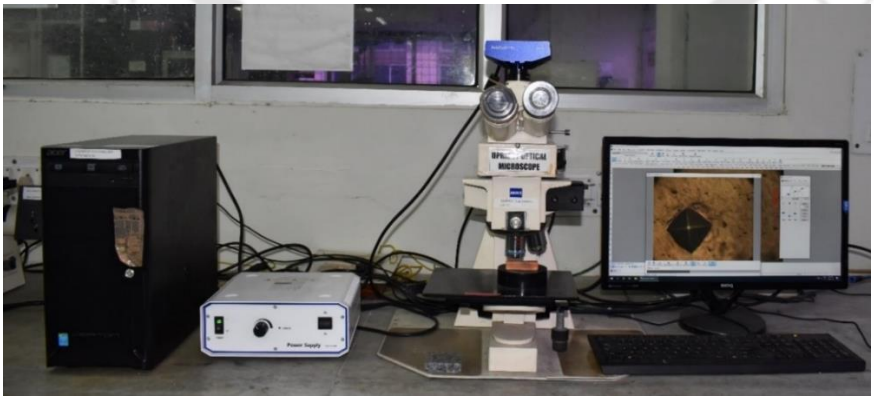

Fig. 3.3 Optical microscope

3.6 Field Emission Scanning Electron Microscope (FESEM)

The morphology of grains, distribution of elements, the phases formed and the change in the composition due to the IS during TLP bonding was investigated using a field emission scanning electron microscope (FESEM) (Make: Zeiss; Model: sigma) equipped with an energy dispersive X-ray (EDS) analysis system. **Figure 3.4** shows the photographs of the FESEM / EDS system. The same sample preparation procedure as that for preparation of OM sample was followed for the preparation of FESEM sample. The distribution of the constituent elements and compositional analysis of the phases formed during TLP bonding were carried out by selected area scanning, line scanning, and elemental mapping methods. In addition, the surfaces of the tensile and fatigue failed samples were investigated by FESEM to reveal the failure mechanism during load application.

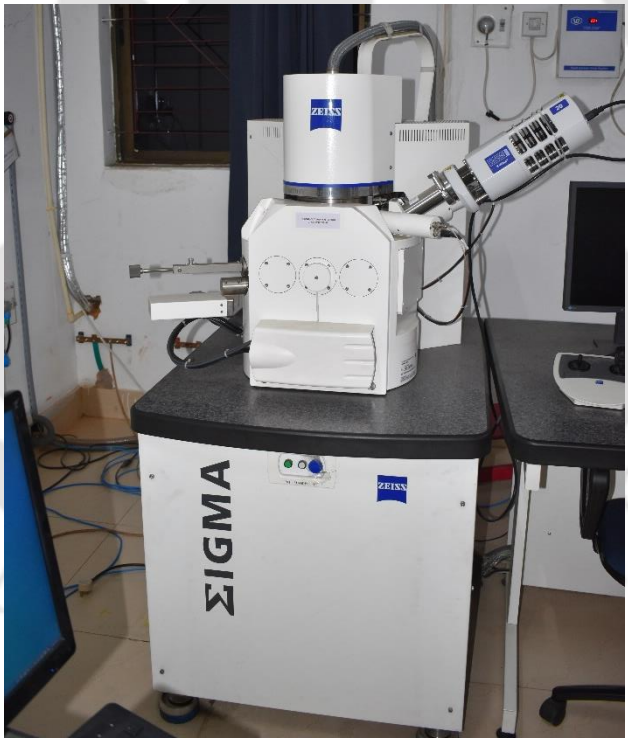

Fig. 3.4 Field emission scanning electron microscope

3.7 Field Emission Transmission Electron Microscope (FETEM)

The formation of nano-crystals of mechanically alloyed powder during the milling process and the structure of the phases formed during TLP bonding were investigated by field emission transmission electron microscope (FETEM) (Make: JEOL, Model: JEM 2100). **Figure 3.5** shows the image of FETEM used for the FETEM analysis. To study the structural characteristic of nano-sized powder particles, the powder was sonicated in an ultrasonic bath and drop casted into a copper grit of 3 mm diameter.

For the TEM sample preparation of the TLP bonded samples, a thin slice of 100 μm thickness was cut perpendicular to the bonded plane by a linear precision saw (Make: Buehler, Model: Isomet 4000) using a diamond-wafering blade. From this a 3 mm diameter disc was punched out using a disc cutting machine (Make: Gatan). The final thinning of the disc specimens was carried out by a double jet electro-polishing machine at a temperature -30 °C a by applying a voltage of 25 V. The electrolyte used for the double jet electro-polishing was a mixture of ethylic alcohol and per-chloric acid at a ratio of 9:1.

Fig. 3.5 Field emission transmission electron microscope

3.8 Laser Particle Size Analyzer (LPSA)

The particle size of the powder mixture, milled for different periods was analyzed by a laser particle size analyzer (LPSA) (Make: M/s Malvern, Model: Mastersizer 2000). **Figure 3.6** shows the photographs of the LPSA. The powder mixture was sonicated for 15 minutes in distilled water before analysis in order to remove the agglomeration of the fine powders.

Fig. 3.6 Photograph of laser particle size analyzer

3.9 X-ray Diffraction (XRD)

Crystal structure characterization and extent of mechanical alloying of the milled powders was carried out using a powder X-ray diffractometer (Make: M/s PAN analytical Model: X'Pert Powder) using Cu Kα radiation (λ = 1.54 Å). The scanning was carried out at a rate of 0.005/s. From the plot of intensity vs. 2θ, the crystal structure and lattice parameter of the alloy powder were determined. The crystallite size, fraction of grain boundaries, and dislocation density in the powder mixture milled for various time periods were determined by the modified Willamson-Hall method **[180]**.

Identification and quantification of different phased present in the TLP boned specimen was carried out by XRD analysis. The peaks in the intensity vs 2θ plot represents the reflections from specific crystallographic planes of the phases. The phases were identified by indexing the 2θ values of the peaks obtained from the XRD study and comparing with the reference patterns of the JCPDS files. The detail of the XRD machine (Make: Rigaku Technologies, Model: Smartlab shown in **Fig. 3.7**) is given in **Table 3.5**. The quantitative

analysis of the phase formed during TLP bonding was carried out by using the area integrated method.

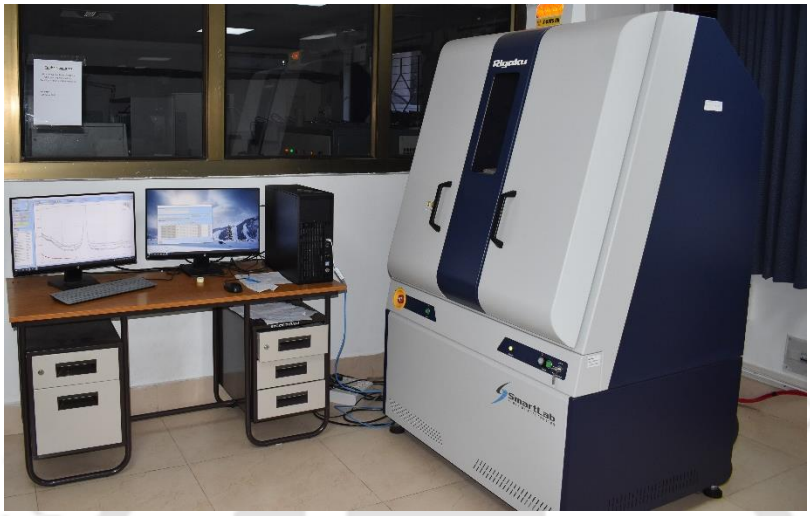

Fig. 3.7 X-ray diffractometer

3.10 Differential Scanning Calorimetry

Differential scanning calorimetry (DSC) is a thermo-analysis technique used to study the thermal characteristic of materials. By this technique, the crystallization, melting/ fusion temperature of the interlayer material could be investigated. The DSC experiments were carried out in the alumina crucibles. The experiments were conducted in an argon gas (99.999 % pure) atmosphere by passing the gas continuously at the rate of 60 ml/min. The melting of the interlayer material was determined from the change of heat flux vs. temperature plot. The change of heat flux was calculated and the melting temperature of the interlayer material was determined. The detail calibration of the DSC equipment is shown in **Table 3.5**. The photograph of the DSC set up is shown in **Fig. 3.8**.

Thermal analysis was performed using a differential scanning calorimeter (DSC) (Make: Netzsch, Model: STA449F3A00). DSC was carried out from room temperature to 1200 °C. The sample powders were heated in an argon atmosphere at three constant heating rates: 20, 15, and 10 °C/min. The activation energy of the melting of the alloy powder was

determined from the heat flow vs. temperature data obtained during the DSC tests using the standard technique.

Fig. 3.8 Differential scanning calorimetry

3.11 Tensile Test

The tensile test is a widely accepted method for determining the bond strength of a joint. In TLP bonding, the tensile test plays an important role in indicating the joint strength compared to the base material strength. Moreover, a measure of ductility obtained from the tensile test can be used as an indicator of the formability of the joint.

The room temperature tensile tests were performed on a servo-controlled hydraulically operated universal testing machine (UTM) as shown in **Fig. 3.9** (Make: BISS; Model MEDIAN 250). Tensile samples were prepared as per the American Society for Testing and Materials (ASTM) E8M-08, as shown in **Fig. 3.10** was used for the testing. The detail of the tensile testing machine is given in **Table 3.5**. During the test, an extensometer with 25 mm gauge length was used to measure the elongation. After fixing the sample in the grips, the sample was loaded monotonically till failure at a cross head speed of 1 mm/min. The load vs displacement data was recorded, from which the stress vs strain plot was obtained, The UTS and % elongation values in each experimental condition is reported. For each experimental condition, two samples were tested and the average value was plotted. In

case the values differ by more than 15 %, another experiment was conducted and the average of the two close values were taken and reported.

Fig. 3.9 Universal testing machine

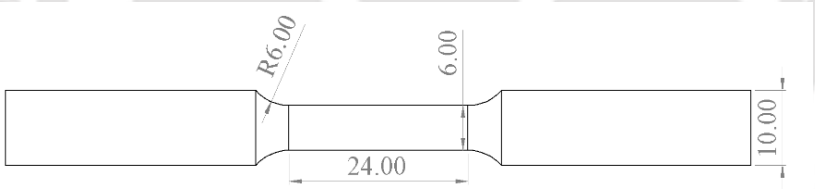

Fig. 3.10 Tensile samples

The high-temperature tensile behavior of the TLP bonded samples was carried out using the same UTM machine. The tensile specimen of the same size as mentioned in **Fig. 3.10** with a modification was used in this current investigation. In the grip section of the tensile specimen, an M10 thread of 25 mm length was fabricated to hold the sample in a sample holder as shown in **Fig. 3.11**. The tensile test was carried out at 650 °C in a muffle furnace. The test was conducted at a cross-head speed of 0.5 mm/min. the post failure fracture surface of the specimens was studied using the FESEM.

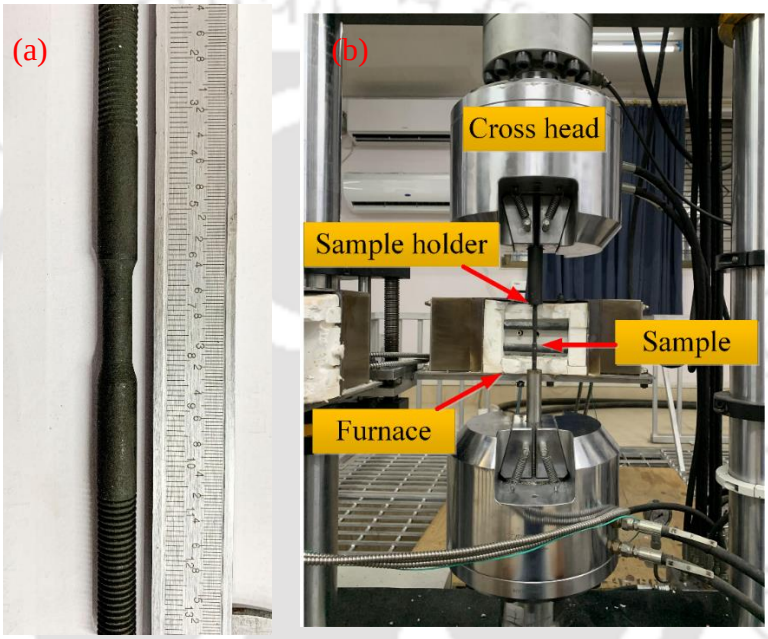

Fig. 3.11 (a) specimen for high temperature tensile test and (b) high temperature tensile fixture

3.12 Hardness Test

The quality of the bond can also be determined by hardness test. The Vickers hardness test is commonly used to measure the variation of hardness value across the joint. The hardness testing was carried out using a microhardness (Make: Omni Tech) tester. The detailed specification of the micro-hardness tester is reported in the **Table 3.5** and the photograph shown in Fig. **3.12 (a).** To measure the micro-hardness variation in the TLP bonded samples, specimen were cut along the transverse direction of the bond using a wire-cut EDM. The cut surfaces were ground by using 240, 320, 400, 600, and 1000 grade Buhler SiC polishing paper. A load of 300 gf was applied on the specimen surface using a diamond

indentor having 136° included angle between opposite faces of the pyramid. The dwell time during the test was fixed at 15 seconds. The two diagonal length of the square impression formed due to the load application was measured and hardens value was determined using the following standard equation:

$$VHN = \frac{1.854 \times P}{L^2} \quad (3.1)$$

Where P is the load applied in kg and L is the average length of the two diagonals in mm. The microhardness values were measured at three different zones viz.; ISZ, DAZ, and BMZ. The micro-photograph of a typical impression obtained during the Micro-hardness testing is shown in **Fig. 3.12 (b)**. The values reported for the hardness are the average hardness values of ten reading taken at each zone.

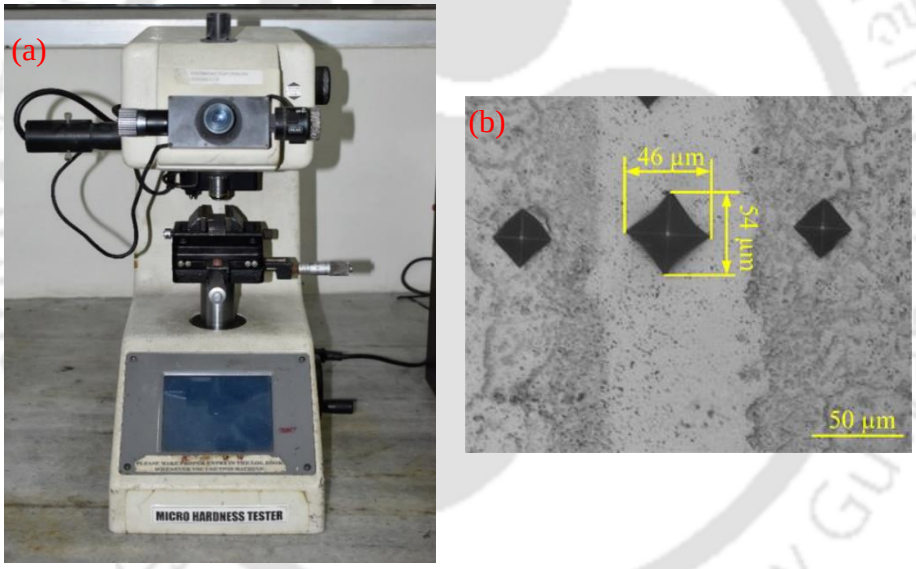

Fig. 3.12 (a) Vickers microhardness tester and (b) sample with indentation marks

3.13 Kinetics of TLP Bonding

Cylindrical Disc samples of 4.5 mm diameter and 1 mm height were prepared from the IN 718 rod by wire-cut EDM. Also, disc shaped interlayer of 4.8 mm diameter was cut from the 40 µm thickness BNi-2 foil by the wire cut EDM. The faying surface of the BM was polished using 320, 400, and 600 grit SiC paper. The BM and interlayer were cleaned

ultrasonically to remove the contaminants like oxides/ oil/grease present on the surfaces. The sides and top of the BM were coated with yttria to restrict the area of interaction of the BM surface with the interlayer as to be the bottom of the BM only. The disc-shaped interlayer was placed in contact with the BM cylinders and the half joint arrangement of the TLP bonding samples required for DSC analysis is shown in **Fig. 3.13**. The weight of the BM cylinder and interlayer disc was 80 mg and 5.1 mg, respectively. Differential scanning calorimetry (DSC) was performed on the IN 718 /BNi-2 couples using a DSC (make: Netzsch, model: STA449F3A00) at a heating and cooling rate of 20 °C/min under a 60 ml/min flowing Ar (99.999 %) atmosphere. The baseline correction of the empty Al_2O_3 crucible was carried out as per the experimental conditions. And, the temperature and enthalpy calibration was carried out by using In, Sn, and Au elements under conditions identical to that used for the sample experiments. The diffusion couple was held at 1050 °C under 99.999 % pure Ar atmosphere as per the program shown in **Fig. 3.14**. In this investigation, an interrupted cyclic method developed by Corbin et al. **[181]** was adapted for determining the enthalpy of solidification during the cooling of the liquid interlayer. The enthalpy of solidification as a function of bonding time is measured via DSC analysis. This cycle was repeated until there was no evidence of solidification measured on the cooling trace. Two separate experiments were carried out for each experimental condition. The post-DSC experiment sample was prepared for microstructural analysis with the usual metallurgical sample preparation procedure and the microstructural and compositional analysis of the post-DSC treated samples are carried out using FESEM.

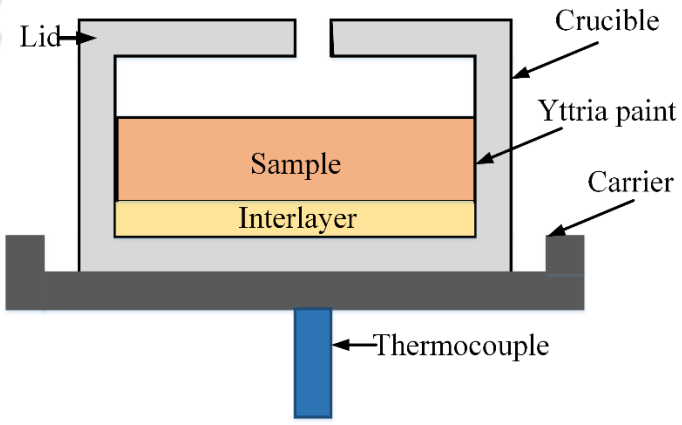

Fig. 3.13 DSC half joint arrangement

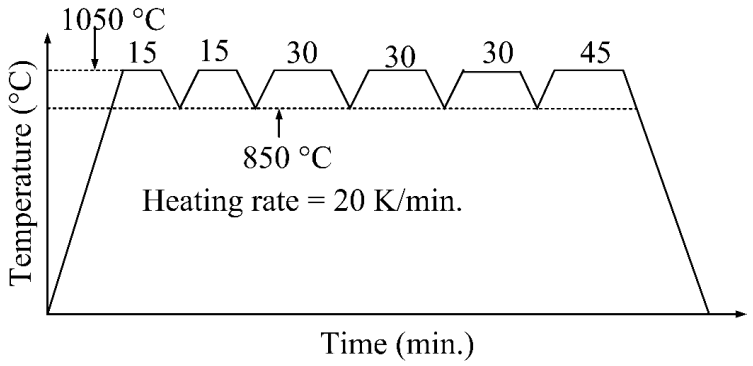

Fig. 3.14 DSC temperature and time program for DSC analysis

3.14 Homogenization of the TLP Bond

To establish homogenized microstructure and remove detrimental second phase particles present in the bond area, homogenization of the TLP bonded samples were carried out. In this investigation, the samples were held at 760˚C for 8 h then cooled down to 660 ˚C and held for 32 h and subsequently furnace cooled to room temperature. To study the microstructural evolution during the homogenization stage, samples are collected after 8, 16, 24, and 32 h, and microstructural characterization was carried out via OM and FESEM. The homogenization stage was performed using a muffle furnace (Make: Daihan scientific furnace, Model: FX: 63). The tensile samples were prepared as per the ASTM E-8M standard and the mechanical properties of the homogenized bond after the removal of detrimental phases were carried out.

3.15 Post Bond Heat-treatment

To enhance the mechanical properties of the IN718 bond two type of heat treatments were carried out. In the first case, the base material and the bonded samples were solution annealed at 1050 °C water quench and in the second case, the samples were solution annealed at 1150 °C water quench, shown in **Fig. 3.15**. In both samples, this was followed by the following sequence: aged 760 °C for 8 hours → furnace cooling to 660 °C at the rate of 55 °C /min → holding at 660 °C for 8 hours → cooling to room temperature. The solution annealing was carried out in a raising-hearth electric furnace (make: BYSAKH & CO.,

Model: 70R4) and precipitation hardening and aging were conducted using a muffle furnace (Make: Daihan scientific furnace, Model: FX: 63).

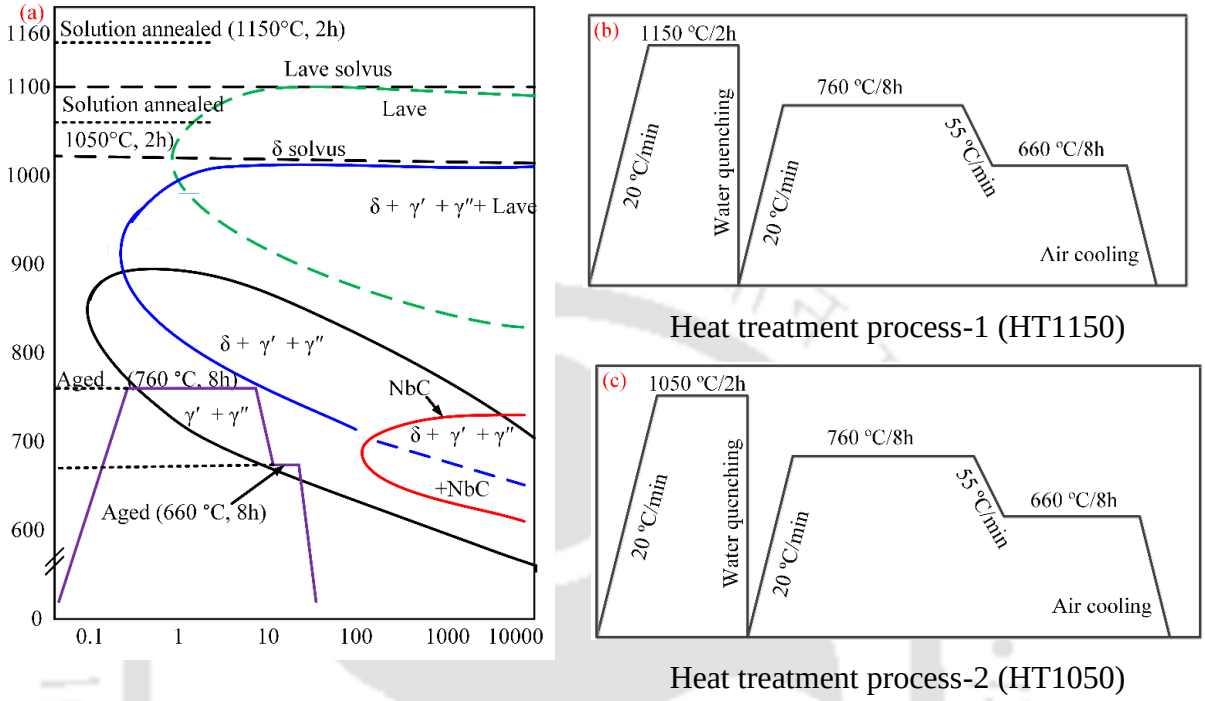

Fig. 3.15 Schematic diagram of PBHT process (a) TTT diagram of IN 718, (b) PBHT process-1 and (c) PBHT process-2

3.16 Fatigue Test

Fatigue is a progressive and localized structural damage that taking place in the material under repeated cyclic loading and unloading conditions. The applied load is usually lower than the yield strength of the material. Generally, the fatigue behavior of a structure is defined in terms of the number of cycles to failure under the specified loading condition. During the fatigue loading, though on a gross scale the stress is elastic, at localized regions of maximum stress concentration the metal deforms plastically. This results in slip-bands and the initiation of micro-cracks. During further cyclic loading, this crack grows and finally results in the rupture of the component. Specimens were prepared to measure the fatigue properties of the TLP bond with the ASTM E-466 standard for the best bonding parameters. The fatigue test specimen is shown in **Fig. 3.16.** A tension-tension fatigue test was conducted at various stress amplitudes, a stress ratio (R) of 0.1, and a loading frequency of 20 Hz using

the BISS-250kN UTM machine as used for tensile test. The load was applied perpendicular to the bonding direction with a stress amplitude of 400, 350, 300, and 250 MPa. The measured fatigue strength is defined in terms of a number of cycles to failure, crack path behaviors, and fracture surface of the specimen for an enhanced assessment of the welded specimens. To observe the mode of failure, the fatigue fracture surfaces were examined by the FESEM.

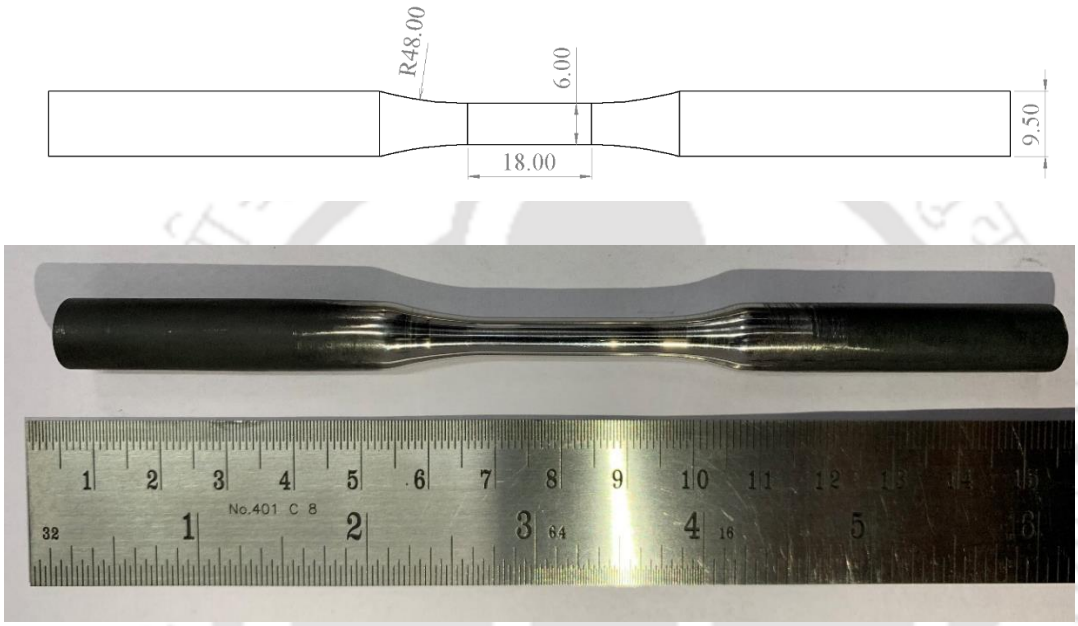

Fig. 3.16 Fatigue specimen

Table 3.5 Detail specification of various machines used for testing of welded specimens		
Machine name	Make & Model	Specification
Servo Hydraulic UTM	BISS, MEDEAN 250	• Capacity: (±) 250 kN, Actuator displacement: 0 to (±) 80 mm • Hydraulic grips of 0.1-27 mm flat specimen and 0.5 27 mm round specimen. • Test: Tension, compression and ¾ point bend test, Low cycle fatigue tests, High cycle fatigue tests, Fatigue crack

		propagation tests, K1c and J1c fracture toughness tests, Creep tests, Stress relaxation tests, shear tests, Constant true strain rate tests. • Control mode: computer controlled Load rate, elongation rate, strain rate, load hold • Hydraulic power pack pumping capacity 25 ltr/min • Testing method: Load control and position control (strain and displacement)
Hardness tester	Buehler, Micromet-2101	• Indentation force: 1, 10, 50, 100, 300, 500, 2000 g force • Dwell time: 5 to 60 s at interval of 5 s
OM	CarlZeiss Axiotech-100HD, 3D	• Magnification: 500X-5kX • Table movement: 3-axis measuring system, reflected light measuring stage 75 mm × 55 mm × 50 mm • Tubes: Binocular phototube (Siedentopf principle), 20°/23, 100 vis /100 doc • Camera: Axio-Cam and Axiovision 4.8.2 software in built
FESEM with OXFORD EDS	Zeiss, Sigma	• Specimen chamber: 330mm inner dia., 270 mm height • Specimen weight: Up to 0.5 kg tilted; up to 2 kg not-tilted • Movement: X/Y = 125 mm, Z = 50 mm, T = –10° to +90°, R = 360° continuous • Specimen stage: 5-axis motorized Cartesian • Chamber detectors: In-lens, SE-2, NEBSD • Magnification range 300 X to 1000 kX
XRD	PANalytical, X-pert	• 3 kW generator and direct optical positioning • Pre-FIX incident and diffracted beam • X-ray lens with attenuator, fixed divergence slits 1/32^{o}. • High-resolution on goniometer with optically encoded sample positioning enables a minimum step size of

		0.0001°. • Tilts of ±90°, rotation of 360°, X and Y translations of 100 mm, and vertical Z displacement of 11 mm
XRD	Rigaku Technologies, Smartlab	• Mode: Powder diffraction, thin film • Technology: Automated high-resolution θ-θ multipurpose X-ray diffractometer (XRD) with expert system Guidance software • Core attributes: 3 kW sealed X-ray tube, CBO optics, D/teX Ultra 250 silicon strip detector • Core: PhotonMax high-flux 9 kW rotating anode X-ray source, in-plane arm (5-axis goniometer), HyPix-3000 high energy resolution 2D HPAD detector, Johansson $K\alpha_1$ optics • Power: 3Ø, 200 V 50/60 Hz, 30 A (sealed tube) or 60 A (rotating anode) • Software: SmartLab Studio II software
FETEM	JEOL, 2100F	• Configuration: High resolution (HR) • Resolution: point, 0.23 nm and lattice: 0.1 nm • Acc. Voltage: 200 kV • Electron source emitter: ZrO/W(100) Schottky • 0.5 nA for 1 nm probe • HR diffraction: 333 nm
DSC	Netzsch, STA449F3A00	• Design: Top-loading • Sensor: S-type thermocouple, range: RT to 1650°C • Heating rate: 1 to 200 k/min • Sensor: TGA, TGA-DTA, TGA-DSC • Vacuum-tight: 10^{-4} mbar • Atmospheres: Inert, oxidizing, static, dynamic, vacuum • Temperature resolution: 0.001 K

		• Maximum sample load: 35000 mg (incl. crucible)
LPSA	M/s Malvern, Mastersizer 2000	• Laser: HeNe gas laser • Max. output power: 4 mW • Beam diameter: 0.63 mm ($1/e^2$) • Beam divergence: 1.5 mrad. • Beam wavelength: 633 nm.
Planetary Ball Mill	Insmart System, PBM 007	• Feed size: up to 10 mm • Output particle size: 1 micron or smaller • Speed: 40 to 400rpm • Direction rotation: programmable (forward/Reverse/Alternate with LED indication) • Time: run time (1-999Min/Sec) + off time (1-999Min/Sec) = 1 cycle, no. of cycles (1 to 999) total time = (run time + off time)*no. of cycle • Number of bowls: 4 (250 ml) • Material construction: Hardened steel with a tough core • Power supply: single phase 230V A.C., 10 Amp • Motor & drive: 1.5Kw (2HP). Microprocessor based variable frequency drive

3.17 Measurement of Residual Stress in the TLP Bonding Process

The X-ray diffraction technique for residual stress measurement is a well-established method. The complete X-ray measurement methods and derivations are discussed in detail in Ref. **[182]**. This method employs Bragg's law of diffraction to evaluate the micro-strain present in the atomic planes. When monochromatic X-rays incidents on the substrate, the reflected beams from successive planes of atoms follow the Bragg's equation given by:

$$n\lambda = 2d \sin\theta \tag{3.2}$$

where λ is the wavelength of X-rays, θ is the angle between the reflected beam and the reflecting planes, d is the inter-planar spacing and n is the order of reflections (n =1, 2, 3,…).

The presence of compressive or tensile residual stress in the substrate changes the inter-planar spacing of the substrate. The change in the *d* value leads to the shift of the X-ray diffraction peaks. The peak shift is used to estimate the residual stress in the sample.

The configurations followed during the measurement of residual stress are shown in **Fig. 3.17 (a-b)**. The planes *L1, L2* and *L3* and *S1, S2* and *S3* refer to the three orthogonal directions relative to the laboratory frame of reference and substrate, respectively. Angle α is the incident angle, Ψ describes the angle between the plane *S3* and *L3*, and ϕ is the angle between *S1* and the projection of *L3* line onto the specimen surface. $\mathrm{Sin}^2\,\Psi$ method is a widely used technique for measurement of residual stress by using several tilt angle Ψ. In this method, the strain along the *L3* direction can be obtained by using the following **equation [182]**.

$$(\varepsilon_{33})_{\phi\psi} = \frac{d_{\phi\psi} - d_0}{d_0} \tag{3.3}$$

where d_0 is the stress free inter-planar spacing, $d_{\phi\psi}$ is the inter-planar spacing at a given $\psi\phi$ direction obtained from the position of diffraction peak for a given *hkl* plane. From equation (3) after tensor transformation, biaxial stress can be determined by using the following equation:

$$\frac{d_{\phi\psi} - d_0}{d_0} = \frac{1+\nu}{E}\sigma_\phi \sin^2\psi - \frac{\nu}{E}\left(\sigma_{11} + \sigma_{22}\right) \tag{3.4}$$

where *E* and *v* are young's modulus and poisons ratio of the lattice plane, respectively, and σ_ϕ is the stress component along the S_ϕ direction (**Fig. 3.17**). It is given by:

$$\sigma_\phi = \sigma_{11}\cos^2\phi + \sigma_{22}\sin^2\phi \tag{3.5}$$

$$\sigma_\phi = \sigma_{11}\cos^2\phi + \sigma_{12}\sin 2\phi + \sigma_{22}\sin^2\phi \tag{3.6}$$

As the $\left(\frac{E}{1+\nu}\right)$ is a constant for a given material plane, the residual stress is calculated by using the linear relationship between the $\sin^2 \Psi$ and the $\frac{d_{\phi\psi} - d_0}{d_0} v$. The surface residual stress is calculated from the gradient of the least square fitted straight line obtained from the plot between the $\partial d/d$ and $\sin^2 \Psi$.

$$\sigma_\phi = \left(\frac{E}{1+\nu}\right) \times m \tag{3.7}$$

where m is the slope of the graph between the $\frac{d_{\phi\psi} - d_0}{d_0} vs \ \sin^2 \psi$.

In the current investigation, samples were cut at a distance of 1 mm from the bond centerline. The X-ray diffraction studies were carried out using a powder XRD (Make: Rigaku, Model: Micromax-007HF). Copper K_α radiation with a wavelength of 1.54 Å was used as the incident beam for the study of residual stress in the IN 718 substrate. The (111) plane was used for the current investigation. The X-ray scan was carried out from 41º to 46º at four different tilt angles i.e. 0, 20, 30, and 45º. The details of the XRD parameters are presented in **Table 3.6**.

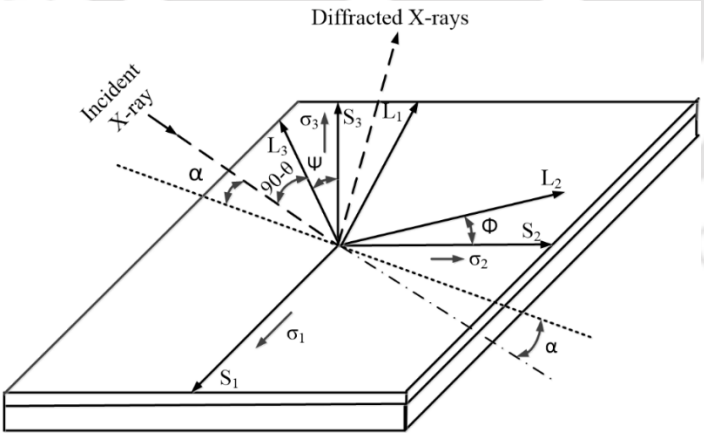

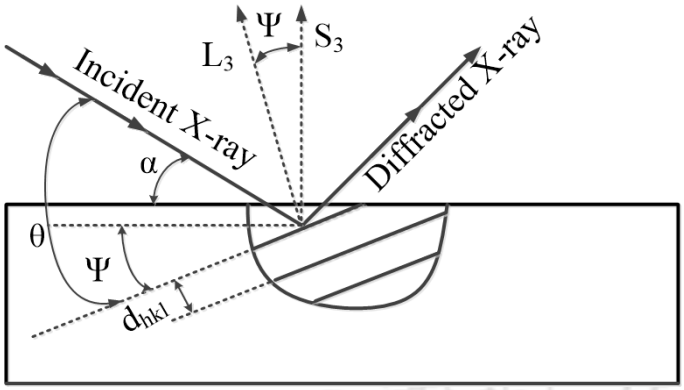

Fig. 3.17 Schematic of residual stress measurement system

Table 3.6 XRD parameters

Structure	Indices (*hkl*)	Diffraction Angle 2θ (°)	Target	Voltage(kV)	Wavelength (Å)
FCC	(111)	43.2	Cu	40	1.5403
Current (mA)	Exposure diameter (mm)	X-ray incident angle (°)	Tilt angle ψ (°)	Rotation angle (°)	Scan rate (°/min)
200	2	5	0, 20, 30, 45	20	1

In the subsequent chapter, the details of the results obtained from the experimental investigations are analyzed and discussed.

Chapter 4
Results and Discussion

4.1 Introduction

Inconel 718 (IN 718) is a precipitation-strengthened nickel-based superalloy suitable for service at temperatures from 650 to 760 °C **[13]**. It has wide application in aero-engines due to its combination of superior mechanical properties, oxidation and corrosion resistance at elevated temperatures, and outstanding weldability **[20]**. Unlike other nickel-based superalloys, this alloy has a high resistance to strain age cracking during welding or post-welding heat treatment **[12]**. However, considering the welding aspects, IN 718 has disadvantages mainly: (i) poor weld penetration (ii) micro-fissuring in the heat-affected zone (HAZ), (iii) poor ductility and impact resistance at the weld fusion zone **[6]**, and (iv) formation of a high amount of segregation and susceptibility to hot cracking in fusion welding process **[9-10]**. TLP bonding is a bonding technique, which eliminates the conventional limitations of the fusion welding process **[106]**. TLP bonding incorporates the advantageous features of both brazing and diffusion bonding techniques. Researchers preferred TLP bonding as a potential joining process for high-temperature gas turbine components, especially superalloys due to its similar bond properties **[13]**, homogeneous microstructure at the bonding area **[14]**, production of robust joint by eliminating centerline eutectics **[15]**, and bond with uniform composition profile. However, due to a lack of proper knowledge of TLP bonding, this process is not used in industries widely. To implement TLP bonding in industries, the influence of process parameters on the bond qualities, and the kinetics of the bond have to be investigated extensively.

This chapter consists of eight main sections. Section 4.2 contributes towards the TLP bonding of IN 718 using BNi-2 interlayer material and the effect of various process parameters on the bond quality. Section 4.3 contributes towards the investigation of the effect of homogenization stage of TLP bonding on microstructure evolution and mechanical property of the bond. Section 4.4 contributes towards the study of the kinetics of TLP bonding and the determination of the isothermal solidification time. Section 4.5 contributes towards the design of a post-bond heat treatment process to enhance the bond quality. Section 4.6 contributes towards determining the high-temperature tensile

properties of the TLP-bonded IN 718 samples. Section 4.7 contributes towards the calculation of residual stress of TLP-bonded joint. Section 4.8 contributes towards the determination of fatigue life of TLP-bonded IN 718 joint. Section 4.9 contributes towards the synthesis of a new nano-sized powder interlayer alloy for TLP bonding of IN 718 by mechanical alloying process.

4.2 TLP Bonding of IN 718 using BNi-2 Interlayer Material

4.2.1 Microstructure of base material

The optical micrograph of the parent metal and BMZ (2 mm from bond centerline) of the as bonded sample (ABS) is shown in **Fig. 4.1 (a-b).** In both cases, the microstructure exhibits an austenite γ-matrix with fine precipitates of metallic carbides dispersed in the matrix. ASTM-E112 standard was followed to determine the grain size of the IN 718 superalloy. The average grain size of the base material and TLP-bonded sample measured by the line intercept method are found to be 18 and 56 µm, respectively. During TLP bonding isothermal stage the samples are exposed to high temperatures which increases the grain size due to recrystallization and grain growth.

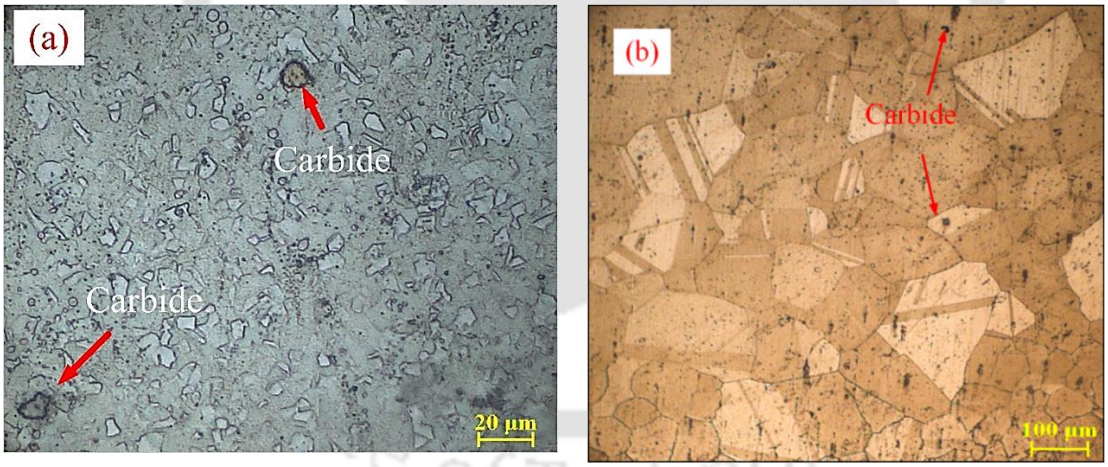

Fig. 4.1 Optical micrograph of (a) base material, and (b) base material after TLP bonding

To study the details of phases present in the IN 718 and the composition of the base material, high magnification FESEM and EDS analysis were carried out. The FESEM microstructures of IN 718 superalloy is shown in **Fig. 4.2 (a-d)**. The microstructure consists of an austenitic γ matrix, irregularly shaped fine precipitates distributed along the grain boundaries and inside the grains, and continuous delta (δ) precipitates distributed along the boundaries of grains. **Figure 4.3 (a)** shows the overall

chemical composition of the IN 718. And **Fig. 4.3 (b-c)** shows the chemical composition of the precipitates present inside the rectangle marked as A and B in **Fig. 4.2 (a)**, respectively. The EDS result reveals that the large size irregular shaped precipitates are of the carbide particles and are mainly Nb, Cr and Ti carbides. As the carbon content in IN 718 alloy exceeds 0.02 wt. %, finely dispersed carbides of Nb, Cr and Ti are observed in the structure.

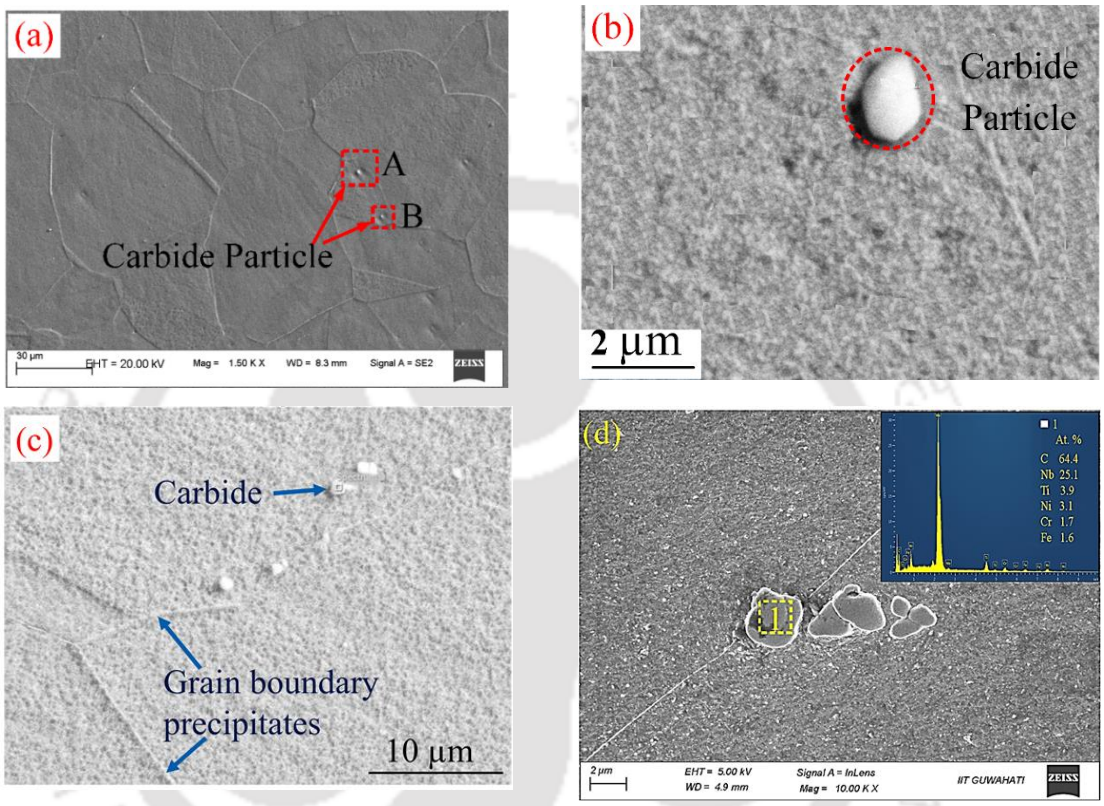

Fig. 4.2 (a) FESEM micrograph of wrought IN 718 and (b) enlarged view of MC carbides, (c) enlarged view of grain boundaries precipitates, (d) enlarge view of the grain boundary carbide

To study the presence of main strengthening phases in the IN 718, a TEM study was carried out. **Figure 4.4 (a)** shows a typical bright-field TEM image of γ′ and γ″ precipitates in the γ matrix. It can be seen that nano-size γ′, γ″ and lave phase are present in the graph along with some dislocation lines. The γ′, γ″ and lave precipitates were present in a spherical, disk, and irregular shapes, with an average particle size of 14, 8, 37 nm, respectively. **Figure 4.4 (b)** illustrates a diffraction pattern produced from a selected area i.e. the rectangle marked as 'A' in **Fig. 4 (a).** The diffraction pattern is composed of strong reflections from the γ phase and superimposed with lesser intensity γ′ and γ″ phases. The γ′ and γ″ particles were found to be coherent with the γ matrix. The diffraction spot in the SAED pattern reveals the crystalline structure of the alloy. The

SAED pattern also revealed FCC with diffraction spots corresponding to the (111), (200), (220), (311), (222), and (400) planes having d-spacing of 20.8, 1.9, 1.3, 1.1, 1.0 and 0.9 Å, respectively. **Figure 4.4 (c)** shows an HTREM image of the sample. An FFT and inverse FFT analysis of the marked area in **Fig. 4.4 (c)** confirmed that the γ′ and γ″ phases lie in the {110} plane along the <110> direction. In addition to the γ′ and γ″ precipitates, δ and carbides precipitates were also observed in the as bonded samples. The δ phase was present in the (001) crystal planes with a d-spacing value of 4.5 Å. Hexagonal MoC was found in the γ matrix along the (105) crystal plane.

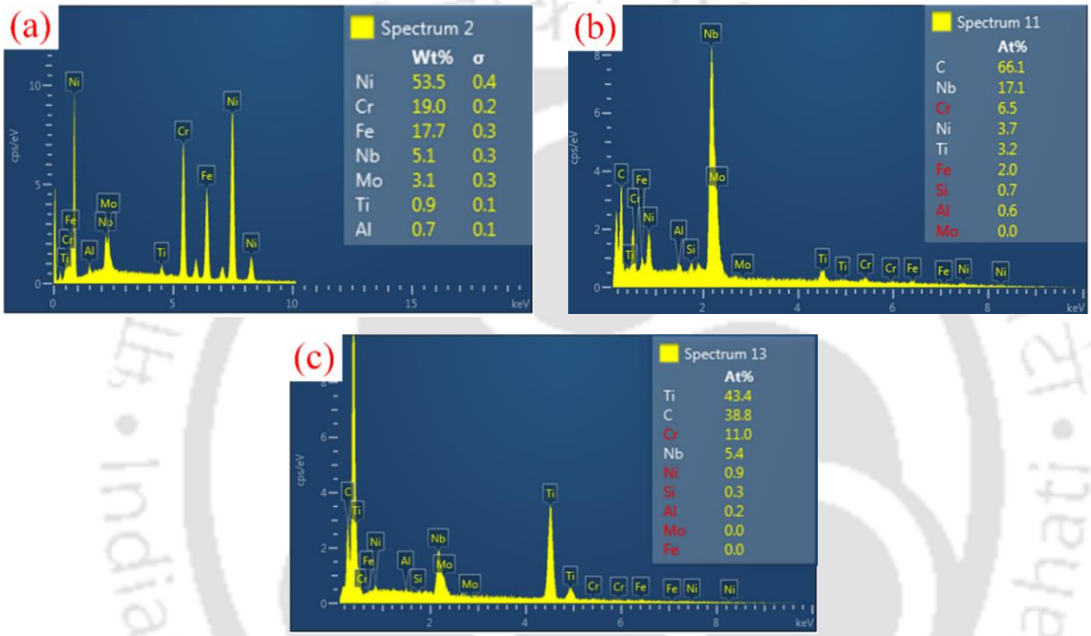

Fig. 4.3 EDS result of (a) IN 718 base material, (b) Carbide present inside rectangle A, and (c) Carbide present inside rectangle B

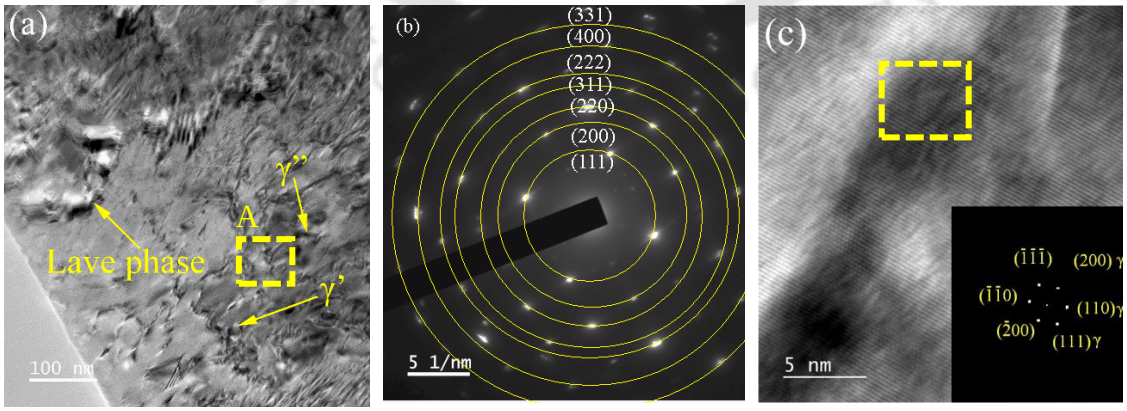

Fig. 4.4 TEM micrograph of TLP-bonded sample (a) bright-field image, (b) SAED pattern, and (c) HRTEM image

4.2.2 Microstructure of TLP-bonded IN 718 joint

Figure 4.5 shows the optical microstructure of the TLP-bonded sample for all experimental conditions. A higher magnified view of the microstructure (as shown in **Fig. 4.6**) shows the bond microstructure is divided into three zones: (i) the isothermal solidification zone (ISZ), (ii) the diffusion-affected zone (DAZ), and (iii) the base material zone (BMZ). In TLP bonding the two substrates are bonded due to a change in the composition of the interlayer. In TLP bonding of IN 718 using BNi-2 interlayer, during isothermal solidification inter-diffusion of elements between the liquid BNi-2 interlayer and the IN 718 takes place. The melting point depressant (MPD) elements viz; B and Si present in the liquid interlayer diffuses into the base material and concurrently elements like Ti, Nb, Al, Mo and Cr from the base material diffuses into the liquid zone. Due to the inter-diffusion of elements the composition of MPD at the interface move away from the eutectic composition and consequently the melting point of the interlayer at the interface rises. As a result, a new interface is formed and the width of the liquid zone decreases. This process continues until the liquid is removed completely. However, at the end of the isothermal solidification there is an MPD concentration pile up at the bond centerline, upon cooling some second phase eutectic compounds forms at the bond centerline. The solidified area formed due to the isothermal solidification is called the isothermal solidified zone. The elements diffused from the liquid interlayer into the base material reacts with base material elements and forms secondary particle. DAZ is the zone where these secondary precipitates are present. After DAZ, unaffected BMZ is formed. In this zone the chemical composition does not change much, however grain growth may occur.

In TLP bonding, due to the inter-diffusion of elements and applied pressure the width of the ISZ is lower than the thickness of the initial interlayer. In experiment no. E.1, the initial thickness of the interlayer was 80 µm, however after isothermal solidification, the width of the ISZ was reduced to 45 µm. Upon increasing the temperatures the width of the ISZ increases. The width of the ISZ for experiment no. E.6 and E.8, were found to be 57 and 71 µm, respectively, whereas their initial interlayer thickness was 80 µm. This may be due to the reason that, at higher temperature more dissolution and widening of the base material occurs and the size of the ISZ increases. In TLP bonding the liquid interlayer wets the base material and the MPD elements present in the liquid zone diffuses into the base material, which increases the concentration of the

MPD elements at the base material interface. When the concentration reaches the eutectic concentration the interface of the base material melts and dissolves.

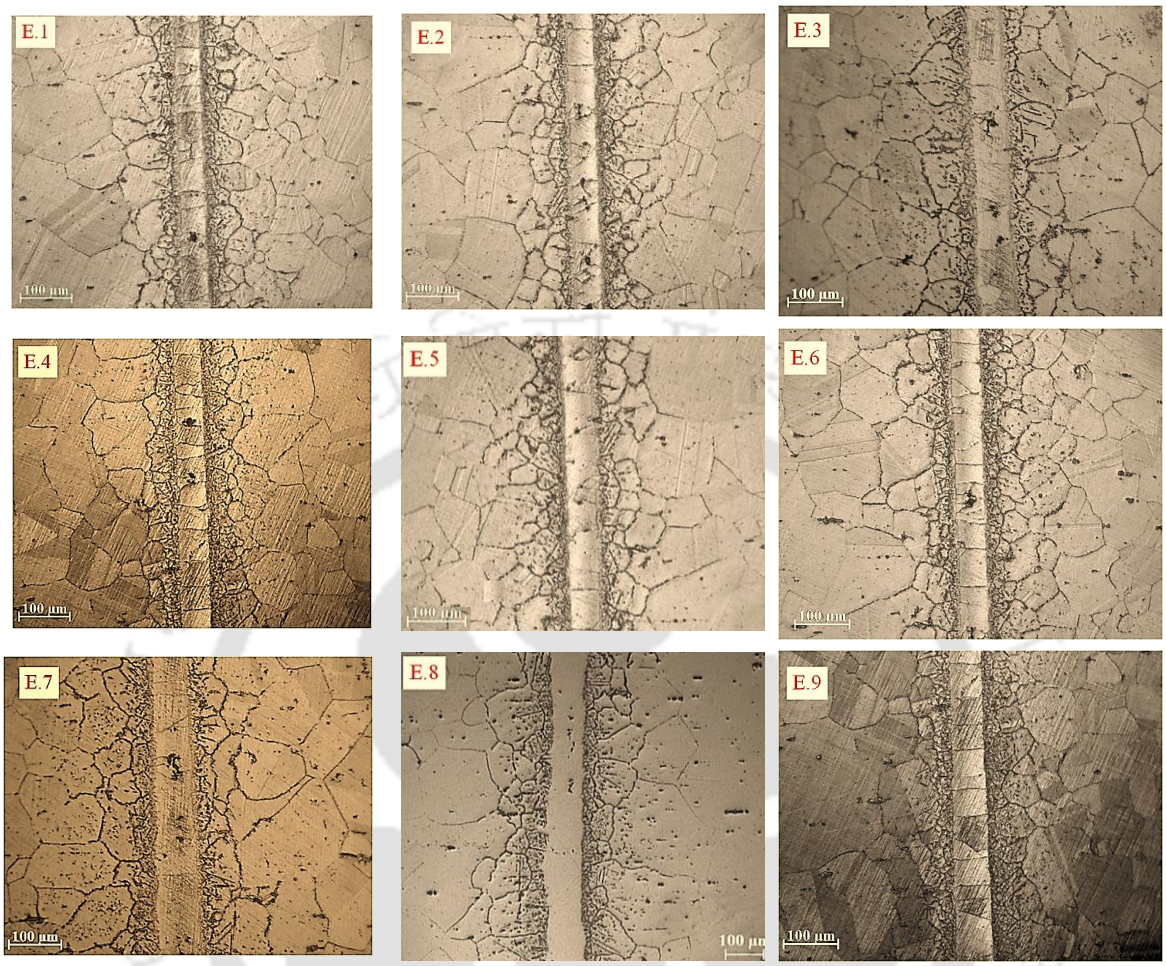

Fig. 4.5 Optical micrographs of TLP-bonded joints, experiment number is depicted inside the image

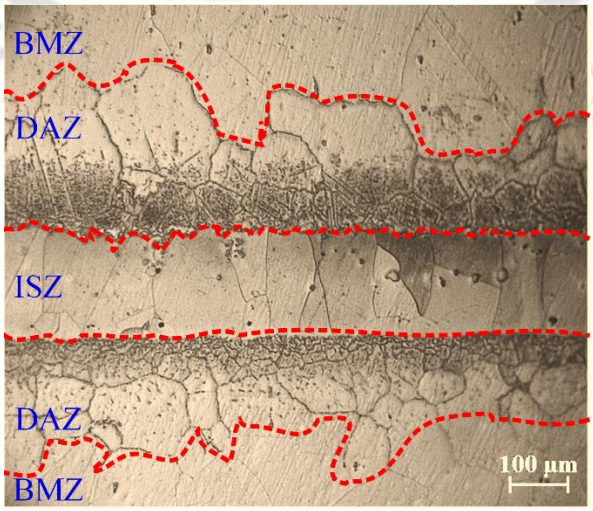

Fig. 4.6 Different zones of TLP-bonded samples for E.5

The FESEM microstructure of the TLP as bonded IN 718 joint is shown in **Fig. 4.7**. The microstructure also comprises three different zones, namely ISZ, DAZ, and BMZ. In the BMZ, the composition of the base material remained same after the bonding process. Diffusion of MPD has not reached to this region. However, microstructural changes were observed in the BMZ. During TLP bonding the base material exposed to high temperature, which is above the nucleation temperature of the δ-phase precipitates that causes formation of large number of δ precipitates along the grain boundaries. Grain boundary δ phase has a detrimental effect on the strength of the joint. To minimize the grain boundary δ-phase, standard heat treatment cycle was performed. The details are discussed in the subsequent section.

The high magnification image of the TLP-bonded sample of E.2 is presented in **Fig. 4.8 (a-c)**. The regions in **Fig. 4.8 (a)**, labelled as 'A' and 'B' corresponds to DAZ and ISZ, respectively, and magnified image is shown in **Fig. 4.8 (b-c). Figure 4.8 (b)** shows that in the DAZ metallic precipitates were formed along the grain boundaries and inside the grain. Needle, coarse irregular shape, and fine blocky morphologies of precipitates were observed at the DAZ, as shown in **Fig. 4.8 (b)**. The EDS analysis results of the precipitates marked in **Fig. 4.8 (b-c)** are presented in **Table 4.1.** The EDS results reveal that the precipitates were borides of Ni, Nb, and Cr. Needle shape and coarse irregular shape borides had higher Nb content compared to the fine blocky borides. The finely dispersed borides were mainly present inside of the grains. In IN 718, as the δ-phases are present in the grain boundaries, the Nb content at the grain boundaries is higher than that of the grains. Besides, the grain boundaries have a high affinity to the diffusion process, hence more borides are formed at the grain boundary areas. The FESEM–EDS analysis confirmed that the precipitates are Nb–Mo– Cr type borides. However, previous studies on Ni-based superalloy suggest that fine blocky, coarse blocky, and chain-type grain boundary borides are of M_3B_2, M_6B, and M_4B_3 **[182-185]** type borides, respectively. In addition to borides, a few silicides were also observed in the DAZ (marked as C). The chemical analysis of the precipitates showed, Cr silicides were formed in the DAZ. During TLP bonding, along with boron, silicon is also diffused into the base material. As the solubility of Si is less in the Ni matrix, the extra Si in the DAZ is rejected out from the matrix, and silicides are formed. EDS analysis was carried out in the ISZ and the results are shown in **Fig. 4.9**. The results reveal that precipitates are rich in B.

These borides are formed due to solidification of the residual liquid in the ISZ. Which indicate that complete isothermal solidification has not been occurred.

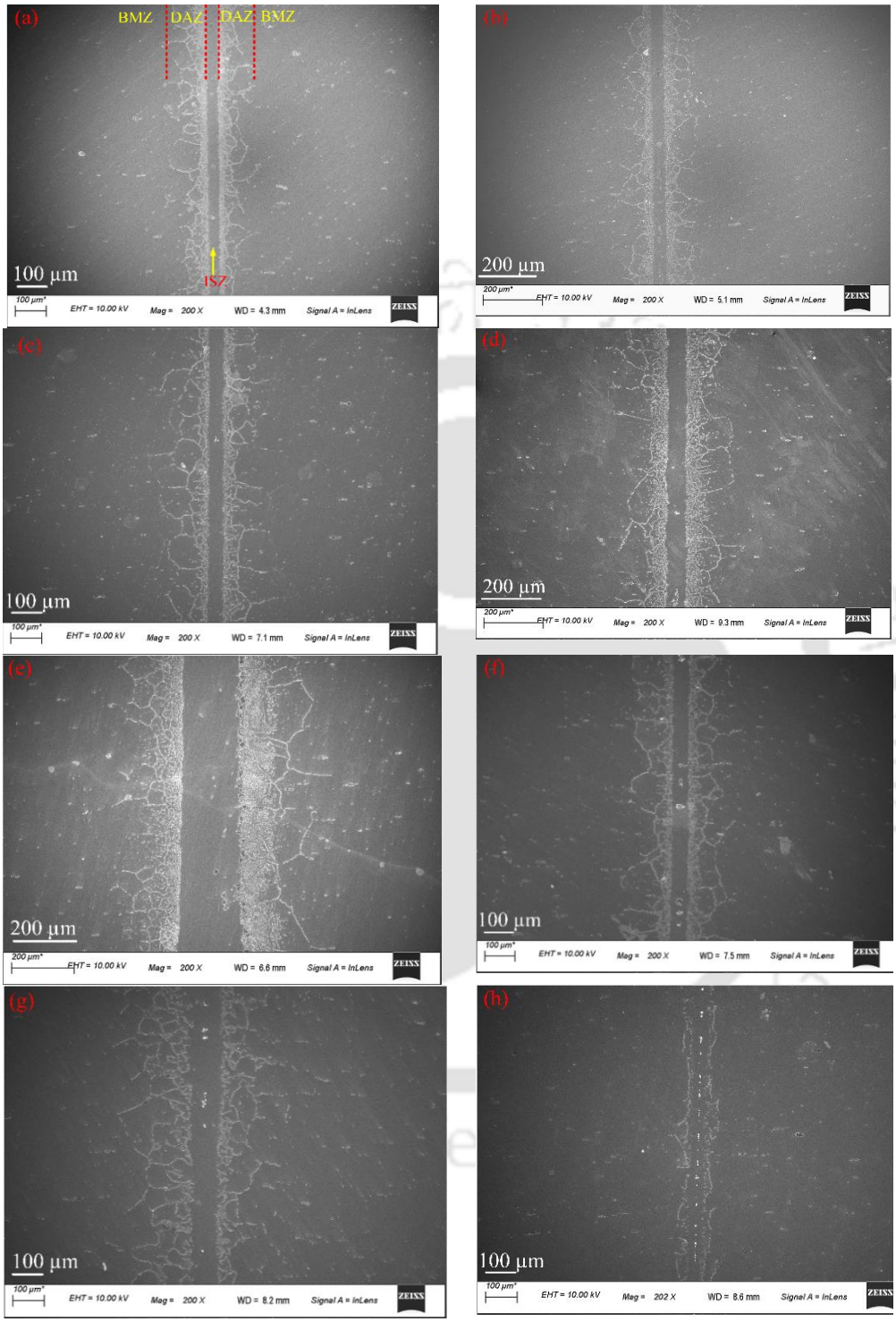

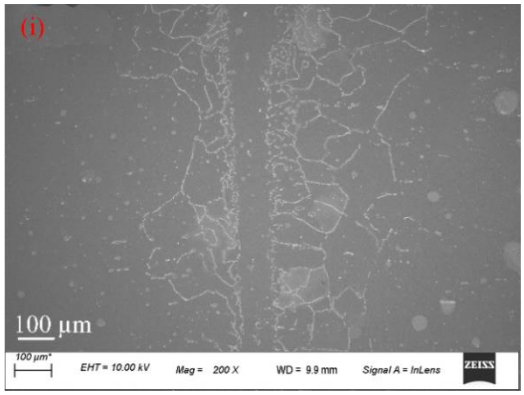

Fig. 4.7 Microstructure of TLP-bonded IN 718 samples (a) E.1, (b) E.2, (c) E.3, (d) E.4, (e) E.5, (f) E.6, (g) E.7, (h) E.8 and (i) E.9

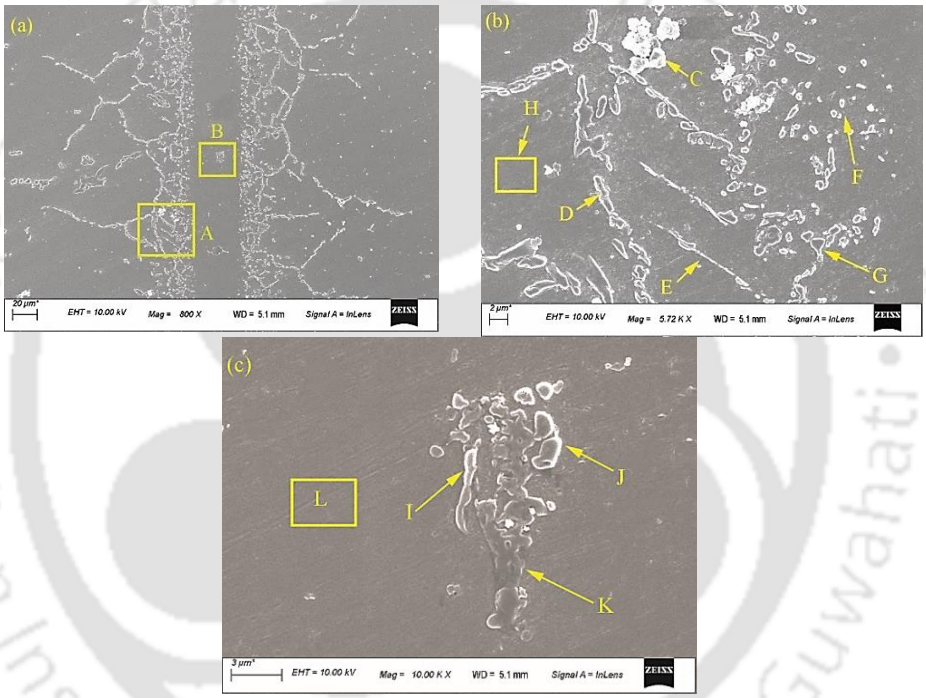

Fig. 4.8 FESEM micrograph of (a) TLP-bonded sample (Exp. No. E.2) (b) Enlarge view of DAZ (region A), and (c) Enlarge view of ISZ (region B)

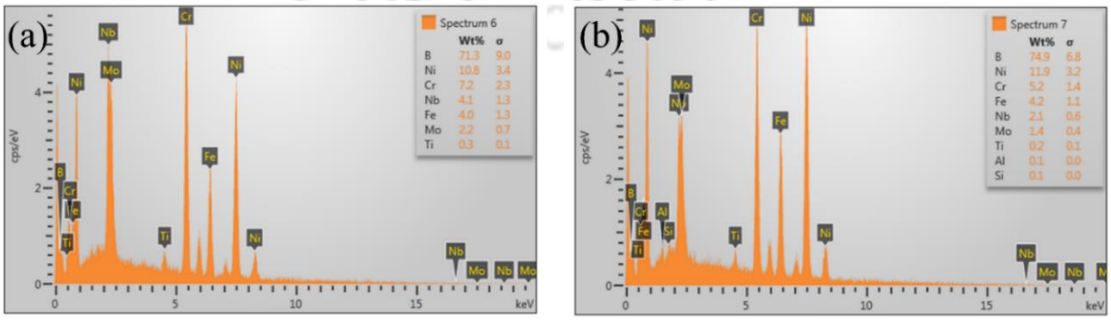

Fig. 4.9 EDS spectrum of (a) area I and (b) area J

Table 4.1 Chemical composition of precipitates that are marked in Fig. 4.8 (b-c)

Elements	Ni	Cr	Fe	Nb	Ti	Mo	Al	Si
C	6.3	46.9	2.7	4.7	0.1	0.0	3.3	36.0
D	11.1	37.9	8.0	23.2	1.5	17.4	0.5	0.4
E	11.7	36.2	8.8	25.1	0.9	16.9	0.3	0.1
F	13.8	35.9	8.1	16.7	0.7	24.2	0.4	0.2
G	5.7	34.0	5.0	37.6	0.8	16.4	0.5	0.0
H	54.5	21.2	19.4	1.8	0.8	1.1	0.9	0.3
I	6.0	44.3	16.4	2.4	30.5	0.3	0.1	0.0
J	31.4	34.7	6.1	8.1	0.0	0.0	0.6	19.1
K	2.0	72.4	11.3	0.1	0.0	0.0	8.9	5.4
L	63.1	18.0	14.8	0.9	0.4	0.5	0.4	1.9

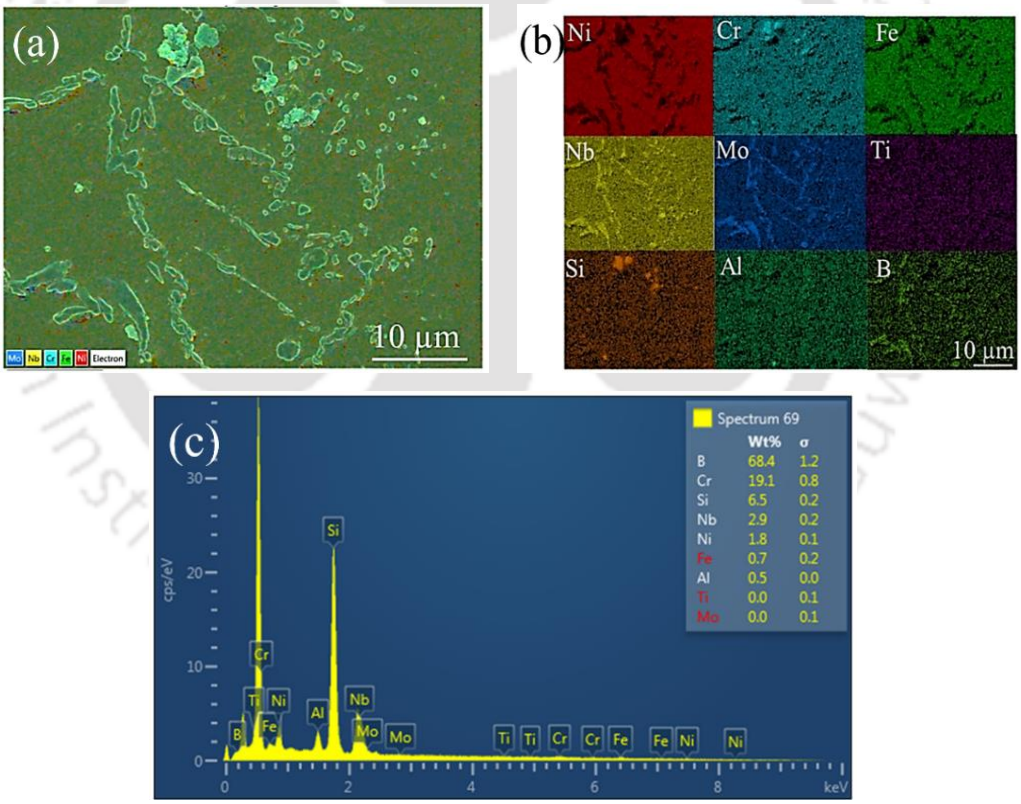

Fig. 4.10 Elemental mapping of the DAZ (Exp. No. E.2) (a) DAZ, (b) DAZ mapping and (c) EDS result of precipitates

To compare the elemental distribution in DAZ and ISZ, the EDS line scan analysis was performed and shown in **Fig. 4.11**. The elemental distribution is almost

steady in all the zones except at the point of intersection of line scan and precipitates. The change can be marked by depletion or rise in the elemental composition. At the point of intersection of precipitate and scan line, Nb, Mo, B, and Si content rose significantly and Fe and Ni content dropped. These fluctuations are due to the presence of precipitates at the DAZ. In the middle of ISZ, there is a significant rise in Al and Si peaks. This can be attributed to the presence of aluminium silicide in the ISZ. Initially, there was no Al content in the interlayer material, during IS Al from the workpiece diffused into the liquid interlayer material which leads to the formation of aluminium silicide in the ISZ.

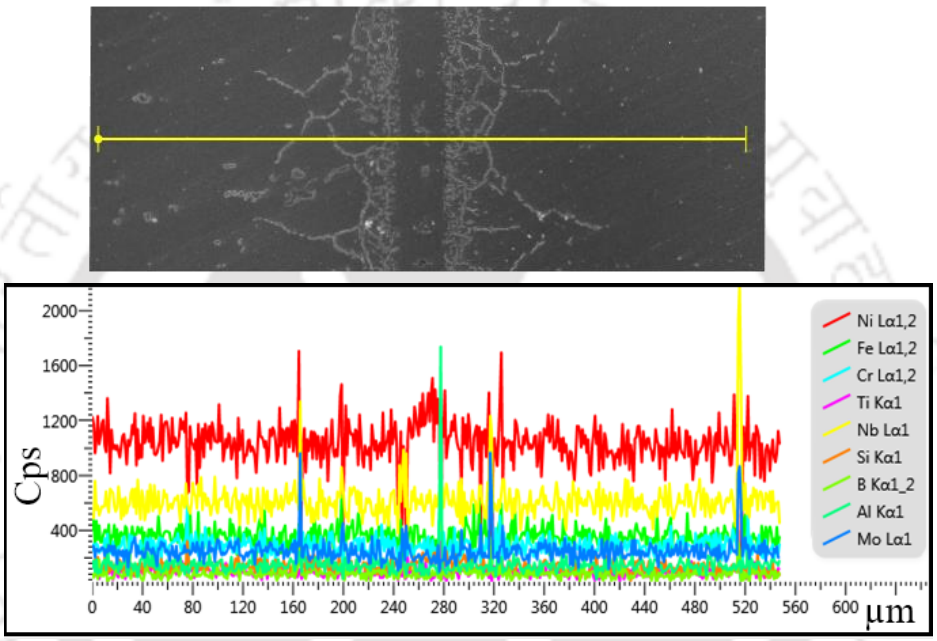

Fig. 4.11 Variation of elemental composition along a line (Exp. No. E.2)

The ISZ was formed at the center of the bond due to composition change at the constant temperature. **Figure 4.8 (c)** shows the enlarged view of ISZ. The ISZ consists of γ matrix, and Nb, Mo, Al, Ti, and Si elements as evident from the EDS results. Since the interlayer material initially did not contain Nb, Mo, Al, and Ti, the presence of these elements at the ISZ indicates the dissolution of the base material during the heating period of the TLP bonding resulting in compositional change. The compositional change resulted in the initiation of the IS. During IS at higher temperatures, elements from the IN 718 diffused into the liquid interlayer, and elements like Si and B diffused into the base material. This inter-diffusion causes variation in the composition on either side. In order to obtain a homogeneous microstructure at the TLP joint region, the bond region has to be held for sufficient time at elevated temperature to complete the IS. If the bonding time is not sufficient for complete IS, then athermal cooling occurs resulting in the

formation of secondary precipitates at the ISZ. The EDS analysis result of the ISZ is presented in **Table 4.1**. The result shows three types of compounds at the ISZ. The EDS analysis result also shows Ni-Cr, and Cr type silicide at the ISZ. In addition to silicide, Cr-Fe-Ti type compounds are also formed at the ISZ. A uniform microstructure was obtained when the bond region was held for longer bonding time and temperature compared to the bond made at the lower bonding time and temperature. EDS elemental mapping of the ISZ was carried out to check the distribution of elements in the ISZ. The EDS mapping of ISZ is shown in **Fig. 4.12**. The elemental mapping reveals that the precipitates were mainly of Cr, Al, Si, Ti, and Si. As discussed above the precipitates are silicides of Cr and Al. Which confirms the formation of silicides at the ISZ due to incomplete IS.

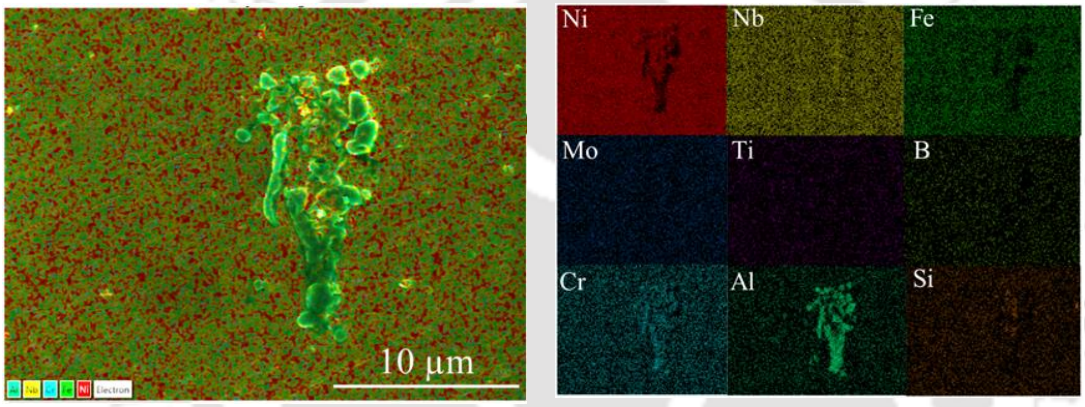

Fig. 4.12 Elemental mapping of ISZ (Exp. No. E.2)

4.2.3 Tensile strength of TLP-bonded joint

Figure 4.13 (a-b) shows tensile test results of as bonded samples. The bond formed at a bonding temperature of 1150 ˚C, holding time of 90 min, interlayer thickness of 80 µm, and a load of 19.6 kg showed maximum ultimate tensile strength (UTS) of 626 MPa. The highest tensile strength obtained in TLP bonding is 86 % of the strength of the base material. The joint strength of TLP-bonded joint depends on the extent of diffusion of solution strengthening elements (like, Mo, Ti, Al, and Nb) from the IN 718 into the bond zone, the volume fraction of strengthening precipitates (viz. γ′ and γ″) and the amount of the eutectics formed due to IS. In the ISZ of the as bonded sample, the composition of solid solution strengthening elements like Nb, Cr, Mo, Al, and Ti were lower than that of the base material. During TLP bonding interdiffusion of elements took place. If the bond is not held at bonding temperature for sufficient time, incomplete IS occurs which result in formation of eutectics in the bond zone and lowers the joint

strength. The lower UTS of the as-bonded sample compared to the base material is the result of the above phenomenon. It was observed that the bond strength at higher bonding temperature is high. At higher bonding temperature more interdiffusion of elements between base material and the liquid interlayer occurs. Which increases the fraction of solid solution element in the ISZ and at the same time reduces the fraction of formation of eutectic. Because of these two reasons the bond strength is higher at higher bonding temperature. It was also observed that the bond strength highly depends upon the IS time. Increasing IS time increases the bond strength. As diffusion is a time depended process, increasing bonding time increases the volume of interdiffusion of elements between the base material and the liquid interlayer. As a result more uniform microstructure is obtained and more strength was observed.

The ductility of the TLP-bonded sample is lower than that of the base material. As discussed in the section 4.3, there are secondary phases in the ISZ. Which are brittle in nature and during plastic deformation these particles breaks and reduces the ductility of the bond zone. Higher tensile strength and ductility were observed for the samples made at high bonding temperature and time. With high bonding temperature, the IS rate increased due to higher diffusivity of MPD elements in the Ni matrix at higher temperature. The higher diffusivity increased the quantity of Nb, Cr, Mo, Al, and Ti in the ISZ. These elements formed a solid solution with the Ni matrix and enhanced the mechanical properties of the bond. At a constant temperature, if the IS time is increased, more amount of alloying elements diffuses from the base material to the ISZ. Which increases the volume of solid solution strengthening elements in the ISZ, as a result tensile strength of the samples increases with increasing bonding time. As more interdiffusion takes place at high bonding time and temperature, the amount of second phase precipitates present at the ISZ decreases. The decrease in the number of brittle precipitates at the ISZ at higher bonding temperature and time increases the ductility of the TLP bond. Though the strength is improved by higher bonding temperature and time, the failure zone is ISZ of the TLP bond. This is due to presence of brittle eutectic phase and lower composition of the solid solution strengthening phase at the ISZ.

4.2.4 Fractography of TLP-bonded joint

The tensile fracture surface features of the as bonded samples are shown in **Fig. 4.14 (a-i)**. The fractographs reveal fine sub- dimples, with cleavage facets at few

localized areas. The dimple and void, and cleavage indicate a mixed-mode of failure of the TLP-bonded IN 718 joints. The dimples indicate the failure by micro-void initiation, growth and coalescence.

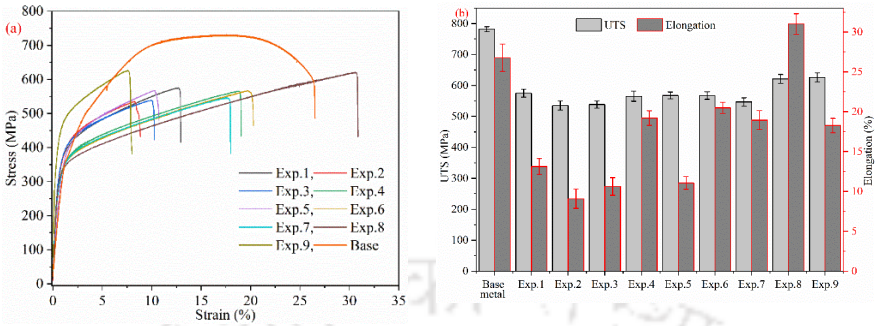

Fig. 4.13 (a) stress vs strain curve of TLP-bonded sample and (b) UTS and % elongation bar chat

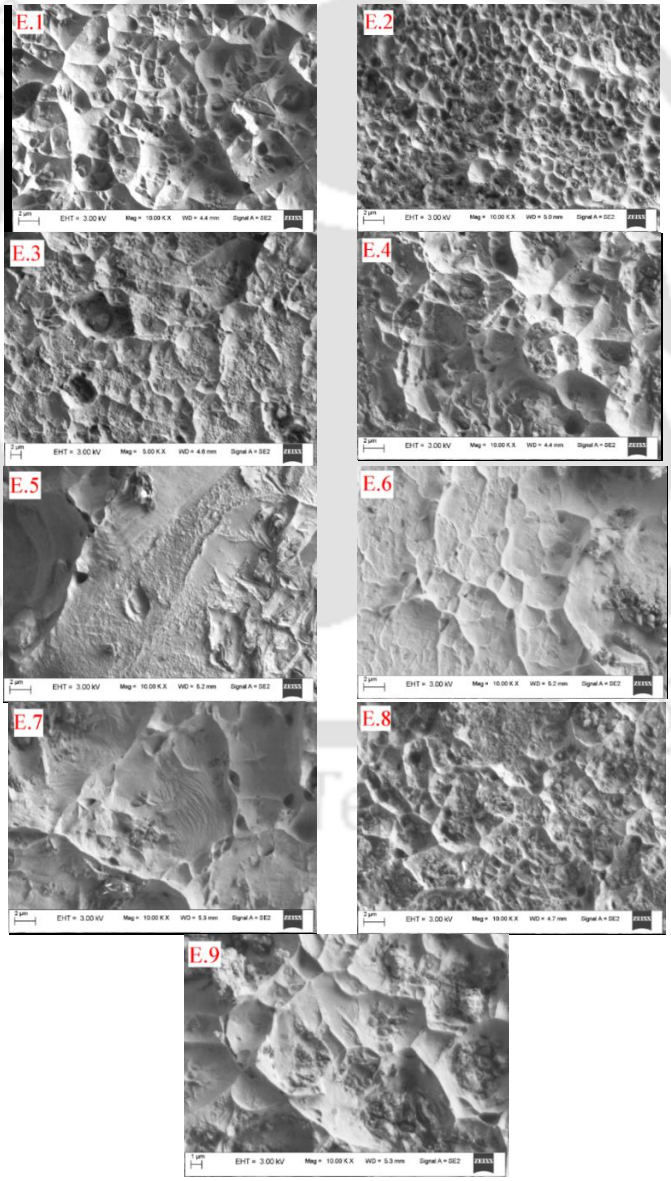

Fig. 4.14 Fractography of as bonded TLP joints

4.2.5 Microhardness result

Hardness profile across the bond area is a measure of mechanical properties of different bond zones. Hardness profile is also a good indicator to assess the degree of homogeneity and the properties of the bond. The variation of microhardness of the as bonded TLP samples across different zones are shown in **Fig. 4.15**. The hardness of TLP-bonded ISZ depends upon two factors. Firstly, the amount of secondary phases present in the ISZ and secondly the amount of solution strengthening elements like Nb, Mo, Al and Ti. The hardness of the ISZ of the bonds made at 1050 ˚C was slightly higher than the BMZ. This is due to the presence of hard brittle secondary precipitates in the ISZ. In TLP bonding, hard brittle secondary precipitates form at the ISZ due to athermal solidification of residual liquid interlayer. If the bonding time is not sufficient residual liquid remains in the ISZ, which increases the hardness of the ISZ. The hardness of ISZ of the bonds made at higher bonding temperature was slightly lower than the hardness of the base material. This is due to the insufficient diffusion of alloying elements during IS **[16, 186]** as the bonding time is less. When the bonding temperature was increased the diffusion rate also increased due to the higher diffusivity of elements at higher temperature. As a result, the volume of residual liquid decreased thereby decrease in the amount of secondary phases. At the same time the amount of solid solution strengthening elements increased. If the bonding time is not sufficient the amount of these phases are less in the ISZ compare to the BMZ. Hence at higher bonding temperature, lower hardness is observed for the ISZ. DAZ hardness was greater than the BMZ and ISZ, which can be related to the presence of Mo–Nb rich boride intermetallic precipitates in this region. As discussed earlier in section 3.2, during TLP bonding borides are formed in the DAZ. The presence of hard boride particle increases the hardness of the DAZ. The BMZ hardness was not affected by the diffusion of MPD elements during the bonding process. The hardness of the BMZ, which was bonded at a higher temperature, was slightly lower than that of the bond made at a lower temperature. This lower hardness values is attributed to the grain growth which occurred at higher bonding temperatures.

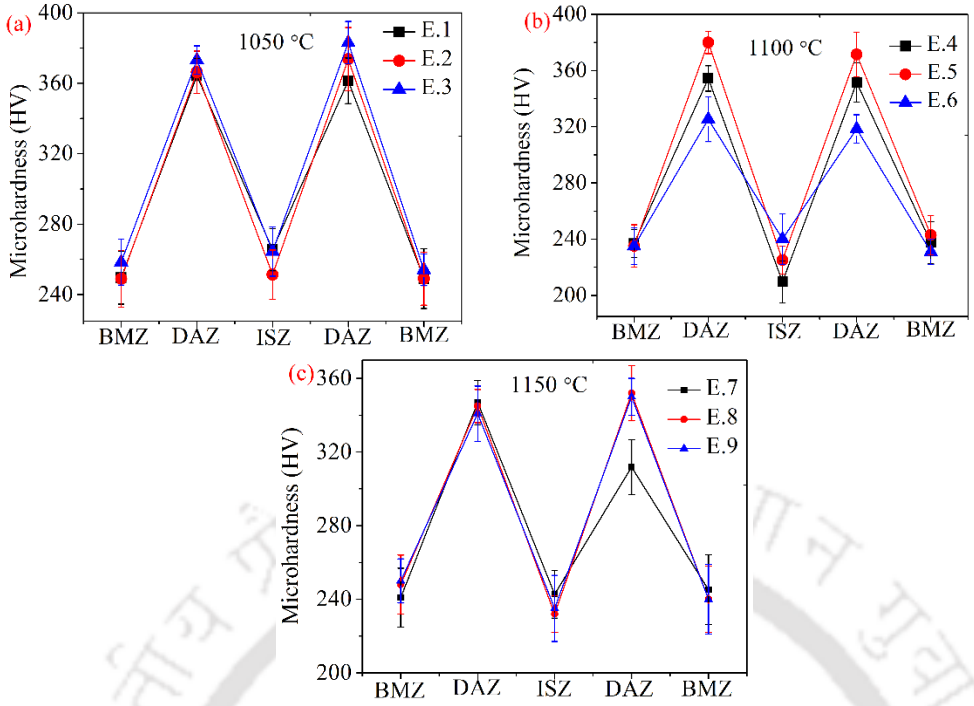

Fig. 4.15 Variation of microhardness in TLP-bonded samples, bonds made at (a) 1050 ˚C, (b) 1100 ˚C and (c) 1150 ˚C

4.3 Effect of Homogenization Stage of TLP Bonding on Microstructure Evolution and Mechanical Property of the Bond

After the isothermal solidification stage, the homogenization stage is a very important stage in TLP bonding. Even after isothermal solidification, there is always a concentration gradient in the bond zone **[106, 105]**. To eradicate the concentration gradient at the centre of the bond, homogenization of the bond has to be carried out for a sufficient amount of time. The homogenization of the TLP bond can be achieved by either extending the bonding time at the same bonding temperature or post-bond heat treatment at some other time, or holding at some lower temperature to minimize the effect of the homogenization on microstructure **[105]**. In all these cases, the TLP bond has to be held for a predetermined time interval to flatten the solute peak formed at the centre of the bond due to isothermal solidification. As the solute peak is smoothened during homogenization the re-melting temperature of the bond increases. Although the re-melting temperature of the bond increases with homogenization, the homogenization time should be programmed in such a way that a high bond strength can be achieved. In the current investigation, homogenization of the TLP bond of IN 718 is achieved as per the TTT diagram and aging response of the IN 718 base material. The homogenization of the

TLP bonding of IN 718 is achieved as per the temperature and time schedule as shown in **Fig. 4.16**.

4.3.1 Microstructure evolution during the homogenization stage

The homogenization is carried out in two temperature-steps. In the first step of homogenization, the samples are held at 760 ˚C for 8 h, during this period the primary strengthening phase γ″, and secondary strengthening phase γ′ precipitates as per the TTT diagram of IN 718 shown in **Fig. 4.16**. However, if the soaking time pasts 8 h at 760 ˚C temperature, δ-phase may start to precipitate. The δ-phase sometimes may deteriorate the mechanical properties of the IN 718. Therefore, the temperature is lowered to 660 ˚C so that the homogenization process can be carried out without forming any harmful phases. Due to this reason, a two-step homogenization was performed in this current study.

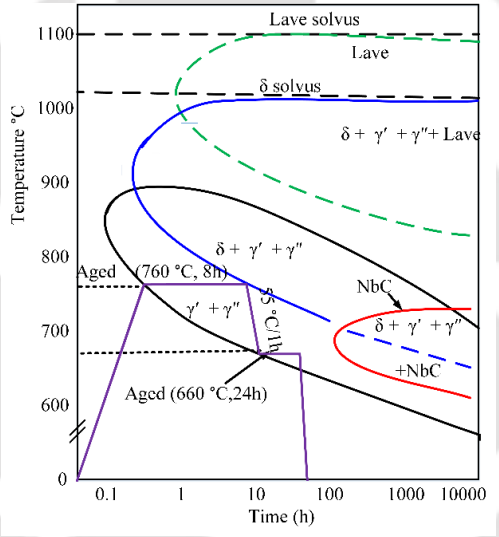

Fig. 4.16 Schematic diagram of homogenization of IN 718 bond

The microstructure of the TLP-bonded samples, homogenized for various time intervals is shown in **Fig. 4.17 (a-e)**. The microstructure of as bonded sample is shown in **Fig. 4.17 (a)**. The figure shows a typical TLP-bonded microstructure consisting of four zones viz.; (i) ASZ, (ii) ISZ, (iii) DAZ, and (iv) BMZ. The microstructure of the as-bonded samples is consisting of intermetallic compounds at the centre of the bond with size ranging from 2 to 10 μm is the ASZ. This zone is formed due to athermal solidification of the residual interlayer liquid. In the DAZ, needle, irregular shaped fine and coarse precipitates are distributed along the grain boundaries and inside the grain. The ISZ is formed at the bond area due to diffusion assisted isothermal solidification. In

this zone, no intermetallic is found. It is only made of austenitic γ-matrix with some solid solution strengthening elements diffused from the base material. **Figure 4.17 (b-f)** shows the microstructure of the TLP bond homogenised for various time intervals. From the figure it can be seen that the size of the ASZ decreases gradually with increasing the homogenization time. After 32 h of homogenisation, the ASZ is almost vanished and only three zones namely; ISZ, DAZ and BMZ is present. Moreover, it was observed that the width of the ISZ+ASZ remained almost same throughout the homogenisation process. During the homogenisation the solute peak that was resulted due to the isothermal solidification was homogenized and a uniform ISZ is obtained. To observe various phases involved during homogenization, high magnification FESEM analysis of different zones are carried out.

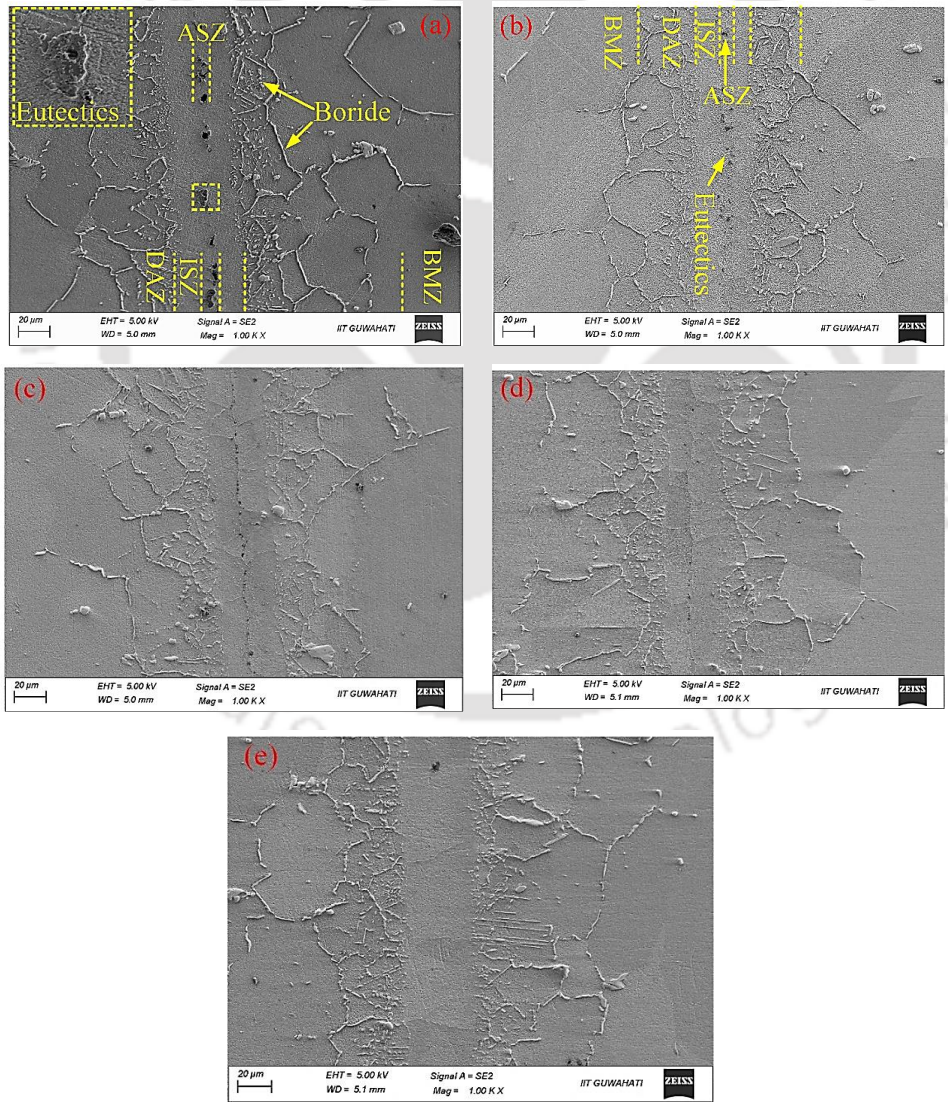

Fig. 4.17 Microstructure of TLP-bonded sample after homogenisation of (a) 0 h, (b) 8 h, (c) 16 h, (d) 24 h and (e) 32 h

The high magnification image of the ISZ of the TLP-bonded samples homogenized for different time intervals are depicted in **Fig. 4.18 (a-e)**. The micrograph shows presence of precipitates like spherical shaped-γ′, disc shaped-γ″, needle shaped-δ and irregular shaped lave phase precipitate in the ISZ of the TLP-bonded samples homogenized for various time intervals. **Fig. 4.18 (a)** shows the microstructure of the ISZ of the as bonded sample. The figure reveals the presence of a large number of lave phase in the as bonded samples. The lave phase are present in irregular shapes and are marked as circle in the **Fig. 4.18 (a)**. The EDS analysis results of the lave phase marked in the **Fig. 4.18 (a)** is shown in **Fig. 4.19 (a)**. The EDS results reveals that the lave phase are Ni-Nb rich particle. Which confirms these particles are lave phase. Moreover, a small amount of δ phase was also observed in the as bonded sample. The size of the δ phase is very small. **Figure 4. 18 (b-e)** shows the high magnification microstructure of the ISZ of TLP-bonded sample homogenized for various time intervals. The micrographs shows presence of γ″, γ′, δ, and lave precipitates in the ISZ of the homogenized sample. It was also observed that the volume of γ″, and γ′ precipitates have increased with homogenization time. As the homogenization temperature is below 750 ˚C, lave and δ-phase do not dissolves completely even after 32 h of homogenisation. However, at elevated temperature the inter-diffusion of elements between the Nb-rich particle and γ-matrix is high. Which results in partial dissolution of lave and δ-phases and formation of γ″, and γ′ precipitates. Moreover, during homogenization stage, the Nb and Al present in the intermetallic of the ASZ diffuses into the γ-matrix of the ISZ. These Nb, and Al combines with the Ni-matrix and forms the γ″, and γ′ precipitates, respectively. This inter-diffusion of elements dissolves the intermetallic phases present in the ASZ and reduces its size to get the homogenised microstructure. Also, during homogenization stage, some Nb and Al diffuse from the base material into the bond area and forms the γ″, and γ′ precipitates. As homogenization time is increased, more γ″, and γ′ precipitates forms at the ISZ, which increases the tensile strength of the TLP bond. However, after 32 h of homogenization the precipitation of γ″, and γ′ are saturated due to unavailability of extra Nb and Al element. As a result, no more precipitation of γ″, and γ′ occurs in the ISZ. The EDS analysis results of lave and δ-phase precipitates marked in the **Fig. 4.18 (e)** is shown in the **Fig. 4.19 (b-c)**. The figure revels these phases are Nb rich lave and δ phase.

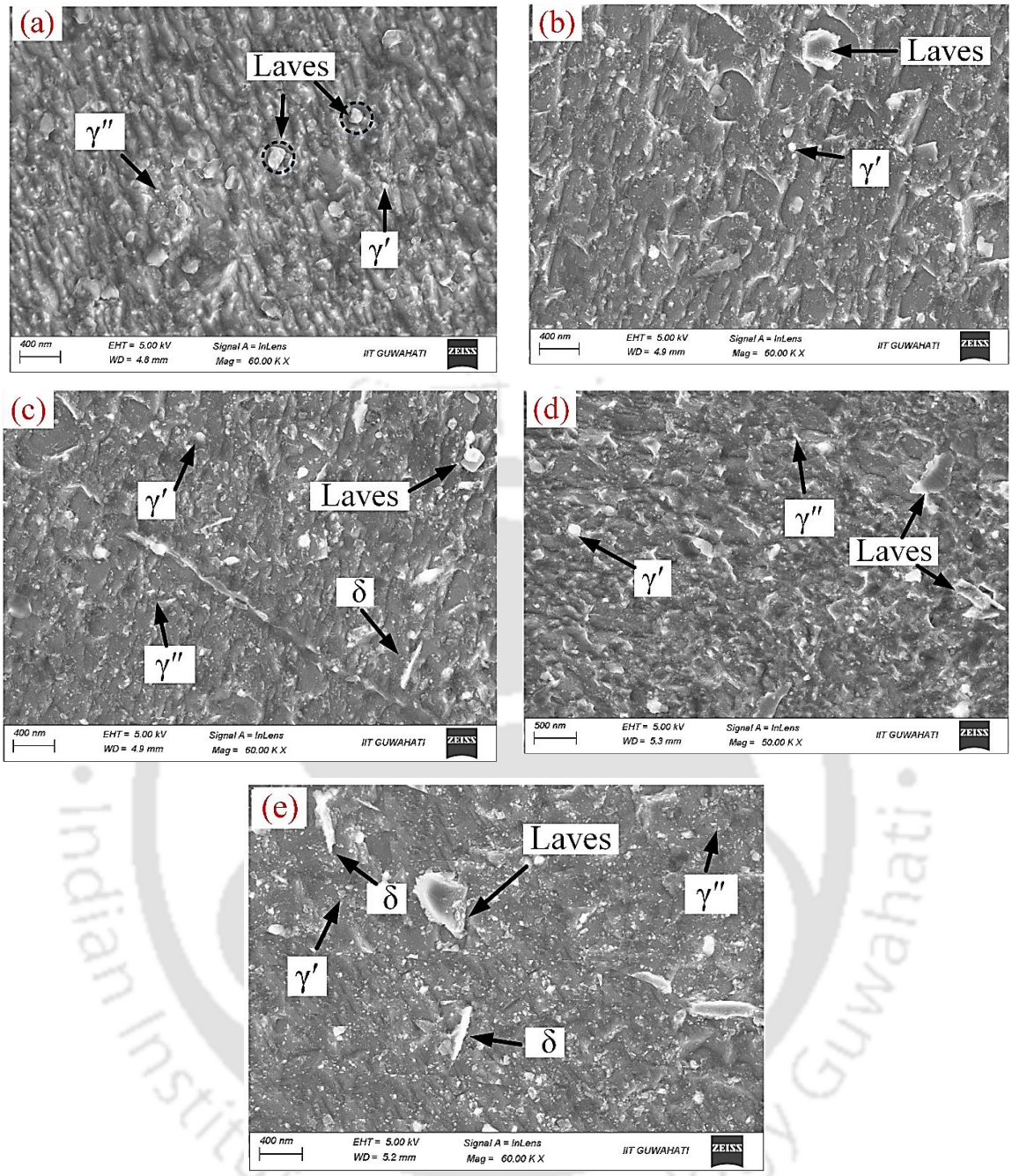

Fig. 4.18 High magnification microstructure of ISZ of TLP-bonded sample after homogenisation of (a) 0 h, (b) 8 h, (c) 16 h, (d) 24 h and (e) 32 h

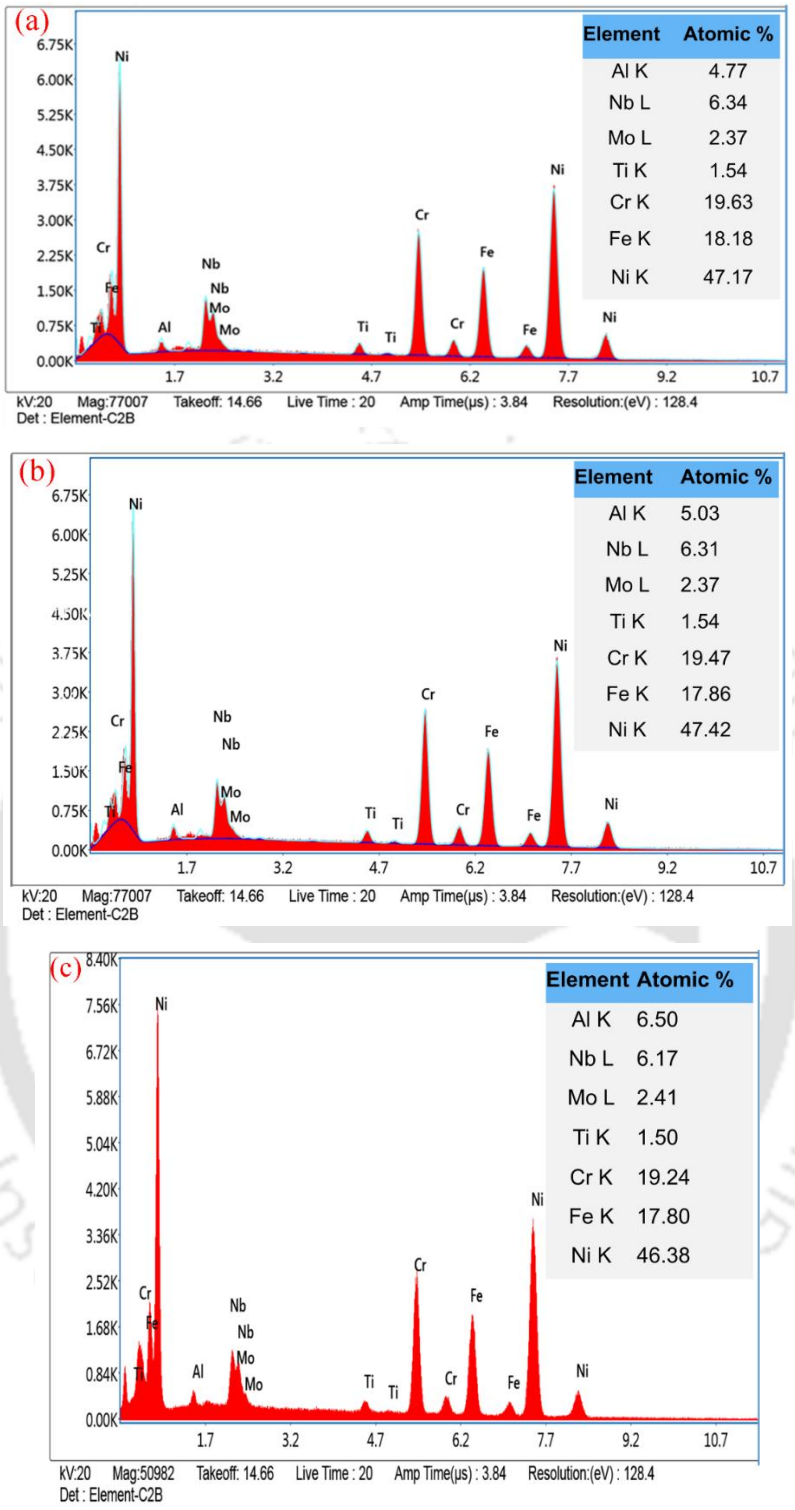

Fig. 4.19 The EDS analysis result of the (a) lave phase of the as bonded sample, (b) lave phase of TLP-bonded sample after 32 h of homogenization, (c) δ phase after 32 h of homogenization

Figures 4.20 (a-b) show the higher magnified image of the DAZ of the as bonded and 32 h homogenized samples, respectively. In the DAZ, in both the samples,

precipitates are observed along the grain boundaries and inside the grain in the shape of needle, fine and coarse irregular shapes. The EDS analysis of the precipitates is presented in **Fig. 4.20 (c)**. The EDS analysis shows the precipitates are Nb-Cr-Mo type borides. In **Fig 4.20 (b)**, it can be seen that there are grooves present in some boride particles, which indicates partial dissolution of the borides. It is also observed that some long-needle-shaped precipitate particles are broken into small pieces. During the homogenization stage, material transportation between the precipitates and the γ-matrix occurs due to the concentration gradient between the precipitate and matrix. This causes partial dissolution and fragmentation of the precipitates. Calculation of the fraction of precipitate by ImageJ software shows that with increasing the homogenization time the fraction of precipitates reduced. The fraction of the precipitate in the DAZ is presented in the **Table 4.2**.

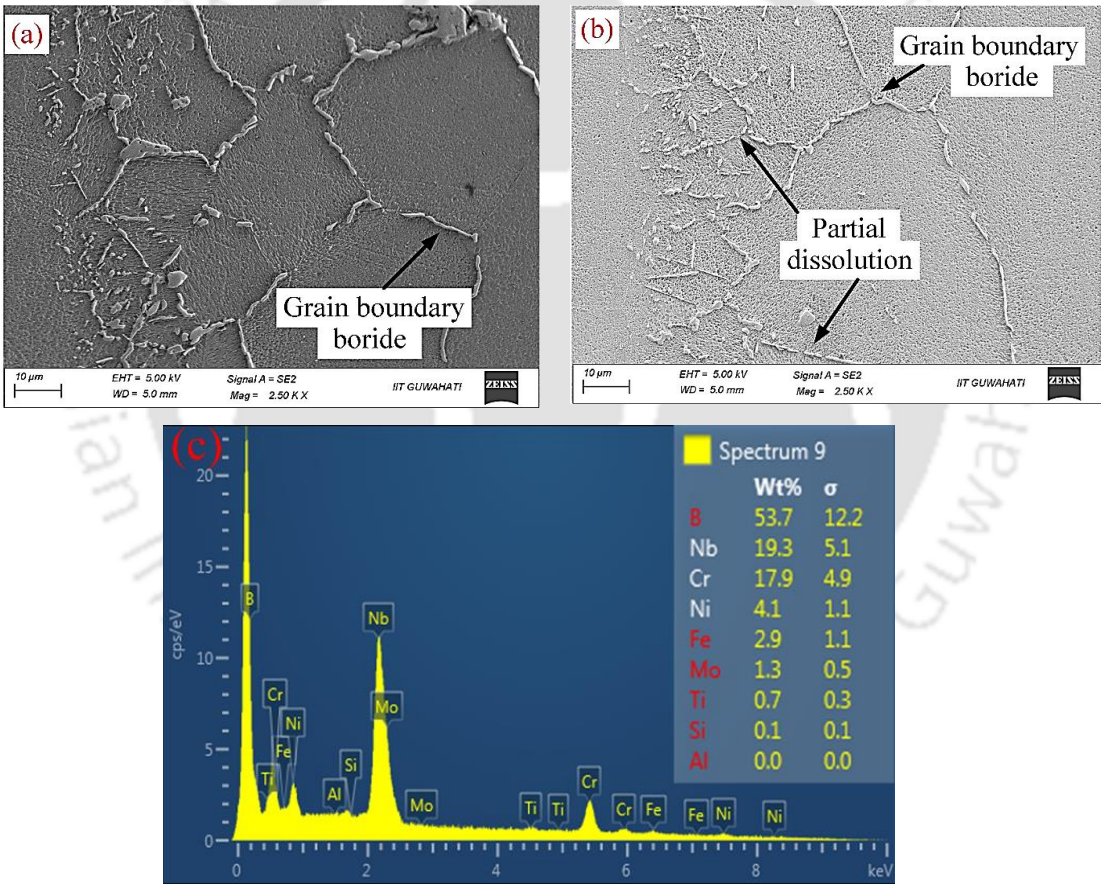

Fig. 4.20 DAZ borides (a) ABS, (b) 32 h homogenized sample, and (c) EDS result of boride

Table 4.2 volume fraction of boride after homogenization

Homogenisation time (h)	Area fraction of boride
0	13.5
8	11.6
16	8.5
24	5.6
32	4.5

The higher magnification microstructure of the BMZ of the homogenized sample is shown in **Fig. 4.21 (a-e)**. The TTT diagram indicates the possible strengthening phases like; γ′ and γ″ may precipitate during homogenization, and δ and lave phase during TLP bonding of IN 718. The microstructure reveals the presence of spherical shaped-γ′, disc shaped-γ″, needle-shaped-δ and irregularly shaped lave phase precipitate in the γ-matrix. The grain boundaries of the as-bonded samples consist of precipitate in a continuous manner (as shown in **Fig. 4.21 (a)**). The EDS analysis result of the grain boundary precipitate (rectangle marked as 'a' in Fig. 4.20 (a)) is shown in **Fig. 4.22 (a)**. The results indicate that the precipitates are Ni-Nb-Al-rich precipitates. However, after homogenization, the δ-phase, and lave phases are found in the grain boundaries in a discrete manner. This indicates the dissolution of the grain boundary δ and lave precipitates during homogenization. The EDS analysis of the grain boundary precipitates and intra-granular precipitate are shown in **Fig. 4.22 (b-c)**. The EDS analysis results shows the grain boundary precipitates and intra-granular precipitates are rich in Nb and Al. Which reaffirms the precipitates are δ-phase, and lave phases. In addition to that, nano-sized disc shapes and spherical shapes precipitates are found in the BMZ of the samples. The EDS analysis at higher magnification of these precipitates indicates that the spherical particles are rich in Al, whereas the disc-shaped particles are rich in Nb. The EDS analysis of the disc and spherical shape precipitates are shown in **Fig. 4.22 (a-b)**. This reaffirms that these precipitates are γ′ and γ″. In the as bonded sample (**Fig. 4.20 (a)**), the fraction of these precipitates is less compared to the homogenized sample. And the fraction of precipitate increases with increasing the homogenization time. During the homogenization time, Nb available in the matrix rearrange themselves in the Ni-matrix to form a coherent Ni_3Nb phase (γ″ precipitate). Similarly, the Al and Ti along with Ni forms a less coherent Ni_3 (Al, Ti) γ′ precipitate. With increasing the soaking time more

and more phases are formed in the γ-matrix. These phases are the strengthening phases which increases the strength of the material.

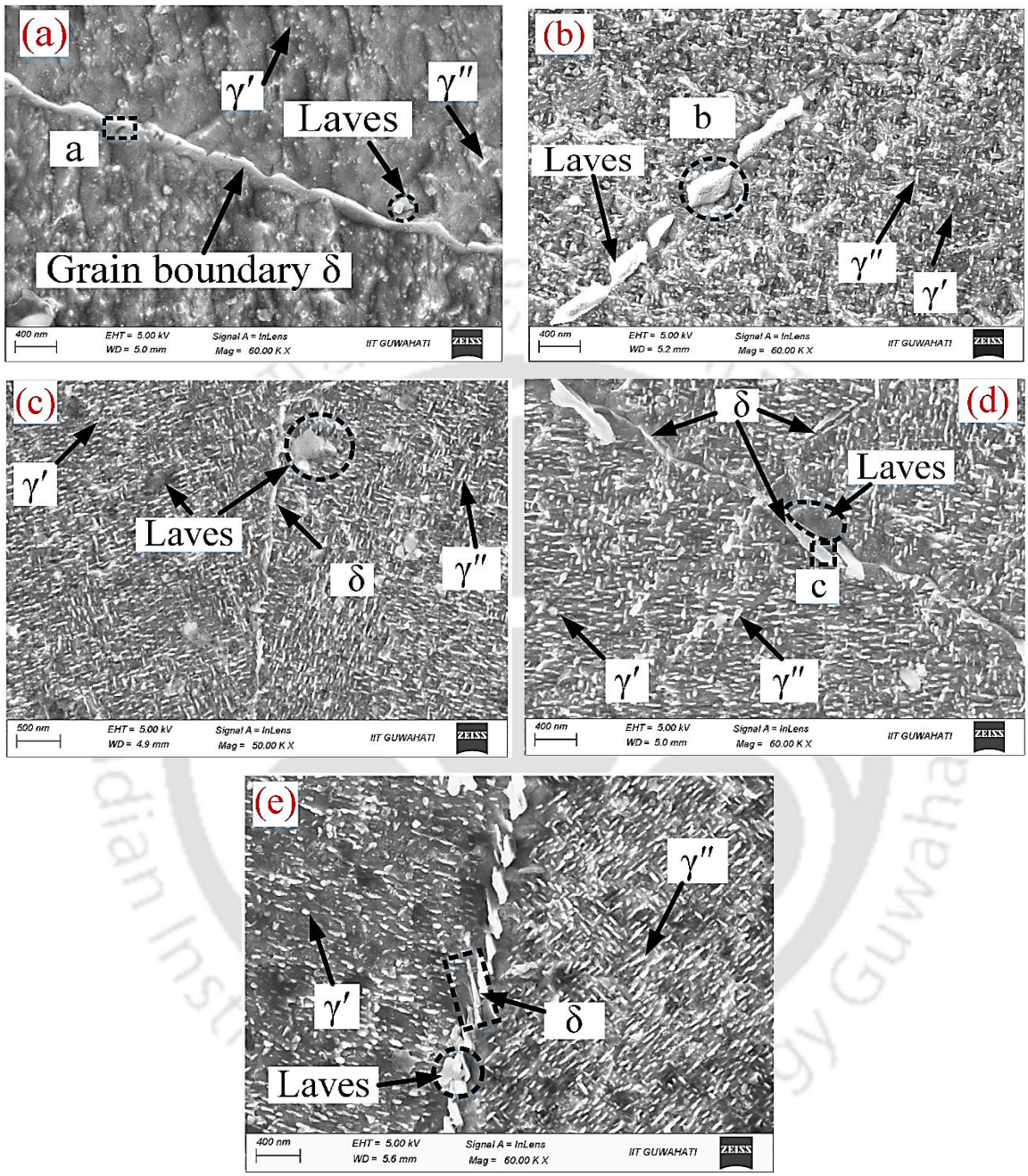

Fig. 4.21 High magnification microstructure of BMZ of TLP-bonded sample after homogenisation of (a) 0 h, (b) 8 h, (c) 16 h, (d) 24 h and (e) 32 h

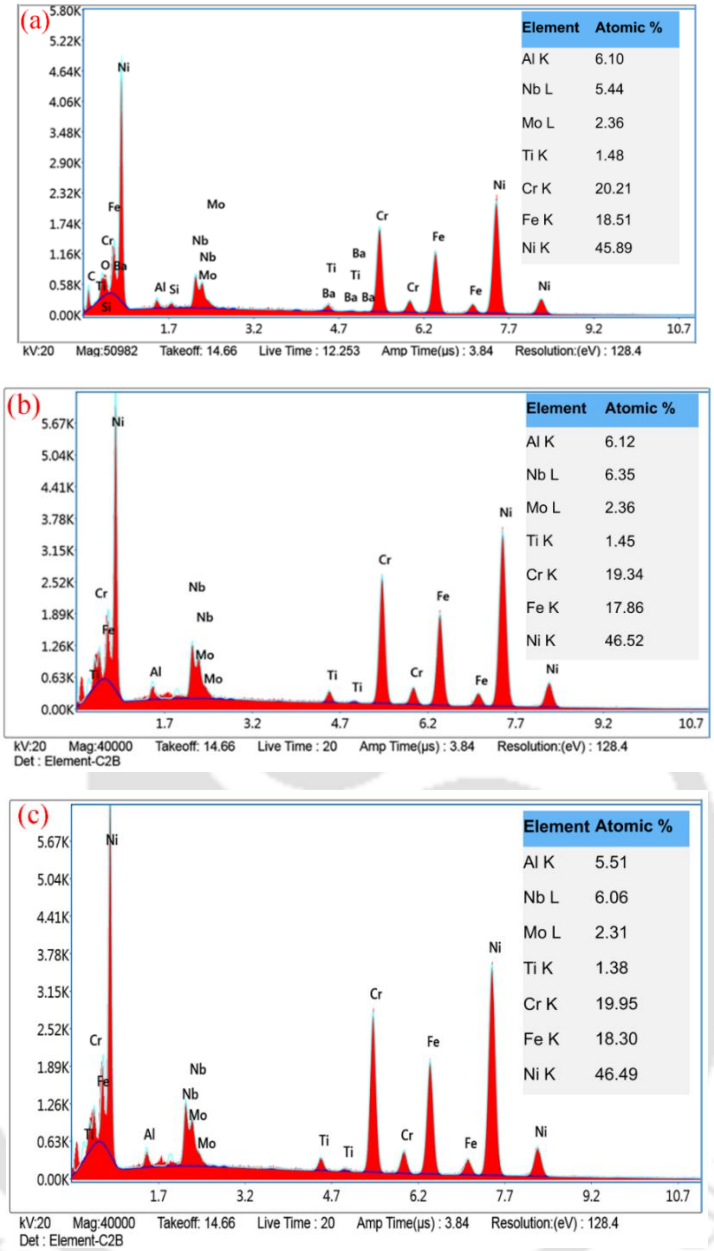

Fig. 4.22 EDS results of (a) Grain boundary δ phase of the rectangular section marked as 'a', (b) lave phase of the circular section marked as 'b' and (c) δ phase of the rectangular section marked as 'c'

4.3.2 XRD analysis

The XRD analysis of the transverse section of the bond zone of the TLP-bonded sample homogenized for different time intervals is shown in **Fig 4.23**. Prominent peaks of γ, γ′ and γ″ phases are evident and are indexed in the figure. In the as-bonded sample, strong diffraction peaks of γ-matrix are observed, mainly dominating in (111) plane ($2\theta \simeq 43.5^{\circ}$). Also, a peak of very small intensity corresponding to NbC at $2\theta \simeq 35.5$ was observed. The peaks corresponding to lave or delta phase were not observed in the

homogenized samples. As γ, γ′ and γ″ phases are the predominant peaks and the volume fraction of carbides, δ and lave phases are very small, reflections from the planes of these phases were not observed in the XRD results. However, the presence of these phases was evident from FESEM studies. In addition to this, there is significant peak shift and broadening of the peak observed with respect to the homogenization time as shown in **Fig. 4.24**. The peak is shifts toward the right side. Which indicate the formation of the secondary phase. The peak broadening was observed due to the presence of micro strain in the samples. During homogenization, there is formation of the γ′ and γ″ phases in the γ matrix. As there is size difference between the γ and γ′, and γ″ phases, there is formation of micro strain in the sample due to lattice miss-match. Which broadens the width of the peak. The figure also, reveals that the diffraction peaks coming from γ, γ′ and γ″ phases are overlapped and are hard to distinguish individually **[187]**. Deconvolution of peaks is carried out for the peak separation. To estimate the volume fraction of γ, γ′, and γ″ phases present in the samples, the integrated area method is followed. The significant peaks corresponding to γ, γ′, and γ″ phases are separated by deconvolution using peak fit-4 software as shown in **Fig. 4.25 (a-e)**. The integrated area of corresponding peaks is determined and the volume fraction of phases is calculated by using the following equation:

$$V_{f,i} = \frac{A_i}{\sum A_i} \tag{4.1}$$

where $V_{f,i}$ is the volume fraction of a phase, A_i is the integral area of that phase, and ΣA_i is the total integral area of all phases obtained from the XRD pattern. The volume fraction of the different phases in the homogenized samples is shown in the **Table 4.3**. It was found that the volume fraction of γ″+ γ′ phases increased with time of homogenization.

Table 4.3 volume fraction of various phases

Phase / Sample	γ	γ′	γ″	γ″+ γ′
0 h	90.4	3.4	6.2	9.6
8 h	88.5	4.6	6.9	11.5
16 h	83.7	6.2	10.1	16.3
24 h	79.0	7.6	12.5	20.1
32 h	75.4	9.5	15.1	24.6

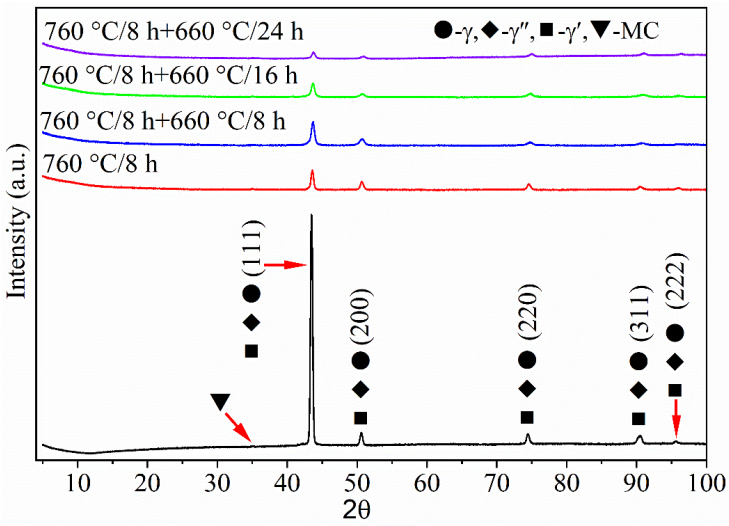

Fig. 4.23 XRD analysis of homogenised samples

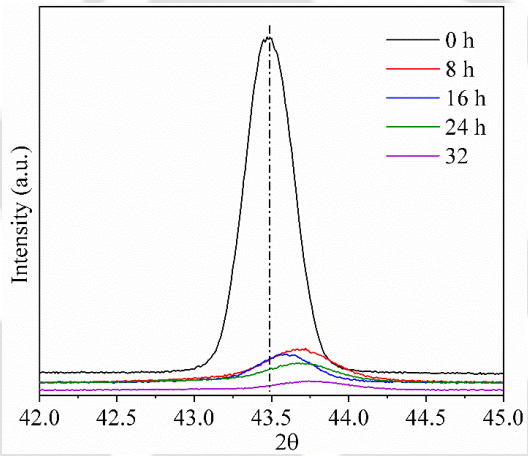

Fig. 4.24 Peak shift and broadening

4.3.3 Hardness variation with homogenization

The hardness variation across the bond regions is a measure of mechanical properties of the bond. The variation of hardness at various zones of TLP-bonded IN 718 joint and homogenized joint is depicted in **Fig. 4.26**. The variation of the harness of the as bonded sample is already explained in section 4.2.5. In this section, the effect of homogenization time on the variation of hardness across bond line is explained in details. From **Fig. 4.26**, it be seen that the hardness of the BMZ increases with homogenisation time and attains some equilibrium after 24 h of homogenisation. The increase in the hardness at the BMZ is due to increase of volume fraction of strengthening precipitates during homogenisation stage. In first stage of homogenisation, the TLP-bonded sample is held at 760˚C for 8 h. During this periods more γ″ and γ′-phase precipitates. As a result

a sharp increase in the hardness is observed in the BMZ. In the second stage of the homogenisation, the sample is held isothermally at 660 ˚C for various time interval. In this periods both γ′ and γ″ precipitates. However, the precipitation rate of γ′ is higher than the γ″. As the formation of γ″ depends upon the availability of Nb content in that area. As the time passes, the content of Nb decreases at the BMZ resulting in reduction of precipitation rate of the γ″. Therefore, with increasing the homogenization time further has little effect on the hardness value of the BMZ and almost attains equilibrium after 24 h of homogenisation.

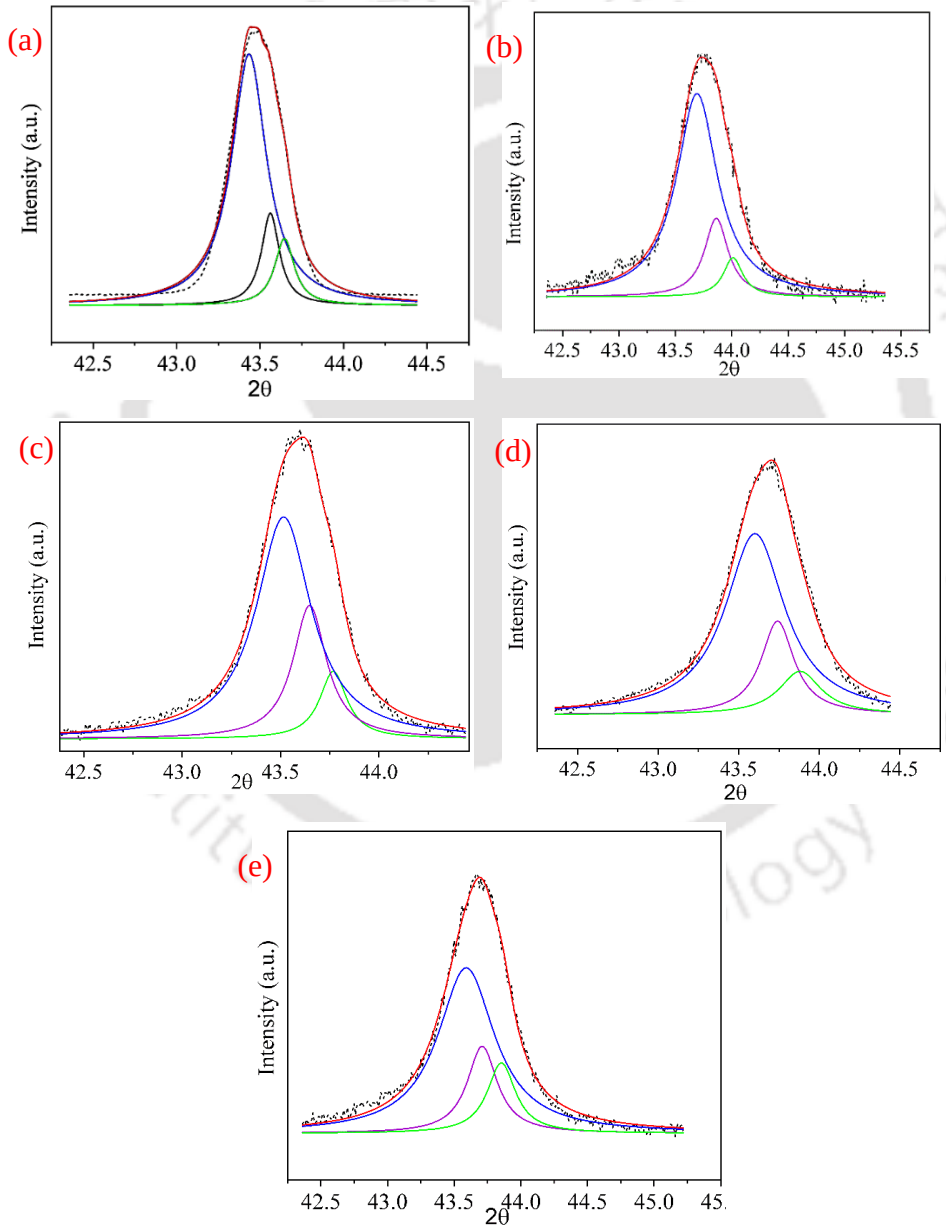

Fig. 4.25 deconvolution of peak corresponding to 2θ of 43.5 (approx.) of the TLP-bonded sample homogenized for (a) 0 h,(b) 8 h, (c) 16 h, (d) 24 h, and (e) 32 h

The hardness of the DAZ at microscopic level is affected by the hardness of the γ-matrix and hardness of boride, γ′ and γ″ precipitates. During homogenization the boride particles dissolves, and breaks into small components and the volume fraction of the boride decreases. At the same time the volume fraction of γ′ and γ″ precipitates increases in the matrix due to precipitation. The combination of these two factors affects the hardness of the DAZ. Initially, up to 16 h of homogenization the hardness value of the DAZ increased greatly, after that there is only a small difference is observed. This is due to the reduction of precipitation rate of the γ′ and γ″ after 16 h of homogenisation. After 16 h of homogenization, due to inter-diffusion of elements, the concentration gradient decreases, resulting in the reduction of the γ′ and γ″ precipitation rate. It is also observed that the micro-hardness of the BMZ is little higher than that of the DAZ. This is due to lower availability of Nb content at the DAZ. As discussed earlier that the borides formed at the DAZ are of Cr-Mo-Nb type borides. Therefore, a fraction of Nb content has been utilized in the formation of boride. Hence, there is less Nb atom available for the formation of the γ″-phase at the DAZ. As a result, a small difference in hardness is observed between the BMZ and the DAZ.

The hardness value of the ISZ is lowest among all zones. However, the hardness value of ISZ has increased significantly with homogenization up to 24 h and then get saturated. The hardness value of the ISZ in as bonded condition depends upon the solution strengthening elements like fraction of Mo, Nb, Ti, Al and Cr. But, during the isothermal holding due to low diffusivity of these elements in Ni, the amount of these solution strengthening elements at ISZ is less compared to the BMZ. This is one of the reason for the lower hardness of the ISZ as compared to other zones. However, during homogenization, along with other solid solution strengthening elements Nb and Al diffuses from the base material into the ISZ. As a result, γ′ and γ″ precipitates in the ISZ. Which increases the hardness of the ISZ. Even after prolonged diffusion, the volume of γ′ and γ″ is lower than that of the BMZ as amount of the Nb and Al in the ISZ is lower compared to that of the BM. Therefore, the hardness of the ISZ is lower than that of the other two zones even after the homogenization.

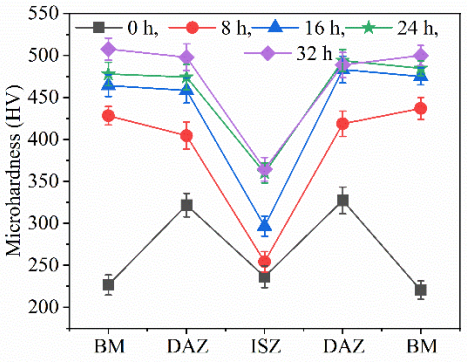

Fig. 4.26 Variation of hardness at various zone of TLP-bonded sample with homogenization time

4.3.4 Tensile strength

Figure 4.27 shows the tensile strength and strain curve of the sample homogenised for various time intervals. The figure reveals that the tensile strength of the TLP-bonded sample increases with increasing the homogenization time. This can be related to the increase of the volume fration of the γ″ and γ′ precipitates with increasing the homogenisatio time. The γ″ is present in the γ-matrix coherently, with increaseing volume fraction of γ″ with homogenization the coherency strain around the γ″ precipitate increases. Which obstruct the movement of dislocation and requires extra load to overcome the obstruction. As a result of this the strength of the IN 718 increases with homogenization time. Moreover, during the homogenisation the solid state inter-diffusion of elements occurs, which dissolves the intermettalic particles present in the ASZ of TLP bonding. Also, increases the solid solution strengthening element content in the bond area. Due to combined effect of these three factors the strength of the TLP bond increases with increasing homogenisation time. After 32 h of homogenisation a 220 % increase in strength is obtained as compared to the as bonded sample strength. At the same time there is loss of 48 % ductility is also oberved. The losss of the ductility can be related to the presence of lave phase and δ-phase in the homogenised sample. These phases are brittle in nature and these are the favorite sites for crack initiation during the deformation.

Figure 4.28 (a-b) shows the tensile behaviour of the TLP-bonded samples prepared at different process parameters and homogenised for 32 h. The **Fig. 4.28 (a)** shows the stress strain curve of samples. The curve shows that the tensile strength of the TLP-bonded samples increased after 32 of homogenization. Maximum UTS of 1374 MPa was observed for the experiment number Exp.6. There is 220 % increase in the UTS observed as compared to the as bonded sample. This increase in the strength can be

related to increase in the volume fraction of γ″ + γ′ phases. After 32 h of homogenization, among all experimental condition a maximum 11 % UTS variation was observed. This is due to the uniform microstructure of the TLP bond after 32 h of homogenization.

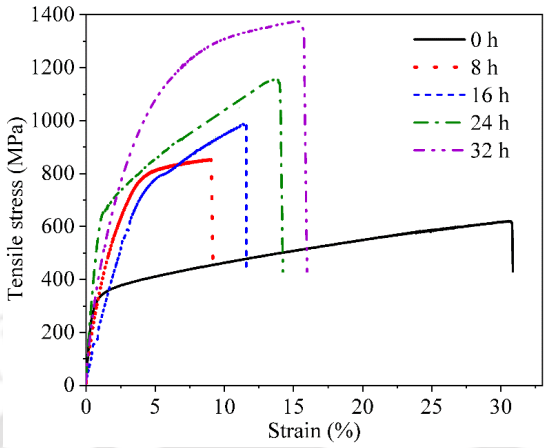

Fig. 4.27 Stress strain curve of TLP bond homogenised for various time interval

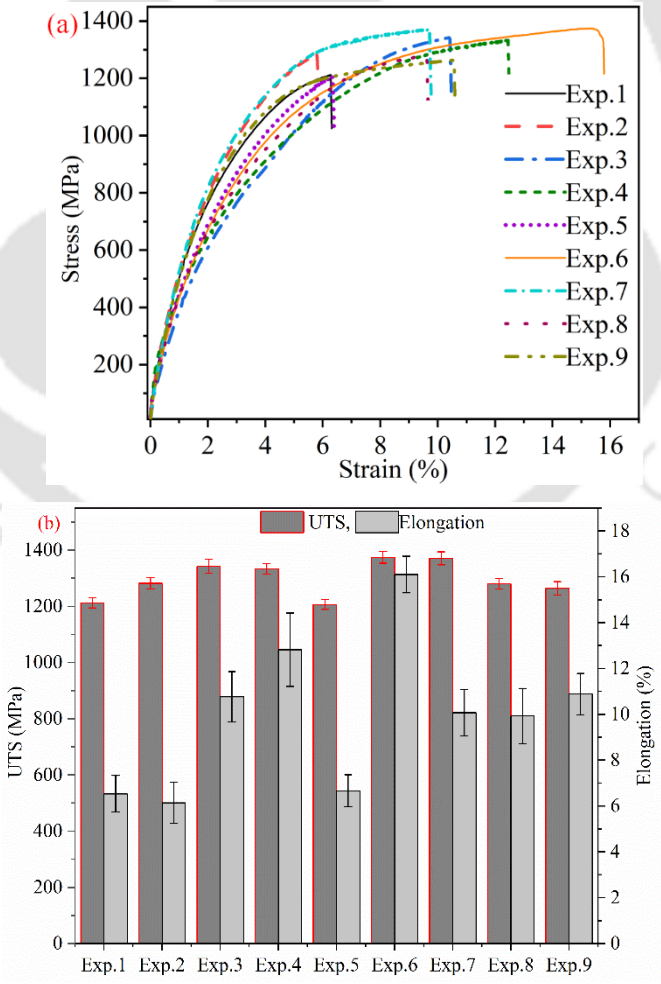

Fig. 4.28 (a) stress strain curve of 32 h homogenized TLP-bonded samples at various experimental condition and (b) bar-chat showing UTS and % of elongation variation

4.3.5 Fractography

The fracture surfaces of the 32 h homogenized TLP-bonded samples of Exp. 2 and Exp.6 are shown in **Fig 4.29 (a-c)** and **Fig. 4.29 (d-f)**, respectively. The low magnification image of the fracture surface of Exp.2 shows two type of fracture surface marked as A and B in Fig. **4.29 (a)**. The higher magnification image of the rectangle marked as A shows intergranular fracture surface, whereas in the rectangle B shows some shallow dimple features and some cleavage surface, which are not distributed uniformly. However, intergranular fracture is dominant in Exp.2, as a result, brittle failure occurs in the samples. Similar features are also observed in the case of Exp. 6 with some deep dimples. The deep dimples indicate a ductile mode of failure. The dimples are formed due to debonding of carbide particles in the grains. As some deep dimples are observed in the sample, the ductility of the Exp.6 increased. The ductility and fracture mode of IN 718 superalloy largely depends upon the relative strength between the grain interior and grain boundary. The presence of the brittle δ and lave particles in the grain boundaries reduces the relative strength of the grain boundaries. During deformation, these particles break and initiate the crack. And the crack propagates in an intergranular manner and reduces the ductility of the sample. The Exp.2, the bond is performed at 1050 ˚C, whereas Exp.6 is performed at 1100 ˚C. Considering the TTT diagram of the IN 718 joint, the dissolution temperature of the δ-phase is 1000 ˚C and lave phase 1100 ˚C. More dissolution of the δ and lave phase occurs in Exp.6 compared to the Exp.2. As a result more δ and lave phase may have precipitated in the grain boundaries of the sample for the case of Exp.2. During uniaxial tensile loading, when the maximum principal stress reaches the uniaxial tensile strength of the brittle particles, the brittle particle fractures and failure of the bond occurs. Which reduces the ductility of the sample.

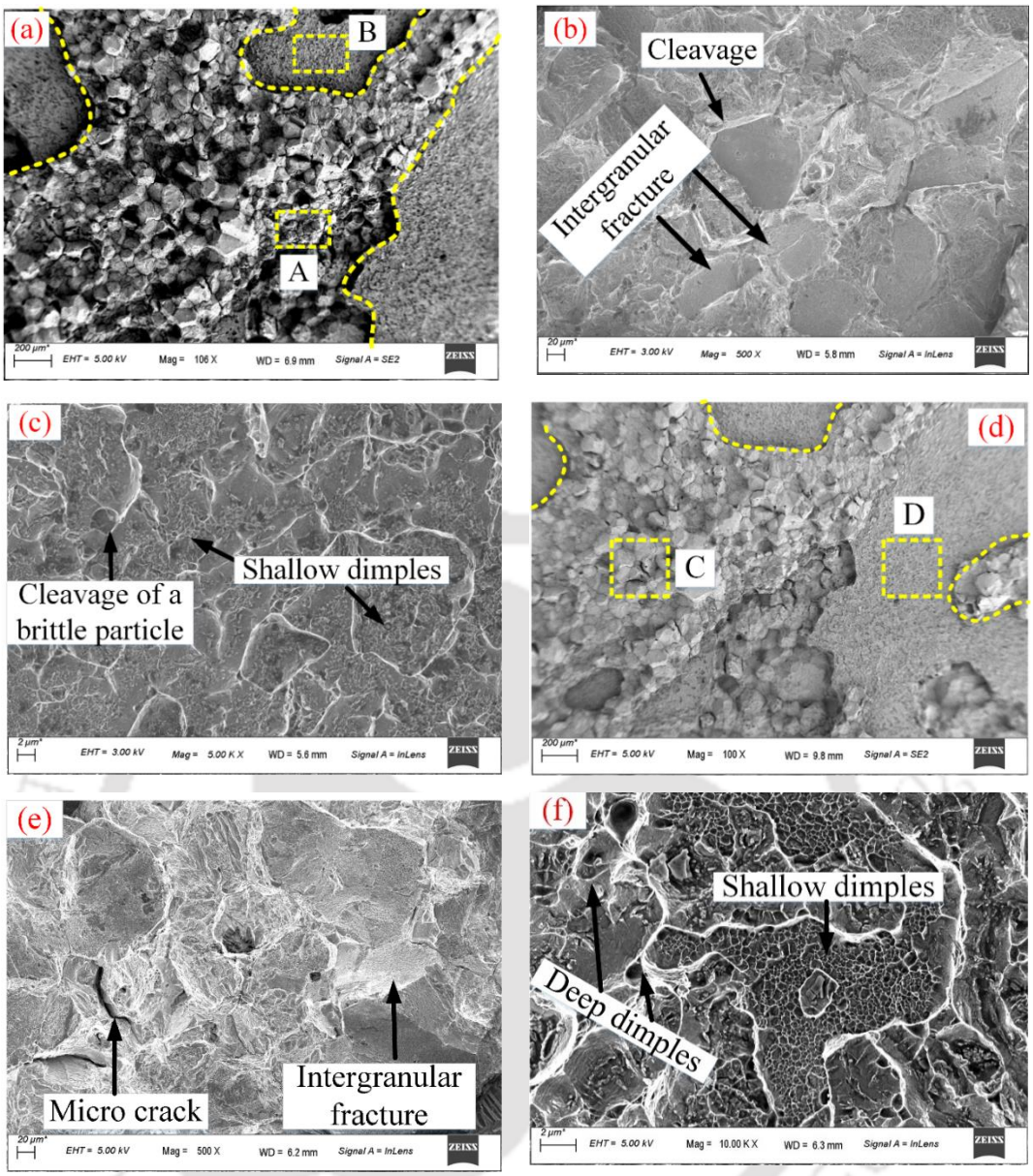

Fig. 4.29 fracture surface of 32 h homogenized TLP-bonded sample (a) for Exp.2, (b) higher magnification of rectangle marked as A, (c) higher magnification of rectangle marked as B, (d) for Exp.6, (e) higher magnification of rectangle marked as C, and (f) higher magnification of rectangle marked as D

4.4 Kinetics of TLP Bonding and Determination of Isothermal Solidification Time by DSC Method

4.4.1 DSC analysis of BNi-2 interlayer

The DSC curve of the BNi-2 interlayer heated up to 1050 ˚C is shown in **Fig. 4.30 (a)**. The figure shows three exothermic peaks between 469 to 612 ˚C, and no such peaks are evident during cooling or second heating. These group of peaks are due to the

transition of the amorphous BNi-2 interlayer into a crystalline structures such as face-centered cubic γ-nickel, orthorhombic Ni_3B phase, and Ni_3Si phases **[188]**. **Figure 4.30 (b)** depicts the enlarged view of the melting and solidification event of the interlayer foil. The figure shows three distinct endothermic peaks within the melting event. Through the first derivative of the DSC curve, the earliest melting point onset temperature of the interlayer was found to be 960 °C and the end-set temperature was found to be 1040 °C. The three distinct endothermic peak in the melting event was due to the melting of ternary eutectic, binary eutectic, and primary phases present in the BNi-2 interlayer material **[188, 189]**.

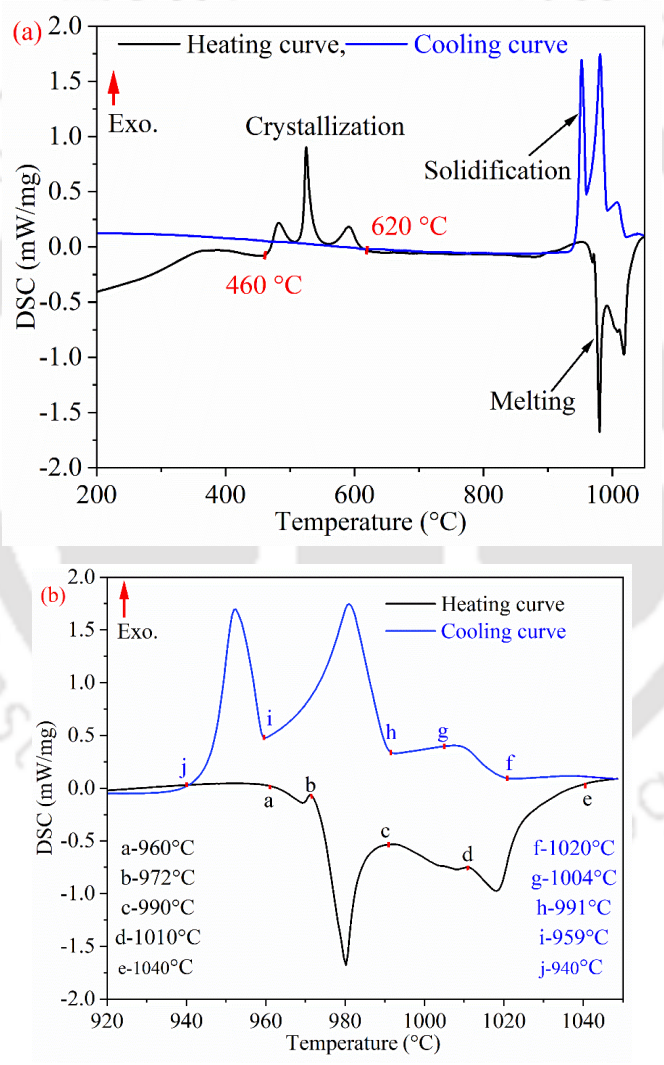

Fig. 4.30 (a) DSC curve of BNi-2 interlayer from room temperature to 1050 °C (b) magnified view of melting endotherm of BNi-2 interlayer

The interlayer material containing Ni-Cr-Fe-B-Si elements, the solidification of the interlayer occurs through the solidification of three phases. The primary γ-Ni, Ni_3B, Cr_3B, and Ni_3Si solidify at different temperatures through eutectic reactions. The sequence of solidification for the BNi-2 interlayer is described below;

$$\text{Primary phase,} \quad L3 \rightarrow Ni(\gamma) \tag{4.2}$$

$$\text{Binary eutectic reaction,} \quad L2 \rightarrow Ni(\gamma) + Ni_3B \tag{4.3}$$

$$L2 \rightarrow Ni(\gamma) + Ni_3B$$

$$\text{Ternary eutectic reaction, } L1 \rightarrow Ni(\gamma) + Ni_3B + Ni_3Si \tag{4.4}$$

The exothermic peaks observed during the solidification of the liquid interlayer were due to these primary, binary and ternary eutectic reactions occurring during solidification of liquid interlayer. The phases in the solidified interlayer can be seen in the microstructure. **Figure 4.31** shows the optical microstructure of the solidified interlayer, which was heated up to 1050 °C. The micrograph reveals the presence of three different phases in the solidified BNi-2 interlayer marked as A, B, and C. These phases are primary γ-Ni, binary eutectic of γ-Ni, nickel boride or γ-Ni, and chromium borides and ternary eutectic of γ-Ni, nickel boride, and nickel silicide **[190]**. During solidification of the BNi-2 interlayer material, the γ-Ni solidified first from the faying surface into the melt as nodular dendrites. This resulted in enrichment of Cr, Si, and B in the residual liquid. As cooling proceeds, solidification of γ-Ni and nickel boride occurs by a eutectic reaction, further enriching the Cr content in the residual liquid. Consequently, further cooling γ-Ni and chromium borides solidify through another binary eutectic reaction. This enriched the residual liquid with more Si elements and solidify as γ-Ni, nickel boride, and nickel silicide by a ternary eutectic reaction. Considering the two binary phase melts simultaneously, the interlayer material exhibits three melting sequences corresponding to the primary γ-Ni solidification, binary eutectic reaction, and ternary eutectic reaction. These three sequences can be seen in **Fig. 4.30 (b)**. This type of reaction was also seen in the case of the DSC experiment conducted for the sample containing interlayer and base material with or without metallurgical contact between the base material and the interlayer material, as shown in **Fig. 4.32**. The DSC experiment conducted for samples containing base material and the interlayer with yttria diffusion barrier between them shows three-stage melting. However, for the samples extracted after the first isothermal holding cycle, the peak corresponding to the primary γ -Ni

solidification disappeared and only the peak corresponds to the binary eutectic and the ternary reaction observed. During the isothermal holding, inter-diffusion between the interlayer and the base material occurs through the interface, resulting in the disappearance of the high-temperature primary γ -Ni solidification event. The initial enthalpy for solidification of the interlayer (in absence of base material) was determined from the DSC-time curve was 6. 4 J/g. However, the enthalpy of solidification for the interlayer in presence of the base material having an yttria barrier between them (i.e. with no metallurgical interrelation between them) was determined to be 5.2 J/g. This value of enthalpy was considered the actual enthalpy required for the solidification of the interlayer. And for the interlayer material having metallurgical interaction with the base material has the enthalpy of solidification 4.16 J/g. There is a reduction of enthalpy of solidification due to metallurgical contact between the interlayer and the base material.

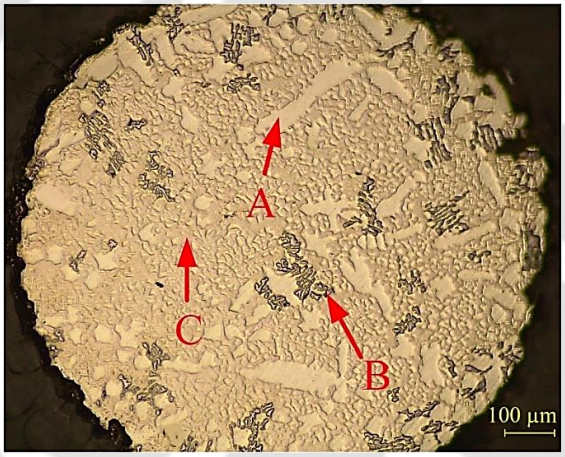

Fig. 4.31 Microstructure of solidified interlayer heated up to 1050 °C

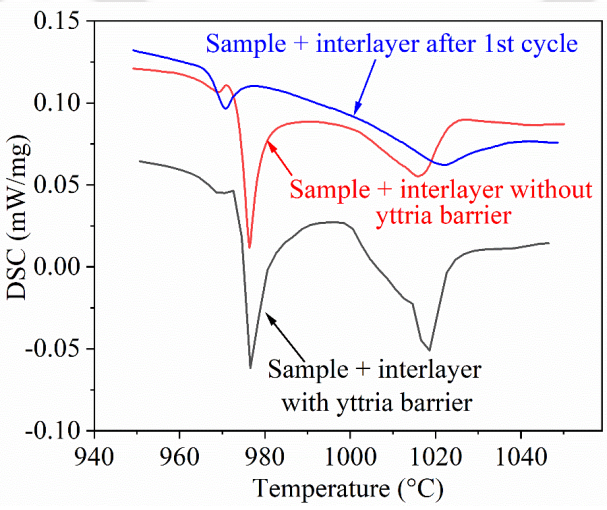

Fig. 4.32 Melting event in the interlayer with various condition

4.4.2 Thermal cycle and microstructure evolution of IN 718/ BNi-2 TLP bonding joint

The temperature, time, and DSC variation of the half TLP joint are shown in **Fig. 4.33 (a-b)**. The heating and cooling trace of a DSC cycle shows endothermic and exothermic peaks during heating and cooling, respectively. The endothermic and exothermic peak observed in the figure was due to the melting and solidification of the interlayer material, respectively. The intensity of these peaks decreased with increasing isothermal holding time. This indicates a decrease in liquid width as isothermal solidification proceeds. A peak shift was observed with increasing the isothermal holding time for both the melting and solidification events. During the isothermal holding inter-diffusion of elements occurs between the IN 718 and BNi-2, which alters the composition of the liquid as a result the melting temperature of the liquid changes. The figure reveals a sharp shoot-out at the end of the heating curve, this shoot-out was due to the higher heating rate of the DSC. At a higher heating rate, the sample can't take up the heat so fast, which results in a shoot-out in the temperature curve.

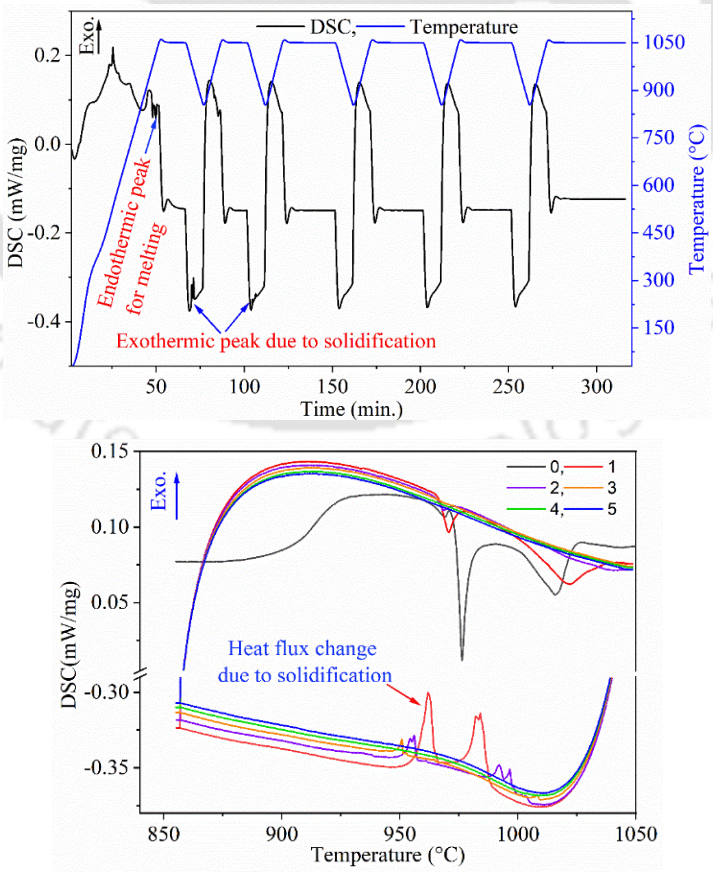

Fig. 4.33 Heat flux variation with (a) time and (b) temperature

4.4.3 Microstructure of the TLP joint

The microstructure of the half TLP bond held for various isothermal holding times is shown in **Fig. 4.34 (a-d)**. **Figure 4.34 (a)** shows the solidified microstructure of the TLP bond held isothermally for 0 min. The microstructure reveals four zones, namely; athermally solidified zone (ASZ), isothermally solidified zone (ISZ), diffusion affected zone (DAZ), and base material zone (BMZ). The ASZ forms due to athermal re-solidification of the residual liquid present in the bond area. The ASZ consists of binary eutectics of γ-Ni, nickel boride and γ-Ni, chromium boride, and ternary eutectics of γ-Ni, nickel boride, and nickel silicide along with some trace of elements diffused from the base material. The microstructure analysis shows the average width of the ASZ after 0, 15, 60, and 120 min of isothermal holding is 32, 20, 10, and 0 µm, respectively. The size of the ASZ decreases with the increase of the holding time and is almost equal to zero after 120 min. of isothermal holding. The ISZ was formed due to the diffusional solidification of the liquid interlayer and the ASZ was formed due to normal cooling of the residual liquid. In the case of 0 min isothermal hold, it was observed that the size of the ASZ+ISZ is 45 µm as shown in **Fig. 4.34 (a)**. The 0-minute hold is corresponding to the heating and melting stage of the interlayer material. Initially, the thickness of the interlayer was 40 µm. However, the size of the ASZ+ISZ is more than that of the initial size of the interlayer material. Moreover, the size of the ASZ is 32 µm. This concludes that the dissolution of the base material and rapid diffusional solidification of the liquid interlayer during the heating and melting stage of the interlayer material occurs simultaneously. The dissolution and the rapid diffusional solidification during this stage are due to the inter-diffusion of elements during the heating and melting stage.

During isothermal holding the inter-diffusion of elements between the base material and the interlayer forms the ISZ. The alloying elements diffused from the base material into the bond zone contribute to solid solution strengthening of the TLP bonding. During the inter-diffusion of elements at high temperatures, the MPD elements like B and Si diffuse from the interlayer into the base material. As time proceeds, the composition of these elements near the bond interface increases and exceeds the solubility limit of the B and Si in the Ni matrix of the interlayer material. Further increasing in time results in the rejection of the extra B and Si atoms from the Ni-matrix. These extra B and Si elements react with the Cr, Mo, and Nb elements to form borides or silicides of respective elements and form the DAZ. These precipitates are of a needle or

irregular shape and are present in the grain boundaries and inside the grain as shown in **Fig. 4.34 (d)**. As per the previous analysis, these borides and silicides are rich in Nb, and Mo.

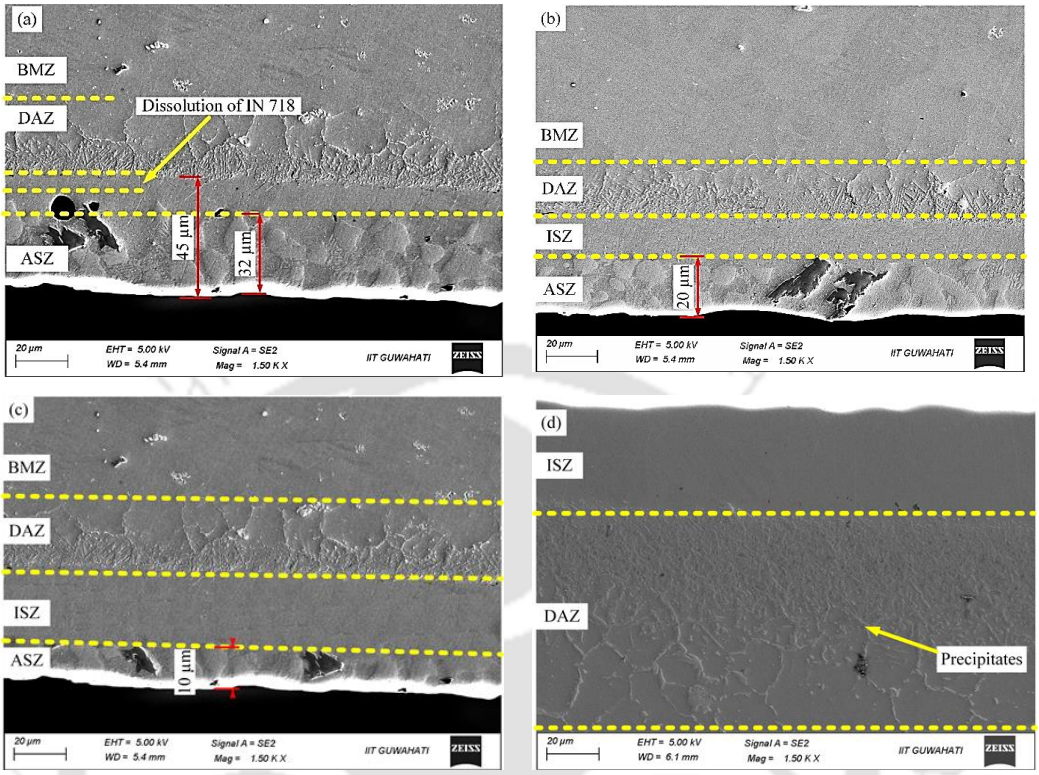

Fig. 4.34 Microstructure of the TLP bond held for (a) 0 min, (b) 15 min, (c) 60 min, (d) 120 min

4.4.4 Solidification peaks for the remaining liquid phase

Figure 4.35 (a-g) shows the exothermic peak corresponding to the solidification of the liquid interlayer held for various time intervals. The curve reveals that the sample in which interlayer material has no metallurgical contact with the base material has three exothermic peaks, whereas the samples which were has metallurgical contact and held isothermally for up to 60 min have two exothermic peaks. Moreover, after 90 min of isothermal holding, only one peak is evident. The peaks in the DSC curves represent the solidification of the phases present in the liquid interlayer. During isothermal holding inter-diffusion of elements occurs which results in the disappearance of some phases. Due to the inter-diffusion of elements the composition of the liquid changes as a result the solidification sequence of the liquid interlayer changes. Therefore, from 0 to 60 min of isothermal holding, solidification of the interlayer occurs due to binary and ternary eutectic reactions. As a result after 90 min of isothermal holding, isothermal solidification of the residual liquid takes place only due to the ternary eutectic reaction. The area under

the curve was calculated and it was also observed that the area under the curve decreased with isothermal solidification time. The area under the DSC versus time is a measure of enthalpy required for the occurrence of the event. The enthalpy for the solidification of the liquid was obtained from the area under the DSC versus the time curve. As the area under the curve decreases, this indicates that the enthalpy of solidification decreases with increasing the isothermal solidification time. This can be related to the decrease of the liquid width with isothermal holding time.

The mass of liquid involved in solidification is given by:

$$\text{Mass of the liquid involved in solidification, } m = \frac{\Delta H_t}{\Delta H_0} \tag{4.5}$$

where ΔH_0 is the enthalpy of solidification measured for the interlayer with the yttria barrier (is a constant) and ΔH_t is the enthalpy of solidification after isothermal holding for a time interval of '*t*'. The enthalpy of formation can be used as a reference to determine the amount of liquid remaining (and thus interface position) in a solid/liquid diffusion couple after an isothermal hold period. Eq. (5) gives this relationship:

$$\%\ \text{Residual liquid in the bond} = \frac{\Delta H_t}{M\Delta H_0} \times 100 \tag{4.6}$$

where M is the mass of the original eutectic interlayer foil.

Considering the wetting area as constant and the density of the liquid constant throughout the DSC experiment, the width of the residual liquid in the joint can be calculated from Eq. (4.5)

$$2w_t = \frac{\Delta H_t}{\Delta H_0} \times 2w_0 \tag{4.7}$$

The initial volume of the interlayer added was V_0, which can be determined as

$$V_0 = w_0 A_0 \tag{4.8}$$

Where w_0 and A_0 are the initial width and area of the interlayer material. As the area of the base material is slightly less compared to the interlayer, the actual width of the interlayer wet the initial area of base material (i.e. A_b) which can be determined as

$$w_0 = \frac{w_0 A_0}{A_b} \tag{4.9}$$

The width of the liquid interlayer was calculated from equation (4.6) and plotted with respect to various isothermal holding times. **Figure 4.36** shows the graph between the liquid width vs the square root of the isothermal holding time. The graph shows that the width of the liquid decreases linearly with the isothermal solidification time. This is a good agreement with the results available in the literature.

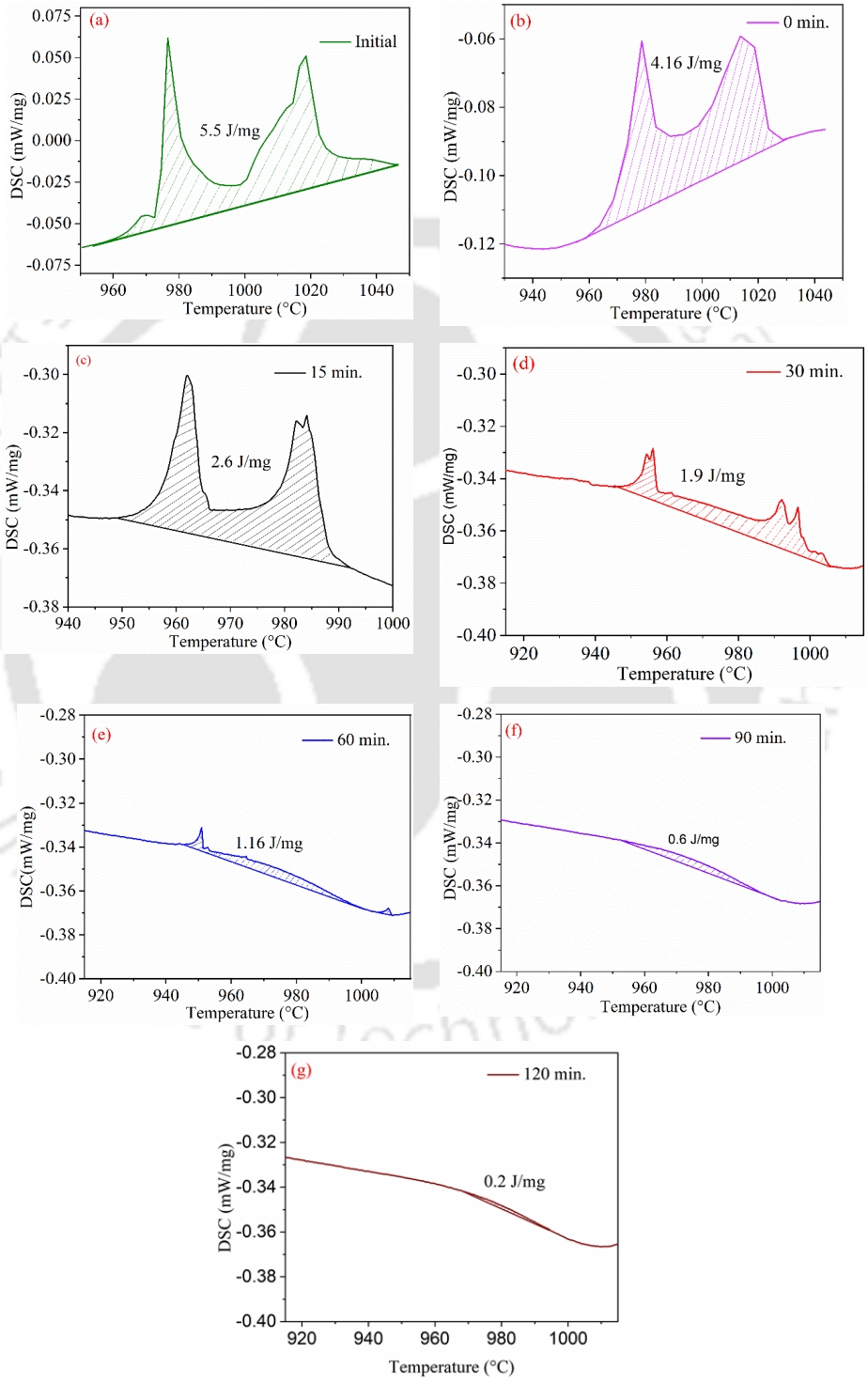

Fig. 4.35 Enthalpy of solidification of liquid, (a) without metallurgical interaction; held isothermally for (b) 0 min, (c) 15 min, (d) 30 min, (e) 60 min, (f) 90 min, and (g) 120 min

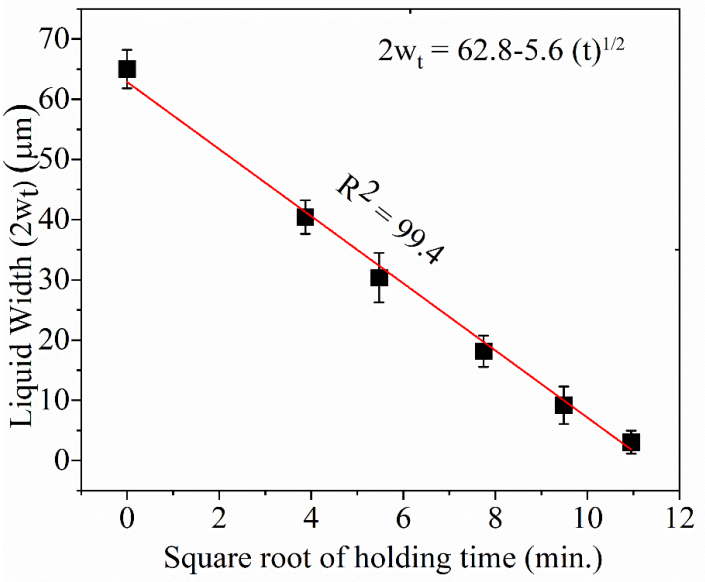

Fig. 4.36 Variation of liquid width with time

The linear regression analysis of the curve between liquid width vs the square root of the isothermal holding time gives an equation to predict the isothermal solidification time for TLP bonding as;

$$2w_t = -C \times (t)^{1/2} + 2w_0 \quad (4.10)$$

where $2w_t$ is the interlayer full width of a TLP bond, t is the isothermal holding time, C is the slope of the $2w_t$ vs $t^{1/2}$ curve and $2w_0$ is the initial interlayer width (i.e. interlayer width for 0 min of isothermal holding) which was obtained from extrapolating the curve to Y-axis intercept. After linear regression analysis of the curve of **Fig. 4.36,** the value of C and $2w_0$ are found to be 5.6 μm/ (min)$^{1/2}$ and 62.8 μm, respectively. Considering the $2w_t$ value as zero for complete isothermal solidification, the time required for the complete isothermal solidification time (tf), can be obtained from Eq. (9) as;

$$t_f{}^{1/2} = \frac{2w_0}{C} \quad (4.11)$$

Putting the value of C and $2w_0$, the time required for complete isothermal solidification of the TLP bond of IN 718 made by using an 80 μm thick interlayer was determined to be 122 min. Ojo et al. **[191]** have predicted for the isothermal solidification during TLP bonding using moving interface modelling technique, they found that the isothermal

solidification time of TLP-bonded sample can be calculated by using the following equation:

$$t_f^{1/2} = \frac{2w_0}{4erf^{-1}\left(\frac{C_S}{C_0}\right)D^{1/2}} \quad (4.12)$$

where D is the equivalent diffusivity of MPD in the base material at the bonding temperature, $C_S$and C_0 are the initial concentration of MPD element in the base material and the interlayer, respectively. Both equation (10) and equation (11) are in the same form and the isothermal solidification rate $C = 4erf^{-1}\left(\frac{C_S}{C_0}\right)D^{1/2}$. For IN 718 and BNi-2 TLP bond the value of C_0 and C_S are 0.3 and 13.7 at. %, respectively. Considering D as constant at a temperature the isothermal solidification rate calculated from the above the formula is in good agreement with

4.4.5 Validation with experimental results

Pouranvaru et al. **[192]** determined the isothermal completion time for TLP bonding of IN 718 joined at a bonding temperature of 1050 ˚C using 50 µm thick BNi-2 interlayer material. They predicted the isothermal solidification time based on the eutectic-free ISZ. They found that the time for completion of isothermal solidification time is 40 min. At a constant temperature and pressure, the isothermal solidification time mainly depends upon the initial thickness of the interlayer material. As there is rapid diffusional solidification occurs in the TLP bonding of Ni-base superalloy during the heating and melting stage, the actual initial thickness of the interlayer before isothermal solidification is different from the original interlayer thickness due to diffusional loss. The extrapolating experimental results of Pouranvaru et al. **[192]**, was found that the thickness of the interlayer material before the start of isothermal solidification is 35.7 µm. Putting $2w_0$ = 35.7 µm, in the equation, the time required for isothermal solidification is calculated to be 41 min. This is a good agreement with the experimental results. Similarly, the results are also in good agreement with other Ni-based superalloys **[40, 192, 193]**.

4.5 Design of PBHT Process to Enhance the Bond Quality

In IN 718 superalloy, γ′ and γ″ are the main hardening precipitates which contributes to the strength of the superalloy. Though the δ precipitate is more stable than the γ″ phase, it does not contribute to the strengthening. Rather its presence in the alloy

causes loss of strength and hardness of the alloy. Precipitation of δ-phase occurs in the temperature range 700-1000 ºC with highest precipitation rate at 900 ºC. According to the TTT diagram of IN 718 **[194]**, very small amount of grain boundary δ phase is formed if it is heated to a temperature above 700 ºC for 1 h. Whereas, the γ′ and γ″ phases precipitates between 600-900 ºC. The maximum precipitation of γ′ and γ″ occurs at 660 °C and 760 °C, respectively. During TLP bonding as the BMZ temperature lies between 700-1000 ºC, the δ particles precipitates along the grain boundaries. Therefore, a heat treatment was carried out to remove the detrimental δ phase and increase the amount of γ′ and γ″ to improve the strength of the TLP-bonded joint. In this investigation two type of heat treatment was employed. In first cycle the sample was solution annealed at 1050 ˚C and in the second cycle the samples are solution annealed at 1150 ˚C. After solution annealed the samples are double aged. The bonded sample was heated to solution annealed temperature at a heating rate of 30 ˚C/min and held for 2 h to dissolve all precipitates present in the alloy. This was followed by water quenching resulting in the formation of only the γ-phase matrix. Subsequently, the samples were heated to 760 ˚C and held for 8 h. At this stage γ″ phase re-precipitates in the matrix. The samples were then furnace cooled to 660 ˚C and held for 8 h, resulting in the formation of γ′ re-precipitates. This heat treatment resulted in a reduction in lave and δ-phase volume fraction and a simultaneous increased in the volume fraction of γ′ and γ″ precipitates in the γ matrix.

4.5.1 Microstructural evolution at the base metal zone

The optical micrographs of the as-received IN 718 (ARIN 718), BMZ of the as bonded sample (ABS) and BMZ of the HT1050 and HT1150 samples are shown in **Fig. 4.37 (a-c)**. The optical microstructure consists of austenite grains, fine dispersed metallic carbides, intra-granular precipitates, and twin boundaries (TB). The average grain sizes of the ARIN 718, BMZ of the ABS, and BMZ of the HT1050 and HT1150 samples, determined by line intercept method, are 18.7, 52, 91, and 112 µm, respectively. The grain size of the as ARIN 718 is very small and there is no evidence of twin boundaries in the sample. During the TLP bonding and PBHT, the IN 718 superalloy was held isothermally at a temperature above its recrystallization temperature. The exposure to higher temperature resulted in grain growth and hence the sharp increase in grain size as evident in the figures. During HT, the number of annealing twin boundaries (TB)

increased. The annealing TB has an advantageous effect in the improvement of strength of the material **[195]**.

Higher magnification FESEM micrographs of the ARIN 718, BMZ of ABS and BMZ of HT1050, and HT1150 samples are shown in **Fig. 4.38 (a-e)**. Earlier studies on the microstructural analysis of IN 718 reveal that γ′, γ″, δ, and lave phases are present in the spherical, disk, needle, and blocky shapes, respectively, in the γ-matrix **[196]**. The higher magnification of ARIN 718 (as shown in **Fig. 4.38 (a)**) reveals the presence of γ′, γ″, δ, and lave phase precipitates in the austenite γ-matrix. The micrograph reveals that the strengthening precipitates viz.; γ′ and γ″ are distributed non-uniformly. Qualitative observation of the micrographs reveals that the volume fraction of the γ′ and γ″ precipitates in the ARIN 718 samples are less compared to the ABS and PBHT samples. In the HT1150, as the solution annealing temperature is 1150 °C. There is a chance of liquation of low melting point eutectic phases. Which may cause the segregation of elements of the low melting point eutectic along the grain boundaries and affect the strength of the IN 718.

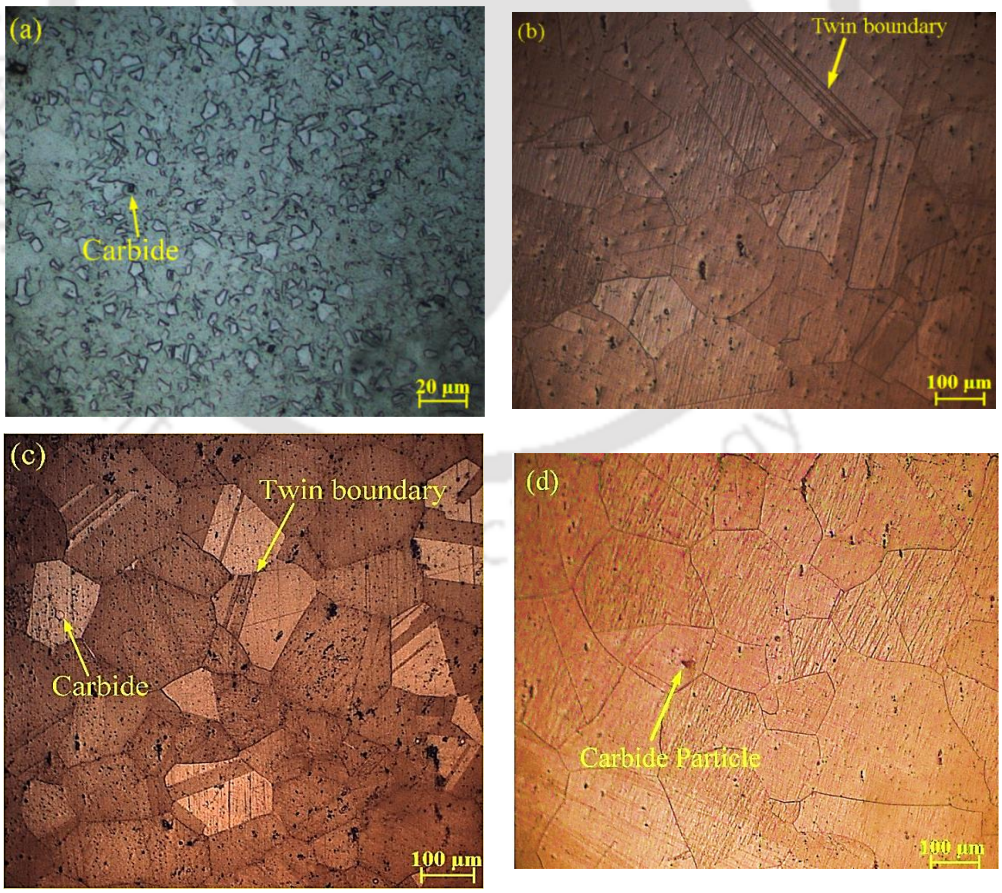

Fig. 4.37 Optical micrograph of (a) as received IN 718 sample, (b) BMZ of as bonded sample, (c) BMZ of the HT1050sample, and (d) BMZ of the HT1150 sample

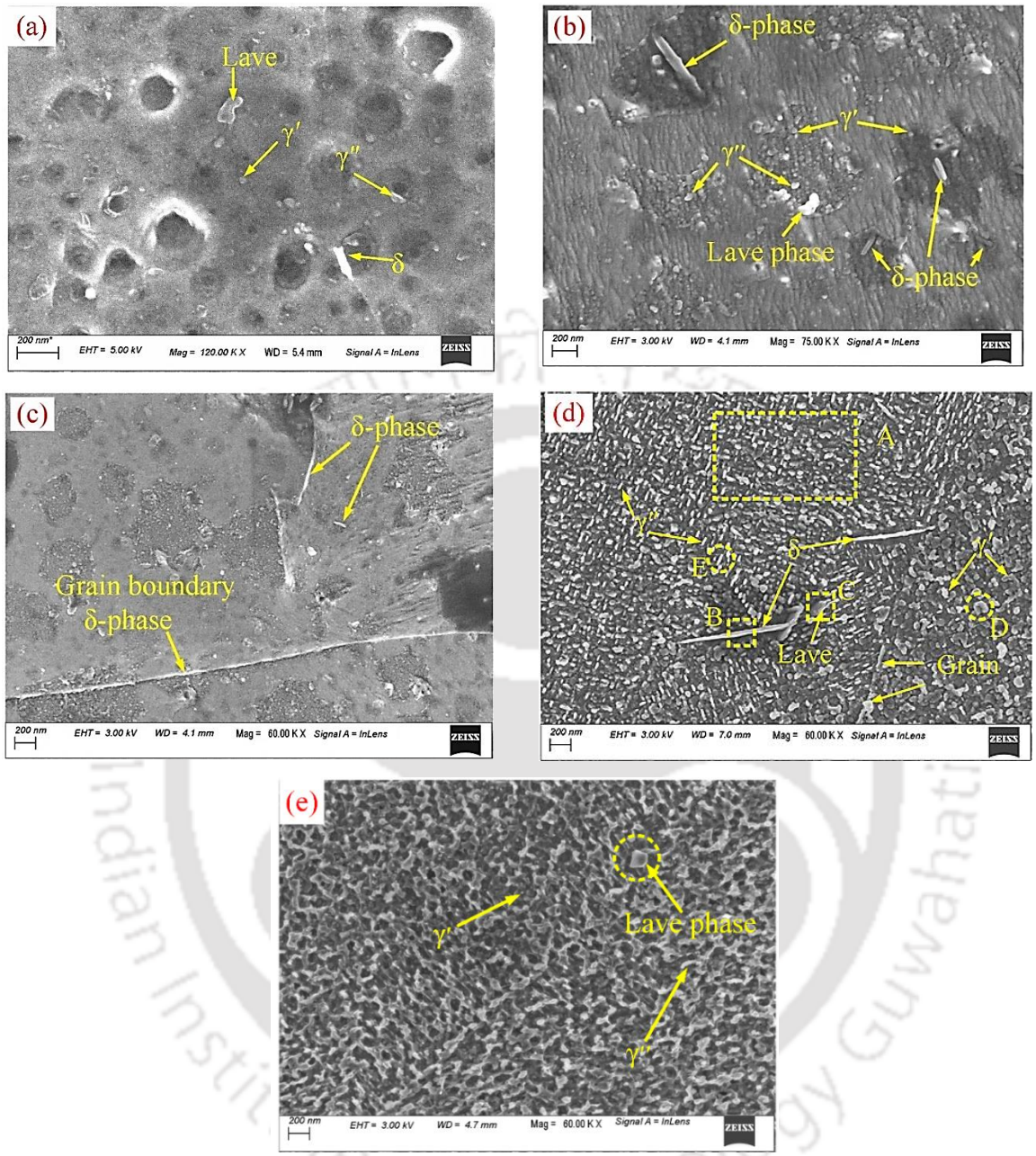

Fig. 4.38 High magnification FESEM micrograph of (a) ARIN 718, (b) ABS sample, (c) ABS sample showing grain boundary δ-phase precipitates, (d) HT1050 samples and (e) HT1150 sample

Higher magnification micrograph of ABS sample, shown in **Fig 4.38 (b)**, shows fine γ′ and γ″ precipitates, needle shaped δ phase along the grain boundaries and inside of the grains, and lave phase. The γ′ and γ″ precipitates here also are not distributed uniformly. However, the qualitative analysis shows the volume fraction of these phases have increased during TLP bonding. The bonding process was carried out at 1100 ºC,

which is well above the dissolution temperature of the δ (i.e. 980ºC), γ′ (i.e. 820º C) and γ″ (i.e. 870 ºC) phases. Hence during the TLP bonding, some of the γ′, γ″, and δ phases present in the ARIN 718 sample should have dissolved. However, during cooling, the γ′, γ″, and δ phases start precipitation as their respective precipitation temperature. Since the γ′ and γ″ precipitation occurs between 590-850 ºC and the time of exposure of the sample while cooling through this temperature range is very less, the volume fraction of these phases formed during TLP bonding are less compared to the PBHT sample. In the case of PBHT process, referring to the TTT diagram, as the samples are held isothermally at 760 °C and 660 °C for a period of 8 h each, precipitation of γ′, and γ″ will occur. As a result, higher amount of γ′, and γ″ precipitates are formed during PBHT. It was also observed that the grain boundary δ and lave phases in the PBHT sample has reduced due to dissolution of these phase during the solution annealing (as shown in **Fig. 4.38 (d)**). The dissolved δ and lave phase re-precipitates into γ′ and γ″ The EDS analysis results of the area rectangle marked as A, needle shaped marked as B, irregular shaped particle marked as C, spherical shaped particle marked as D, and disk shaped particle marked as E are presented in **Fig. 4.39**. The EDS analysis results show that the Nb content in the δ, lave and γ″ phases (7.5, 4.4 and 5.8 atomic percentages, respectively) is higher than the Nb content of matrix (marked as rectangle A). Therefore, these Nb-rich particles can be considered as δ, lave, and γ″ phases by observing the shape of the particle. Moreover, the Al and Ti content in the spherical precipitate is also higher than that of the matrix, which confirms these spherical particles are γ′ precipitates. However, as the volume interaction of electron is large FESEM EDS analysis, obtaining exact composition of nano precipitates is very difficult. For higher accurate analysis TEM / EDS analysis was carried out and the results are presented in the subsequent section. The size of the γ′, γ″, δ and lave precipitates present in the various samples are measured by ImageJ software and are presented in **Table 4.4**. It was observed that the size of the precipitates increases with thermal exposure. During the aging process new strengthening phases nucleates from the matrix in expense of lave and the δ phases and the existing phases grows. As a result the volume fraction of the strengthening phases increased and which can be beneficial for the strength of the bond.

Table 4.4 The size of the various precipitates (in nm)

Phase / Sample	γ′	γ″	δ		Lave	
			Length	Width	Length	Width
ARIN 718	20-32	28-48	142-165	32-43	134-147	46-60
ABS	33-46	39-58	580-632	86-94	164-182	62-78
PBHT	42-62	43-76	711-1041	29-42	142-158	79-88

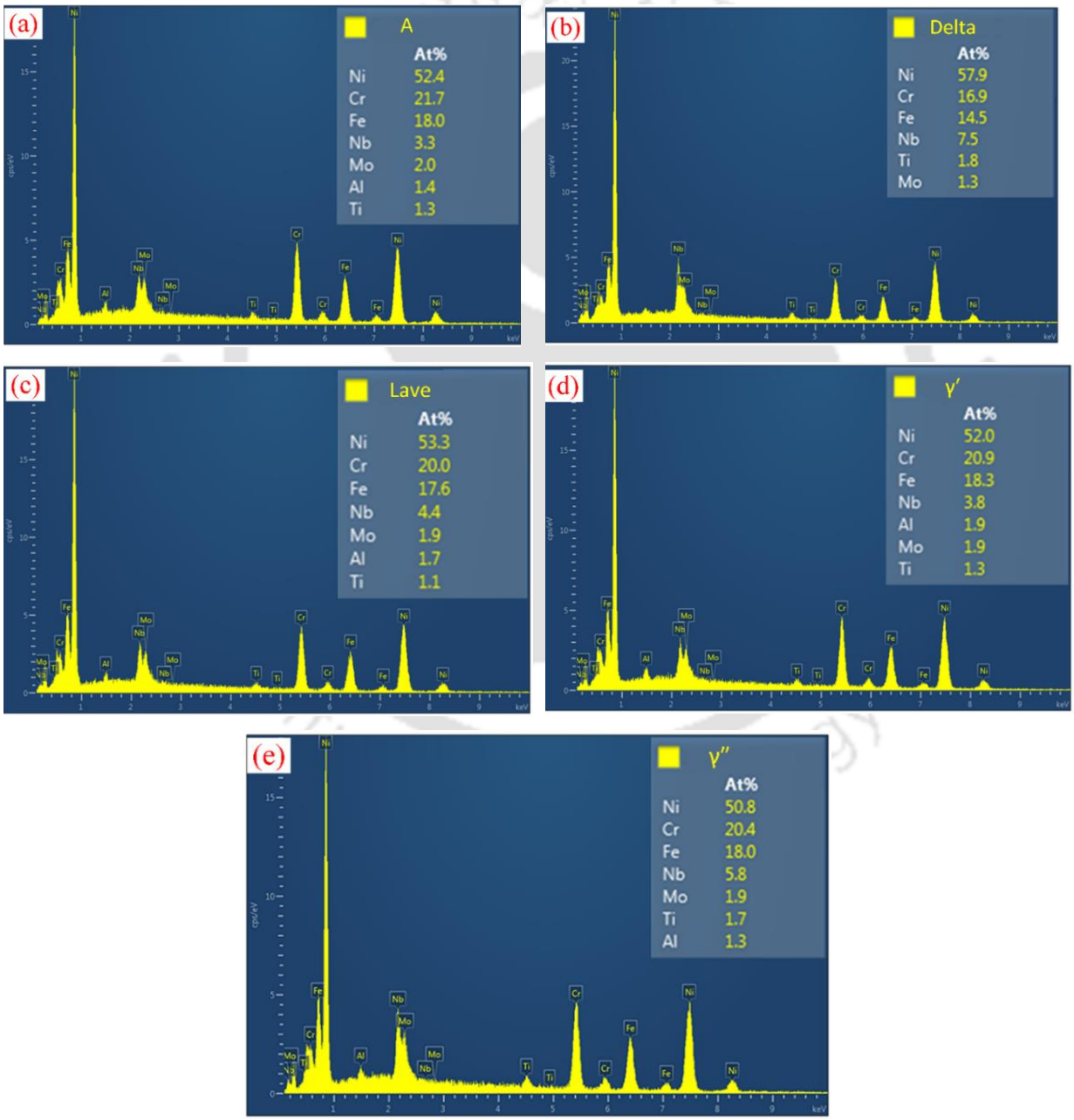

Fig. 4.39 EDS result of (a) matrix, (b) δ phase (c) lave (d) γ′ phase and (e) γ″ phase

4.5.2 Phase analysis

4.5.2.1 XRD analysis

Figure 4.40 illustrates the XRD results of the ARIN 718, ABS, HT1050, and HT1150 samples. Prominent peaks of γ, γ′ and γ″ phases are evident and are shown indexed in the figure. The figure reveals that the diffraction peaks coming from γ, γ′ and γ″ phases are overlapped and are hard to distinguish individually **[197]**. Deconvolution of peaks are carried out for the peak separation. In the case of ARIN 718, small intensities of carbides, δ phase and lave phase were also evident in addition to the above peaks. For ABS and HT1050, and HT1150 samples, peaks corresponding to lave or delta phase were not observed. As γ, γ′ and γ″ phases are the predominant peaks and since the volume fraction of carbides, δ and lave phases are very small, reflections from the planes of these phases were not observed in the XRD results. However, the presence of these phases was evident from TEM studies. During TLP bonding and heat treatment, the strengthening phases, as well as particles present in the areas of segregation may dissolved in the matrix under high temperature. During the cooling state, dissolved γ′ and γ″ phases re-precipitate in the matrix as strengthening phases with different sizes and shapes. Furthermore, as the time available to re-precipitate lave and δ phases is very less, the volume fraction of these phases is less in the case of ABS and PBHT samples. No noticeable peak shifts were observed in the major XRD peaks of the samples. However, the relative peak intensity of XRD peaks corresponding to γ, γ′ and γ″ have changed in the PBHT sample. The peak intensity of a material depends upon its structure and symmetry. During heat treatment, phase transformation occurred by changing the order of Nb and Ni atoms in the δ and lave phases to precipitate a body-centered tetragonal structured γ″ phase. This phase transformation resulted in the change in relative intensities of the different planes in PBHT samples.

Two extra peaks (at $2\theta \simeq 87.2^{\circ}$ and 94.1°) corresponding to γ″ was observed in the PBHT sample. During precipitation hardening of IN 718, the Nb atoms present in the γ matrix combines with Ni atoms to forms metastable γ″ phases. As a result, more γ″ phases are evolved in the PBHT samples. To estimate the volume fraction of γ, γ′, and γ″ phases present in the samples, integrated area method is followed. The significant peaks corresponding to γ, γ′, and γ″ phases are separated by deconvolution using origin software

as shown in **Fig. 4.41**. The integrated area of corresponding peaks are determined and the volume fraction of phases are calculated by using the following equation:

$$V_{f,i} = \frac{A_i}{\sum A_i} \tag{4.13}$$

where $V_{f,i}$ is the volume fraction of a phase, A_i is the integral area of that phase, and ΣA_i is the total integral area of all phases obtained from XRD pattern. The volume fraction of the different phases in the ARIN 718, ABS and PBHT samples are shown in the **Table 4.5**. It was found that the volume fraction of γ″+ γ′ phases increased with PBHT. Similar results were also achieved after heat treatment of the IN 718 superalloy **[198, 199]**.

Table 4.5 Volume fraction of various phases

Phase / Sample	γ	γ′	γ″	γ″+ γ′
ARIN 718	91.6	3.3	5.1	8.4
ABS	90.4	3.4	6.2	9.6
HT1050	76.4	8.1	15.5	23.6
HT1150	76.8	7.9	15.3	23.2

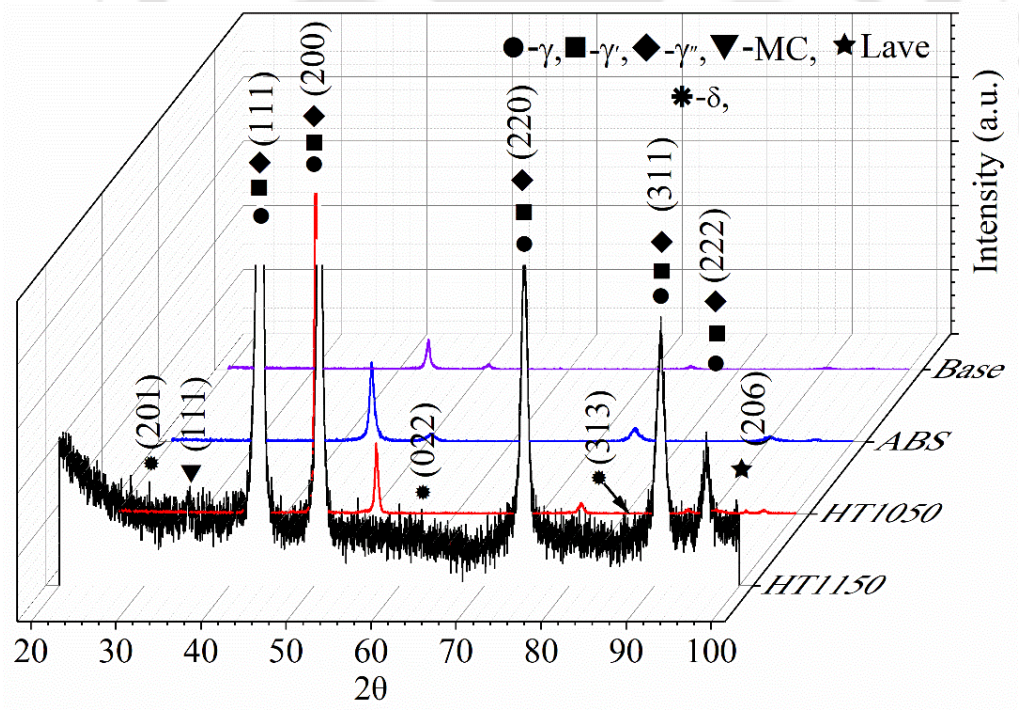

Fig. 4.40 XRD diffraction patterns of base material, ABS and HT1050, HT1150 specimens

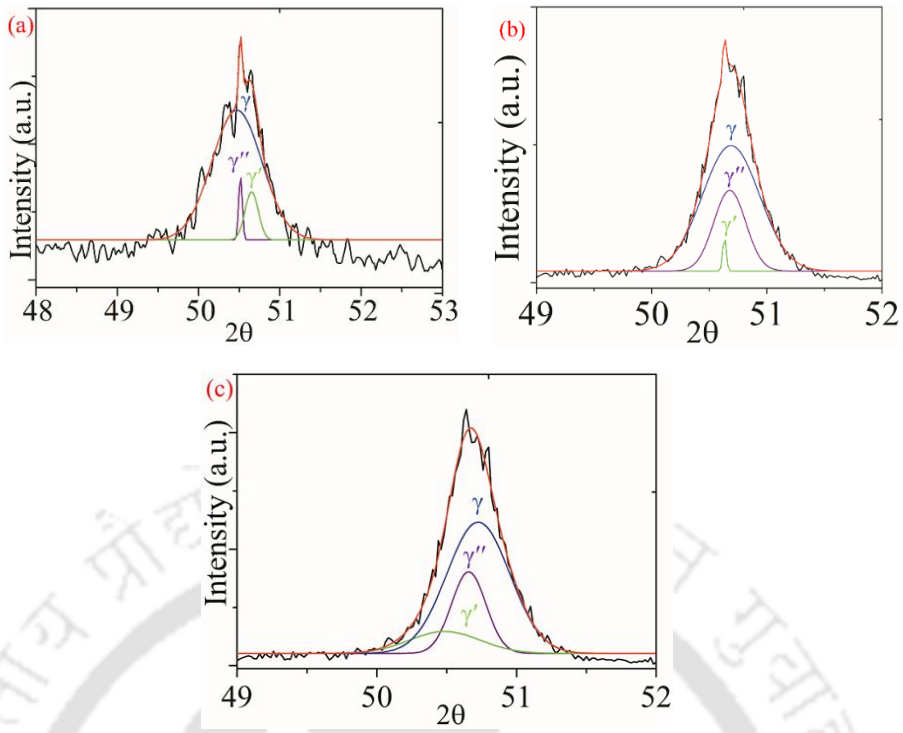

Fig. 4.41 Peak separation of (a) ARIN 718, (b) ABS and (c) PBHT sample

4.5.2.2 TEM analysis

Figure 4.42 (a-c), shows the bright field, selected area energy diffraction (SAED) pattern and high resolution TEM (HRTEM) image of the ABS sample. The bright field TEM image shows circular γ′ phase, disc like γ″-phase, fine block shaped lave phase and irregular block shaped metal carbides distributed in the austenite γ matrix. The average particle sizes of γ′, γ″ and lave phases are 14, 8, and 37 nm, respectively. The SAED pattern and HRTEM image of the ABS samples are shown in **Fig. 4.42 (b)** and **Fig 4.42 (c)**, respectively. Indexing the diffraction spots indicates that the γ matrix has an FCC crystal structure with a lattice parameter of 3.6 Å. The diffraction pattern consists of strong reflections from γ phase superimposed with weaker reflections from the γ′ and γ″ phases. The γ ′ and γ ″ particles were found to be coherent with the γ matrix. SAED pattern shows spots indicating crystalline nature of the material. Indexing of SAED pattern reveals FCC structure, with sports are corresponding to in (111), (200), (220), (311), (222) and (400) planes having *d*-spacing values of 2.08, 1.9, 1.3, 1.1, 1.0 and 0.9 Å, respectively. An HTREM graph of IN 718 is shown in **Fig. 4.42 (c)**. An FFT and inverse FFT analysis were carried out to detect the orientation of γ′ and γ″ phases. The result revealed that the γ′ and γ″ phases lie in the {110} plane along the <110> direction. In addition to the γ′ and γ″ precipitates, δ and carbides precipitates were also observed in

the as bonded samples. The δ phase was present in the (001) crystal planes with *d*-spacing value of 4.5 Å. Hexagonal MoC was found in the γ matrix along the (105) crystal plane**.**

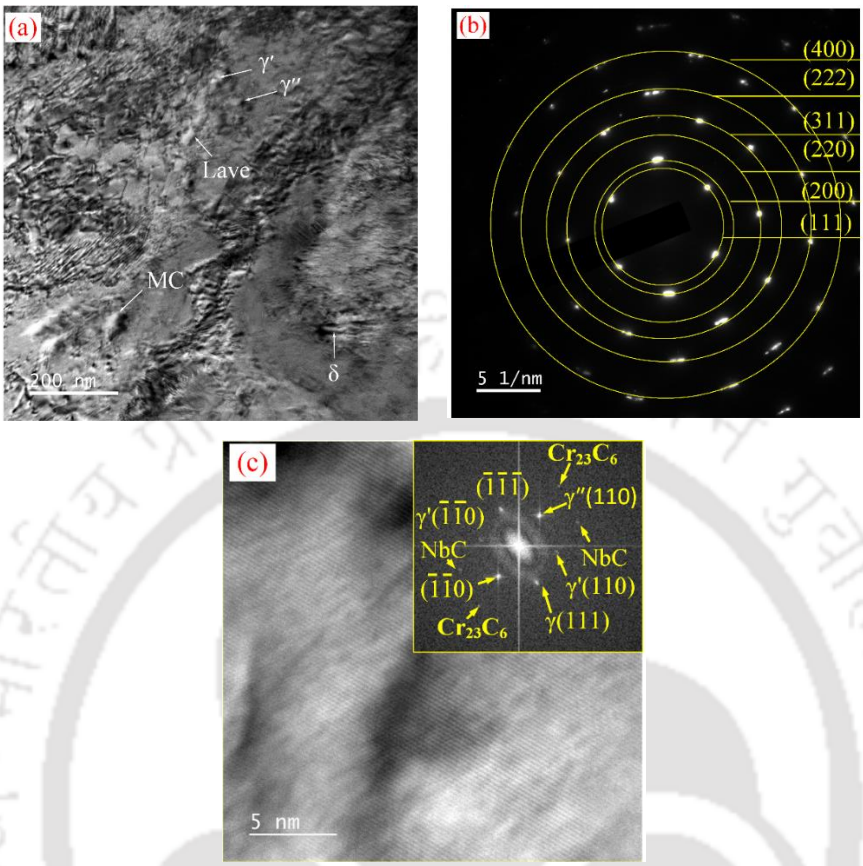

Fig. 4.42 TEM micrograph of ABS (a) bright field image, (b) SAED pattern and (c) HRTEM

Figure 4.43 (a-c) represents typical TEM micrograph of PBHT sample. The bright field image in **Fig. 4.43 (a)** reveals large volume fraction of spherical γ′ and γ″ disk shape precipitates with size of 14 and 25 nm, respectively. In the PBHT samples more uniformly distributed γ′, and γ″ phases were observed. The increase in volume fraction of the γ′ and γ″ precipitates were due to double aging of the PBHT samples. During TLP bonding, the IN 718 was exposed to high temperature, which causes the increase in particle size due to recrystallization and grain growth. The coherency strain observed in the as bonded samples has been reduced as shown in **Fig. 4.43 (a)**. Similar to as bonded samples, cubic crystal structure was also obtained after PBHT. The SAED pattern of the PBHT samples is shown in **Fig. 4.43 (b)**. Spot in SAED pattern indicates the material is crystalline. The SAED pattern reveals FCC structure with spots corresponding to (111), (200), (220), (311), (222) and (400) planes. The HRTEM image is shown in **Fig 4.43 (c)**. The figure reveals that γ′ and γ″ precipitates are superimposed

with each other in the {110} planes along the <110> crystal direction. Furthermore, some γ′ and γ″ exists in the (210) and (202) planes, having *d*-spacing of 1.59 and 1.6, respectively. Cr_7C_3 type carbides with orthorhombic crystal structure was observed in the PBHT samples. To confirm the formation of the precipitates, the TEM-EDS analysis was carried out and is shown in **Fig. 4.44 (a-c)**. The Nb content in the particle shows formation of γ′ and γ″ phases in the γ matrix.

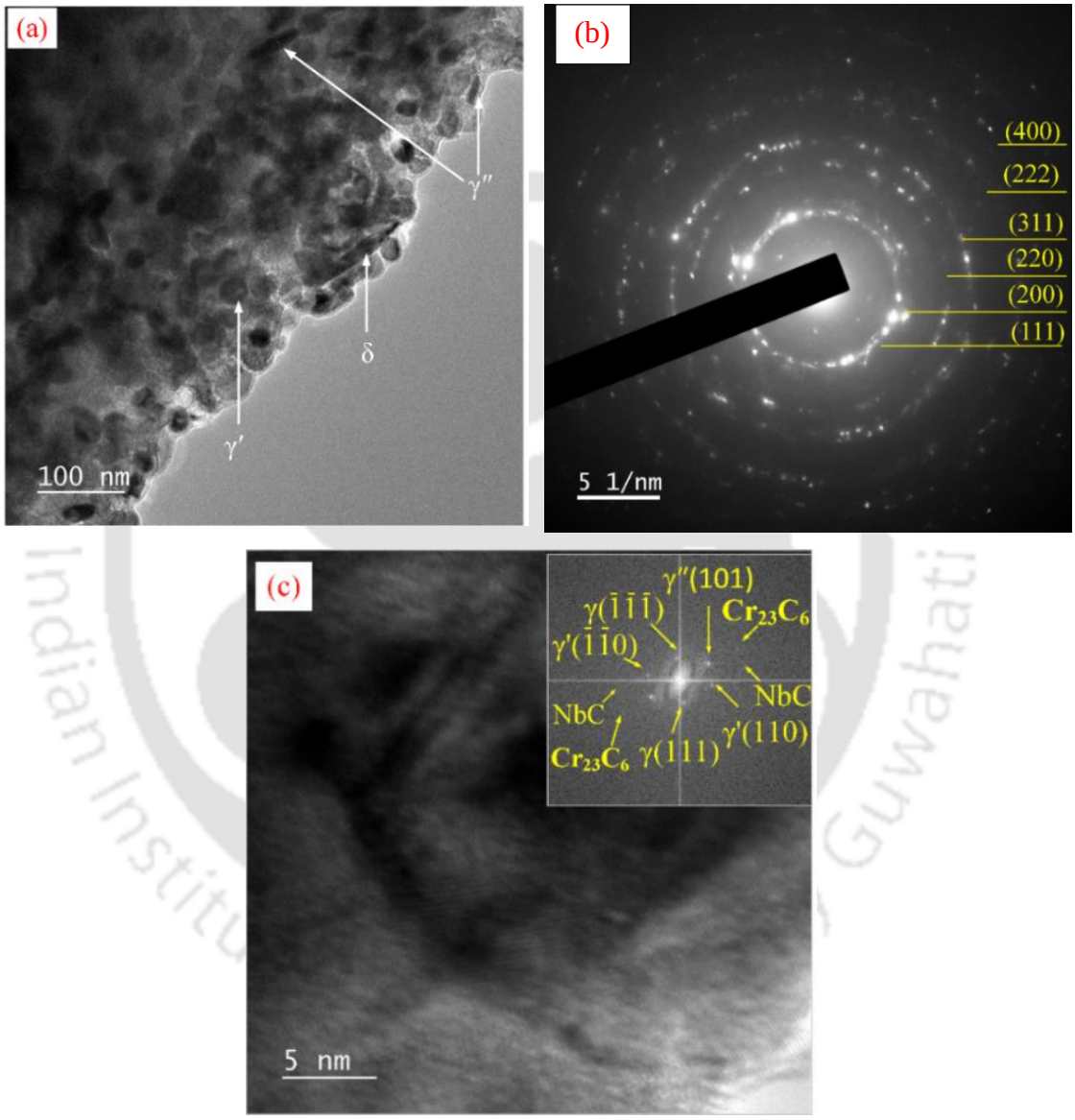

Fig. 4.43 TEM micrograph of HT1050 sample (a) bright field image, (b) SAED pattern and (c) HRTEM image

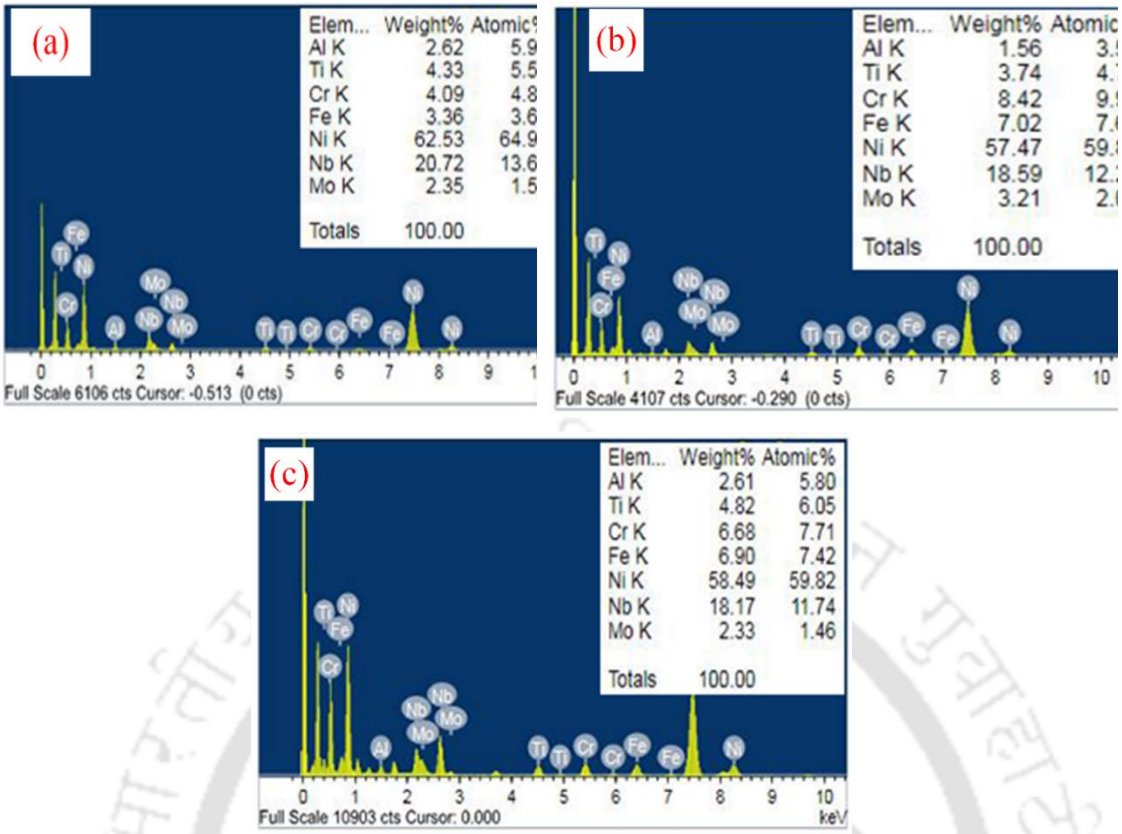

Fig. 4.44 TEM-EDS analysis of (a) γ″-phase, (a) γ′-phase and (c) δ -phase

Figure 4.45 (a) represents typical TEM micrograph of the BMZ of the HT1150 sample. The bright field image in **Fig. 4.45 (a)** reveals large volume fraction of spherical shaped γ′ and disk shaped γ″ precipitates with size of 16 and 22 nm, respectively. The increase in volume fraction of the γ′ and γ″ precipitates were due to double aging of the PBHT samples. During TLP bonding, the IN 718 was exposed to high temperature, which causes the increase in particle size due to recrystallization and grain growth. Similar to the as bonded samples cubic crystal structure was also obtained after PBHT. The SAED pattern of the rectangle marked as 'B' in **Fig. 4.45 (a)** is shown in the **Fig. 4.45 (b).** The SAED pattern revealed crystalline FCC structure with diffraction spot corresponding to the (111) (111), (200), (220), (311), (222) and (400) planes. The HRTEM image is shown in **Fig 4.45 (c)**. The figure revealed the γ′ and γ″ precipitates are superimposed with each other in the {110} planes along the <110> crystal direction. Furthermore, some γ′ and γ″ existed in the (210) and (202) planes, having d-spacing of 1.59 and 1.6 Å, respectively. Cr_7C_3 type carbides with orthorhombic crystal structure was observed in the PBHT samples.

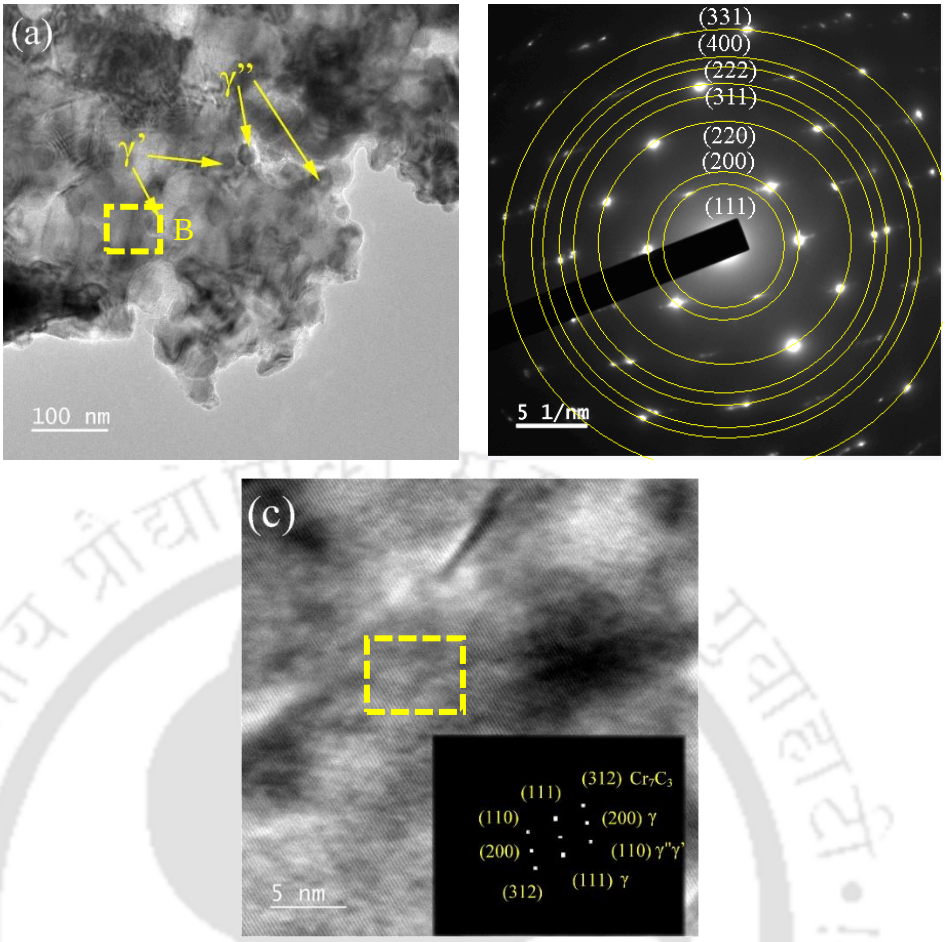

Fig. 4.45 TEM micrograph of PBHT sample (a) bright field image, (b) SAED pattern and (c) HRTEM image

4.5.3 Microstructure of TLP bond

Microstructure of the bond area of the ABS is shown in **Fig. 4.46**. The bond microstructure consists of four regions: (i) isothermal solidification zone (ISZ), (ii) Athermal solidification zone (ASZ) (iii) diffusion affected zone (DAZ), and (iv) un-affected base material zone (BMZ). The ISZ forms by isothermal solidification (IS) mechanism. On holding at the bonding temperature for sufficient time, interdiffusion of atomic elements between the liquid interlayer and the parent alloy occurs. On isothermal holding, composition of interlayer changes at the interface due to interdiffusion of elements. This raises the melting temperature of the interlayer at the interface. That leads to IS and formation of a new solid-liquid interface. This phenomenon continues until complete removal of the liquid in the bond area i.e. the completion of IS. The IS starts from the base metals surface and progresses toward the center of the bond. During IS, the grains nucleates from the workpiece surface and grows towards the center of the bond by

epitaxial solidification. However, cooling down the bond assembly before complete IS leads to athermal solidification of the remaining liquid present in the interlayer and forms ASZ. The ASZ is present in the centerline of the TLP bonding due to unsolidified residual liquid. In the ASZ, the second phase precipitates were observed in the form of blocky shape and forms a continuous line in the bond centerline.

Figure 4.46 (b-c), depicts the microstructures and the elemental mapping of the DAZ. Needle shape and irregular shape Fine and coarse second phase particles are observed in the DAZ. The precipitates were present as a discontinuous network along the grain boundaries and also dispersed inside the grains near to the ISZ. From the microstructure, it was observed that the volume fraction of the second phase particles decreased while moving away from the bond interface toward the BMZ. Near to the bond interface area, the grain size was very fine and the concentration of second phase particles were high. This is attributed to the fact that grain boundaries are regions of higher energy compared to the grains due to which the rate of atomic diffusion along the grain boundary is high compared to that inside the grains. This results in higher concentration of second phase particles at the grain boundaries compared to inside the grains. Results of the EDS analysis presented in **Table 4.6** reveals the precipitates as Cr-Nb-Mo rich particles. As the atomic number and quantity of boron in the alloy is small, accurate detection of boron by EDS was very difficult and hence not included. However, the elemental mapping shown in **Fig. 4.46 (c)**, reveals Fe, Cr, Si and Ti are distributed uniformly in the Ni-matrix and the second phases particles consist of Nb, Mo and B atoms indicating these phases as borides of Nb and Mo. During IS, the boron diffuses from the liquid interlayer diffuse into the base alloy through the grain and along the grain boundaries. As Mo, Cr, and Nb have high boride promoting elements, these elements react with the boron to form borides during IS.

Table 4.6 EDS result of DAZ precipitates

Element (at. %)	Ni	Cr	Fe	Nb	Ti	Mo	Al
Needle	11.6	35.3	3.7	30.4	0.8	17.4	0.3
blocky	26.2	30.8	12.8	12.3	1.1	16.1	0.1
Grain boundary precipitates	8	47.2	15.1	15.3	–	13.8	0.2

The elemental mapping of ASZ (marked as "O" in **Fig. 4.46 (a)**) is shown in **Fig. 4.47** The spatial distribution of elements in the second phase precipitates shows higher contrast for Nb, Mo, Si, and Al elements. The presence of Nb, Mo, Al and Ti elements at the ASZ indicates dissolution of base alloy and interdiffusion of elements between the liquid interlayer and the base alloy. Initially, these elements were not present in the interlayer. At high temperatures, interdiffusion of elements from the base material into the liquid interlayer zone resulted in the formation of second phase particles. The high magnification micrograph of ISZ reveals the presence of four contrast colors in the ASZ such as light grey, black, white and dark grey, which are labelled as 1, 2, 3 and 4, respectively, in **Fig. 4.47 (a)**. This could be due to presence of four different phases at the ASZ. The EDS of the marked areas were carried out to determine the composition of the second phase particles. The EDS results are presented in the **Table 4.7**. The light grey particles are Ni-Nb-Si rich particles, the black particles are Ni-Al-Ti rich particles, the white particles are Ni-Nb-Al-Si rich particles and the dark grey are Al- Ni-Cr-Fe rich particles. The light grey and white particles are could be silicides of Ni-Nb and Ni-Nb-Al, respectively. The dark grey and black particles are Al rich second phases. The second phase precipitates present in the ASZ are $Ni_{54.7}Si_{21.7}Nb_{17.9}Cr_{1.7}Fe_{1.7}Al_{1.3}Ti_{1.1}$, $Al_{65.2}Ni_{16.8}Ti_{8.0}Si_{3.4}Cr_{3.4}Fe_{1.9}Nb_{1.2}$, $Ni_{41.3}Al_{22.7}Si_{15.1}Nb_{11.7}Ti_{4.7}Cr_{2.4}Fe_{2.1}$ and $Al_{44.2}Ni_{33.1}Cr_{11.3}Fe_{8.1}Si_{1.9}Nb_{1.5}Ti_{1.2}Mo_{0.7}$

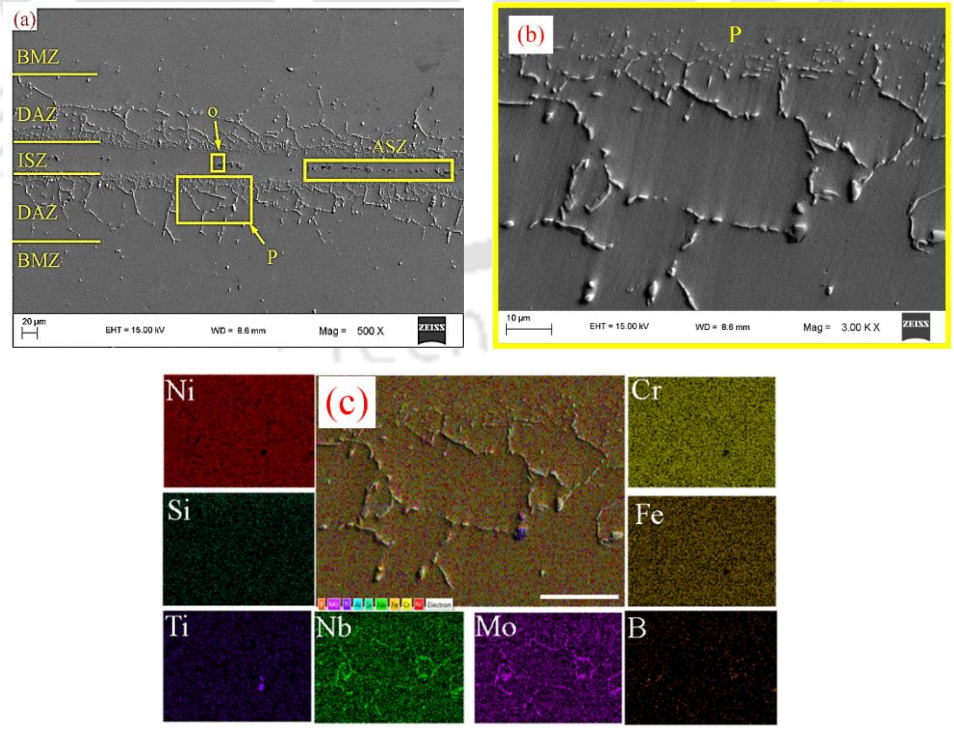

Fig. 4.46 Microstructure of (a) ABS, (b) DAZ and (c) elemental mapping of DAZ

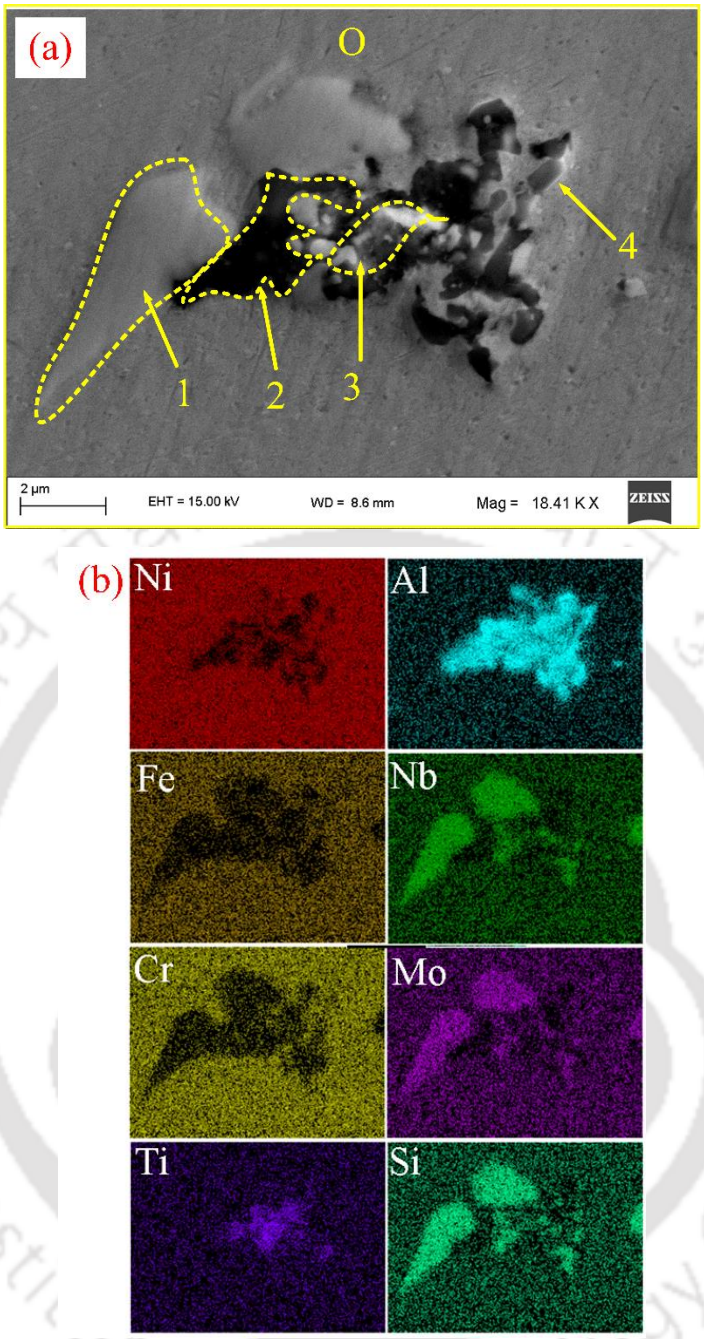

Fig. 4.47 (a) Enlarged view of section O and (b) elemental mapping of ASZ

Table 4.7 EDS analysis result of different precipitates of ISZ

Element (at. %)	Ni	Cr	Fe	Nb	Al	Ti	Mo	Si
1	54.5	1.7	1.7	17.9	1.3	1.1	–	21.7
2	16.8	3.4	1.9	1.2	65.2	8	–	3.4
3	41.3	2.4	2.1	11.7	22.7	4.7	–	15.1
4	33.1	11.3	8.1	1.5	42.2	1.2	0.7	1.9

4.5.4 Microstructure of post bond heat treated (PBHT) sample

4.5.4.1 Microstructure of HT1050 process

Previous section indicated presence of second phase particles at DAZ in the ABS. This will degrade the mechanical properties of the joined components. PBHT is considered to be a necessary process to improve the microstructural homogeneity and mechanical properties of the TLP-bonded samples. Usually, two stages of heat treatment processes are recommended for nickel based superalloys: solution heat treatment (annealed) and precipitation heat treatment (aged) **[198]**. The PBHT was carried out as per the reported heat treatment processes for IN 718 superalloy **[199]**. The following four steps were considered: (i) solution heat treatment carried out at 1050 ˚C for 120 min in order to dissolve δ phase in the base alloy matrix, (ii) quenching the sample to form γ matrix, (iii) aging at 760 ˚C for 8 h to precipitate γ″ to contribute to strengthening of the alloy and (iv) double aging at 660 ˚C for 8 h to precipitate γ′ which are the secondary strengthening precipitates. After double aging, the sample was furnace cooled so that the required microstructure is obtained.

The microstructure of the PBHT sample is shown in **Fig. 4.48 (a-e)**. Compared to the ABS, more uniform microstructure is obtained after HT1050 heat treatment. Similar to the TLP-bonded sample, three zones were observed in the PBHT sample. However, the ASZ is almost eliminated by the PBHT process. In the ISZ fine circular and irregular shaped precipitates were observed. The size of the ISZ is increased and at the same time, the concentration of Nb, Ti, Al, and Mo in the ISZ has increased due to more inter-diffusion of these elements. The magnified view of the ISZ is presented in the **Fig. 4.48 (b)**. Very small precipitates are observed in this zone. The EDS analysis of the precipitates are presented in the **Table 4.8**. The EDS analysis shows a decrease in the Si content in the silicides. During the PBHT process, as the sample was held for prolonged period, more Si atoms diffuse from the ASZ and the Nb, Mo and Ti are distributed uniformly in the ISZ. The sizes of the ASZ decreased and ISZ size increased during the PHBT. Two types of precipitates are observed in the ISZ after PBHT. The precipitates marked as C, D, and H in **Fig 4.48 (b)** have higher Al and Si content compared to E, F, and G. These are the second phase particles formed due to inter-diffusion of atoms during the PBHT process. As the diffusivity of Si in Ni is less compared to B, the time required for complete diffusion of Si from the interlayer is more. As a result, some Si based second

phases are observed at the ISZ. The secondary phases formed during PBHT are Ni-Cr-Nb rich silicide and Al–Cr rich secondary phase.

The magnified view of the DAZ of the PBHT sample is shown in **Fig. 4.48 (c)**. Compared to ABS, wider DAZ zone was formed during the PBHT process. During PBHT process the diffusion length of B atoms increased and they reacted with the boride promotor elements like Nb, Cr and Mo to form second phase particles. That increased the size of the DAZ. Due to prolonged high temperature diffusion during PBHT process, some portion of the borides dissolve in the Ni matrix resulting in fragmentation of the needle shape and large bulky borides. In addition to this, as the concentration of boride promotors like Nb, Cr and Mo is less in the base matrix as compared to the precipitates, therefore, these atoms diffuses from the precipitates into the base matrix. As a result, the boride fraction in the DAZ zone decreases during PBHT process. The fraction of the borides decreased from 15.2 % in ABS to 7.5 % after PBHT. The EDS of different shapes of borides is presented in **Table 4.9.** The EDS analysis result shows that Nb-Cr-Mo rich phases are formed in the DAZ.

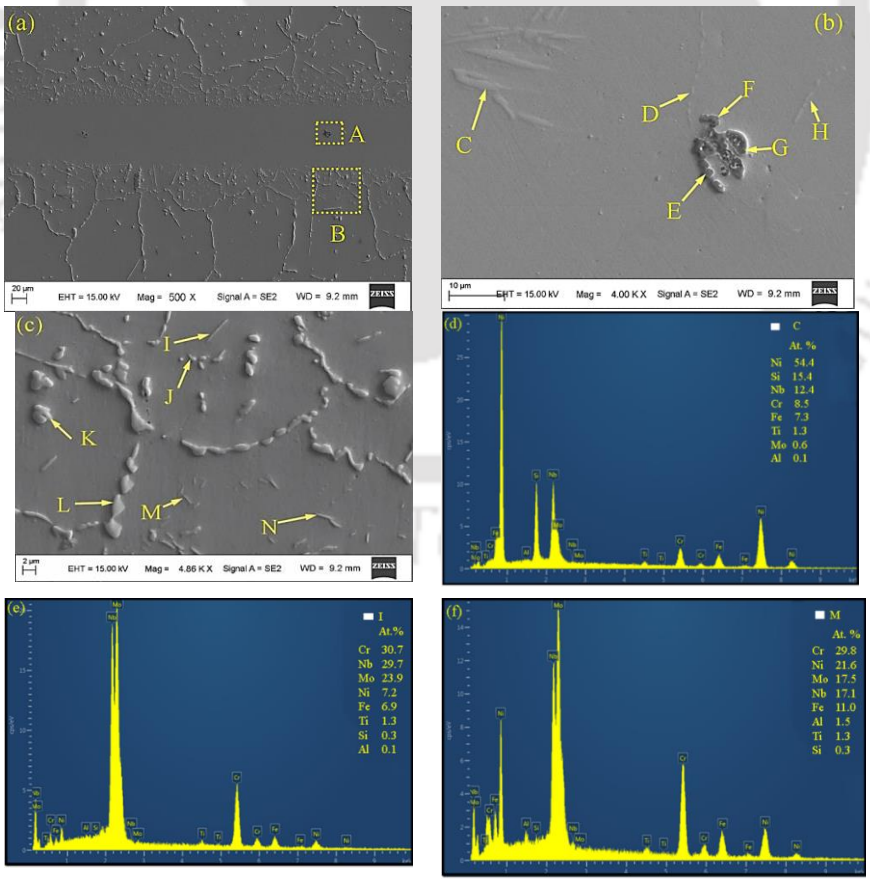

Fig. 4.48 Microstructure of (a) PBHT sample, (b) magnified view of ISZ, (c) DAZ, (d) EDS result of particle "C", (e) EDS result of particle "I", and (f) EDS result of particle "M"

Table 4.8 EDS analysis results of ISZ precipitates

Element (at. %)	Ni	Cr	Fe	Nb	Al	Ti	Mo	Si
C	54.4	8.5	7.3	15.4	0.1	1.3	0.6	12.4
D	53.8	10.3	8.5	11.8	0.4	1.1	0.7	13.3
E	10.6	4.9	3.4	0.7	78.6	0.9	0.4	0.7
F	6.2	48.6	3.7	0.8	30.3	4.2	1.1	5.1
G	8.2	3.3	2.5	00.6	76.4	7.5	0.3	1.1
H	54.4	6.2	5.7	15.2	5.5	0.8	0.0	12.2

Table 4.9 EDS results of various precipitate present at DAZ

Element (at. %)	Ni	Cr	Fe	Nb	Al	Ti	Mo	Si
I	7.2	30.7	6.9	29.7	0.1	1.3	23.9	0.3
J	12.0	49.0	6.5	21.3	0.5	1.5	8.9	0.2
K	12.2	45.6	6.3	24.1	0.8	2.2	8.8	0.0
L	10.4	26.8	7.6	32.1	0.3	1.5	21.2	0.1
M	21.6	29.8	11.0	17.1	1.5	1.3	17.5	0.3
N	19.3	35.2	10.6	16.1	0.7	1.1	17.0	0.1

4.5.4.2 Microstructure of HT1150 process

The FESEM micrograph of the BMZ and DAZ of the post-bond heat-treated TLP-bonded sample (HT1150 process) is shown in Fig. **4.49 (a-b)**. The microstructure shows three different zones similar to the as bonded TLP bonding samples. As mentioned earlier, at BMZ, γ′ and γ″ precipitates were formed at the expense of δ-phases. Metallic carbides of Nb and Ti were also observed in the BMZ. The microstructure of the PBHT sample seems to be more uniform compared to the as-bonded sample. The higher magnification image of the DAZ of the PBHT sample is shown in **Fig. 4.49 (b)**. The EDS results of different borides are presented in **Table 4.10**. The EDS analysis results are similar to the as bonded samples, Nb-Cr-Mo type borides were formed in the DAZ. However, the following changes are observed in the DAZ; (i) the size of the DAZ increased to 138 µm compared to 105 µm for the as-bonded sample, (ii) The volume fraction of borides decreased from 15 % in the as-bonded sample to 6 % in PBHT sample,

(iii) continuous network type borides present in the grain boundaries were dissolved and transformed into fine blocky type borides (as marked M) in **Fig. 4.49 (b)**, and (iv) some of the fine blocky shape borides observed in the as bonded sample were dissolved in the matrix.

The dissolution of borides is diffusion-controlled process. Prolonged annealing of the bonded samples at higher temperatures causes diffusion of boron from precipitates to BMZ. Which leads to an increase in the DAZ area in PBHT samples. In addition to that, the concentration of Nb, Cr, and Mo is very high in the precipitates compared to the surrounding matrix. These elements diffuse from the precipitates to the adjacent matrix during the PBHT stage resulting in the decrease of boride promoting elements in the DAZ. Hence the volume fraction of borides decreases after PBHT. Due to the matrix-precipitate interfacial energy and curvature difference in grain boundary precipitates, a chemical potential is build-up across a grain boundary boride and matrix according to Gibbs–Thomson effect **[200]**. This chemical potential setups a diffusion flux, which leads to particle break-up during PBHT. As a result of this, the coarse grain boundary borides were broken down in to fine particles.

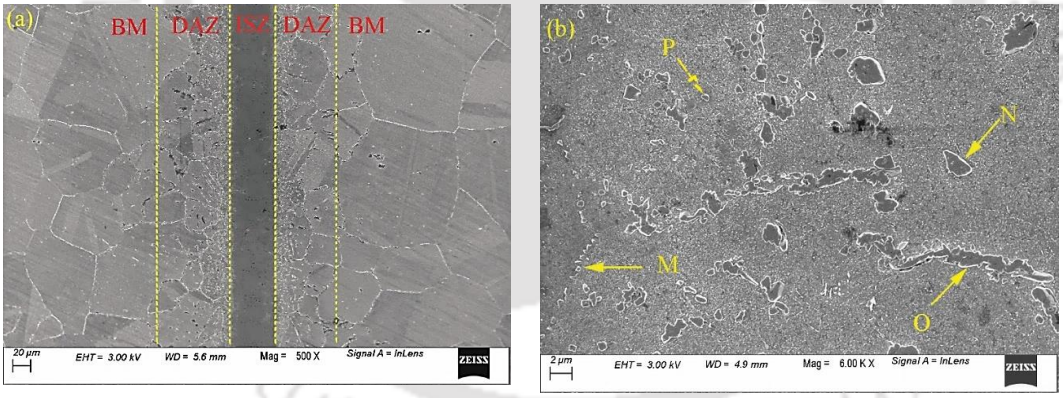

Fig. 4.49 FESEM micrograph of (a) heat-treated sample (Exp.2) and (b) DAZ precipitate

Table 4.10 Compositions of DAZ precipitates

Element	Ni	Cr	Fe	Nb	Ti	Mo	Al	Si
M	18.6	30.1	12.6	20.1	1.0	16.9	0.6	0.1
N	40.4	25.6	16.2	7.5	0.5	8.8	0.6	0.4
O	18.3	30.1	8.4	32.1	1.4	9.0	0.6	0.1
P	18.3	29.0	8.5	20.9	1.1	20.9	0.8	0.6

4.5.5 Tensile properties of PBHT samples

The stress-strain curve of the PBHT sample is shown in **Fig. 4.50 (a-c)**. The graph reveals that the strength of the heat-treated sample is more than that of the as-received and as-bonded samples. The strength of the base material also increased significantly after heat-treatment. However, the ductility of the heat-treated sample has reduced significantly. In IN 718 superalloy, the mechanical properties mainly depend on the size, volume fraction and morphology of the coherent ordered BCT-γ″ phase and ordered FCC-γ′ phase. As the nano sized γ″ precipitates are present coherently with the γ-matrix. It produces coherency strain due to lattice mismatch. The coherency strain will obstruct the movement of the dislocation which increases the strength of the IN 718 joint. Moreover, the ordered FCC-γ′ phase contributes the strengthening process by order hardening mechanism. With heat treatment, the volume fraction of the γ′+ γ″ phase increased in the IN 718 alloy causing an increase in the UTS in the heat-treated samples. During solution treatment, holding above 1050 ºC for 2 h, the δ-phase completely dissolved, and on immediate water quenching, as the available time for precipitation of δ-phase was very little, a very small amount of δ precipitates was observed in the PBHT samples. On double aging the samples resulted in the formation of more γ′ and γ″ phases. Which are the main precipitation strengthening phases of IN 718 superalloy. The increased in the volume fraction of γ′ and γ″ phases contributed to the strength of the material. In addition to this, on holding the bond at elevated temperature for longer time, the homogenization stage of TLP bonding was accomplished, which resulted in diffusion of more alloying elements during PBHT and assured solid solution strengthening of the alloy. Both precipitation strengthening and solid solution strengthening contributed to the higher tensile strength of PBHT samples, as reported by **Chang et al. (2014)**. Moreover, during post bond heat treatment the secondary phases present in the ISZ dissolves and uniform microstructure is obtained. This factor also contributes the higher strength of the PBHT sample than the ABS. Also, the volume fraction of boride decreased during PBHT which partially contributed in the strengthening of PBHT samples. The precipitation of more γ′ and γ″ phases in the bond zone reduced the ductility of the samples. As these precipitates are brittle in nature, the overall ductility of the bond decreases. In addition to this, as the γ′ and γ″ phases are distributed closely in the sample. Coalescence of crack occurs quickly as less space available for crack growth. Which results in less ductility of the PBHT samples.

The UTS and percentage of elongation of the (as received IN 718) ARIN 718, heat-treated base material (HT IN 718), as bonded sample (ABS), HT1050, and HT1150 samples are shown in **Fig. 4.51 (a-b)**. The UTS of ABS, HT1050 and HT1150 samples (for Exp. 6) were 567 MPa, 1220 MPa, and 1124, respectively. After PBHT it was observed that more than 100 % of strength increased as compared to the ABS. At the same time, there is a 40 % reduction in ductility. The maximum UTS observed in case of HT1050 heat-treatment cycle is 1233 MPa, whereas for HT1150 heat-treatment cycle the maximum UTS observed is 1124 MPa. In IN 718 superalloy, at 1150 °C temperature, liquation of low melting point grain boundary eutectic phase occurs. At that temperature the lave phase liquefies and segregates at the grain boundaries. Which later affects the strength of the superalloy. This is the main reason for lower strength of the HT1150 samples compared to HT1050 sample.

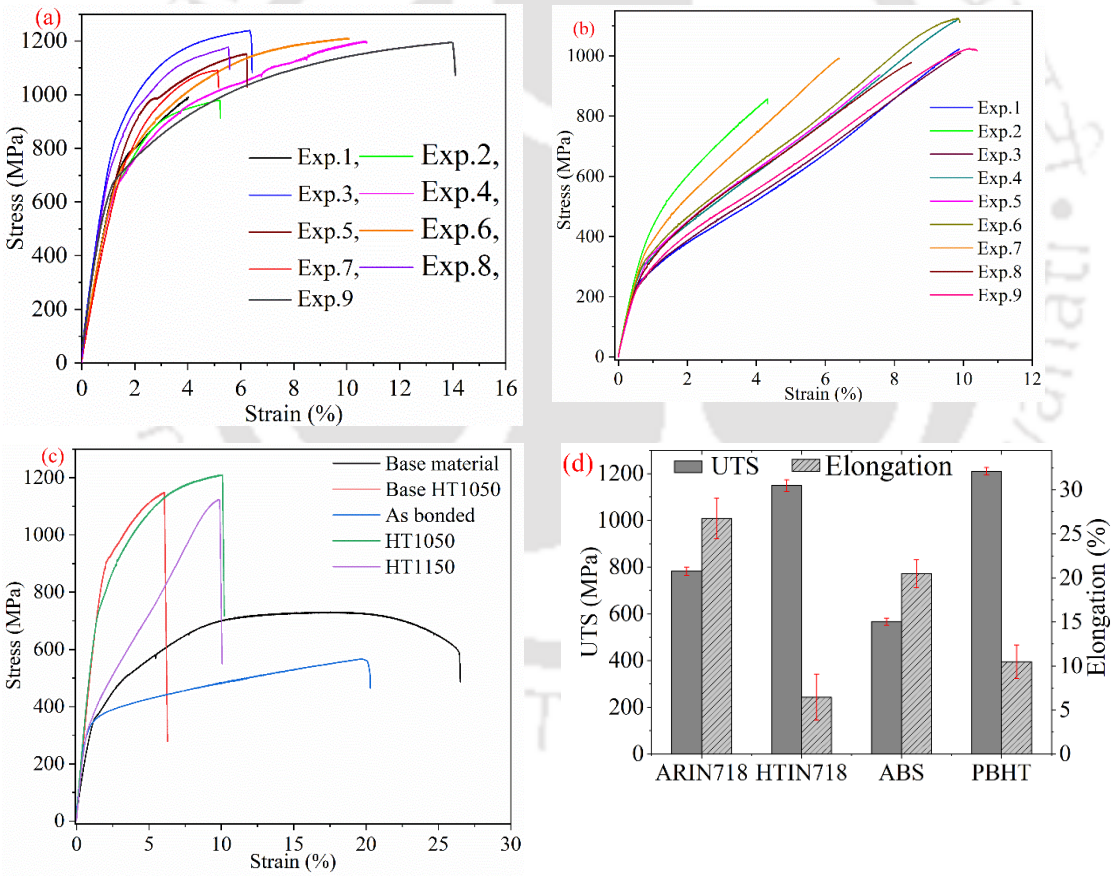

Fig. 4.50 Tensile properties of the PBHT sample for heat treatment cycle (a) HT1050, (b) HT1150, (c) comparison of all sample, and (d) UTS and elongation bar chart

4.5.6 Fractography

The percentage of elongation and fracture mode of IN 718 superalloy largely rely on the relative strength between the grain boundaries and interior of the grains. Two

factors possibly will account for the higher ductility of the ARIN 718 and ABS samples. Firstly, the yield strength of the ARIN 718 and ABS samples is lower than that of the HT1050 and base HT1050 samples thereby facilitating larger plastic deformation before failure.

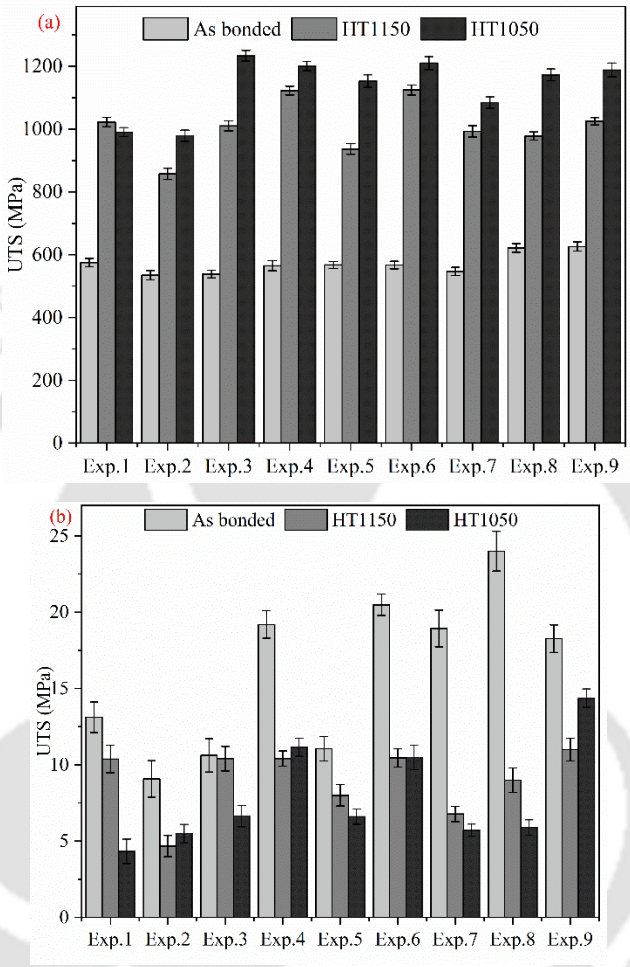

Fig. 4.51 Variation of tensile properties with various experimental condition (a) UTS and (b) Ductility

Secondly, the grain boundary strength of the ARIN 718 and ABS samples was greater than that of the PBHT and HT samples. As a result, direct dimple mode of failure was observed in the ARIN 718 and ABS samples and the intergranular fracture was dominated for all the heat treated samples (shown in **Fig. 4.52**. A low magnification fractography image of the ARIN 718 and PBHT samples are shown in Fig. **4.53 (a-b)**. It shows dimple features indicating transgranular failure for the ARIN 718 samples whereas intergranular failure is the mechanism for the PBHT sample. The dimples features in the ARIN 718 sample indicate that the failure is by the nucleation of micro-voids inside the grains of second phase particles, subsequent growth and followed by coalescence of these voids. The percentage elongation and fracture behaviour of material under study depend

on the type and nature of the constituent phases at the grain boundaries (GB) and inside the grains. It also depends on the strength of the grains and GB. During the solution treatment stage of the HT and PBHT samples, carbides precipitated at the grain boundaries, which decreased the grain boundary strength of the HT and PBHT samples.

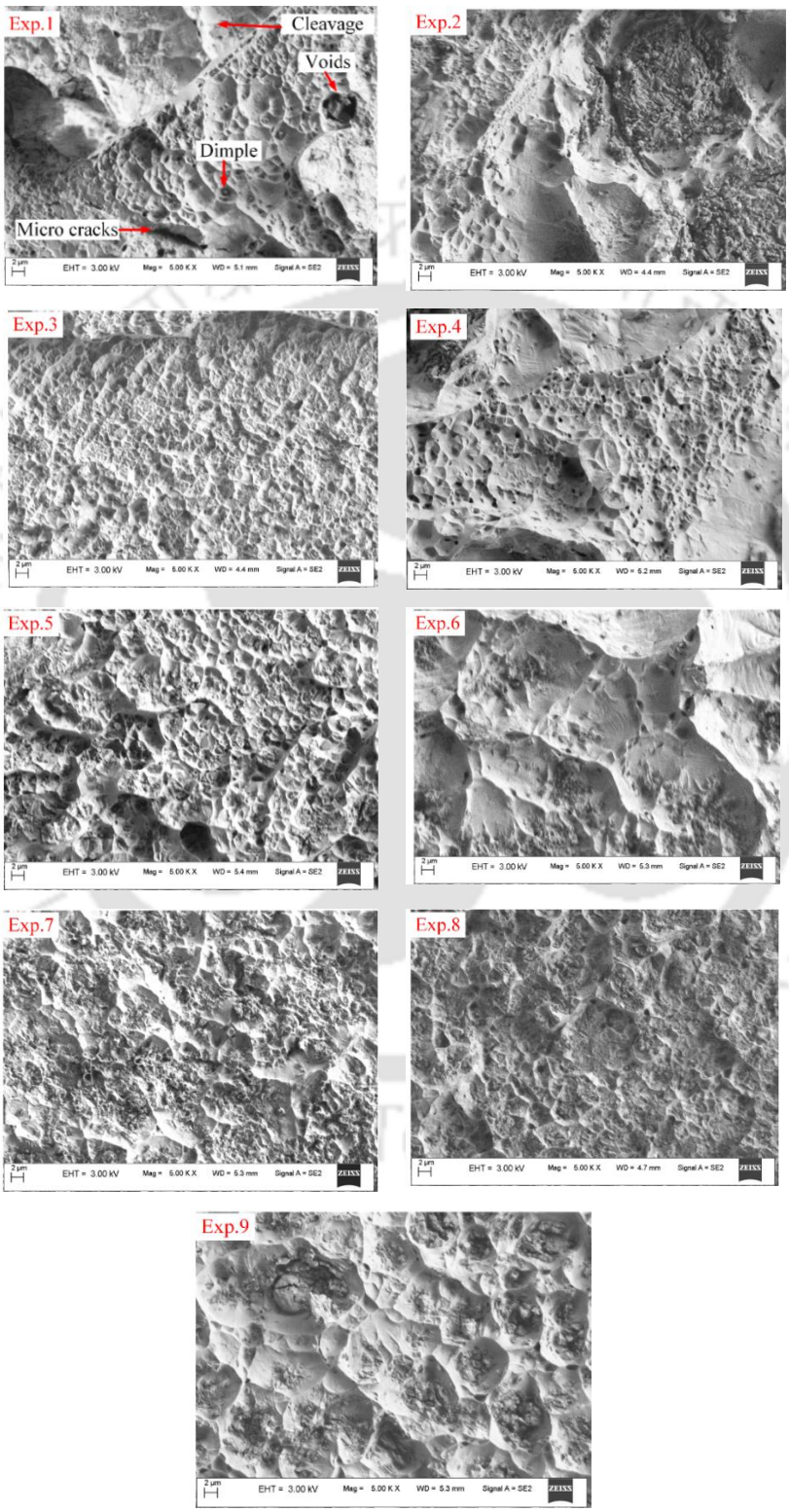

Fig. 4.52 Fracture surface of HT 1050 tensile samples

As a result brittle failure was observed in these samples. The presence of hard second phase particles at the grain boundary regions in the PBHT samples makes the grain boundary regions weak and at the same time makes these regions brittle. During the external loading, the failure initiates at the GB and propagates through the GB regions due to the high brittleness compared to inside the grains.

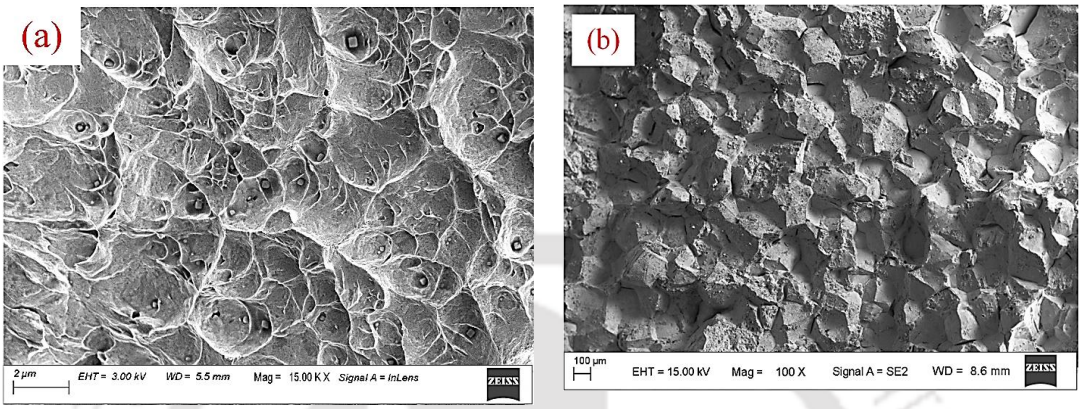

Fig. 4.53 Fractograph of (a) as received sample and (b) PBHT sample

Figure 4.54 shows the fracture surface of the HT1150 tensile samples. The low and high magnification of the fracture surface are shown in **Fig. 4.55 (a-b)**. The fracture surface reveals the following; (i) low magnification observation reveals fine dimples with an average size of around 2 µm as the major feature and fractured second phase particles having size varying between 6-15 µm, and (ii) high magnification fractographs reveals features of intergranular fracture, secondary micro-cracks and cleavage are several areas Samples corresponding to Exp. Nos. E.4, E.5, and E.6 showed more volume of dimples compared to other samples. This is mainly due to a more uniform microstructure of the samples. The inter-granular fracture produced was mainly due to fracture propagation along the grain boundaries since these are regions of high energy. In addition, the presence of the brittle δ-phase and borides at the grain boundaries promoted de-cohesion of the grain boundaries. This phenomenon is mainly observed in grain boundary favoured diffusion processes. The presence of cleavage, inter-granular fracture, and dimples in the fracture facets indicates mixed type of failure.

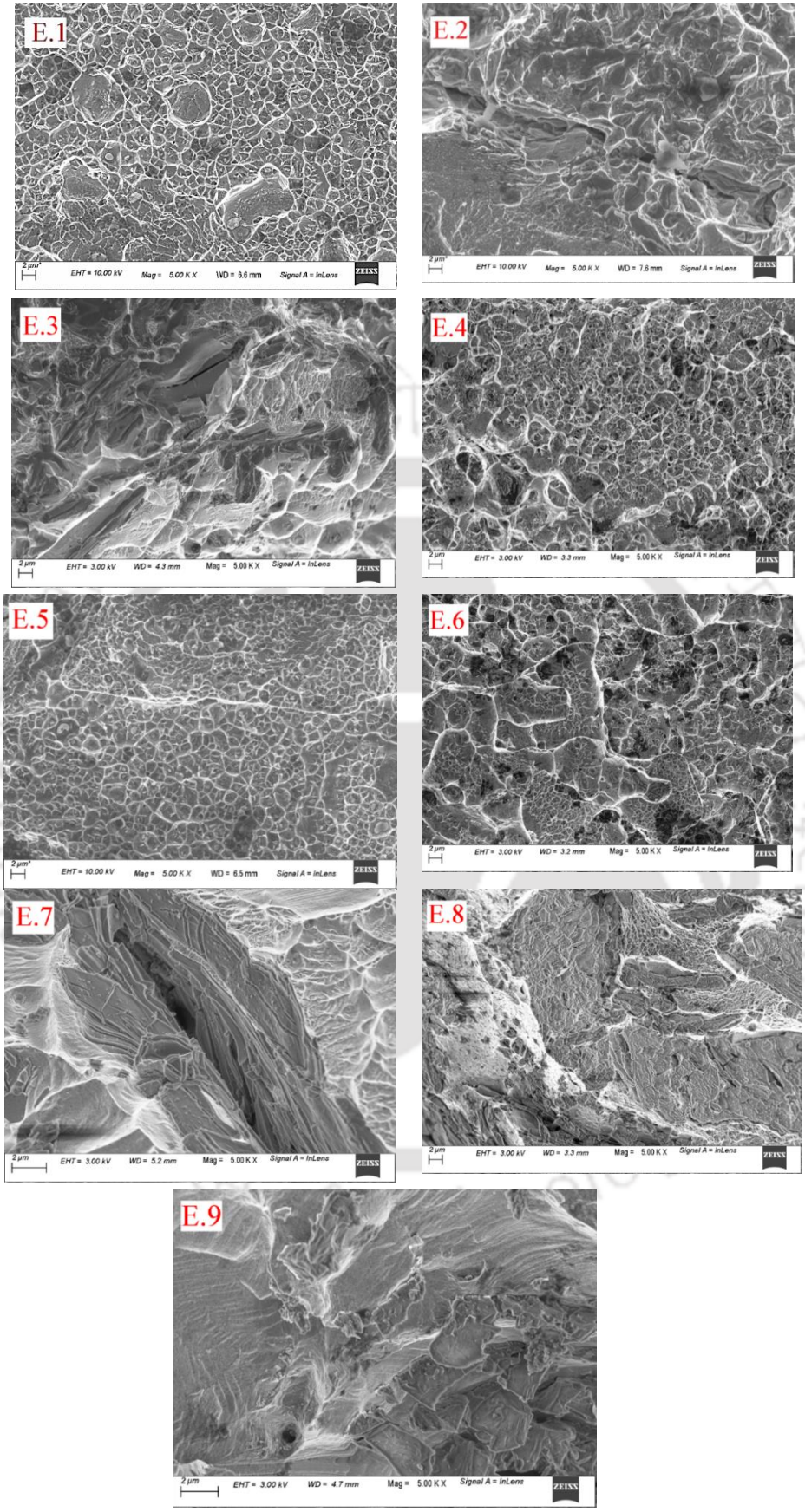

Fig. 4.54 Fracture surface of post bond heat treated tensile samples

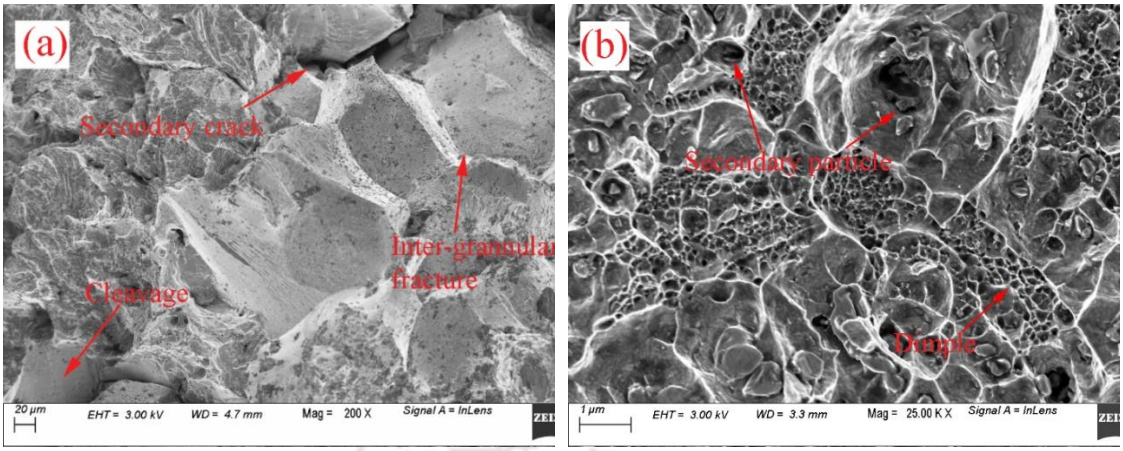

Fig. 4.55 Fracture surface of PBHT sample (a) low and (b) high magnified views

4.5.7 Microhardness result

The hardness variation of the HT1050 and HT1150 samples are shown in **Fig. 4.56** and **Fig.4.57**, respectively. The hardness of ISZ, BMZ and DAZ increased in both the cases. The volume percentage of γ″+ γ′ precipitates increased during heat treatment, which is the primary cause of higher hardness of the PBHT samples. During PBHT, the volume fraction of boride phases also decreased as the samples were exposed to prolonged high temperature diffusion. The difference in hardness between the DAZ and the BMZ was decreased because of the reduction of boride fraction in the DAZ and precipitating more γ″ and γ ′ phases in the BMZ. The volume of second phase precipitates present in the ISZ in the as bonded sample was reduced after PBHT due to more diffusion of alloying elements. At the same time the fraction solid solution strengthening phases and γ″+ γ′ precipitates increases in the ISZ. This increases the hardness of the PBHT samples. It was also observed that the hardness of the ISZ is lower than that of the BMZ and DAZ. This is attributed to low fraction of solution strengthening elements and γ″+ γ′ precipitates at the ISZ compared to other two zones.

It was observed that the hardness variation between the HT1050 and HT1150 cycle is very marginal. However, the hardness of the DAZ of the HT1050 is more compared to that of the HT1150. In the case of HT1150, as the annealing temperature is high, more boride dissolve during heat treatment. As a result of this the hardness of the DAZ is slightly lower than that of the BMZ.

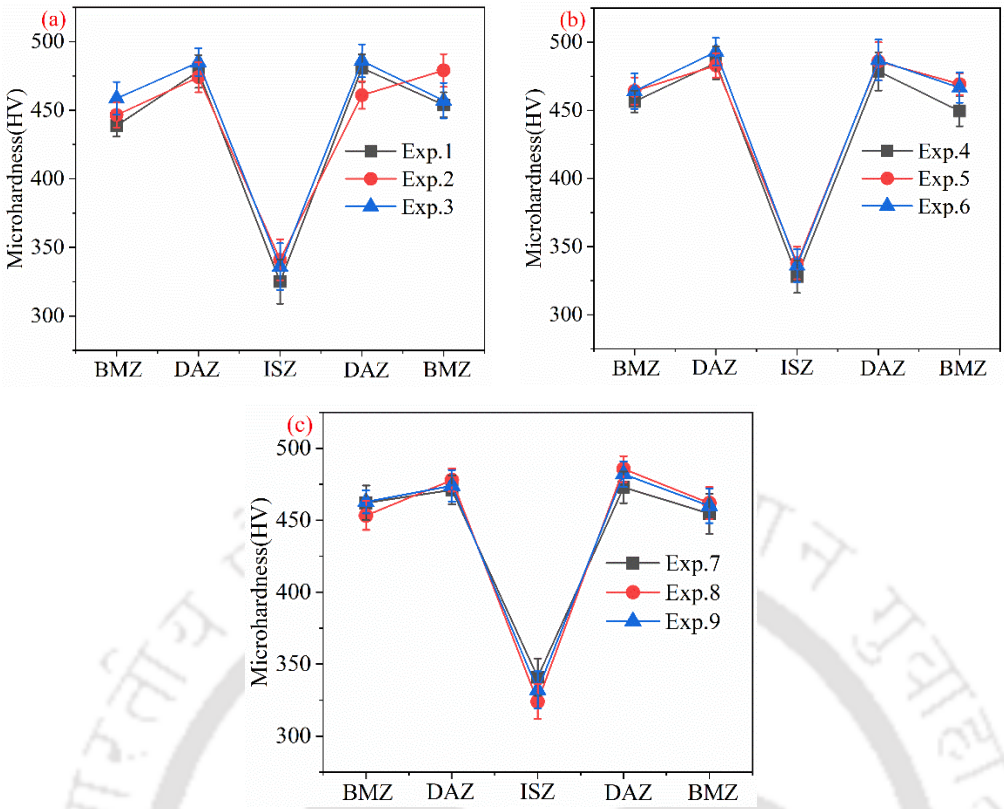

Fig. 4.56 Microhardness variation of HT1050 samples, (a) bond made at 1050, (b) bond made at 1100, and (c) bond made at 1150

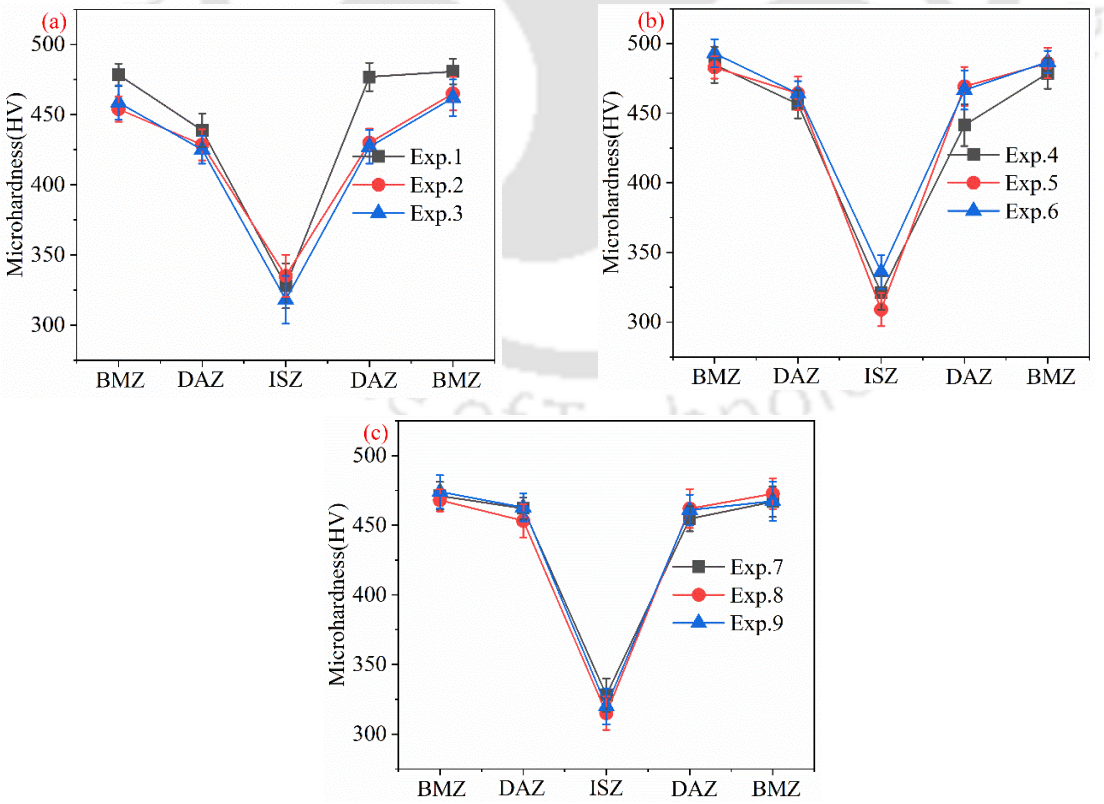

Fig. 4.57 Variation of microhardness of PBHT-2 samples bonded at (a) 1050 ˚C, (b) 1100 ˚C and (c) 1150 ˚C

4.6 Determining of High-Temperature Tensile Properties of PBHT Sample

IN 718 is most often used for manufacturing the hot section components of aero-engines. These components are usually subjected to high-temperature loadings **[2]**. Therefore, the evaluation of the high-temperature mechanical properties of the IN 718 joint is very important. As discussed previously, TLP bonding can be an emerging technique to join IN 718 superalloy **[105, 106, 111]**. Investigating the mechanical properties of the TLP-bonded IN 718 joint at elevated temperatures is the most important work. From the previous section (i.e. 4.4.3), the mechanical properties of the TLP-bonded joint has been improved by the PBHT process. Therefore, in this section, the elevated temperature mechanical properties of the PBHT samples have been studied and compared with that of the heat-treated base material.

4.6.2 Tensile property of PBHT samples at 650˚C

Figure 4.58 (a) shows the engineering stress vs strain curve of the PBHT samples tested at 650 ˚C. The graph reveals a brittle type of failure in all the cases. The tensile strength of the post bond heat treated (PBHTed) TLP-bonded sample is lower than that of the base material strength. Necking is not observed during the test sample till failure. **Figure 4.58 (b)** shows the variation of UTS and % of elongation at different bonding parameters. The graph reveals that the tensile strength corresponds to Exp.6 shows maximum UTS of 1029 MPa, whereas the base material UTS is 1064 MPa. With PBHT a bond efficiency of 95 % is achieved at elevated temperatures. Moreover, the elevated temperature strength of the PBHTed TLP-bonded sample is lower than the room temperature tensile strength of the PBHTed TLP-bonded samples. The UTS of the PBHTed samples tested at room temperature has 1210 MPa, whereas the UTS of the PBHTed samples tested at 650 ˚C has 1029 MPa. A 15 % softening was observed in the TLP-bonded samples as the temperature was raised from room temperature to 650 ˚C. This is due to the lower strength of the grain boundaries and the interior of the grain at elevated temperatures. During the room temperature tensile test, the dislocations get tangled and piled up at grain boundaries and also around the primary strengthening phase γ″ and secondary strengthening phase γ′. This obstructs the dislocation motion. To trigger the multiplication and movement of dislocation, a higher load needs to be applied in order to increase the shear stress of the dislocation slipping. As a result, higher strength is

obtained during room-temperature tensile testing of the PBHT samples. At room temperature, the strength of grain boundaries is higher than that of the interiors of the grains. However, at the high-temperature tensile test, the heat input given to the material will thermally activate the atoms and vacancies present inside the material. This results in the annihilation of vacancies and dislocations thereby reducing the impediments to the movement of existing dislocations. Since grain boundary regions are regions of higher energy, this phenomenon is more pronounced at grain boundaries thereby reducing the grain boundary strength are elevated temperatures **[201]**. This reduces the tensile strength of the PBHTed sample at high temperatures. The % of elongation of the-heat treated base material and the PBHTed TLP-bonded samples are almost equivalent. At elevated temperatures, a maximum of 4.7 % elongation was observed in the samples corresponding to Exp.4, Exp.6 and base material. There is a sharp reduction in the % of elongation in the samples at elevated temperatures. The reduction in % of elongation is due to intermediate temperature embrittlement.

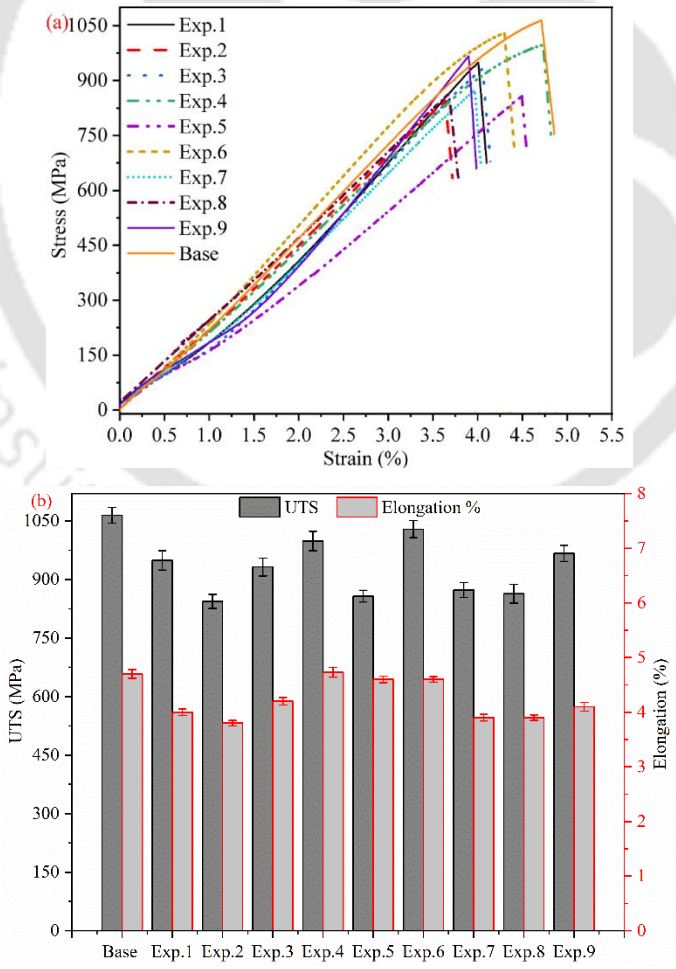

Fig. 4.58 (a) stress-strain curve of PBHT TLP-bonded sample tested at 650 ˚C and (b) bar-chat of UTS and % of elongation

4.6.3 Fractography

The overall fracture surface of the TLP-bonded IN 718 joint (for Exp. 6 and Exp.4) after uniaxial tensile tests at 650 ˚C is shown in **Fig. 4.59 (a-f)**. The low magnification micrograph of Exp. 6 predominantly reveals intergranular fracture along with, discrete micro-voids, and fine deep dimples (as shown in **Fig. 4.59 (a)**). Moreover, the fracture path is almost perpendicular to the applied tensile force. High magnification of the fracture surface of the rectangle marked A indicates intergranular fracture as shown in **Fig. 4.59 (b)** and also fine equiaxed and shallow dimple indicating transgranular fracture. This indicates the fracture is due to a combination of both brittle and ductile failure. The high magnification microscopic analysis of the rectangle marked as B shows some deep dimples containing fragments of carbides and Nb-rich particles. Some needle shape Nb-rich particles are clearly visible on the fracture surface which indicates that the particles are δ-precipitates that are formed during the PBHT process. To confirm this EDS analysis was carried out. The EDS result of the particles marked as rectangles 1, 2, and 3 in **Fig. 4.59 (b-c)** is shown in **Fig. 4.60 (a)**, **(b)**, and **(c)**, respectively. The result reveals that the particle present in rectangles 1 and 3 are rich in Nb. From the morphology and the EDS analysis, it is clear that these broken particles in rectangles 1 and 3 are lave and δ-precipitate, respectively. The particle present in rectangle 3 is needle shape and rich in Nb, which reaffirms that it is a δ-precipitate. And the particle present in rectangle 2 is rich in carbon and Ti, this confirms that the particle is a Ti-rich carbide particle. The broken carbide, lave, and δ-precipitates inside the dimples indicate these precipitates cracked during deformation before final failure. The voids which were observed in the fracture surface are due to the interfacial debonding of the carbide, lave, δ-precipitates, and γ-matrix **[202]**.

The low magnification micrograph of Exp. 4 is shown in **Fig. 4.59 (d)**. The micrograph predominantly reveals intergranular fracture along with, discrete micro-voids, and fine deep dimples. The magnified view of the rectangle marked as C is shown in **Fig. 4.59 (e)**. The microscopic view of the fracture surface shows that the fracture is a transgranular mode with shallow dimples containing fragments of carbides and Nb-rich particles indicating ductile failure. The EDS analysis result of the broken particle present inside the rectangle marked as a, b, and c are shown in **Fig. 4.61 (a-c)**, respectively. The EDS analysis results reveal that these particles are rich in Nb and C. As discussed earlier these particles are carbide, lave, and δ-precipitates. In IN 718, carbides, lave, and δ phases

are present inside the grain and also at grain boundaries. These particles are brittle in nature. During deformation at elevated temperatures, these particles can't cope with the γ-matrix of the IN 718. As a result, the debonding of these particles occurs at the particle and γ-matrix interface which results in the nucleation of voids in the γ-matrix.

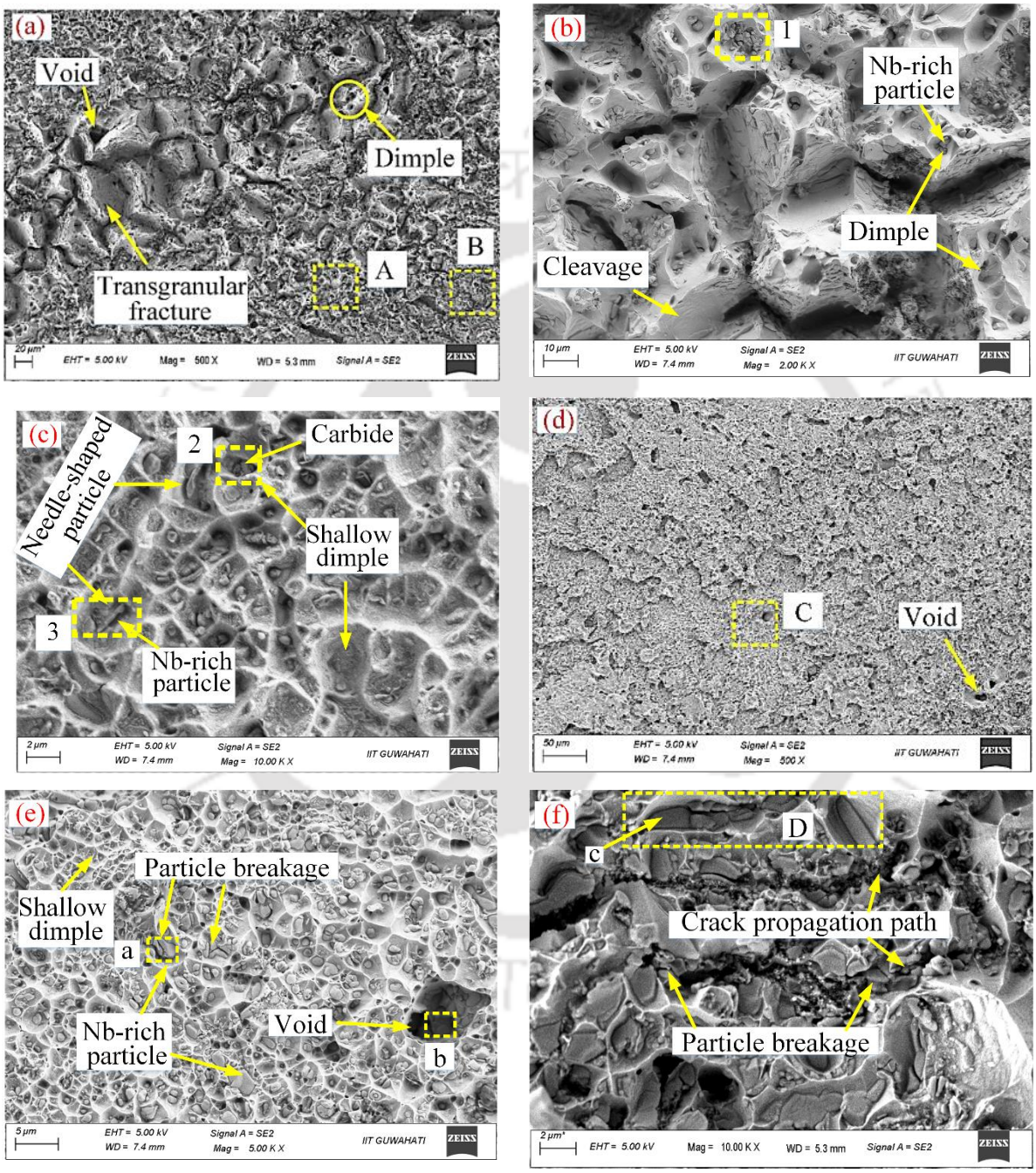

Fig. 4.59 Fracture surface of the tensile tested sample (a) fracture surface of Exp.6, (b) high magnification micrograph of rectangle marked as A, (c) high magnification micrograph of rectangle marked as B, (d) fracture surface of Exp.4, (e) high magnification micrograph of rectangle marked as C, and (f) high magnification micrograph showing the crack path and particle breakage

During tensile deformation, the cracks initiated at the particle and γ-matrix interface propagate and coalescence in the failure of the samples. No slip lines around the crack were observed, which indicates less plastic deformation before failure. Crack initiation and propagation method is another important feature in deformation. The crack propagation of the high-temperature tensile testing of the TLP-bonded sample of Exp. 4 is shown in **Fig. 4.59 (f)**. The graph reveals that along the crack broken particles are present. These broken particles are Nb-rich particles. In **Fig. 5.59 (b)** and **(f)**, it can be observed that the cracks initiated at the interface of the particle-matrix interface, respectively. As these sites are the region where slip bands accumulate and tangle, cracks usually initiate from these areas. Later, these cracks connect with one another and propagate in a transgranular manner. Moreover, at elevated temperature cracks also initiates from the grain boundaries and propagate intergranular manner.

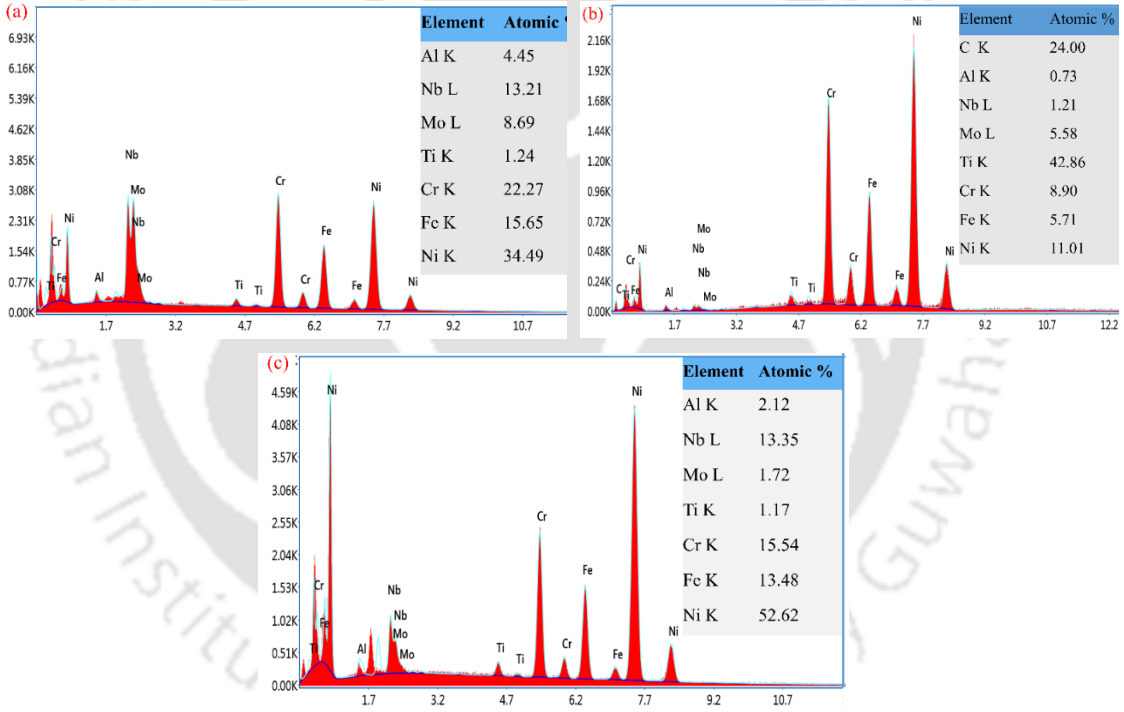

Fig. 4.60 EDS analysis result of particle present in rectangles (a) 1, (b) 2, and (c) 3

In polycrystalline material, the strength of the grain boundaries is higher than that of intragranular strength at low temperatures. At low temperatures (i.e. $T<0.5T_m$), the grain boundaries act as a strong dislocation barrier, therefore, it is difficult to deform grain boundaries during plastic deformation. At low temperatures, the large precipitate particles act as dislocation motion barriers **[202, 203]**. During plastic deformation, the precipitates (like carbide and δ-phase) and grain boundaries impede the dislocation

movements. This results in a dislocation pile-up in these regions. When the strain increases, stress concentration around these regions increases due to the dislocation pile-ups. Once the stress concentration attains a certain level, cracks or voids generate from these regions and propagate in a transgranular way across the width of the sample and the final failure of the samples occurs.

At elevated temperatures, along with temperatures, the microstructure features of the samples are also important factors that affect the mechanism of deformation during tensile loading. The size, volume, and distribution of precipitates (like γ″, γ′, δ, carbides, and lave-phase), and the structure of grain boundaries also affect the deformation mechanism. Therefore, the interaction of precipitates and grain boundaries with the local dislocations is responsible for the initiation and propagation of the crack **[204, 205]**.

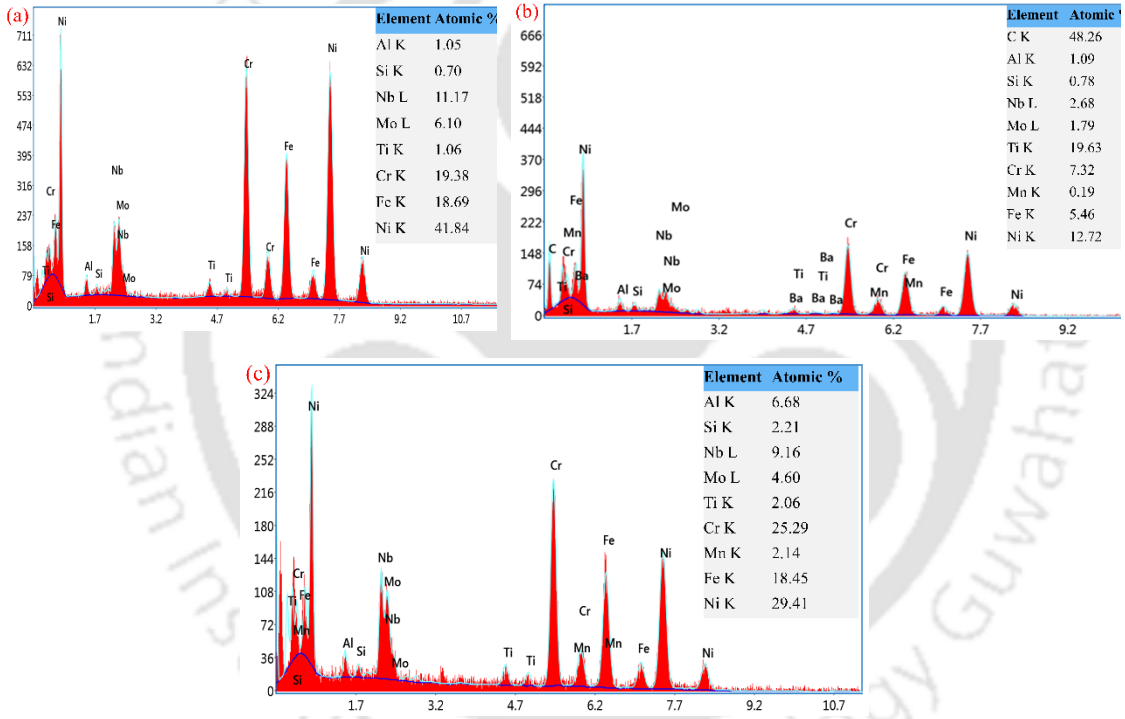

Fig. 4.61 EDS analysis result of particle present in rectangles (a) a, (b) b, and (c) c

The ductility of the TLP-bonded IN 718 joint tested at 650 ˚C is lower than the room temperature ductility. This is mainly due to the intermediate temperature embrittlement of Ni-based superalloys **[206]**. The cohesive strength of the grain boundaries gets weakened due to thermal activity at elevated temperatures **[207]**. When an external load is applied at elevated temperatures, the grain boundary cleavage forms easily, and as a result, intergranular cracks form. Later, the cracks propagate quickly along the grain boundaries and lower the ductility of the sample. With increasing temperature, the movement of dislocations rises and which induce the inhomogeneity in

localized strains as additional dislocations are trapped at the γ/ γ′ and γ/ γ″ interface in the IN 718. The increase in the mobility of dislocations rises stress concentration at the γ/ γ′ and γ/ γ″ interface. This finally leads to decohesion of the glide plane and reduces the ductility of the samples. Along with these two factors, the presence of the δ-phase and carbide precipitate at the grain boundaries reduces the ductility of the IN 718 samples at high temperatures. At higher temperatures, the size of these precipitates increases due to thermal activity and breaks suddenly as a result the ductility of the IN 718 decreases at elevated temperatures.

4.7 Residual Stress Evaluation

The X-ray diffraction patterns of the TLP-bonded IN 718 joint are shown in **Fig. 4.62**. The figure reveals that the major peaks are corresponding to the γ, γ´ and γ″ phases. In this superalloy phases like δ, lave, and metal carbide also exist in the matrix, however, as their volume fraction is very small, their corresponding diffraction peaks are indistinguishable. The highest peak intensity is observed for the (111) plane corresponding to 2θ of 43.2˚. This peak is corresponding to the diffractions from γ, γ´, and γ″ phases **[208]**. The highest peak intensity plane is taken to measure the residual stresses in the TLP-bonded IN 718 samples. The strained samples are subjected to X-ray beams at various tilt angles for residual stress assessment. The 2θ value corresponding to the (111) plane shifts to the right when the samples are tilted against the X-ray incident angle as displayed in **Fig. 4.63**. When the samples are tilted, diffraction of the X-ray will take place from the (111) planes of strained grains which causes a change in the *d*-spacing value and that shifts the peaks after tilt.

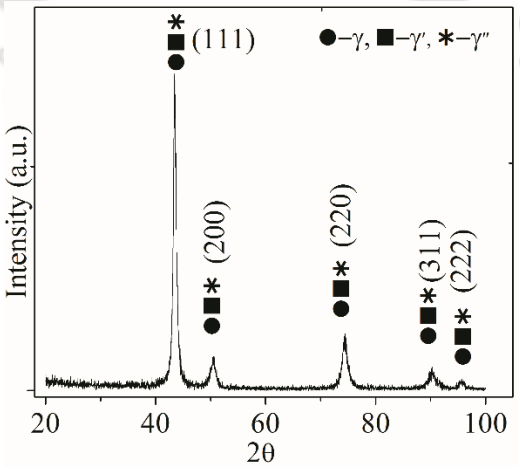

Fig. 4.62 XRD analysis of IN 718

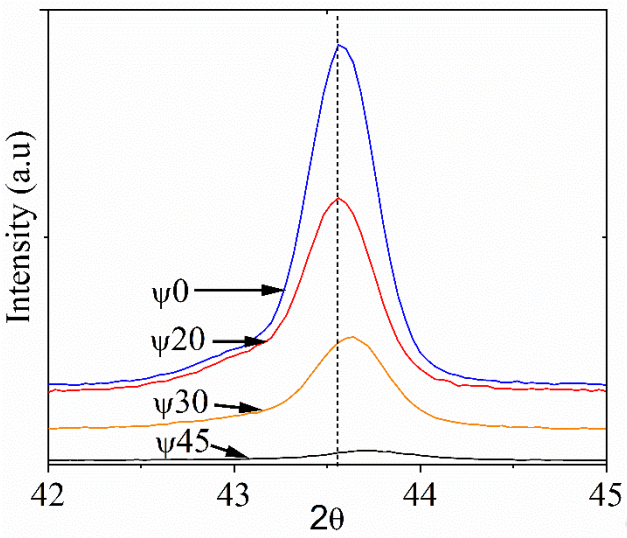

Fig. 4.63 Peak shift of E.2

A graph plotted between the d-spacing values for various tilt angles vs the respective $Sin^2 \Psi$ value. **Figure 4.64** shows the *d* vs $Sin^2 \Psi$ graph of the TLP-bonded IN 718 samples. The best least-square line fitted to the curve shows a linear graph fitting with a negative slope. The residual stress is calculated from the slope of the *d* vs $Sin^2 \Psi$ curve using **equation (3.7).** The variation of the residual stress in different TLP-bonded IN 718 samples are shown in **Fig. 4.65**. A compressive residual stresses are developed during TLP bonding. During TLP bonding, a large amount of heat is applied to the bond area through the induction heating source (in the current investigation). The temperature distribution is not uniform though out the length of the sample and induces different magnitudes of thermal strains in the bond region. Due to the different thermal expansion coefficient between the IN 718 superalloy and BNi-2 interlayer **[209]**. The properties of the bond zone are different. Moreover, due to the interdiffusion of elements between IN 718 and BNi-2 interlayer, various phases are formed during the isothermal and athermal solidification in the bond zone **[32]**. The above factors causes inhomogeneous volume change at the bond area. In order to adjust the different strains in the TLP bond, elastic strains or plastic strains are developed and residual stress are produced **[209]**. In all the samples the residual stress developed is maximum at the bond centerline and decreased with distance away from it. Due to thermal shrinkage after isothermal solidification and restraint by the applied load, a compressive residual stress is developed in the bond area of TLP-bonded samples **[209, 210]**. The values of the residual stress at the bond centerline for different bonding conditions are shown in **Fig. 4.65 (b)**. The figure reveals that with

increase in bonding temperature, the value of the residual stress increased. As temperature rises, higher temperature gradient is established between the bond centerline and the base material as a result more residual stress are developed at elevated temperatures **[211]**.

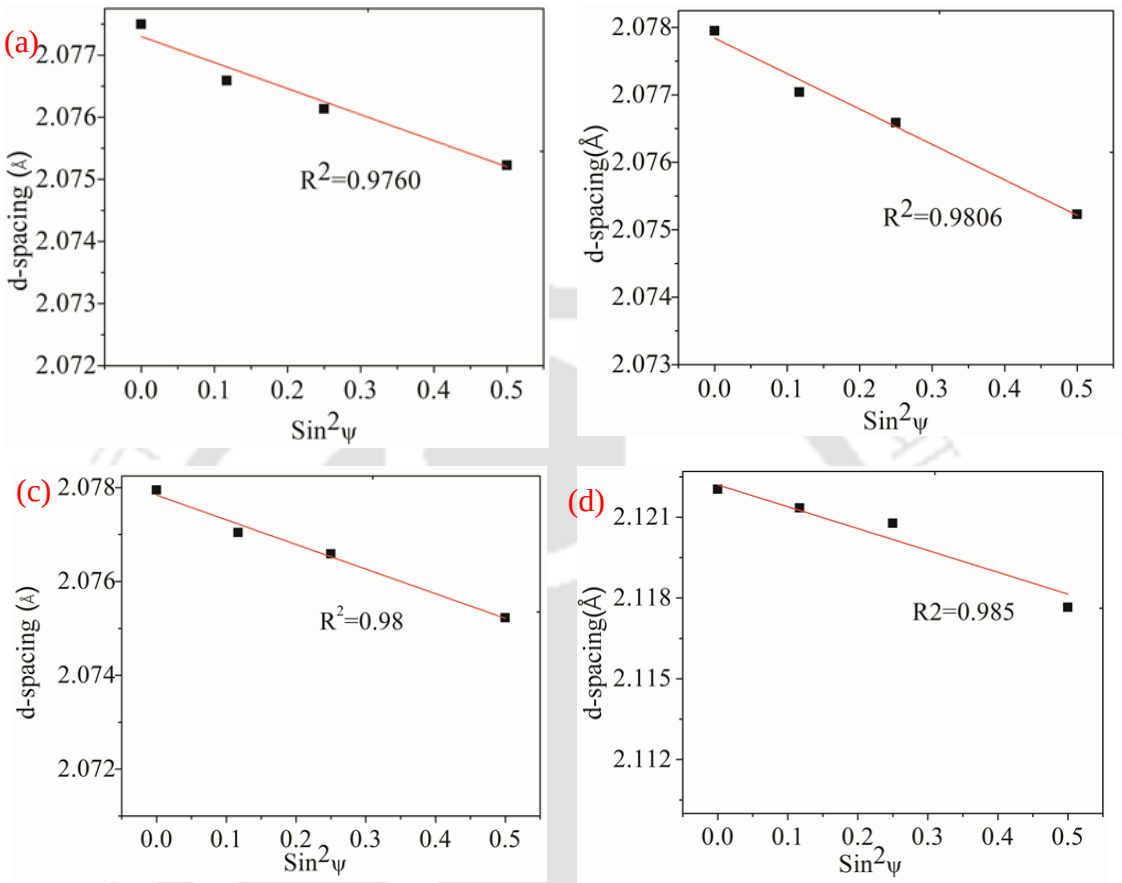

Fig. 4.64 *d* vs $\sin^2\psi$ graph at centerline of (a) Exp. 3, (b) Exp. 6, (c) Exp. 8, (d) Exp. 9

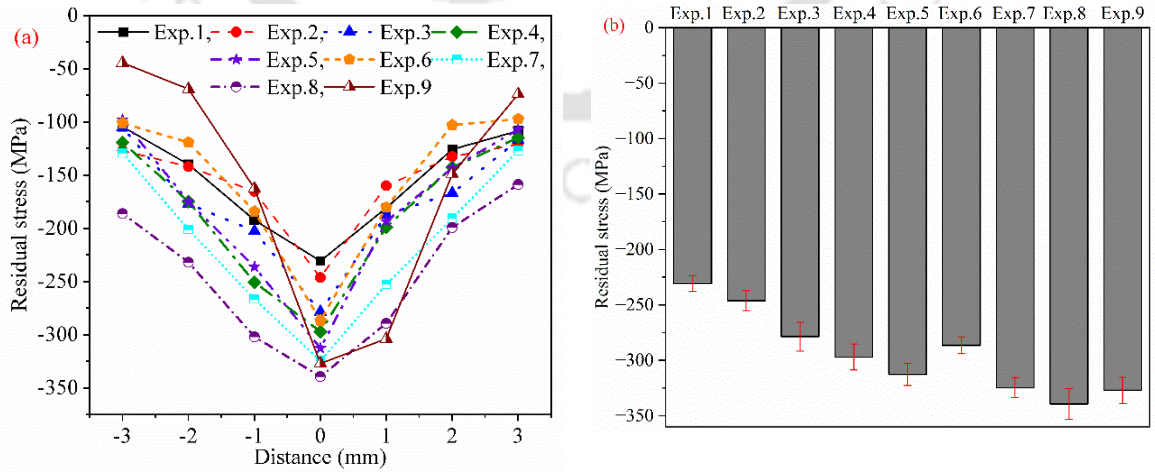

Fig. 4.65 (a) Distribution of residual stress in TLP-bonded samples, and (b) bar-chat of maximum residual stress developed in the TLP-bonded samples

4.8 Determination of Fatigue Life of TLP-bonded IN 718 Joint

4.8.1 Fatigue performance of TLP-bonded IN 718 joint

Figure 4.66 shows the high cycle fatigue performance of TLP-bonded IN 718 joint, PBHT sample, and heat-treated (HT) base material. The figure has two regimes, (i) high cycle fatigue (HCF) regime corresponds to medium applied stresses and lies in the range between 450 and 880 MPa for the heat-treated base material and PBHT sample, and 250 to 550 MPa for the as-bonded sample and (ii) fatigue endurance limit regime (FEL) which correspond to low applied stresses and it is below 450 MPa for the heat-treated base material and PBHT and 250 MPa for the as bonded sample for a stress ratio of R = 0.1. The SN-curve of the PBHT, HT base material, and the as-bonded sample is fitted following the Basquin equation **[212]**.

$$\sigma = \sigma_f (2N_t)^b \tag{4.14}$$

where σ is the nominal stress amplitude (MPa), σ_f is the fatigue strength coefficient (MPa), N_t is the number of cycles to failure, and b is the Basquin exponent. The fatigue strength of the TLP-bonded IN 718 joint is significantly increased after PBHT compared to the as-bonded sample. However, there is a small difference in fatigue life between the PBHT sample and the HT base material. The average fatigue life of the TLP-bonded joint at 450 MPa is 3×10^5 cycles, whereas for HT base material and PBHT sample, it's more than 2×10^6 cycles (i.e. the sample does not fail). The fatigue life of a bonded sample is mainly affected by the surface quality, residual stresses, inclusions, grain size, strengthening phases, brittle precipitates, other stress concentration factors, etc. The lower fatigue strength of the as-bonded TLP sample is mainly attributed to the presence of a large amount of the brittle intermetallic phases at the ISZ of the TLP-bonded IN 718 joint. These phases are formed due to incomplete isothermal solidification in a TLP-bonded sample. As these intermetallic phases are brittle they are not easily deformed when the material is subjected to external forces and are potential sources of crack initiation sites. Therefore, the fatigue failure of the sample occurs at the ISZ of the TLP bonding. However, after heat treatment, the samples undergo recrystallization, dissolve deleterious lave and δ-phase, and form strengthening phases which reduce the probability of crack initiation (as discussed earlier in section 4.4). Moreover, during PBHT due to the inter-diffusion of elements, the intermetallic phases present in the ISZ dissolve, and

a homogeneous microstructure is achieved. As a result, the probability of crack initiation from these intermetallic phases decreases. The absence of these coarse intermetallic phases results in the delayed threshold value for crack initiation. The presence of nano-sized strengthening phases formed during the heat treatment impedes crack propagation during fatigue loading. As a result of the above factors, the fatigue strength of the PBHT sample improves significantly.

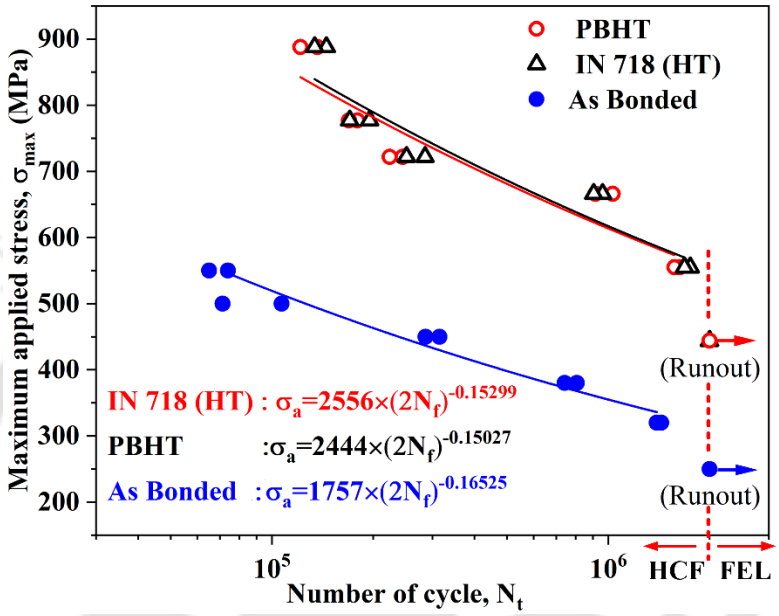

Fig. 4.66 SN curve of fatigue samples, blue circle for TLP-bonded IN 718 joint, black triangle for HT base material, and black rectangle for PBHT sample

4.8.2 Fractography

Figure 4.67 (a-d) shows the macroscopic and microscopic characteristics of the fatigue fracture surface of heat-treated base material (σ_a =400 MPa, N_t =1.45× 10^5). The macroscopic features exhibit three zones of fatigue fracture. Zone-I is marked as the crack initiation site showing ratchet marks due to the nucleation of multiple micro-cracks. The zone-II fracture is marked as the propagation region, where beach marks are visible. And the final failure zones are marked showing the failure of the sample.

Figure 4.67 (b) shows the FESEM microscopic image of the crack initiation zone. From the figure, it appears that the fatigue cracks have initiated from near the surface of the sample. The high magnification FESEM image of the crack initiation zone shows debonding at the particle-matrix interface, particle breakage, and secondary micro-cracks (as shown in **Figure 4.67 (c))**. These particles correspond to the brittle phases like lave,

carbide, and δ-phase present in the γ-matrix of the IN 718 superalloy. **Figure 4.67 (d)** shows features of fatigue striations. To confirm the particle nature the EDS analysis of the debonded particle in **Fig. 4.67 (c)** was carried out and the result is shown in **Fig. 4.68 (a)**. The result shows the particle is rich in C and Ni. From the EDS analysis, we can confirm that the crack has initiated due to the debonding of carbide particles present near the surface of the base material.

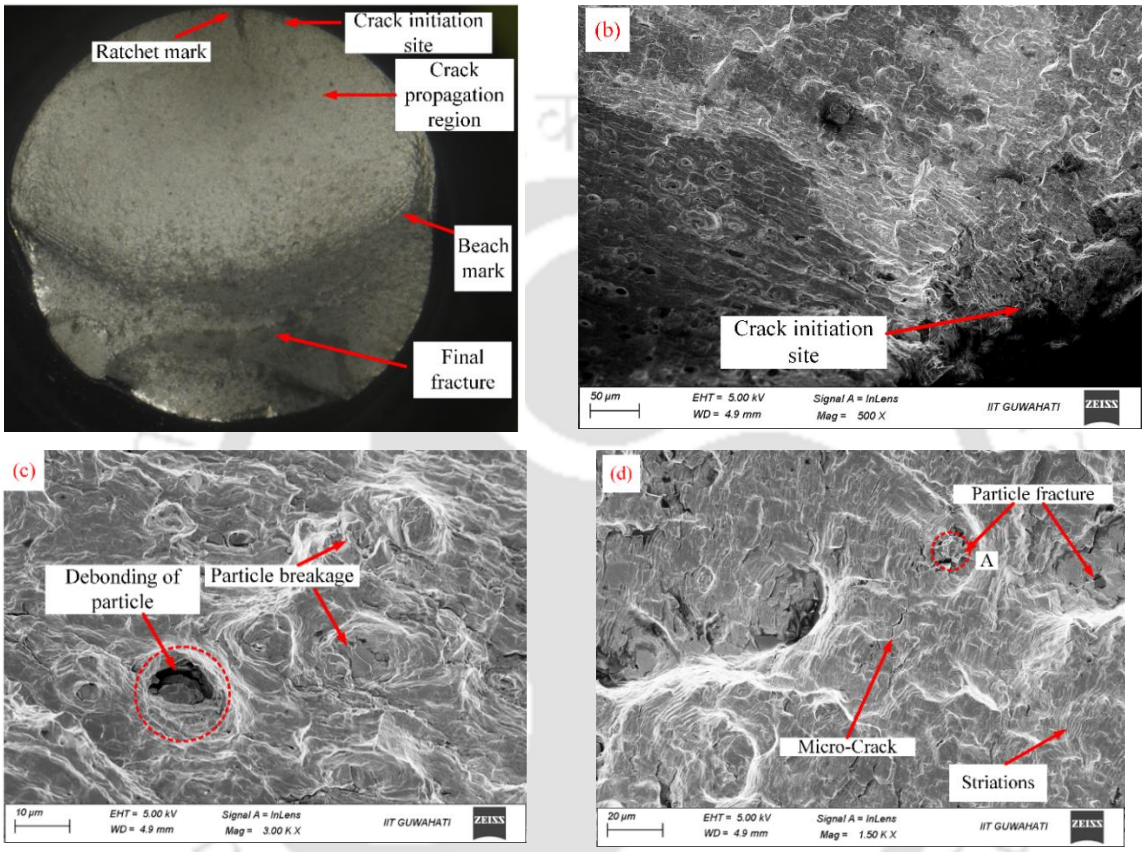

Fig. 4.67 Fracture surface of HT base material sample (a) macroscopic image, (b) microscopic image of crack initiation, (c) High magnification image of crack initiation site showing particle debonding (d) higher magnification image showing Paris zone striations

In the Paris region, features of fatigue striations are evident (**Fig. 4.67 (d)**) indicating an almost constant crack growth rate. In addition to this, some fragmentation of second-phase particles are observed. The EDS analysis of the fragmented particle (as shown in **Fig. 4.68 (b)**) shows that these particles are rich in Nb. This indicates that these particles may be lave or δ-phase. In IN 718 lave and δ-phase are present in the matrix. During fatigue loading these brittle particles brakes during crack propagation. These cracks are initiated from the edge and the internal cracks propagates and final failure of the samples occurs.

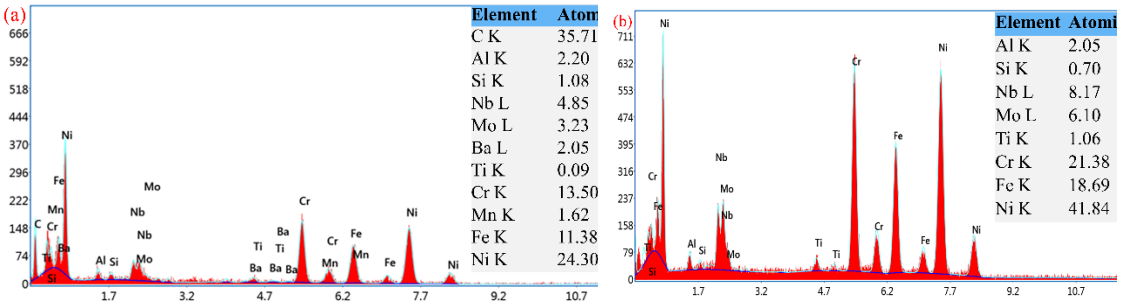

Fig. 4.68 EDS analysis result of the debonded particle (a) carbide particle, and (b) Nb-rich particle

Figure 4.69 (a-c) shows the macroscopic and microscopic image of the as-bonded fracture surface sample. The photograph of the fracture surface of the sample is shown in **Fig. (a)** (σ_a =250 MPa, N_t =7.4× 10^4). The macrograph indicates crack initiation points at the surface followed by propagation along the length and fails on the other end. Close analysis of the crack initiation zone is carried out by FESEM and shown in **Fig. 4.69(b)**. The fractographs reveal river patterns, voids, and cleavages which are typical of brittle failure. Which indicates crack initiation from multiple sites. The EDS analysis of the second phase present in the crack initiation site shows is shown in **Fig. 4.69 (d)**. The result reveals that the particles are rich in Si and Al. As discussed earlier, in the as bonded sample second phase intermetallic are present due to incomplete isothermal solidification. The presence of a brittle intermetallic compound at the ASZ generates stress concentration around it. With further fatigue loading the stress concentration around the brittle particle increases and the particle gets fractured and creates a void or micro crack. These micro-cracks propagate and the coalescence of these micro-cracks results in the final fracture of the material. In the as-bonded sample pseudo cleavage was also observed near-threshold fatigue fractures. The cleavage facets observed in the as-bonded samples are the result of cross slip during the crack growth.

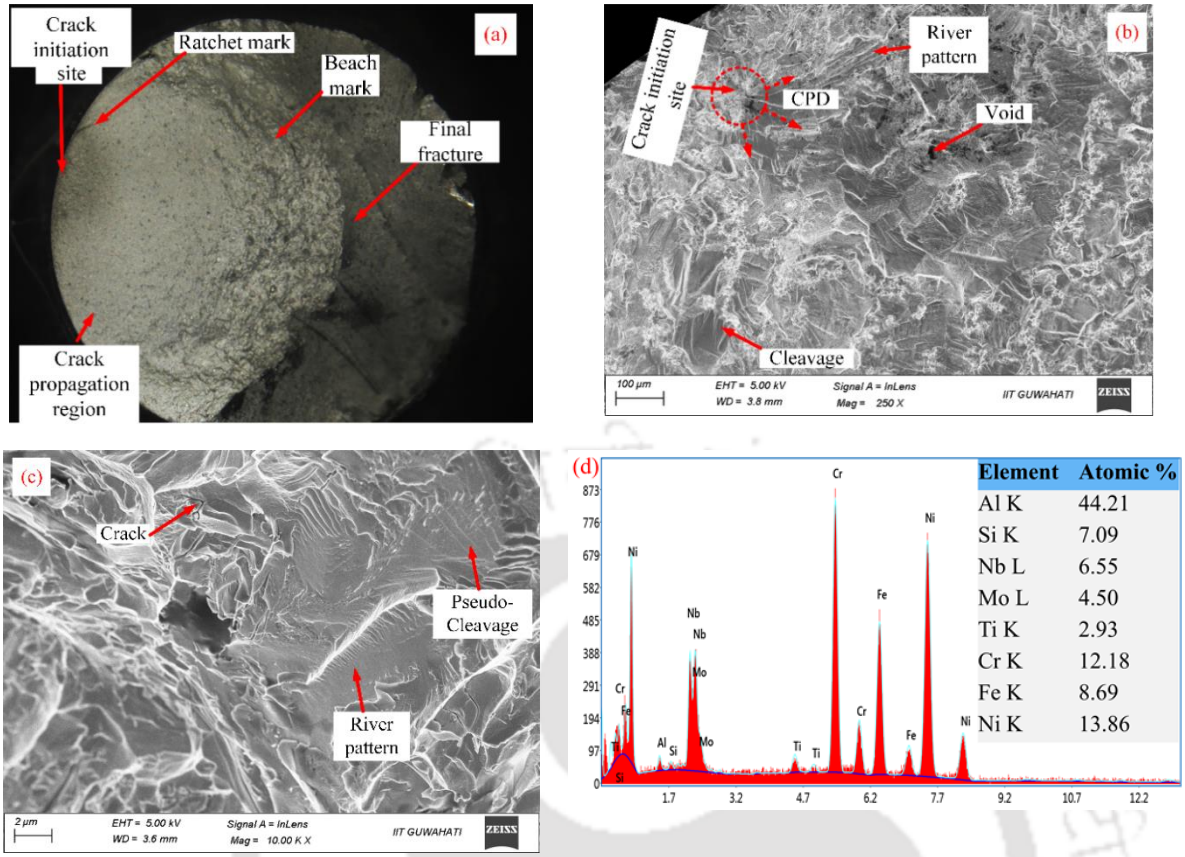

Fig. 4.69 Fracture surface of TLP-bonded sample (a) macroscopic image, (b) microscopic image of crack initiation, (c) higher magnification image showing Paris zone striations, and (d) EDS result of the second phase particle

Figure 4.70 (a-c) shows the image of the fracture surface of the PBHT samples. At the macroscopic level, as shown in **Fig. 4.70 (a)**, the images show ratchet and beach marks indicating crack initiation and propagation, respectively. The macroscopic image shows the crack is initiated at the edge of the sample and propagates to other ends. However, at the microscopic level (as shown in **Fig. 4.70 (b)**), close analysis of the crack initiation site confirms the presence of multiple crystallographic facets in the fracture surface of the PBHT sample. The multiple crystallographic facets formed due to the initiation and growth of the micro-cracks. The cracks are initiated either from the triple point of the high-angle grain boundaries or from the grain boundary precipitates This indicates that the crack initiates due to persistent slip bands **[213]**. In the PBHT sample, the fatigue fracture surface shows dense and well-defined river patterns near the crack initiation point. **Figure 4.70 (c)**, shows the high-magnification image of the second-stage crack propagation site. In this region, striations are present in the entire area indicating a constant crack propagation rate typical for ductile materials. Features of fine micro-

cracks and particle debonding at a few localized regions are also evident. The EDS analysis result of the particle marked inside the circle is presented in **Fig. 4.70 (d)**. The result shows that the particle is an Nb-Ni-rich particle. As discussed earlier, these particles can be lave or δ-phase and are present along the grain boundaries of the-heat treated samples. During fatigue loading, these brittle phases initiate micro-crack which propagates at a uniform rate finally resulting in fracture. Since the PBHT to a great extent reduces the coarse and brittle second-phase particles and results in homogeneous microstructure due to recrystallization thereby improving the ductility. All these results in higher fatigue life for the PBHT samples.

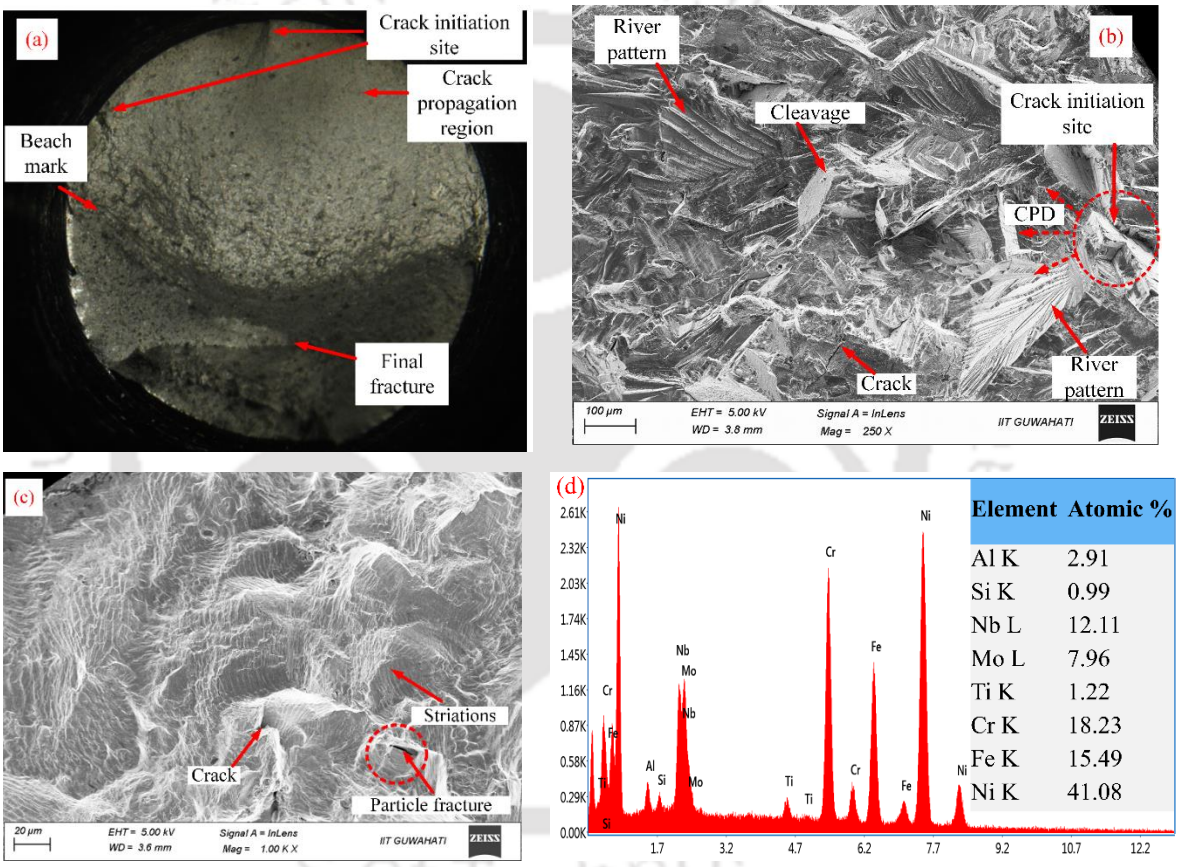

Fig. 4.70 Fracture surface of PBHT sample (a) macroscopic image, (b) microscopic image of crack initiation site, (c) higher magnification image showing Paris zone striations, and (d) EDS result of the second phase particle

4.9 Synthesis of Nano-sized Powder Interlayer Alloy for TLP Bonding of IN 718 by Mechanical Alloying Process

4.9.1 FESEM and LPSA Results

The morphology of the powder mixture milled for various periods has been shown in **Fig. 4.71 (a-h)**. Milling time vs average particle size, obtained by LSPA is presented in **Fig. 4.72**. The photomicrographs of the initial powder mixture revealing spherical and coarse nickel powders (~ 100 μm diameter) along with other elements are shown in **Fig. 4.71 (a)**. From **Fig. 4.71 (b)**, it is evident that the morphology of the nickel has changed from spherical shape to flake shape after 2 h of milling. This was due to the severe plastic deformation during the milling process. The fine powder particles of Cr, Fe, Si, and B have been found embedded in the coarse nickel particle as shown in **Fig. 4.73**. The mean size of the powder mixture milled for 2 h is 113 μm. **Figure 4.71 (c)** depicts the FESEM micrographs of the powder particles milled for 5 h. The powder surface feature reveal flake morphology with a considerable reduction in powder particle size and has an average size of 70 μm. The photograph reveals bimodal particle size distribution with coarse powder flakes and a large number of fine powder flakes. Milling of the powder mixture for 10 h reveals almost spherical powders, as shown in **Fig. 4.71 (d)**. Results of LSPA of 10 h milled reveals an average powder size of 37 μm and 20 volume percent of the powders are having a size above 70 μm. The presence of coarse powder is due to the agglomeration of fine powders as a result of the high surface energy due to the very fine size of milled powders. Continuous milling of the powder beyond 10 h does not alter the morphology of the milled powders. However, milling resulted in a continuous reduction in the particle size. **Figure 4.72** reveals that the average size of the powders reduced to 13 μm when milled for 50 h. Though the results indicate a marginal increase in the average size to 15.4 μm when milled for 60 h, the FESM photographs reveal that this is mainly due to the slight increase in the size of the agglomerations.

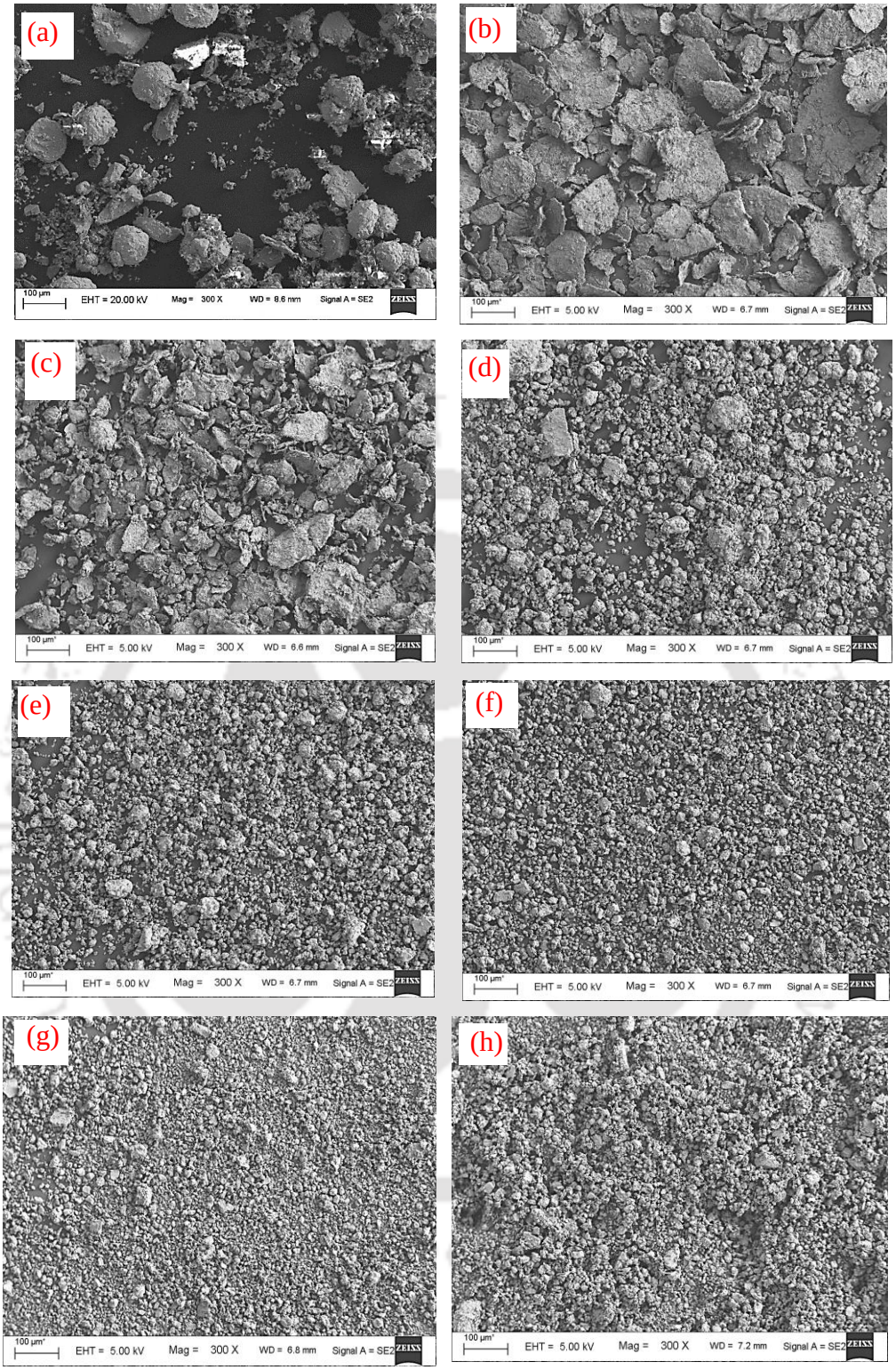

Fig. 4.71 FESEM morphology of powder with various milling time, (a) 0 h, (b) 2 h, (c) 5 h, (d) 10 h, (e) 20 h, (f) 35 h, (g) 50 h and (h) 60 h

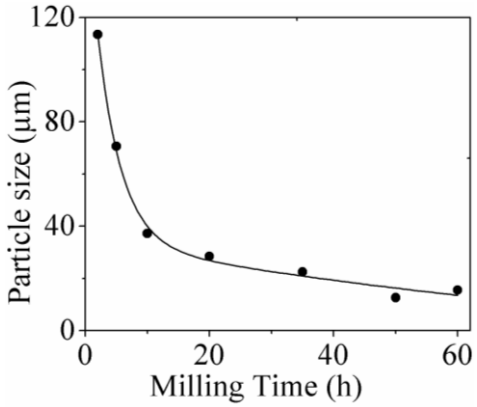

Fig. 4.72 Change of powder size with milling time

The results of the particle size analysis and the FESEM study reveals that with increasing milling time, the powder particle size reduces. The process of MA during milling of powder mixture is mainly due to three mechanisms: (i) plastic deformation of the ductile powders, (ii) cold welding of particles and (iii) fracturing of brittle constituent particles. During the initial phase of milling, individual powder particle(s) are impacted between the milling balls. The ductile powder particles undergo severe plastic deformation whereas the brittle particles undergo fracturing. Due to the severe plastic deformation, the ductile particle strain hardens and becomes brittle. The brittle particle during the impact, either gets embedded inside the ductile particles and forms a composite powder or remains in the fragmented form. The ductile particles can also get cold welded. During subsequent milling, the three processes viz. plastic deformation, cold welding, and fracturing continue. This stage is marked by a sharp reduction in the particle size. After some period, the powder mixture can no longer be plastically deformed due to the loss of ductility as a result of the prior plastic deformation. The process dominating at this stage is cold welding and fracturing. A stage will be attained when equilibrium is attained between the rate of fracturing and cold welding. At that point, the particle size almost remains constant. The continuous cold welding and fracturing processes result in uniform distribution of the elements at the atomic level leading to the formation of the mechanically alloyed powder. The plot of the average particle size vs milling time as displayed in **Fig. 4.72** is attributed to the above reasons.

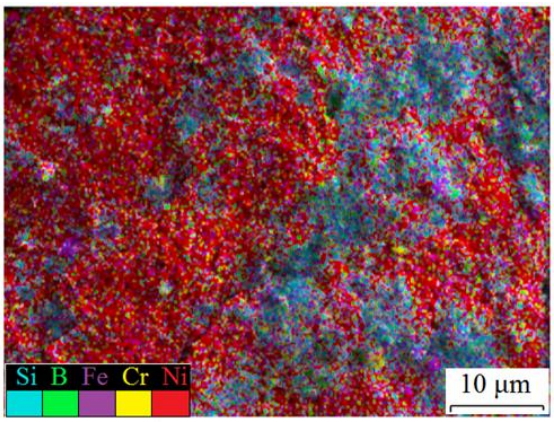

Fig. 4.73 Different particle embedded in single Ni powder particle after 2 h milling

Figure 4.74 shows the X-ray elemental mapping of the 60 h milled powder. The figure reveals uniform distribution of Cr, B, Fe, and Si in the nickel powder particles. During the milling process, the brittle particles fragment and gets distributed in the Ni particles at the atomic level. The results of the elemental X-ray mapping indicate that after 60 h of milling, the alloying elements like Cr, Si, B, and Fe fragments into very fine particles and distributed uniformly in the nickel matrix. The evolution of single phase solid solution alloy could be ascertained by the XRD and TEM studies. These are explained in detail in subsequent sections.

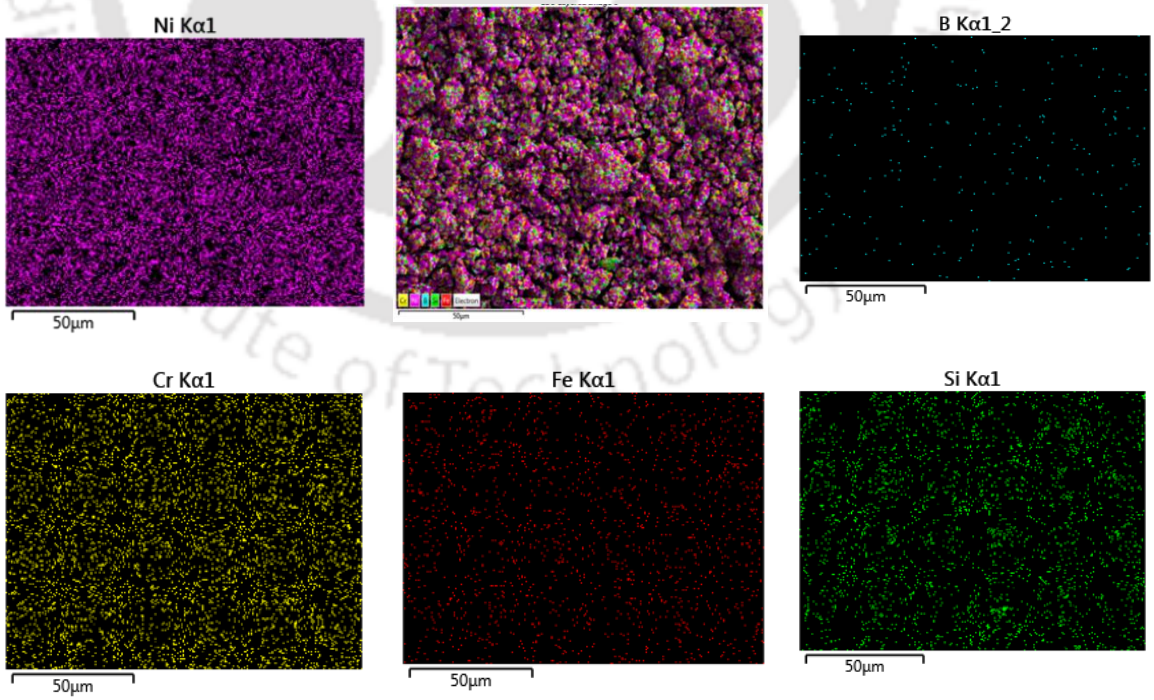

Fig. 4.74 Elemental X-ray mapping of 60 h milled powders

4.9.2 XRD analysis

In order to establish the formation of a single phase Ni-Cr-B-Si-Fe solid solution alloy the XRD data of the powder milled for different time periods were analyzed. The XRD spectrums of the Ni-Cr-B-Si-Fe alloyed powders before and after milling for different periods are shown in **Fig. 4.75** and **4.76**, respectively. The XRD spectra of the powder mixture before milling (**Fig. 4.75**) reveal sharp peaks due to reflections from planes of constituent elements viz. Ni, Cr, Si, B, and Fe. **Figure 4.76** reveals that milling of the powder mixture for 5 h results in complete disappearance of the peaks corresponding to reflections from planes of Si and B. Only peaks corresponding to reflections from Ni, Cr and Fe were evident. This indicates the possible dissolution of Si and B in Ni, Cr and Fe powders forming one or more of non-equilibrium solid solutions. With further milling, Cr and Fe also diffuses into Ni matrix and forms meta-stable FCC solid solution of Ni (Cr, B, Si, Fe). The peak intensity at 2θ value of ~ 44.5° for the powder mixture before milling is the sum of the intensities from the planes of Ni, Cr, and Fe. During the powder milling, some of the reflections from any of these elements may disappear during the alloying process. From **Fig. 4.76**, it is evident that on increasing milling time, the relative intensity of the peak at 2θ value of ~ 44.5° decreased compared to the peaks at other 2θ values. The XRD patterns show that the elements Ni, Cr, Fe, Si, and B gradually transformed into single phase solid solution alloy during the milling process. Measurement of the full width at half maximum (FWHM) of all peaks revealed peak broadening with an increase in milling time. The peak broadening observed is a consequence of dislocation density generated in the particle and mean crystallite size reduction on account of the high energy MA process. The 2θ angles from the reflecting peaks indicate that crystal structure of the interlayer alloy is FCC structure.

The XRD pattern after 60 h milled powder reveals: (i) complete disappearance of the peaks corresponding to Cr, Si, B, and Fe, (ii) broadening of the peaks corresponding to the nickel element, and (ii) peak shifts. Comparison with the data of JCPDS file, the peak at a 2θ value of ~ 44.5° corresponds to the reflections from (111) planes of Ni, Cr, and Fe. In the present powder mixture, since Fe content is very low (1.5 wt. %), the contribution of intensity from reflections from (111) plane of Fe is marginal. The sharp peak observed at the 2θ value of ~ 44.5° in the XRD pattern for the initial powder mixture can be the sum of the intensities from the planes of Ni and Cr. The XRD peaks

corresponding to reflections from Cr, B, and Si were not observed for the 60 h milled powder. The complete disappearance of these peaks indicates the possible dissolution of Cr, Fe, Si, and B in Ni powder. The dissolution of these elements in nickel leads to the formation of non-equilibrium, meta-stable FCC solid solution of Ni (Cr, Fe, Si, B). An in-depth analysis of 60 h milled powder revealed peak broadening and peak shift corresponding to the reflections from planes of nickel. The peak broadening observed is a consequence of dislocation density generated in the particle and mean crystallite size reduction on account of the high energy mechanical alloying process **[214, 215]**. The peak shift observed after 60 h of milling indicates the lattice strains due to the dissolution of the Cr, Si, B, and Fe in the Ni matrix, resulting in the formation of an FCC solid solution of Ni (Cr, Si, B, Fe). The transformation of the initial powder mixture into a single-phase FCC Ni (Cr, Si, B, Fe) is the consequence of the sequence of the milling process. During the high-energy ball milling, some amount of powder particles is trapped in between the colliding hardened steel balls. The ductile powder particles undergo severe plastic deformation, whereas the brittle particles undergo fracturing. Due to the severe plastic deformation, the ductile particle strain hardens and becomes brittle. The brittle particle during the impact either gets embedded inside the ductile particles and forms a composite powder or remains in the fragmented form. The ductile particles can also get cold-welded. During subsequent milling, powder particles are repeatedly plastically deformed, cold-welded, fractured and re-welded. This stage is marked by a sharp reduction in the particle size **[216]**. After some period, the powder mixture can no longer be plastically deformed as it loses its ductility because of the prior plastic deformation. The processes dominating during this stage are fracturing and cold welding. A stage will be attained when equilibrium is achieved between the rate of fracturing and cold welding. At this stage, the particle size almost remains constant. The continuous cold welding and fracturing processes result in uniform distribution of the elements at the atomic level, and thereby mechanically alloyed powder is formed.

It was necessary to establish the formation of single-phase solid solution alloy. Since the major element was Ni, the change in Ni lattice parameter with milling time was determined and shown in **Fig. 4.77**. The lattice parameter fluctuations during milling process signifies the existence of the atomic disorder. Up to 2 h of milling, the lattice parameter of the alloy mixture decreased and subsequently increased with an increase in milling time. Substitutional dissolution of Si and B in the Ni matrix is the reason for an

initial decrease in the lattice parameter. As the atomic radius of Si (1.11 Å) and B (0.9 Å) are smaller than that of Ni (1.24 Å), the lattice parameter decreases. After 5 h of milling, a significant amount of Cr and Fe atoms replaces the lattice sites of nickel matrix resulting in the formation of a substitutional solid solution. This is possible since the atomic radius of Fe (1.26 Å) and Cr (1.28 Å) are larger than the atomic radius of Ni. With higher milling time, more Cr and Fe atoms dissolve in the Ni lattice. The results reveal that, after 60 h of milling, a single phase solid solution alloy with FCC structure with lattice parameter of 3.53 Å is formed. The d spacing of the 60 h milled alloyed powder was evaluated from the XRD data using XPERT software. The d-spacing value corresponding to the plane (111), (200), (220), and (311) were 2.0356, 1.775, 1.2468, and 1.0733 Å respectively.

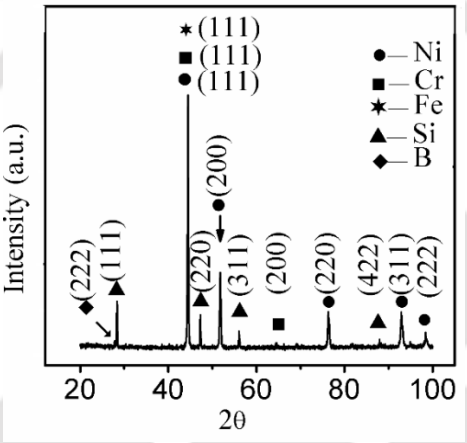

Fig. 4.75 XRD pattern of as mixed powder

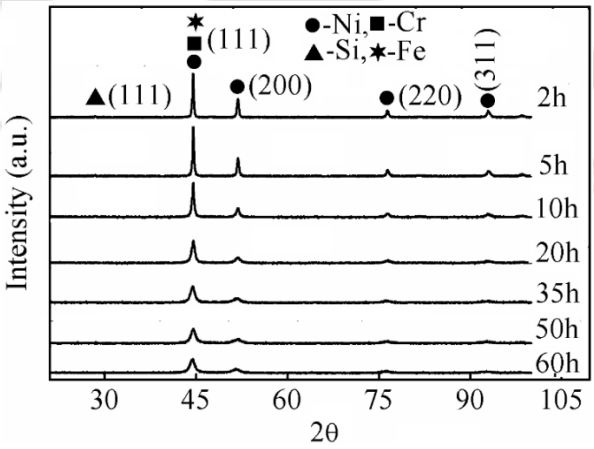

Fig. 4.76 XRD spectra of Ni-Cr-Fe-Si-B powders milled for different milling times

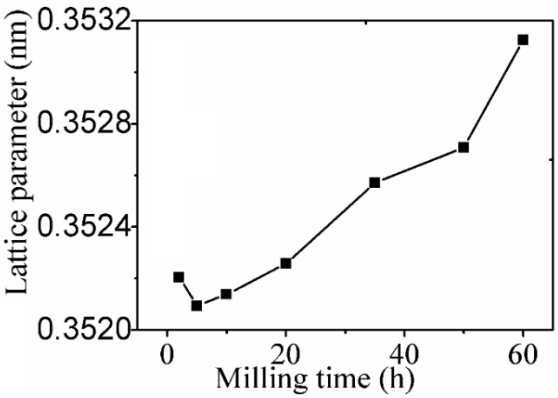

Fig. 4.77 Variation in lattice parameters with time

The dislocation density (ρ) and average crystallite size (D) of the milled powders were determined from the X-ray peak profiles by modified Williamson-Hall plot (MWHP) method **[217]**. This was obtained using the expression

$$(\Delta K)^2 = \left(\frac{0.9}{D}\right)^2 + \left(\frac{\pi b^2 \rho}{2B}\right) K^2 C_{hkl} \quad (4.15)$$

where $\Delta K = (2cos\,\theta B\,\Delta\theta_B)/\lambda$, θ_B is Bragg angle of reflection (in degree), $\Delta\theta_B$ is peak's FWHM, λ is the X-rays wavelength, b is the modulus of dislocation Burger's vector taken as $b = \frac{\sqrt{3}}{2}a$, for FCC crystal, a is the lattice constant, $K = 2 \sin \theta_B/\lambda$, B is a constant (=10), and C_{hkl} is the dislocation contrast factor, where (hkl) represents Miller indices. The following C_{hkl} values were determined for four prominent Bragg reflections from the XRD spectrum of the as-milled powders. C_{hkl} was determined using the relation **[218]**.

$$C_{hkl} = C_{h00}\,(1 - qH^2) \quad (4.16)$$

where,

$$H = (h^2k^2 + h^2l^2 + k^2l^2)/(h^2 + k^2 + l^2)^2 \quad (4.17)$$

$$C_{h00} = \alpha\left(1 - \exp^{-\frac{Ai}{\beta}}\right) + \gamma Ai + \delta \quad (4.18)$$

$$q = L\left(1 - \exp^{-\frac{Ai}{M}}\right) + NAi + O \quad (4.19)$$

$$Ai = \frac{2C_{44}}{C_{11} - C_{12}} \quad (4.20)$$

C_{44}, C_{11} and C_{12} are the elastic constants of Ni taken from literature **[219]**. $\alpha, \beta, \gamma, \delta$, L, M, N, and O values are constant for screw dislocation and depends upon elastic constants for edge dislocation. These values were taken from the work of Ungar et al. **[218]**. C_{hkl}, value was evaluated for both edge and screw dislocations. Considering equal amount of edge and screw dislocations, arithmetic average value of C_{hkl} was used to compute the crystallite size and dislocation density. The values of ρ and D were determined from slope and intercept of the linear fit of the plot, respectively, by plotting $(\Delta K)^2$ against $K^2 C_{hkl}$. **Figure 4.78 (a-b)** illustrates the plot of mean crystallite size and dislocation density vs milling time. Up to 50 h of milling, the mean crystallite size decreased rapidly and then slowly tends to saturate. The average dislocation density as shown by **Fig. 4.78 (b)** increased with increasing milling time.

Mechanical alloying is a simple technique to manufacture a variety of solid state nano-structured alloy powders. The external energy supplied for the milling process is transferred to the milling balls. The constituent metal powders collide in between the high energy balls resulting in either: (i) intense plastic deformation of ductile powders or (ii) fragmentation of brittle powders. It has been reported that dissolution rates of the constituent alloying element are directly associated with the dislocation density generated by MA **[220]**. The dislocation density is a key structural element that affects the final microstructure of the nano-crystalline. The crystallite size and dislocation density can be correlated as follows **[221]**,

$$\rho = 2\sqrt{3}\,\frac{\langle \eta_{rms} \rangle}{Db} \tag{4.21}$$

where $\langle \eta_{rms} \rangle$ is the lattice strain root mean square, b is the Burgers vector modulus of dislocations. From the above equation, it is clear that large dislocation density increases the tendency to form extremely refined nano-crystallite structures. Once the dislocation density in the powders attains saturation, additional milling will not generate more dislocations since it forms dislocation tangles and finally dislocation substructure. At this time, the material becomes brittle and the crystallite size attains a minimum value. Once this happens the rate of particle fracturing and rate of cold welding attains an equilibrium state. Hence, further reduction in particle size will not be possible. The present study reveals that the crystallite size of 4 nm was attained after milling for 60 h and at this time

the equilibrium condition was almost achieved. However, at this point, some prevailing dislocations may rearrange and some may be extinguished because of prolonging milling **[222]**. This mechanism encourages the evolution of sub-grain boundaries in the final nano-crystalline alloys. The rise in dislocation density by large deformation is the main reason for grain refinement. The dislocations produce an array of walls. Further deformation transforms these walls into grain boundaries. Crystallites in the extremely deformed alloy are split into sub-crystallites and separating from one another by a low-angled grain boundary. These boundaries significantly affect the displacement of dislocations. The mean crystallite size of the 60 h milled powders is only a few nanometers. The fraction of grain boundaries (f_{GB}) in the deformed powders was estimated by the relationship **[222]**,

$$f_{GB} = 1 - \frac{(D - d_{eGB})^3}{D^3} \quad (4.22)$$

Where d_{eGB} is the thickness of effective grain boundary, d_{eGB} is determined using the expression **[222]**,

$$d_{eGB} = 84\, D_{aad} - 21.7 \quad (4.23)$$

where (D_{aad}) is the average atomic diameter and both d_{eGB} and D_{aad} are in nanometer scale. **Figure 4.79** shows the plot of value of f_{GB} vs milling time. It is clear that during the initial stages of milling f_{GB} increases rapidly and with further milling, it increases at a decreasing rate. After milling for about 50 h, the fraction of grain boundary formed almost attains saturation.

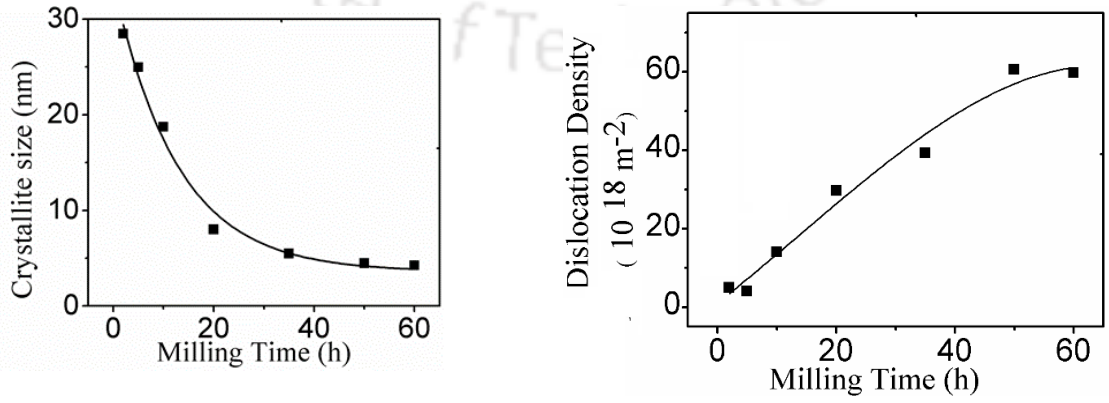

Fig. 4.78 Variation in (a) average crystallite size and (b) dislocation density with milling time

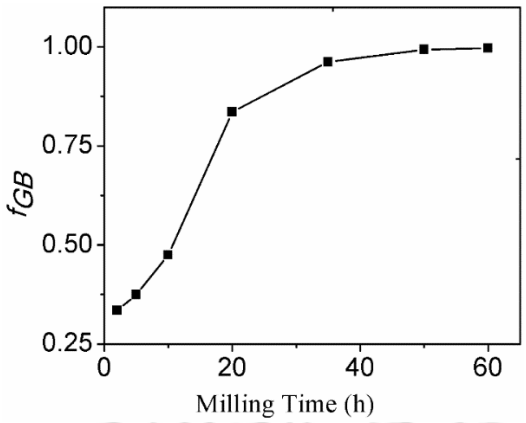

Fig. 4.79 Variation of grain boundaries with milling time

The obtained X-ray peak profile could be approximated to a Gaussian curve. Multiple Gaussian curves were used to analyze the overlapping peaks. **Figure 4.80** shows a typical Gaussian curve fit in which the black solid line corresponds to the XRD data, the blue solid line corresponds to the sum of the multiple Gaussian profiles, and the violet, green and red solid lines represent the individual Gaussian fits for the multiple peaks. The peak analysis of the individual Gaussian profile confirms small intensity peaks with corresponding 2θ values of 44.3°, 44.4°, 51°, 51.3°, and 51.7° as shown in **Fig. 4.80**. Comparing these 2θ values with JCPDS files shows formation of Ni, B and Si type eutectic compounds during MA process. BNi2, B3Ni4 and Ni2Si type of eutectic constituents are formed during the MA processes.

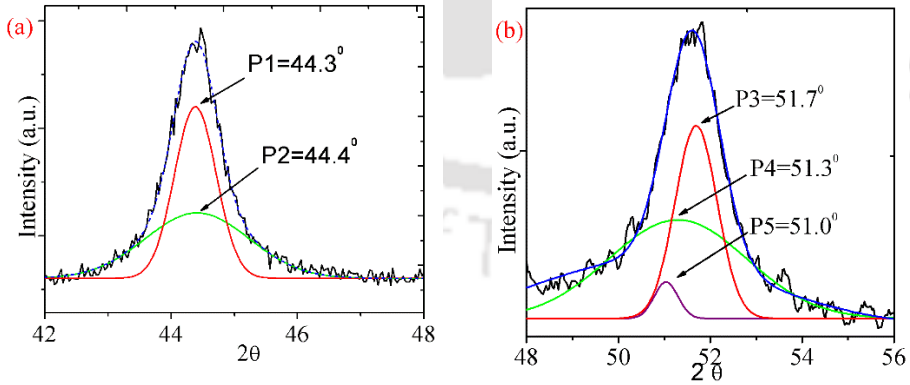

Fig. 4.80 Gaussian curve fitting and peak separation for 60 h milled powder (a) peak 1, and (b) peak 2

4.9.3 TEM results

The extent of alloying during milling of Ni-Cr -B-Si-Fe powder mixture was also analyzed by TEM study. **Figure 4.81 (a-h)** show typical selected area electron diffraction (SAED) patterns and bright-field TEM (BF-TEM) micrographs of powder mixture milled for 35, 50 and 60 h.

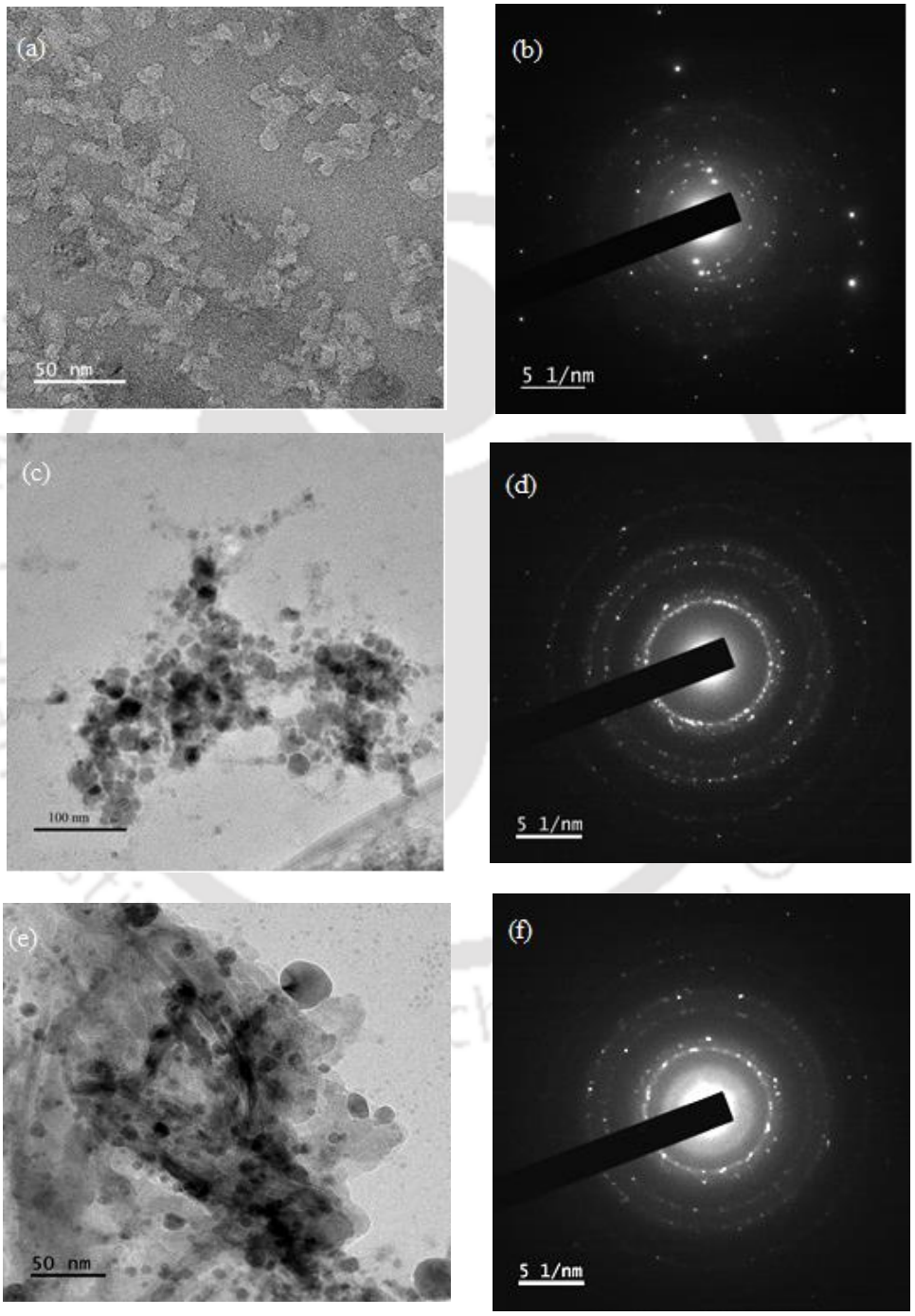

Fig. 4.81 TEM micrograph (a) BF 35 h, (b) SAED 35 h, (c) BF 50 h, (d) SAED 50 h, (e) BF 60 h, and (f) SAED 60 h milling

The micrographs reveal that the milled powders are mainly nano-sized grains. The particle size of the alloyed powder was calculated by Image J software taking at least 20 particles. The analysis revealed an average particles size of around 20.93 nm when milled for 35 h whereas the corresponding value is around 12.88 nm and 12.37 nm after milling for 50 and 60 h, respectively. Though there is a very small difference in particle size between 50 h and 60 h milled powders, 60 h powder shows more alloying as compared to the 50 h milled powder. The SAED patterns indicated crystalline nature for the powder mixture. The SAED pattern obtained for the 35 h milled powder mixture consists of several weak diffraction spots corresponding to reflections from the planes of Ni, Fe, Si, B, Cr and indicating incomplete alloy formation. The SAED pattern obtained for the powder mixture milled for 50 h and 60 h show diffraction ring pattern indicating formation of a single phase crystalline alloy. The diffraction pattern revels reflection from (111), (200), (220), and (311) planes of a face centered cubic structured solid solution alloy. Analysis reveals the d-spacing for the (111), (200), (220), and (311) planes as 2.067, 1.82, 1.278, and 1.091 Å respectively and which in agreement with the value obtained from XRD analysis.

4.9.4 DSC Results

The DSC was carried out to study the thermal properties of the milled alloy powder. The DSC thermograms of alloy powders milled for different time periods is shown in **Fig. 4.82 (a-b)**. Up to 20 h of milling, no peaks were observed. The result indicates a gradual exothermic nature till 1016 °C in the milled powder. This is attributed to the crystallization of the amorphous milled powder during heating. The extensive plastic deformation induced during mechanical alloying produces amorphization of many crystalline materials by introducing a large number of defects **[223]**. As a result of this exothermic nature of thermogram is observed until 1016 °C. **Fig. 4.82 (b)** shows the DSC heat flow vs. temperature plot of powder milled for 35 h, 50 h, and 60 h. The DSC curves reveal the endothermic peak for powders milled for more than 35 h, approximately at 1026 °C. In order to obtain the peak start, peak maximum and peak end temperatures, the first derivative of the DSC curve was carried out. The first derivative of the 35 h milled powder DSC thermogram is shown in **Fig. 4.82 (c)**. Form the first derivative vs. temperature curve, the peak start, peak maximum and peak end temperatures for 35 h milled powder was 1019 °C, 1026.3 °C and 1032.3 °C, respectively. Similarly, the peak start, peak maximum and peak end temperatures of 50 h and 60 h milled powder were

obtained to be 1014 °C, 1025.495 °C, and 1032 °C and 1008 °C, 1023.974 °C, and 1031.4 °C, respectively. The endothermic peaks observed after 35 h of milling is due to the melting of the alloyed powders. After 35 h of milling, nano-crystalline non-equilibrium solid solutions form. At elevated temperature, these solid solution melts to form Ni-B-Si ternary eutectic. This results in a lowering of the alloy melting temperature. The points corresponding to the peak start and peak ends are the solidus and liquidus temperatures of the respective alloy mixtures. Increasing milling time increases the amount of eutectic formed during milling, thereby further lowering of the melting temperature. The variation of the solidus, peak maximum, and liquidus temperature are shown in **Fig. 4.82 (d)**. The graph shows that with increasing milling time, the solidus and peak maximum and liquidus temperature of the alloy powder decreases. However, for powders milled for a period below 20 h, the melting temperature is high since proper alloying of the powder mixture has not taken place. Data obtained from **Fig. 4.83** indicates that as the heating rate increases, the endothermic peak shifts towards higher temperatures. The variation of the peak maximum (P_{max}) with a heating rate is shown in **Fig. 4.83 (b)**. This higher side shift is attributed to less time availability at a specific temperature **[224]**.

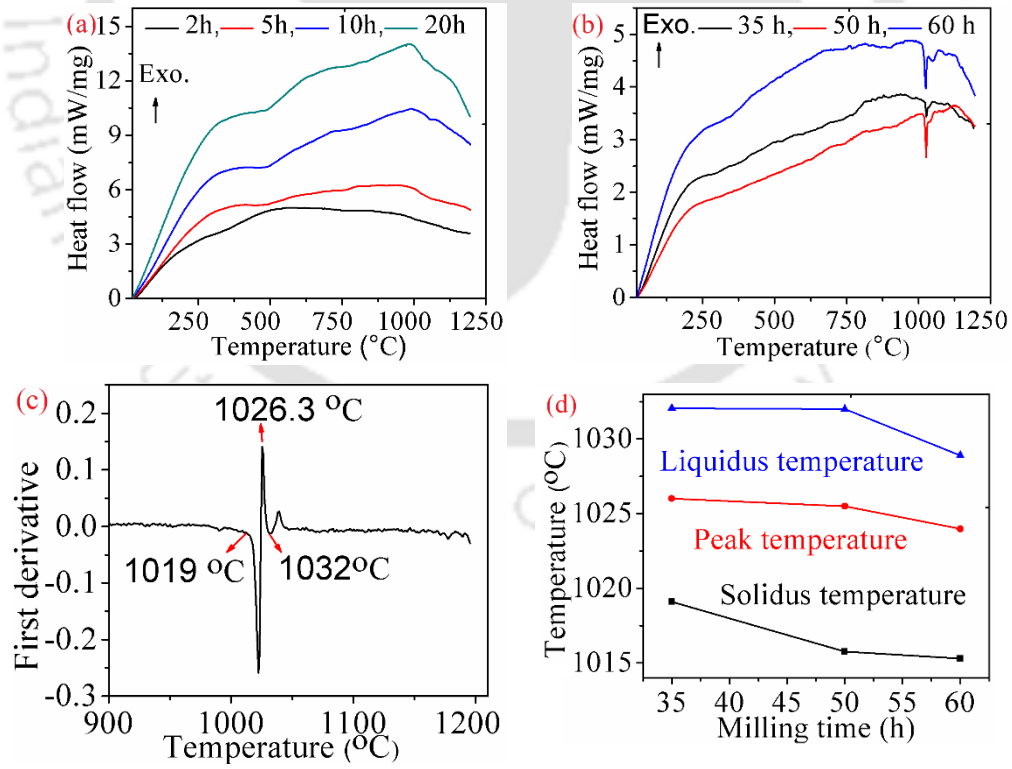

Fig. 4.82 DSC thermogram of powders (a) milled up to 20 h showing no peaks and (b) more than 20 h showing endothermic peaks, (c) first derivative of 35 h milled powder, (d) variation of peak temperature with milling time

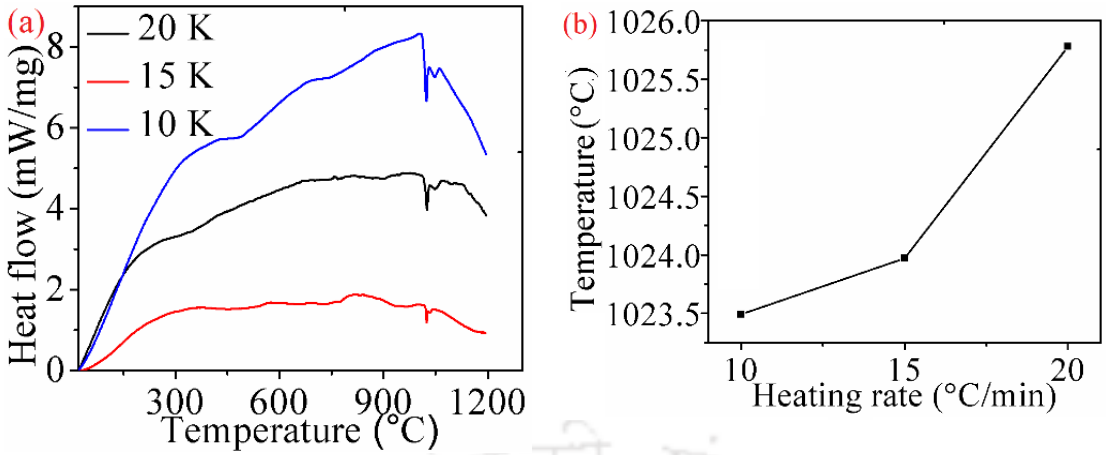

Fig. 4.83 (a) DSC curve of 60 h milled powder heated different heating rate and (b) variation of peak maximum with heating temperature rate

The activation energy for the powders milled for 35, 50, and 60 h have been calculated using the Kissinger equation **[225, 226]**:

$$ln\left(\frac{\emptyset}{Tp^2}\right) = \left(\frac{-Ea}{RTp}\right) + lnK_0 \qquad (4.24)$$

where $\emptyset$ is heating rate, T_p is peak transformation temperature, E_a is activation energy of the process, R is universal gas constant, and K_0 is constant. From the Kissinger plot, shown in **Fig. 4.84**, the activation energy ($-Ea$) was determined from the slope of the $ln\left(\frac{\emptyset}{Tp^2}\right)$ and $1/Tp$ plot. The activation energy for the melting of the milled powder reduces with increasing milling time, which is mainly due to the introduction of a large number of imperfections like grain boundaries, sub-grain boundaries, free surfaces, dislocations, etc. during mechanical alloying **[227]**. Lowering of the activation energy facilitates inter-diffusion of the atoms between interlayer material and bond zone, thereby reduces the time required for the bonding of IN 718 alloy.

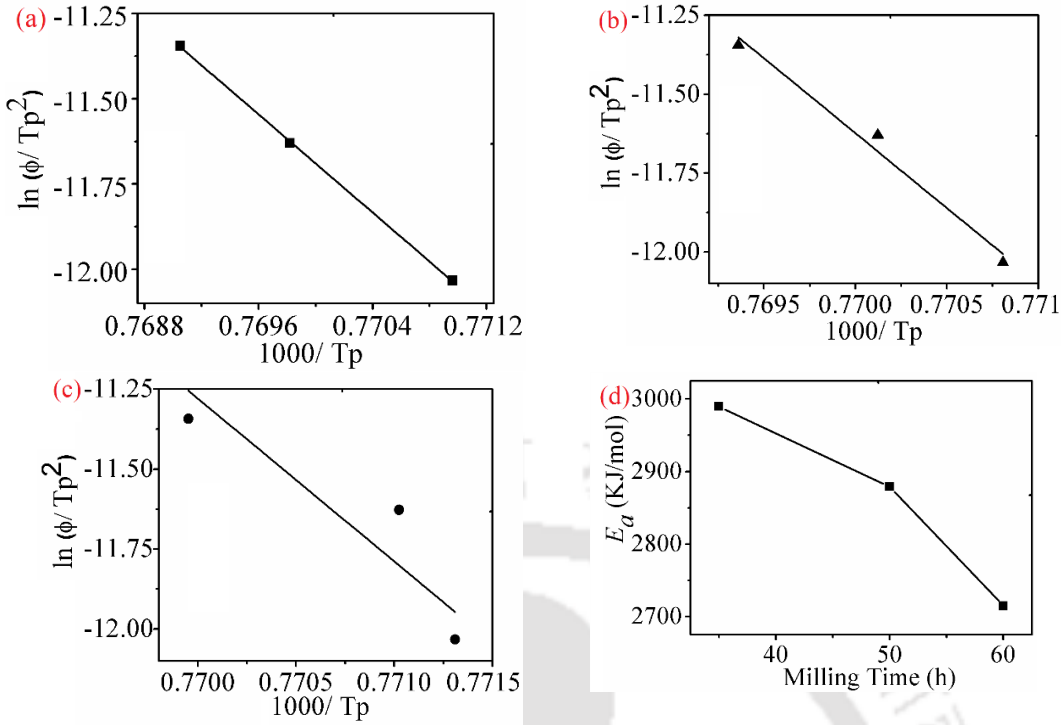

Fig. 4.84 Kissinger plot of (a) 35 h, (b) 50 h, (c) 60 h milled powder and (d) variation of activation energy with milling time.

4.9.5 Microstructure of TLP bond

Figure 4.85 shows typical TLP-bonded IN 718 microstructures made at 1050 ˚C held for 1 h. The bond region consists of three zones: (i) ISZ, (ii) DAZ and (iii) BMZ. Isothermal solidification begins from the parent alloy surface and advances towards the joint centerline. The ISZ forms by the nucleation and growth of grains from base material surface to middle of liquid phase. As the melted interlayer completely wets the base material, the growth process of the isothermal solidification technique is epitaxial **[228]**. During the isothermal holding period, elements Nb, Ti and Al diffuse from the parent alloy into the molten interlayer. Simultaneously Si and B diffuse into the parent alloy from the molten filler material. The diffusion of Si and B from the interlayer reduces the concentration of these elements in the eutectic interlayer. This leads to a rise in the liquidus temperature of the interlayer. As the liquidus temperature, raise above the holding temperature, isothermal solidification begins. The isothermal bonding will attain completion if the joint is held at a fixed holding temperature for sufficient time. If the assembly is cooled down before complete isothermal solidification, the remaining liquid solidifies athermally. During the athermal solidification, due to the little solubility of Si and B in the solidifying phase, they are rejected into the liquid interlayer region. Continuous enrichment of liquid interlayer by B and Si during athermal solidification

would result in the formation of eutectic constituents, i.e. brittle and hard boride and silicide phases solidification.

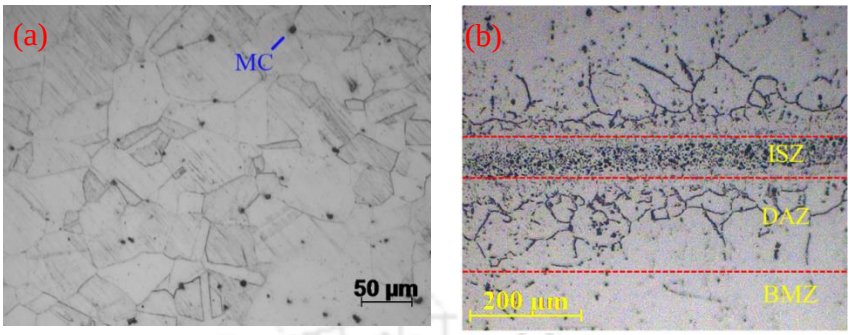

Fig. 4.85 Microstructure of (a) IN 718 superalloy and (b) TLP-bonded joint (1050 ˚C, 1 h)

Figure 4.86 shows the FESEM micrograph of TLP-bonded sample made at 1100 ºC and bonding time of 60 min. The microstructure shows three zones, viz., (i) unaffected base metal zone (BM), (ii) diffusion affected zone (DAZ), and (iii) isothermally solidified zone (ISZ). During the bonding process, in the BM zone, the composition remains the same as the base material. Elements of the MPD have not diffused up to this region. In the DAZ zone, metallic precipitates are found inside the grain and along grain boundaries. In the ISZ, different types of second phase labeled as “B”, “C”, “D”, “E” and “F” are observed. Along with second phase, some voids are also evident in the ISZ. The voids are mainly due to air entrapped between the powder particles during the application of the interlayer between base materials. The micrograph of different bonding conditions is depicted in **Fig. 4.87**. From the micrograph, it was found that with increasing bonding time and temperature, more amount of boron precipitates was observed along the grain boundaries than inside the grain. At lower temperatures and time, bigger second phase particles were single-phase in the ISZ. This is attributed to the lower diffusivity of boron at a lower temperature in comparison with high temperatures.

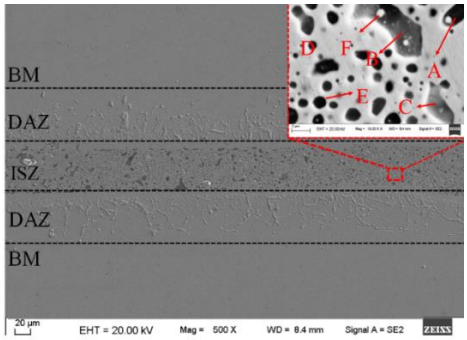

Fig. 4.86 TLP-bonded sample made at 1100 ºC, 60 min.

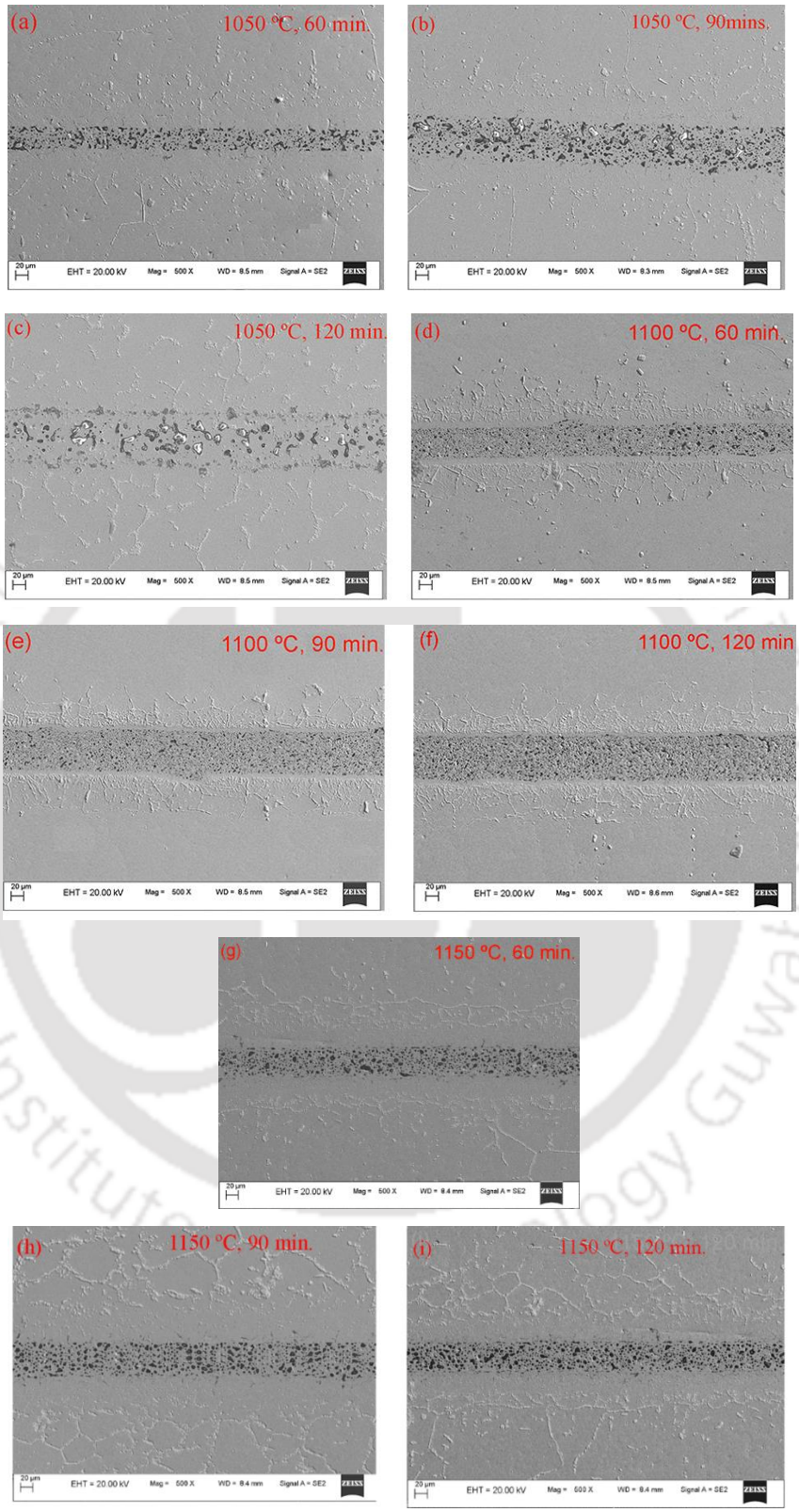

Fig. 4.87 FESEM micrographs of TLB bonded samples made at (a) 1050 ºC, 60 min., (b) 1050 ºC, 90mins., (c) 1050 ºC, 120 min., (d) 1100 ºC, 60 min., (e) 1100 ºC, 90 min., (f) 1100 ºC, 120 min., (g) 1150 ºC, 60 min., (h) 1150 ºC, 90 min., and (i) 1150 ºC, 120 min.

The X-ray mapping of TLP-bonded sample is shown in **Fig. 4.88**. The mapping indicates the presence of the high amount of Al and Ti along with the interface between the ISZ and the DAZ. This signifies the dissolution of the base metal during TLP bonding. Trace of O and Si was observed at the ISZ. During ball milling, Si fractures into nano level, which increases the surface energy of the Si particles. These nanoparticles are very active, reacts with oxygen to form silicon oxides, which are very stable particles. As a result of which silicon oxides are observed in the ISZ, and very less amount of Si participates in the diffusion during TLP bonding of IN 718 superalloy. A small amount of Ta, Nb, and Al were also observed at ISZ, which confirms the inter-diffusion of the atoms during TLP bonding.

Elemental line scanning for various elements across a TLP bond processed at 1050 ºC and holding time of 120 min is shown in **Fig. 4.89**. The result indicates significant amounts of B along with Nb and Mo at the grain boundaries in the DAZ. During IS, B diffuses from the interlayer into the DAZ and forms borides. Higher amounts of Al and Ti are evident at the ISZ – DSZ interface regions, as observed by the sharp peaks for these elements. Similarly, the line scan depicts the depletion of Ni, Cr, and Fe at ISZ-DSZ interface regions, indicating diffusion of these atoms from the base material to the interlayer. The result also confirms the presence of the higher amount of Si at ISZ, revealing the negligible amount of diffusion of Si from the filler material into the IN 718. This is attributed to the very low diffusivity of Si in Ni compared to B **[229]**. Composition variation of various elements at different zones of the TLP bond region is illustrated in **Fig. 4.90**. The results reveal the high atomic percentage of B at the DAZ and a very low percentage of B at the ISZ, which confirms the diffusion of B from the melted filler material into DAZ. The results also reveal the presence of Ti, Nb, and Al at the ISZ. From the results obtained, one can conclude inter-diffusion of Ti, Nb, Al, and B across interlayer and IN 718 alloy during TLP bonding. **Figure 4.91** shows the distribution of different elements obtained by elemental x-ray mapping at DAZ. The figure shows a uniform distribution of elements except Nb, Mo, and B in the DAZ. The figure also reveals enrichment of grain boundaries by Nb, Mo, and B with concomitant depletion of elements Ni and Fe. From the figure, it is evident that Mo, Nb, and B are present at the precipitates in high concentration, which confirms the formation of borides of Mo and Nb. The presence of Si in the DAZ was negligible. As the diffusivity of B (1.67×10^{-10} m^2/sec) is four orders higher than the diffusivity of Si ($2.11\times$

10^{-14} m^2/sec), B diffused from the interlayer area into the IN 718 whereas the Si particle remained in the ISZ. It appears that silicon can diffuse from the interlayer to the base material only with prolonged exposure time, which is much beyond that required for TLP bonding.

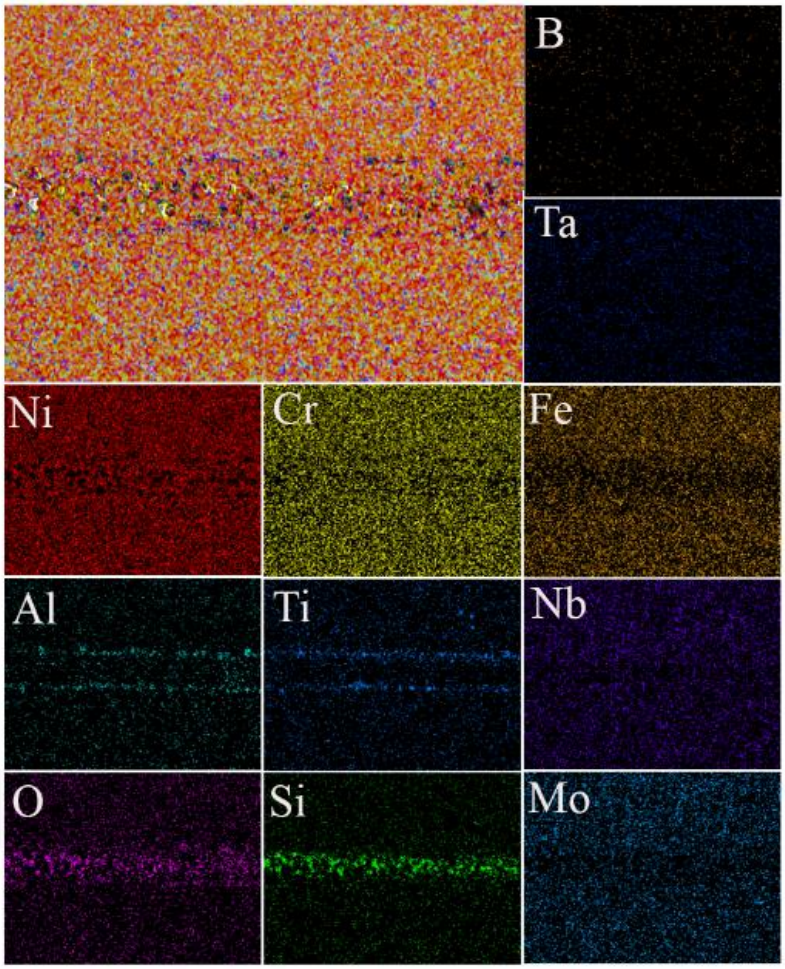

Fig. 4.88 X-Ray mapping of TLP-bonded sample made at 1050 ºC, 120 min

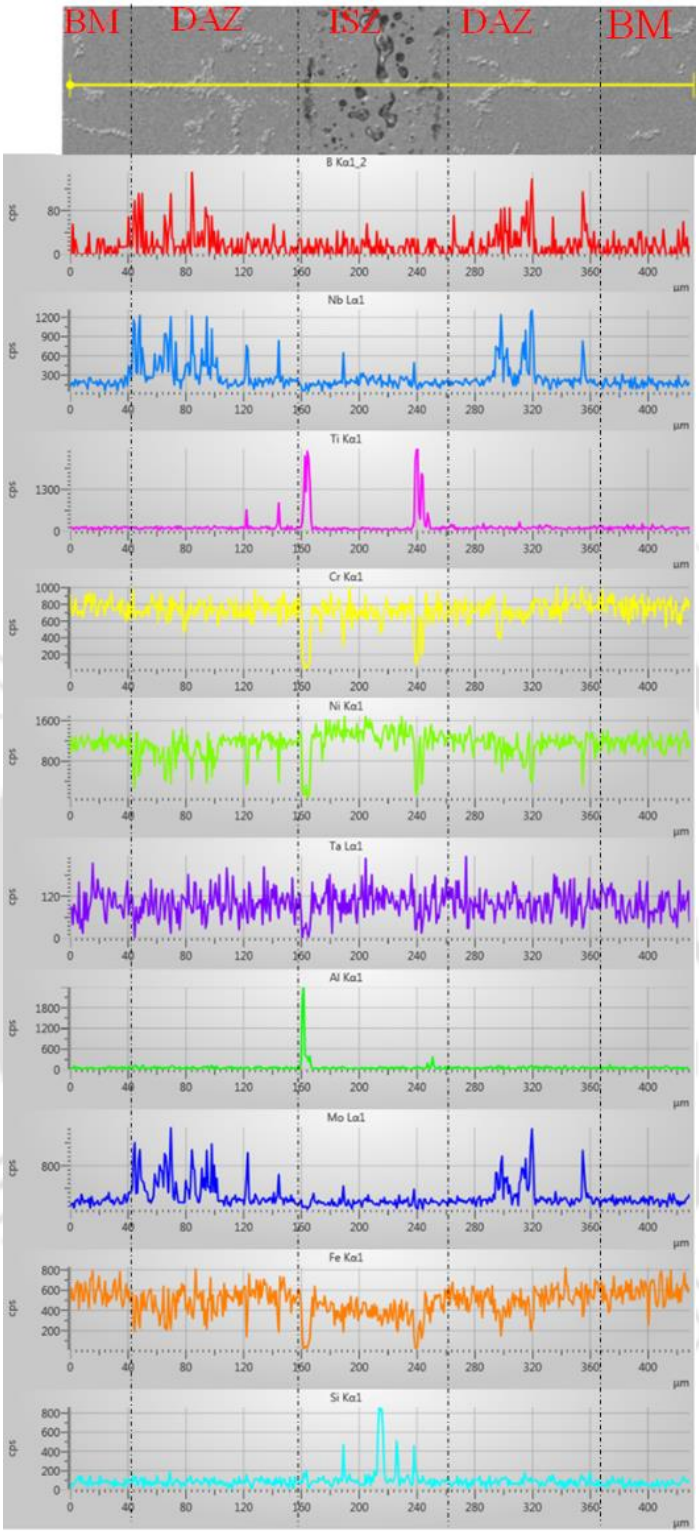

Fig. 4.89 Distribution of elements along the bond zone (made at 1050 ºC, 120 min)

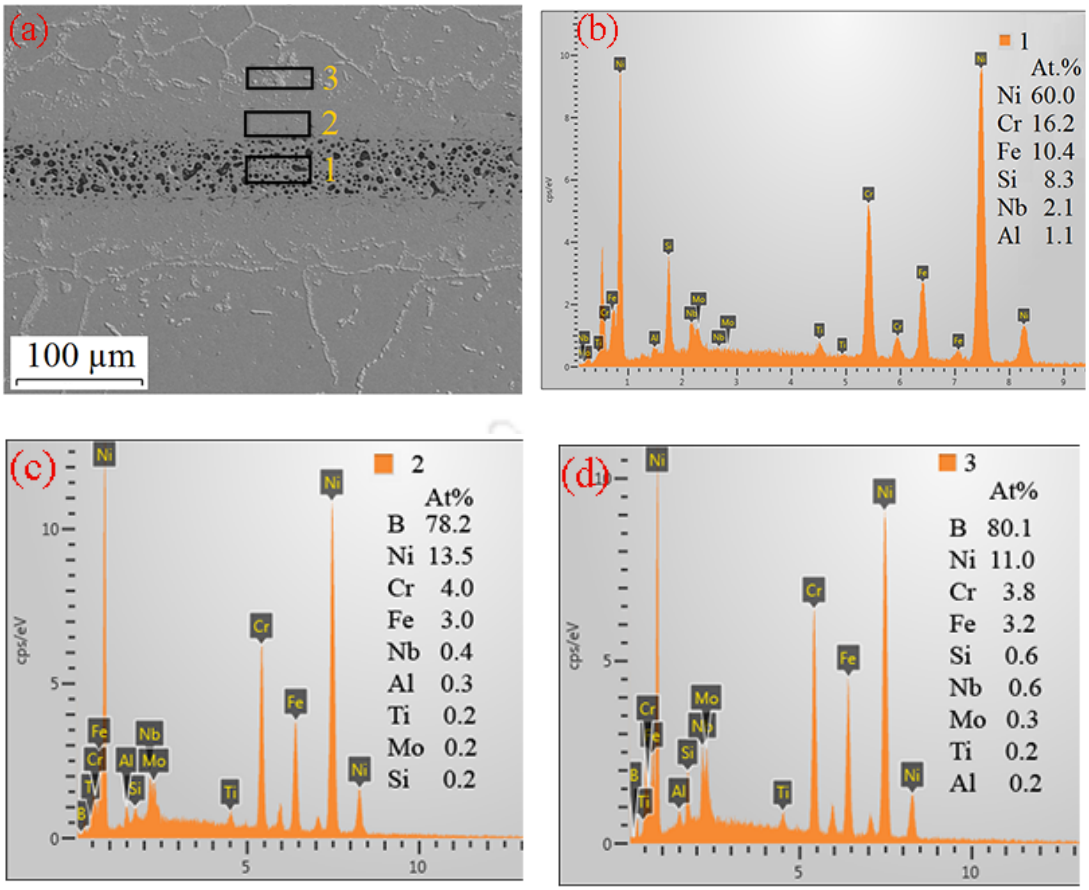

Fig. 4.90 Variation of elements along the different zones of TLP-bonded joint (a) TLP bond made at 1150 ºC, 120 min., (b) EDS of spot marked as 1, (c) EDS of spot marked as 2, and (d) EDS of spot marked as 3

The EDS spectrum of grain boundary phase marked as A is also shown in **Fig. 4.91**. The analysis revealed the grain boundary phase has 87 % B (in at. %) with small amounts of Ni, Nb, Fe, Mo, and Cr. It is also observed that the Nb and Mo in the grain are lower than that in the grain boundary phase. The results confirm the presence borides of Nb and Mo at the boundaries of grains in the DAZ. The ISZ is formed at the center of the joint due to the compositional variation during the isothermal holding. The ISZ consist of the γ-Ni matrix, along with the presence of Ti, Al, Nb, Mo and Si elements. The presence of some amount of voids (marked as "A" in **Fig. 4.86**) has also been observed. Though the initial interlayer material did not contain Ti, Al, Nb, and Mo, these elements diffuse from IN 718 superalloy into the interlayer region during TLP bonding. Concomitantly, B and Si diffuse into the IN 718 superalloy. This inter-diffusion of elements is the primary mechanism of IS in TLP bonding. The bond formed at higher bonding time and temperature has a more uniform microstructure than the bond made at lower bonding time and temperature.

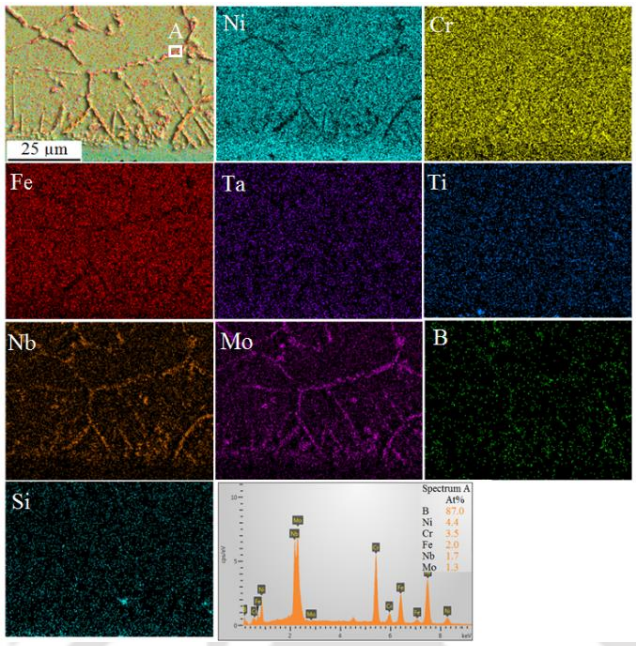

Fig. 4.91 X-ray mapping of DAZ of TLP bond made at 1100 ºC, 120 min

The magnified view of the ISZ of TLP bond is shown in **Fig. 4.92**. The micrograph shows different phases are present at the ISZ. The composition of various constituents seen in the micrograph analyzed by EDS is depicted in **Table 4.11**. The result reveals a higher concentration of Nb, Cr, Ti, and Fe in ISZ as compared to the matrix. Also, the amount of Si in all phases is more than the initial concentration of interlayer material. Which signifies the formation of Nb, Cr, Ti, and Fe silicide during TLP bonding. During the cooling induced athermal solidification, as the solubility of Si in the solidifying γ phase is low, Si atoms are rejected to the unsolidified liquid interlayer. Si enrichment in the liquid interlayer causes the solute concentration of the residual liquid to surpass the solubility limit of the γ phase. Therefore, the remaining liquid transforms into eutectic-type hard and brittle silicides phases of Nb, Cr, and Fe. In TLP bonding, interdiffusion of atoms takes place between the base material and the interlayer material. In the isothermally solidified zone, different phases are formed due to the interdiffusion of elements. Some phases have a very high concentration of Si (81.2 at. %). EDS analysis of some phases shows Ni silicide and precipitates containing Cr, Nb, and Ti. Silicon diffuses from the interlayer to the base material during isothermal solidification. If the isothermal holding time is insufficient, diffusion of complete silicon to the base metal will not take place, resulting in the presence of silicide at the bond zone after the isothermal solidification. The EDS analysis revealed the presence of Ni3Si at the bond

zone. The other phases present at the ISZ due to interdiffusion of elements are $Ti_{33.9}Al_{36.5}Cr_{16.5}Fe_{0.7}Nb_{3.7}Si_{6.3}$, $Cr_{39.1}Ni_{22.5}Fe_{2.5}Nb_{6.2}Ti_{16.8}Al_{2.8}Si_{10}$, and $Ni_{18.1}Cr_{7.9}Fe_{4.0}Si_{67.9}Ti_{0.5}Al_{1.5}$.

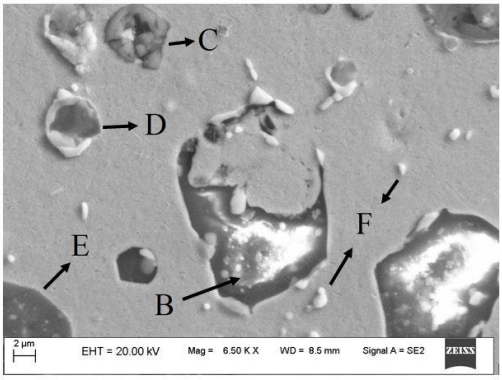

Fig. 4.92 Magnified view of ISZ of TLP joint (bond made at 1050 ºC, 120 min)

Table 4.11 EDS analysis results of different phases present in the ISZ.

Concentration /Precipitate	Ni (at.%)	Cr (at.%)	Fe (at.%)	Nb (at.%)	Ti (at.%)	Al (at.%)	Si (at.%)	Mo (at.%)
B	5.5	7.6	0.8	---	2.5	2.3	81.2	---
C	2.4	16.5	0.7	3.7	33.9	36.5	6.3	---
D	22.5	39.1	2.5	6.2	16.8	2.8	10	---
E	18.1	7.9	4.0	---	0.5	1.5	67.9	---
F	53.4	8.8	5.8	14.3	0.1	0.2	16.8	0.5

In DAZ, almost similar types of phases are formed when bonded by BNi-2 interlayer and present interlayer material. A similar kind of borides of Cr, Nb, and Mo was also found in the DAZ of TLP-bonded IN 718 joint made by using BNi-2 interlayer material **[37, 230]**. As boron acts as the main diffusing elements in BNi-2 and present interlayer material, it reacts with the high boride promoter elements like Nb, Cr, and Mo to form borides of respective elements. Whereas, binary eutectic borides of Ni and Cr, ternary eutectic compound of Ni-B-Si and Ni-silicides observed in the ISZ of TLP-bonded sample made by using BNi-2 interlayer material **[37, 130]**. However, no borides

are evident in the ISZ of the TLP-bonded sample made by using present interlayer material. This is mainly due to lower holding time for complete isothermal solidification and low diffusivity of BNi-2 interlayer elements in IN 718 superalloy.

Figure 4.93 (a-b) shows the FESEM micrograph of TLP-bonded joint. Microstructure of the DAZ of samples bonded at 1100 ˚C and 1050 ˚C are shown in **Fig. 4.93 (c-d)**, respectively. The bonding was carried out at a holding time of 1 h. The features of the DAZ bonded at 1100 ˚C is characterized by the formation of continuous second phases at the grain boundaries (**Fig. 4.93(c)**). These phases exist as either in needle form or small block forms. In addition, few second phase particles can be seen inside the grains. **Figure 4.93(e-f)** shows the EDS spectra of the second phase practical of the DAZ. The EDS analysis (**Fig. 4.93 (e-f)**) reveals these second phase particles as borides of Fe, Cr, Nb, and Ni. The average composition of second phase particles is shown in **Table 4.12** indicating a high concentration of boron (~93 at. % B). Grain boundary regions act as initial nucleation sites for the second phase particles since these areas have higher energy **[40]** compared to regions inside the grains. At 1100 ˚C, the diffusivity of B through the grain boundary is very high and hence boron can diffuse faster through the grain boundary regions resulting in the formation of borides. Second phases are also observed in the DAZ of joint bonded at 1050 ˚C. The second phases formed were fine particles with almost equiaxed morphology. These second phase particles were distributed across the grains instead of at grain boundaries. This is attributed to the low grain boundary diffusivity of B at low temperature. The silicon concentration in these phases is less than 0.1 at. %. Studies have revealed that at 1100 ˚C the diffusion rate of B and Si in Ni are 6.22×10^{-11} m/sec and3.09×10^{-14} m/sec, respectively **[231]**. The high concentration of B in the second phase particles is attributed to the high diffusivity of B in Ni, which is three orders of magnitude greater than that for Si in Ni.

Elemental X-ray mapping of the DAZ, shown in **Fig. 4.94**, reveal the presence of boron, niobium, aluminium and molybdenum in the precipitates at grain boundary regions. The X-ray mapping of base metal also revealed the presence of Nb, Al, and Mo at grain boundaries though boron was not present. The results indicate formation of borides of niobium and molybdenum at grain boundary regions after TLP bonding. The isothermal solidification in TLP bonding of IN 718 using the present interlayer material is favoured by the high diffusivity of boron in Ni.

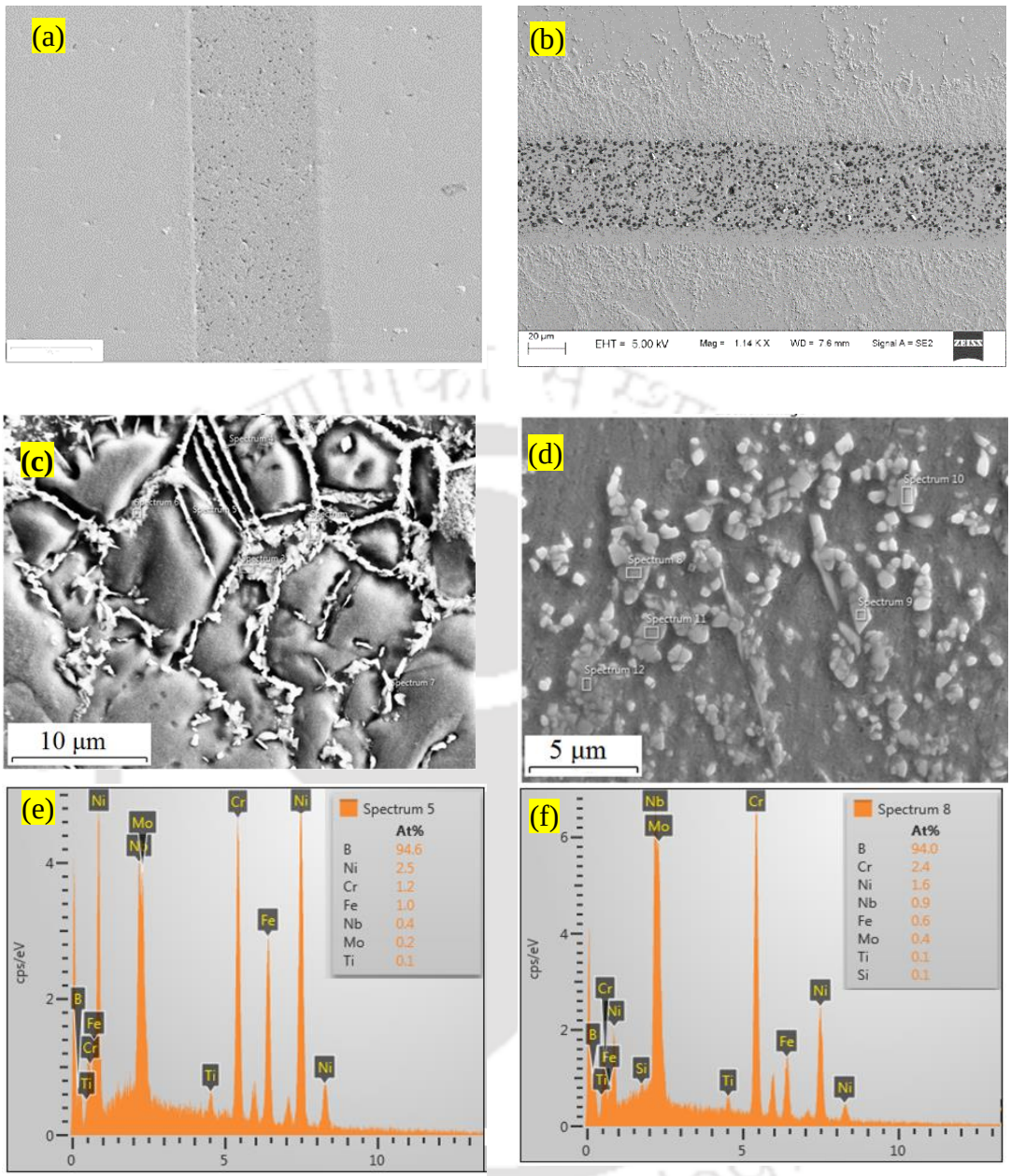

Fig. 4.93 FESEM micrograph of the TLP-bonded joint made at (a) 1100 ˚C, 1 h, (b) 1050 ˚C, 1 h and (c) DAZ of (d) DAZ of bond made at 1150 ˚C (e) EDS of point 5 and (f) EDS of point 8.

Table 4.12 Average elemental concentration of DAZ precipitates

Elements	B	Ni	Cr	Fe	Nb	Mo	Ti	Si	Al
Concentration (at.%)	93.511	2.511	2.022	0.989	0.55	0.294	0.089	0.013	0.089

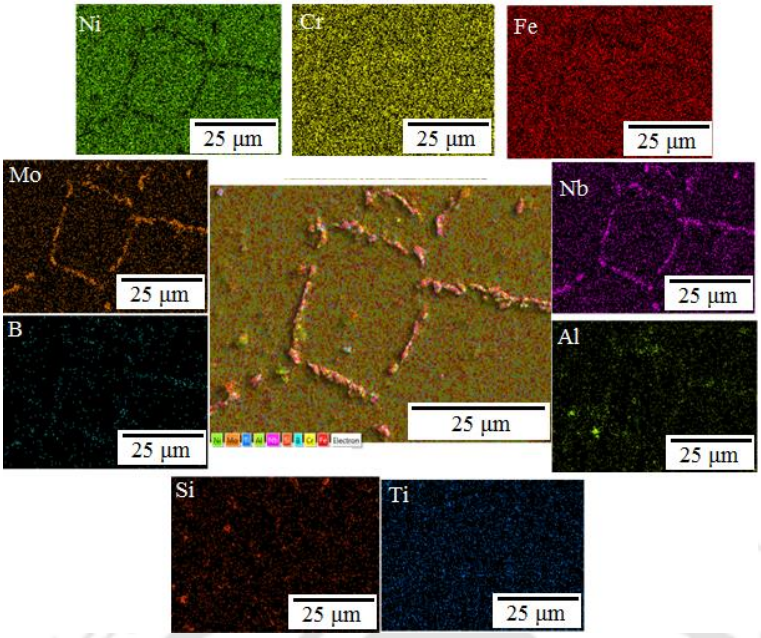

Fig. 4.94 X-ray mapping of DAZ

The EDS spectrum for ISZ of the joint is shown in **Fig. 4.95**. The result reveals (i) decrease in Ni and Si concentration, (ii) concomitant increase in Fe and Cr and (ii) presence of a small amount of niobium (Nb) and titanium (Ti). Boron was not detected in the ISZ of the TLP joint region. As the diffusivity of boron is very high, boron diffuses quickly into the base metal region as compared to other elements. It is also observed that the amount of Nb and Ti in the interlayer region increase on increasing bonding time and temperature. From the results, it can be inferred that isothermal solidification takes place as a result of interdiffusion of elements across the bond interface. **Figure 4.96** shows X-ray line scan of IN 718 sample made at 1100 ˚C. The micrograph shows compositional variation across different bonding zones. Boron concentration was very significant at DAZ which also confirms to **Fig. 4.93**.

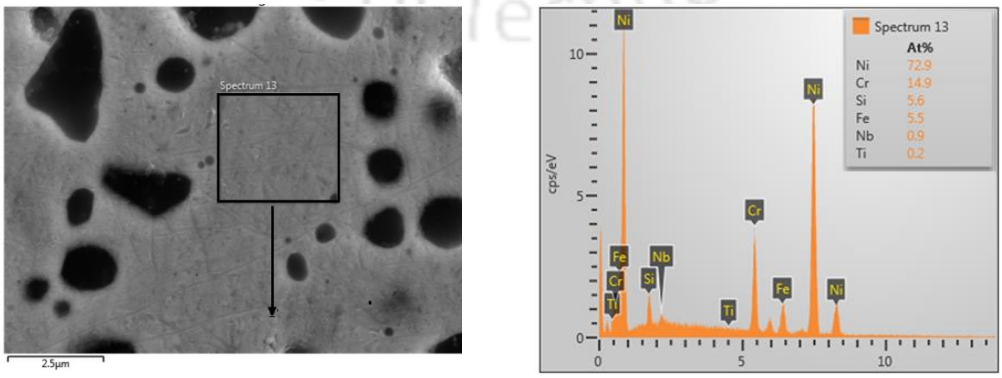

Fig. 4.95 EDS micrograph TLP-bonded ISZ

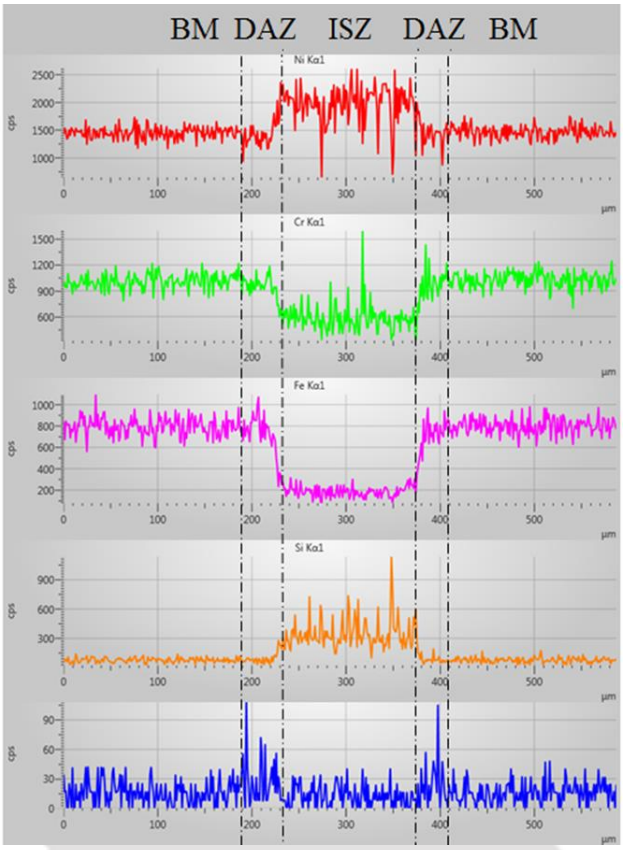

Fig. 4.96 Variation of different elements across TLP bond line (bonded at 1100˚ C and 1 h)

4.9.6 Shear strength

The ultimate shear strength variations of the bonded samples processed at different combination of temperature and time are presented in **Fig. 4.97**. The shear stress vs. ram displacement at 1050 ºC, 1100 ºC, and 1150 ºC for an isothermal holding time of 90 min are shown in **Fig. 4.98 (a)**. When the bonding temperature was increased from 1050 ºC to 1150 ºC, the ultimate shear strength increases from 381 MPa to 460 MPa. This is attributed to the depletion in the eutectic amount formed during isothermal holding **[232]**. In TLP bonding, the joint quality depends upon the degree of inter-diffusion of elements **[233]**. At higher temperatures, the diffusivity of the MPD is high as compared to lower temperatures leading to enhanced inter-diffusion of atoms between the liquid interlayer and base material. This results in the formation of less eutectic at the bonding zone leading to higher strength at the higher bonding temperature. **Fig. 4.98 (b)** reveals higher shear strength with an increase in bonding time at a constant bonding temperature. Higher bonding time allows more volume of elements to inter-diffuse between the base

and the interlayer material. This results in a homogenous distribution of elements at the bond regions, thereby reducing the amount of eutectic formed by athermal solidification.

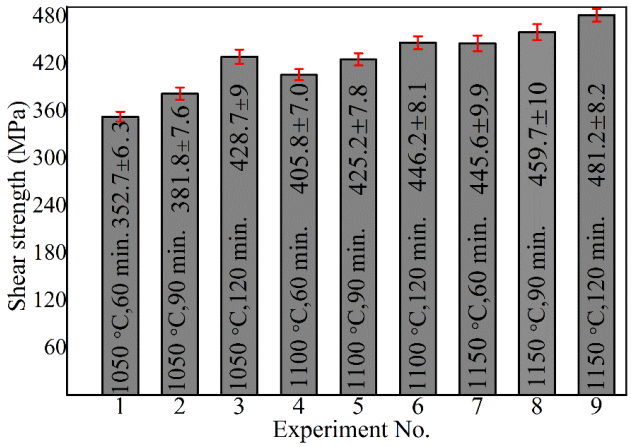

Fig. 4.97 Ultimate shear strength of the different experimental conditions.

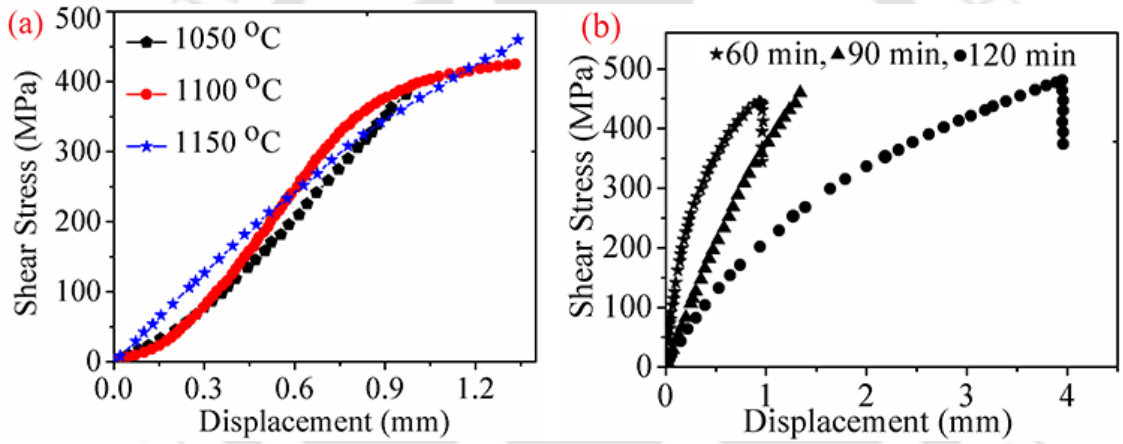

Fig. 4.98 Shear stress variation with (a) temperature and (b) time.

4.9.7 Microhardness

Hardness profile in TLP joint is an excellent indicator to evaluate the degree of homogenization achieved during the bonding process. The variation of micro-hardness at the three distinct zones of TLP-bonded samples are shown in **Fig. 4.99 (a-c)**. Hardness at ISZ is lower as compared to the base material hardness. The hardness of ISZ is determined by inter-diffusion of alloying elements between the base material and bond region. The low hardness value of ISZ is attributed to the inadequate diffusion of alloying elements **[234, 235]** during the bonding process due to the unavailability of sufficient time for completion of IS. The hardness of ISZ, in bonds produced at elevated temperature, is high as compared to bonds formed at a lower temperature, as shown in

Fig. 4.99 (d). As mentioned in the earlier section, this is attributed to the higher rate of inter-diffusion of Nb, Mo, Al, and Ti, at a higher temperature. The hardness of DAZ is higher than the hardness of BM, due to the enrichment of Mo–Nb borides in this region. During the TLP bonding, the hardness of the BM region is not changed much by the diffusion of MPD elements. The BM zone hardness obtained at higher bonding temperature is slightly lower than that achieved at lower temperatures. The grain size of the BM increases with increasing bonding temperature. The decrease in hardness of BM with an increase in bond temperature is attributed to the grain growth at elevated temperature.

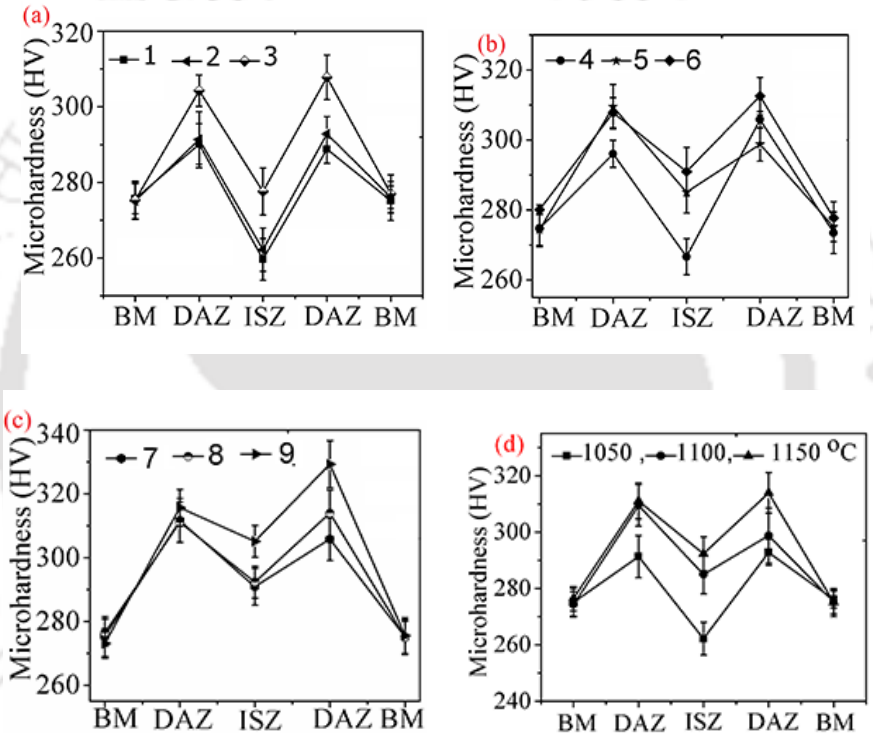

Fig. 4.99 Microhardness variation at different zones (a) Exp. No. 1- 3, (b) Exp. No. 4- 6, (c) Exp. No. 7- 9 and (d) variation of hardness with bonding temperature

IN 718 is precipitation strengthened nickel based superalloy, the hardness of the material is influence by its alloying elements like Cr, Fe, Nb, Ti, and Al. The Cr and Fe act as solid solution strengthening elements, and the Nb, Ti, and Al act as the precipitation strengthening elements. During TLP bonding Nb, Ti, and Al diffuse from the base material into the bond zone. Due to insufficient isothermal solidification time, the amount of elements which has diffused in to the ISZ is low compared to base material. As a result, less γ′ and γ″ precipitates forms, and the hardness of the ISZ decreases.

Chapter 5

Conclusion and Future Scope

5.1 Conclusions of the Present Work

In the present work, detailed experimental investigations were carried out to evaluate the influence of process parameters on the bond properties of the TLP-bonded IN 718 joint. The effect of homogenization stage of TLP on the bond quality and mechanical properties was investigated. The kinetics of the TLP bonded sample was studied by the interrupted DSC technique. Post-bond heat treatment was designed to improve bond quality. The residual stress present in the TLP-bonded sample was determined and its effect was analyzed. A new Ni-Cr-Fe-B-Si base interlayer material was also developed and investigated for TLP bonding of IN 718. The conclusions that can be derived from the present research work are described in the following paragraphs.

The experimental investigation of TLP bonding revealed that bonding temperature, isothermal solidification time, and thickness of the interlayer material determine bond quality. In the present investigation, the maximum bond strength that was obtained by TLP bonding of IN 718 was 86 % of the base material's strength. The presence of secondary precipitates viz. silicides of Ti and Al in the ASZ reduced the bond strength. A higher bonding time and temperature give higher strength due to a more uniform microstructure and chemical homogeneity. A higher bonding temperature and time can be beneficial in obtaining high bond strength. Dissolution of the base material and solidification of the liquid interlayer occur concurrently during the heating and melting stages of TLP bonding. The time duration for IS depends upon the actual width of the interlayer material. Due to diffusion, the actual width of the interlayer material prior to IS was less than the initial width of the interlayer material. Therefore, while calculating the IS time, the industries should know the kinetics of the TLP bonding of the base material.

Homogenization stage of TLP bonding results in the dissolution of deleterious precipitates and borides present in the ISZ and HAZ, respectively, and produced a bond with uniform microstructure and chemical homogeneity. The volume fraction of boride decreased from 13 % to 4.5 %, and the volume fraction of strengthening precipitates i.e.

γ″+γ′ increased from 9 to 23 % after 32 hours of homogenization. This resulted in a 220 % increase in strength in the current investigation. As this process is recommended for joining superalloys in aero-engines, and the parts are subjected to severe lading conditions, homogenization of bond should be carried out at elevated temperature. At the same time industries should consider TTT diagram during selection of homogenization time and temperature.

The post-bond heat treatment improved the chemical homogeneity in the TLP bond by reducing the ASZ size and boride fraction in the DAZ. The strength of the TLP-bonded sample increased by 113 %, the ductility reduced by 48 %, and also improved the hardness due to PBHT.–PBHT improved the high-temperature tensile strength of the bond. At 650 °C, the PBHT sample exhibited 85 % of the heat-treated base material strength with a concomitant reduction in ductility.-The room temperature fatigue strength of the PBHT sample is comparable to that of the base material fatigue strength. TLP bond resulted in compressive residual stresses at the bond region. Isothermal solidified zone (i.e. bond center line) exhibited maximum residual stress and decreased with distance away from it. The residual stress increased with increasing bonding temperature.

A new solid solution face-centered cubic structured Ni-Cr-B-Si-Fe alloy was developed by powder ball milling technique for use as interlayer material for TLP bonding of IN 718 superalloy. The lattice parameter of this alloy powder was 3.53 Å and had a melting point of 1023 °C. The strength of the TLP bonded sample using the developed interlayer material is lower than the base material strength. This is attributed to the presence of voids in the ISZ. Insufficient diffusion of alloying elements from the BM to ISZ resulted in lowering the hardness of ISZ compared to BM. Nb-Ti-Mo borides increased the hardness of DAZ.

5.2 Future scope

Based on this work, the following areas are suggested for further research. As IN 718 is usually used in high temperature application in aero-engines, seeing the requirement of high strength in modern aero-engine industries, the existing interlayer materials may be coated with nano-sized Mo, Nb, Ti, and Al particles to improve the volume fraction of γ″+γ′ strengthening phases at the ISZ of TLP bonded IN 718 joint. The elevated temperature fatigue behaviour of the TLP-bonded IN 718 may be

investigated in depth. Also, viability of TLP bonding of dissimilar materials like Ti-Ni, Ni-stainless steels, etc. may be explored.

As the newly developed interlayer can be beneficial for the industries. Therefore, investigation of bond quality may be carried out using the newly developed interlayer material in foil form. Analytical or numerical models may be developed to predict the bonding time as a function of interlayer materials, bonding time and temperature.

Reference

[1] Gasson, P.C., 2008. The Superalloys: Fundamentals and Applications RC Reed Cambridge University Press, The Edinburgh Building, Shaftesbury Road, Cambridge, CB2 2RU, UK, 2006. 372pp. Illustrated. £ 80. ISBN 0-521-85904-2. The Aeronautical Journal, 112(1131), pp.291-291.

[2] Gowthaman, P.S. and Jeyakumar, S., 2019. A review on machining of high-temperature aeronautics super-alloys using WEDM. Materials Today: Proceedings, 18, pp.4782-4791.

[3] Backman, D.G. and Williams, J.C., 1992. Advanced materials for aircraft engine applications. Science, 255(5048), pp.1082-1087.

[4] Cao, X., Rivaux, B., Jahazi, M., Cuddy, J. and Birur, A., 2009. Effect of pre-and post-weld heat treatment on metallurgical and tensile properties of Inconel 718 alloy butt joints welded using 4 kW Nd: YAG laser. Journal of Materials Science, 44(17), pp.4557-4571.

[5] Ni, M., Liu, S., Chen, C., Li, R., Zhang, X. and Zhou, K., 2019. Effect of heat treatment on the microstructural evolution of a precipitation-hardened superalloy produced by selective laser melting. Materials Science and Engineering: A, 748, pp.275-285.

[6] Miller, S., 1996. Advanced materials mean advanced engines. Interdisciplinary Science Reviews, 21(2), pp.117-129.

[7] Oshobe, O.E., 2012. Fiber laser welding of nickel-based superalloy Inconel 718. University of Manitoba (Canada).

[8] Kataria, R., Singh, R.P., Sharma, P. and Phanden, R.K., 2021. Welding of super alloys: a review. Materials Today: Proceedings, 38, pp.265-268.

[9] Singh, S.R., Mote, R.G. and Mishra, S.K., 2022. The effect of microstructures and precipitates (γ', γ ″, δ) on machinability of Inconel-718 nickel-based superalloy in turning process. Journal of Manufacturing Processes, 82, pp.374-389.

[10] Ozer, S., Bilgin, G.M., Davut, K., Esen, Z. and Dericioglu, A.F., 2022. Effect of post fabrication aging treatment on the microstructure, crystallographic texture and elevated temperature mechanical properties of IN718 alloy fabricated by selective laser melting. Journal of Materials Processing Technology, 306, p.117622.

[11] Huang, X. and Miglietti, W., 2012. Wide gap braze repair of gas turbine blades and vanes—a review. Journal of Engineering for Gas Turbines and Power, 134(1).

[12] Kumar, D.P. and Kumaran, S., 2020. Mechanical and corrosion behaviour of Inconel 718 processed through SPS diffusion bonding and double aging treatment. Materials Today: Proceedings, 27, pp.2582-2585.

[13] Thompson, R.G., 1988. Microfissuring of alloy 718 in the weld heat-affected zone. JOM, 40(7), pp.44-48.

[14] Prager, M. and Shira, C.S., 1968. Welding of precipitation-hardening nickel- base alloys (Welding precipitation hardenable Ni base alloys noting heat treatment, microfissuring, strain age cracking and other intricacies). Welding Research Council Bulletin, (128).

[15] Vishwakarma, K.R., Richards, N.L. and Chaturvedi, M.C., 2005. HAZ microfissuring in EB welded allvac 718 plustm alloy. Superalloys, 718, pp.625-706.

[16] Tarai, U.K., Robi, P.S. and Pal, S., 2020. Thermal Properties of Ni–Cr–Si–B–Fe Based Interlayer Material and Its Application in TLP Bonding of IN 718 Superalloy. Acta Metallurgica Sinica (English Letters), 33(12), pp.1666-1680.

Reference

[17] Zalawadia, J. and Lamba, K.K., 2017. Experimental Investigation on Metallurgy of High Vacuum Electron Beam Welded Ni Base Alloy Inconel 718. Indian Welding Journal, 50(3).

[18] Manikandan, S.G.K., Sivakumar, D. and Kamaraj, M., 2019. Welding the Inconel 718 superalloy: Reduction of micro-segregation and laves phases. Elsevier.

[19] Ajay, V., Babu, N.K., Ashfaq, M., Kumar, T.M. and Krishna, K.V., 2021. A review on rotary and linear friction welding of inconel alloys. Transactions of the Indian Institute of Metals, 74(11), pp.2583-2598.

[20] Nakkalil, R., Richards, N.L. and Chaturvedi, M.C., 1993. The influence of solidification mode on heat affected zone microfissuring in a nickel-iron base superalloy. Acta metallurgica et materialia, 41(12), pp.3381-3392.

[21] Song, K.H. and Nakata, K., 2010. Microstructural and mechanical properties of friction-stir-welded and post-heat-treated Inconel 718 alloy. Journal of Alloys and Compounds, 505(1), pp.144-150.

[22] Venukumar, S., Sarkar, P., Sashank, J.S., Sampath, P. and Saikiran, K., 2018. Microstructural and mechanical properties of Inconel 718 TIG weldments. Materials Today: Proceedings, 5(2), pp.8480-8485.

[23] Hanning, F., 2018. Weld cracking in precipitation hardening Ni-based superalloys (Doctoral dissertation, Chalmers Tekniska Hogskola (Sweden)).

[24] Thejasree, P., Manikandan, N., Raju, R., Narasimhamu, K.L., Surendranatha, G.M. and Damodaram, A.K., 2022. Investigations on laser beam welded Inconel 718 weldments. Materials Today: Proceedings, 68, pp.1757-1761.

[25] Sahu, A.K. and Bag, S., 2021. Influence of current pulsation on solidification parameters during micro-plasma arc welding of thin sheet Alloy 718. Welding in the World, 65(12), pp.2403-2419.

[26] Ghaffari, R. and Naffakh-Moosavy, H., 2022. Investigation of macrostructure, microstructure, and hot cracking susceptibility of laser-welded Inconel-718 superalloy under various post-cold treatment environments. CIRP Journal of Manufacturing Science and Technology, 37, pp.110-124.

[27] Ram, G.J., Reddy, A.V., Rao, K.P., Reddy, G.M. and Sundar, J.S., 2005. Microstructure and tensile properties of Inconel 718 pulsed Nd-YAG laser welds. Journal of Materials Processing Technology, 167(1), pp.73-82.

[28] Gordine, J., 1971. Some problems in welding Inconel 718. WELD J, 50(11), p.480.

[29] Jung, D.H., Sharma, A., Mayer, M. and Jung, J.P., 2018. A review on recent advances in transient liquid phase (TLP) bonding for thermoelectric power module. Reviews on advanced materials science, 53(2), pp.147-160.

[30] Li, Wenchao, et al. "Homogenization stage during TLP bonding of RAFM steel with a Fe–Si–B interlayer: microstructure evolution and mechanical properties." Materials Science and Engineering: A 780 (2020): 139205.

[31] Li, W., Li, X., Liu, Y., Wang, Z., Liu, C. and Li, H., 2020. Homogenization stage during TLP bonding of RAFM steel with a Fe–Si–B interlayer: microstructure evolution and mechanical properties. Materials Science and Engineering: A, 780, p.139205.

[32] Pouranvari, M., Ekrami, A. and Kokabi, A.H., 2014. Diffusion brazing of cast INCONEL 718 superalloy utilising standard heat treatment cycle. Materials Science and Technology, 30(1), pp.109-115.

[33] Xia, C., Zhao, M., Sun, W., Li, H. and Liu, P., 2018. Microstructure and properties of 3D printed Inconel 718 joint brazed with BNi-2 amorphous filler metal. Materials Research, 22.

[34] Asadi, J., Sajjadi, S.A. and Omidvar, H., 2021. New insights into microstructural changes during transient liquid phase bonding of GTD-111 superalloy. Transactions of Nonferrous Metals Society of China, 31(9), pp.2703-2715.

[35] Pouranvari, M., Ekrami, A. and Kokabi, A.H., 2008. Microstructure development during transient liquid phase bonding of GTD-111 nickel-based superalloy. Journal of alloys and compounds, 461(1-2), pp.641-647.

[36] Lee, B.K., Song, W.Y., Kim, D.U., Woo, I.S. and Kang, C.Y., 2007. Effect of bonding temperatures on the transient liquid phase bonding of a directionally solidified Ni-based superalloy, GTD-111. Metals and materials international, 13(1), pp.59-65.

[37] Pouranvari, M., Ekrami, A. and Kokabi, A.H., 2013. Transient liquid phase bonding of wrought IN718 nickel based superalloy using standard heat treatment cycles: Microstructure and mechanical properties. Materials & Design, 50, pp.694-701.

[38] Yan, G., Bhowmik, A., Nagarajan, B., Song, X., Tan, S.C. and Tan, M.J., 2019. The bonding time effects on the transient liquid phase bonding of Inconel 718 using nickel-based sintered brazing preform. Applied Surface Science, 495, p.143465.

[39] Egbewande, A.T., Chukwukaeme, C. and Ojo, O.A., 2008. Joining of superalloy Inconel 600 by diffusion induced isothermal solidification of a liquated insert metal. Materials characterization, 59(8), pp.1051-1058.

[40] Jalilian, F., Jahazi, M. and Drew, R.A.L., 2006. Microstructural evolution during transient liquid phase bonding of Inconel 617 using Ni–Si–B filler metal. Materials Science and Engineering: A, 423(1-2), pp.269-281.

[41] Tokoro, K., Wikstrom, N.P., Ojo, O.A. and Chaturvedi, M.C., 2008. Variation in diffusion-induced solidification rate of liquated Ni–Cr–B insert during TLP bonding of Waspaloy superalloy. Materials Science and Engineering: A, 477(1-2), pp.311-318.

[42] Doroudi, A., Pilehrood, A.E., Mohebinia, M., Dastgheib, A., Rajabi, A. and Omidvar, H., 2020. Effect of the isothermal solidification completion on the mechanical properties of Inconel 625 transient liquid phase bond by changing bonding temperature. Journal of Materials Research and Technology, 9(5), pp.10355-10365.

[43] Arafin, M.A., Medraj, M., Turner, D.P. and Bocher, P., 2007. Transient liquid phase bonding of Inconel 718 and Inconel 625 with BNi-2: Modeling and experimental investigations. Materials Science and Engineering: A, 447(1-2), pp.125-133.

[44] Pilehrood, A.E., Omidvar, H., Shamsipur, A. and Sajuri, Z., 2020. Influence of transient liquid phase bonding followed by homogenization on the fatigue lifetimes of inconel 738 at elevated temperature. Journal of Manufacturing Processes, 55, pp.348-358.

[45] Wikstrom, N.P., Ojo, O.A. and Chaturvedi, M.C., 2006. Influence of process parameters on microstructure of transient liquid phase bonded Inconel 738LC superalloy with Amdry DF-3 interlayer. Materials Science and Engineering: A, 417(1-2), pp.299-306.

[46] Jalilvand, V., Omidvar, H., Shakeri, H.R. and Rahimipour, M.R., 2013. Microstructural evolution during transient liquid phase bonding of Inconel 738LC using AMS 4777 filler alloy. Materials Characterization, 75, pp.20-28.

[47] Ghaderi, S., Karimzadeh, F., Ashrafi, A. and Hosseini, S.H., 2020. Effect of pressure, temperature and homogenization on the dissolution behavior and mechanical properties of IN718/AISI 304 during transient liquid phase bonding. Journal of Manufacturing Processes, 60, pp.213-226.

[48] Arafin, M.A., Medraj, M., Turner, D.P. and Bocher, P., 2007. Transient liquid phase bonding of Inconel 718 and Inconel 625 with BNi-2: Modeling and experimental investigations. Materials Science and Engineering: A, 447(1-2), pp.125-133.

[49] Jiao, Y., Sheng, G., Zhang, Y., Xu, C. and Yuan, X., 2022. Transient liquid phase bonding of Inconel 625 with Mar-M247 superalloy using Ni–Cr–B interlayer: Microstructure and mechanical properties. Materials Science and Engineering: A, 831, p.142204.

[50] Jincheng, L., Bangyang, X., Lili, X., Yanying, H., Panpan, L., Tiesong, L., Peng, H. and Weiqi, Y., 2022. Partial transient liquid phase diffusion bonding of ZrC-SiC and 304 stainless steel by Ti/Ni interlayer: Microstructure and properties. Journal of the European Ceramic Society, 42(9), pp.3708-3719.

[51] Ghahferokhi, A.I., Kasiri-Asgarani, M., Ebrahimi-kahrizsangi, R., Rafiei, M., Bakhsheshi-Rad, H.R., Amini, K. and Berto, F., 2022. Effect of bonding temperature and bonding time on microstructure of dissimilar transient liquid phase bonding of GTD111/BNi-2/IN718 system. Journal of Materials Research and Technology, 21, pp.2178-2190.

[52] Das, N., 2010. Advances in nickel-based cast superalloys. Transactions of the indian institute of metals, 63(2), pp.265-274.

[53] Akca, E. and Gürsel, A., 2015. A review on superalloys and IN718 nickel-based INCONEL superalloy. Periodicals of Engineering and Natural Sciences (PEN), 3(1).

[54] Lingenfelter, A., 1989. Welding of Inconel alloy 718: A historical overview. Superalloy, 718, pp.673-683.

[55] Jappes, J.W., Ajithram, A., Adamkhan, M. and Reena, D., 2022. Welding on Ni based super alloys–A review. Materials Today: Proceedings, 60, pp.1656-1659.

[56] Akca, E. and Gürsel, A., 2015. A review on superalloys and IN718 nickel-based INCONEL superalloy. Periodicals of Engineering and Natural Sciences (PEN), 3(1).

[57] Umbrello, D., 2013. Investigation of surface integrity in dry machining of Inconel 718. The International Journal of Advanced Manufacturing Technology, 69(9), pp.2183-2190.

[58] Kuo, C.P., Ling, C.C., Chen, S.H. and Chang, C.W., 2006. The prediction of cutting force in milling Inconel-718. The International Journal of Advanced Manufacturing Technology, 27(7), pp.655-660.

[59] Ohadi, M., Zhang, X., Keramati, H., Arie, M., Singer, F., Tiwari, R. and Shooshtari, A., 2018. Recent developments in high temperature heat exchangers: A review. Frontiers in Heat and Mass Transfer (FHMT), 11.

[60] Sonar, T., Balasubramanian, V., Malarvizhi, S., Venkateswaran, T. and Sivakumar, D., 2021. An overview on welding of Inconel 718 alloy-Effect of welding processes on microstructural evolution and mechanical properties of joints. Materials Characterization, 174, p.110997.

[61] Xiao, H., Li, S., Han, X., Mazumder, J. and Song, L., 2017. Laves phase control of Inconel 718 alloy using quasi-continuous-wave laser additive manufacturing. Materials & Design, 122, pp.330-339.

[62] Paulonis, D.F., Oblak, J.M. and Duvall, D.S., 1969. Precipitation in Nickel-base Alloy 718. Pratt and Whitney Aircraft, Middletown, Conn.

[63] Cozar, R. and Pineau, A., 1973. Morphology of y'and y" precipitates and thermal stability of inconel 718 type alloys. Metallurgical Transactions, 4(1), pp.47-59.

[64] Chaturvedi, M.C. and Han, Y.F., 1983. Strengthening mechanisms in Inconel 718 superalloy. Metal science, 17(3), pp.145-149.

[65] Oblak, J.M., Paulonis, D.F. and Duvall, D.S., 1974. Coherency strengthening in Ni base alloys hardened by DO22 γ′ precipitates. Metallurgical and Materials Transactions B, 5(1), pp.143-153.

[66] Uçak, N. and Çiçek, A., 2018. The effects of cutting conditions on cutting temperature and hole quality in drilling of Inconel 718 using solid carbide drills. Journal of Manufacturing Processes, 31, pp.662-673.

[67] Mei, Y., Liu, Y., Liu, C., Li, C., Yu, L., Guo, Q. and Li, H., 2015. Effects of cold rolling on the precipitation kinetics and the morphology evolution of intermediate phases in Inconel 718 alloy. Journal of Alloys and Compounds, 649, pp.949-960.

[68] Mantri, S.A., Dasari, S., Sharma, A., Alam, T., Pantawane, M.V., Pole, M., Sharma, S., Dahotre, N.B., Banerjee, R. and Banerjee, S., 2021. Effect of micro-segregation of alloying elements on the precipitation behaviour in laser surface engineered Alloy 718. Acta Materialia, 210, p.116844.

[69] Slama, C., Servant, C. and Cizeron, G., 1997. Aging of the Inconel 718 alloy between 500 and 750 C. Journal of materials research, 12(9), pp.2298-2316.

[70] Slama, C. and Abdellaoui, M., 2000. Structural characterization of the aged Inconel 718. Journal of alloys and compounds, 306(1-2), pp.277-284.

[71] Oshobe, O.E., 2012. Fiber laser welding of nickel-based superalloy Inconel 718. University of Manitoba (Canada).

[72] Srinivasan, D., Lawless, L.U. and Ott, E.A., 2012. Experimental determination of TTT diagram for alloy 718Plus®. Superalloys 2012, 3, pp.759-768.

[73] Anderson, M., Thielin, A.L., Bridier, F., Bocher, P. and Savoie, J., 2017. δ Phase precipitation in Inconel 718 and associated mechanical properties. Materials Science and Engineering: A, 679, pp.48-55.

[74] Lawitzki, R., Hassan, S., Karge, L., Wagner, J., Wang, D., von Kobylinski, J., Krempaszky, C., Hofmann, M., Gilles, R. and Schmitz, G., 2019. Differentiation of γ′-and γ ″-precipitates in Inconel 718 by a complementary study with small-angle neutron scattering and analytical microscopy. Acta Materialia, 163, pp.28-39.

[75] Munther, M., Tajyar, A., Holtham, N., Hackel, L., Beheshti, A. and Davami, K., 2022. An investigation into the mechanistic origin of thermal stability in thermal-microstructural-engineered additively manufactured Inconel 718. Vacuum, 199, p.110971.

[76] Ferreri, N.C., Vogel, S.C. and Knezevic, M., 2020. Determining volume fractions of γ, γ′, γ ″, δ, and MC-carbide phases in Inconel 718 as a function of its processing history using an advanced neutron diffraction procedure. Materials Science and Engineering: A, 781, p.139228.

[77] Radavich, J.F., 1989. The physical metallurgy of cast and wrought alloy 718. Superalloy, 718(33), pp.229-240.

[78] Fu, S.H., Dong, J.X., Zhang, M.C. and Xie, X.S., 2009. Alloy design and development of INCONEL718 type alloy. Materials Science and Engineering: A, 499(1-2), pp.215-220.

[79] Hagel, W.C. and Beattie, H.J., 1959. Iron and Steel Institute Special Report. London, 64, p.98.

[80] Candioto, K.C.G., Caliari, F.R., Reis, D.A.P., Couto, A.A. and Nunes, C.A., 2015. Characterization of the superalloy Inconel 718 after double aging heat treatment. In Mechanical and Materials Engineering of Modern Structure and Component Design (pp. 293-300). Springer, Cham.

[81] Hasani, N., Dharmendra, C., Sanjari, M., Fazeli, F., Amirkhiz, B.S., Pirgazi, H., Ram, G.J. and Mohammadi, M., 2021. Laser powder bed fused Inconel 718 in stress-relieved and solution heat-treated conditions. Materials Characterization, 181, p.111499.

[82] Ran, R., Wang, Y., Zhang, Y.X., Fang, F., Xia, Y.K., Zhang, W.N., Yuan, G. and Wang, G.D., 2022. Two-stage annealing treatment to uniformly refine the microstructure, tailor δ precipitates and improve tensile properties of Inconel 718 alloy. Journal of Alloys and Compounds, 927, p.166820.

[83] Singh SR, Mote RG, Mishra SK. The effect of microstructures and precipitates (γ', γ ″, δ) on machinability of Inconel-718 nickel-based superalloy in turning process. Journal of Manufacturing Processes. 2022 Oct 1; 82:374-89.

[84] Lewis, A.C., Bingert, J.F., Rowenhorst, D.J., Gupta, A., Geltmacher, A.B. and Spanos, G., 2006. Two- and three-dimensional microstructural characterization of a super-austenitic stainless steel. Materials Science and Engineering: A, 418(1-2), pp.11-18.

[85] Lan, B., Wang, Y., Liu, Y., Hooper, P., Hopper, C., Zhang, G., Zhang, X. and Jiang, J., 2021. The influence of microstructural anisotropy on the hot deformation of wire arc additive manufactured (WAAM) Inconel 718. Materials Science and Engineering: A, 823, p.141733.

[86] Antonov, S., Chen, W., Lu, S., Isheim, D., Seidman, D.N., Feng, Q., Sun, E. and Tin, S., 2019. The effect of phosphorus on the formation of grain boundary laves phase in high-refractory content Ni-based superalloys. Scripta Materialia, 161(C).

[87] Tao, P., Li, H., Huang, B., Hu, Q., Gong, S. and Xu, Q., 2019. The crystal growth, intercellular spacing and microsegregation of selective laser melted Inconel 718 superalloy. Vacuum, 159, pp.382-390.

[88] Cieslak, M.J., Knorovsky, G.A., Headley, T.J. and Romig Jr, A.D., 1989. The solidification metallurgy of alloy 718 and other Nb-containing superalloys (No. SAND-89-0264C; CONF-890646-1). Sandia National Lab. (SNL-NM), Albuquerque, NM (United States).

[89] Cao, X., Rivaux, B., Jahazi, M., Cuddy, J. and Birur, A., 2009. Effect of pre-and post-weld heat treatment on metallurgical and tensile properties of Inconel 718 alloy butt joints welded using 4 kW Nd: YAG laser. Journal of Materials Science, 44(17), pp.4557-4571.

[90] Jose, P.J. and Anand, M.D., 2018. Comprehensive Analysis of TIG Welded Inconel–718 Alloy for Different Heat Input Conditions. International Journal of Engineering & Technology, 7(3.6), pp.206-209.

[91] Segerstark, A., Andersson, J., Svensson, L.E. and Ojo, O., 2018. Microstructural characterization of laser metal powder deposited Alloy 718. Materials Characterization, 142, pp.550-559.

[92] Radhakrishna, C.H. and Prasad Rao, K., 1997. The formation and control of Laves phase in superalloy 718 welds. Journal of Materials Science, 32(8), pp.1977-1984.

[93] He, J., Tang, X.Y., Fukuyama, S. and Yokogawa, K., 1995. Boundary in γ ″precipitates in inconel 718 nickel-base superalloy. Acta metallurgica et materialia, 43(12), pp.4403-4409.

[94] Wagner, H.J. and Hall, A.M., 1965. Physical metallurgy of alloy 718 (Vol. 217). Defense Metals Information Center, Battelle Memorial Institute.

[95] Brochu, M., Chiocca, A., Navalon-Cabanes, R. and Fournier, J., 2013, June. Solidification cracking of IN 718 TIG welds. In 13th International Conference on Fracture (pp. 1-10).

[96] Fayed, E.M., Brailovski, V., Jahazi, M. and Medraj, M., 2022. Stability of the microstructure and elevated-temperature mechanical properties of additively manufactured Inconel 718 superalloy subjected to long-term in-service thermal cycling. Materials Science and Engineering: A, 838, p.142790.

[97] Lee, J.H., Lee, C.M. and Kim, D.H., 2022. Repair of damaged parts using wire arc additive manufacturing in machine tools. Journal of Materials Research and Technology, 16, pp.13-24.

[98] Mei, Y., Liu, Y., Liu, C., Li, C., Yu, L., Guo, Q. and Li, H., 2016. Effect of base metal and welding speed on fusion zone microstructure and HAZ hot-cracking of electron-beam welded Inconel 718. Materials & Design, 89, pp.964-977.

[99] Vishwakarma, K.R., Richards, N.L. and Chaturvedi, M.C., 2008. Microstructural analysis of fusion and heat affected zones in electron beam welded ALLVAC® 718PLUS™ superalloy. Materials Science and Engineering: A, 480(1-2), pp.517-528.

[100] Agilan, M., Krishna, S.C., Manwatkar, S.K., Vinayan, E.G., Sivakumar, D. and Pant, B., 2012. Effect of welding processes (GTAW & EBW) and solutionizing temperature on microfissuring tendency in inconel 718 welds. In Materials Science Forum (Vol. 710, pp. 603-607). Trans Tech Publications Ltd.

[101] Singh, M., Morscher, G.N., Shpargel, T.P. and Asthana, R., 2008. Active metal brazing of titanium to high-conductivity carbon-based sandwich structures. Materials Science and Engineering: A, 498(1-2), pp.31-36.

[102] Stankowski, A., 2002, January. Advanced thermochemical cleaning procedures for structural braze repair techniques. In Turbo Expo: Power for Land, Sea, and Air (Vol. 36088, pp. 1181-1195).

[103] Li, H. and Li, Z.X., 2008. Research on Transient Liquid Phase Diffusion Bonding of Steel Sandwich Panels Under Small Plastic Deformation. Journal of materials engineering and performance, 17(6), pp.849-856.

[104] Cai, X.Q., Wang, Y., Yang, Z.W., Wang, D.P. and Liu, Y.C., 2016. Transient liquid phase (TLP) bonding of Ti2AlNb alloy using Ti/Ni interlayer: microstructure characterization and mechanical properties. Journal of Alloys and compounds, 679, pp.9-17.

[105] Zhou, Y., Gale, W.F. and North, T.H., 1995. Modelling of transient liquid phase bonding. International materials reviews, 40(5), pp.181-196.

[106] MacDonald, W.D. and Eagar, T.W., 1992. Transient liquid phase bonding. Annual review of materials science, 22(1), pp.23-46.

[107] Islam, T. and Sharif, A., 2019. Transient liquid phase bonding. Harsh Environment Electronics: Interconnect Materials and Performance Assessment.

[108] Miśta-Jakubowska, E., Czech Błońska, R., Duczko, W., Gójska, A.M., Kalbarczyk, P., Żabiński, G. and Trela, K., 2019. Archaeometric studies on early medieval silver jewellery from Central and Eastern Europe. Archaeological and Anthropological Sciences, 11(12), pp.6705-6723.

[109] Loepp, D., 2021. Some observations on the replication of precious metal artefacts in experimental archaeology. Journal of Archaeological Science: Reports, 37, p.102870.

[110] Mustain, H.A., Brown, W.D. and Ang, S.S., 2010. Transient liquid phase die attach for high-temperature silicon carbide power devices. IEEE transactions on components and packaging technologies, 33(3), pp.563-570.

[111] Reeks, W., Davies, H. and Marchisio, S., 2020. A review: Interlayer joining of nickel base alloys. Journal of Advanced Joining Processes, 2, p.100030.

[112] Owczarski, W.A., 1962. Eutectic brazing of Zircaloy 2 to type 304 stainless Steel. Welding J.(NY), 41.

[113] Bartholomew, H. and Bernstein, L., 1966. Applications of solid-liquid interdiffusion (SLID) bonding in integrated-circuit fabrication. Trans metall soc aime, 236(1), pp.405-412.

[114] Norris, B., 1986. Liquid Interface Diffusion (LID) Bonding of Titanium Structures. The Institute of Metals, pp.83-86.

[115] Hoppin, G.S and Berry, T.F., 1970. Activated Diffusion Bonding. Welding Journal, 49(1), pp.505-509.

[116] Wells, R.R. and Mikus, E.B., 1968. Thin Film Diffusion Brazing Titanium Members Utilizing Copper Intermediaries. U.S.Patent #3,417,461.

[117] Niemann, J.T. and Garrett, R.A., 1974. Eutectic bonding of boron--aluminum structural components. II. Development and application of the process. Weld. J.(NY), 53(8), pp.351s-360s.

[118] Duvall, D.S., Owczarski, W.A., Paulonis, D.F. and King, W.H., 1972. Methods for diffusion welding the superalloy Udimet 700. Balance, 15(4.95), pp.18-7.

[119] Nakao Y., 1989. Theoretical Research on Transient Liquid Insert Metal Diffusion Bonding of Nickel Base Alloys, Trans. Japan Welding Soc., 20(1), pp.60-65.

[120] Ramirez, J.E. and Liu, S., 1992. Diffusion brazing in the nickel-boron system. Welding Journal-New York-, 71, pp.365-s.

[121] Tuah-Poku, I., Dollar, M. and Massalski, T.B., 1988. A study of the transient liquid phase bonding process applied to a Ag/Cu/Ag sandwich joint. Metallurgical Transactions A, 19(3), pp.675-686.

[122] Liu, M.C., Sheng, G.M., He, H.J. and Jiao, Y.J., 2017. Microstructural evolution and mechanical properties of TLP bonded joints of Mar-M247 superalloys with Ni-Cr-Co-W-Ta-B interlayer. Journal of Materials Processing Technology, 246, pp.245-251.

[123] MacDonald, W.D. and Eagar, T.W., 1998. Isothermal solidification kinetics of diffusion brazing. Metallurgical and materials Transactions A, 29(1), pp.315-325.

[124]

[125] Gale, W.F. and Butts, D.A., 2004. Transient liquid phase bonding. Science and technology of welding and joining, 9(4), pp.283-300.

[126] Pouranvari, M., Ekrami, A. and Kokabi, A.H., 2009. Effect of bonding temperature on microstructure development during TLP bonding of a nickel base superalloy. Journal of Alloys and Compounds, 469(1-2), pp.270-275.

[127] Cook, G.O. and Sorensen, C.D., 2011. Overview of transient liquid phase and partial transient liquid phase bonding. Journal of materials science, 46(16), pp.5305-5323.

[128] Gale, W.F. and Orel, S.V., 1996. A microstructural investigation of NiAl/Ni-Si-B/NiAl transient liquid phase bonds. Journal of materials science, 31(2), pp.345-349.

[129] Pouranvari, M., Ekrami, A. and Kokabi, A.H., 2013. TLP bonding of cast IN718 nickel based superalloy: process–microstructure–strength characteristics. Materials Science and Engineering: A, 568, pp.76-82.

[130] Pouranvari, M., Ekrami, A. and Kokabi, A.H., 2013. Solidification and solid state phenomena during TLP bonding of IN718 superalloy using Ni–Si–B ternary filler alloy. Journal of Alloys and Compounds, 563, pp.143-149.

[131] Idowu, O.A., Richards, N.L. and Chaturvedi, M.C., 2005. Effect of bonding temperature on isothermal solidification rate during transient liquid phase bonding of Inconel 738LC superalloy. Materials Science and Engineering: A, 397(1-2), pp.98-112.

[132] Cooke, K.O., Khan, T.I. and Oliver, G.D., 2011. Nanostructure Particle-Reinforced Transient Liquid Phase Diffusion Bonding: a Comparative Study. Metallurgical and Materials Transactions A, 42(8), pp.2271-2277.

[133] Lee, B.K., Song, W.Y., Kim, D.U., Woo, I.S. and Kang, C.Y., 2007. Effect of bonding temperatures on the transient liquid phase bonding of a directionally solidified Ni-based superalloy, GTD-111. Metals and materials international, 13(1), pp.59-65.

[134] Malekan, A., Farvizi, M., Mirsalehi, S.E., Saito, N. and Nakashima, K., 2019. Influence of bonding time on the transient liquid phase bonding behavior of Hastelloy X using Ni-Cr-B-Si-Fe filler alloy. Materials Science and Engineering: A, 755, pp.37-49.

[135] Shamsabadi, A.Y. and Bakhtiari, R., 2016. TLP bonding of IN738/MBF20/IN718 system. Journal of Alloys and Compounds, 685, pp.896-904.

[136] Atieh, A.M. and Khan, T.I., 2014. TLP bonding of Ti-6Al-4V and Mg-AZ31 alloys using pure Ni electro-deposited coats. Journal of Materials Processing Technology, 214(12), pp.3158-3168.

[137] Khakian, M., Nategh, S. and Mirdamadi, S., 2015. Effect of bonding time on the microstructure and isothermal solidification completion during transient liquid phase bonding of dissimilar nickel-based superalloys IN738LC and Nimonic 75. Journal of Alloys and Compounds, 653, pp.386-394.

[138] Jin, Y.J. and Khan, T.I., 2012. Effect of bonding time on microstructure and mechanical properties of transient liquid phase bonded magnesium AZ31 alloy. Materials & Design, 38, pp.32-37.

[139] S.S. Sayyedain, and H.R. Salimijazi, Microstructure and mechanical properties of transient liquid phase bonding of Al2Op3/Al nano composite using copper interlayer. Materials and Design, 53 (2014) 275–282.

[140] Kenevisi, M.S. and Khoie, S.M., 2012. An investigation on microstructure and mechanical properties of Al7075 to Ti–6Al–4V Transient Liquid Phase (TLP) bonded joint. Materials & Design, 38, pp.19-25.

[141] Wen Lin and Tao Jin, transient liquid phase bonding of Ni- based Single crystal superalloy. Journal of Material Science and Technology. 18 (2002) 442-448.

[142] Maity, J. and Pal, T.K., 2012. Transient liquid-phase diffusion bonding of aluminum metal matrix composite using a mixed Cu-Ni powder interlayer. Journal of materials engineering and performance, 21(7), pp.1232-1242.

[143] Ellis, M.B.D., 1996. Joining of aluminium based metal matrix composites. International Materials Reviews, 41(2), pp.41-58.

[144] Zhai, Q., Xu, J., Lu, T. and Xu, Y., 2014. Research on interlayer alloys for transient liquid phase diffusion bonding of single crystal nickel base superalloy DD6. Journal of Materials Science and Chemical Engineering, 2(09), p.12.

[145] Abdelfattah, M., 2008. An experimental and theoretical study of transient liquid phase bonding of nickel based materials (Master's thesis).

[146] Zakipour, S., Samavatian, M., Halvaee, A., Amadeh, A. and Khodabandeh, A., 2015. The effect of interlayer thickness on liquid state diffusion bonding behavior of dissimilar stainless steel 316/Ti-6Al-4V system. Materials Letters, 142, pp.168-171.

[148] Yuan, X., Kim, M.B. and Kang, C.Y., 2011. Microstructural evolution and bonding behavior during transient liquid-phase bonding of a duplex stainless steel using two different Ni-B-based filler materials. Metallurgical and Materials Transactions A, 42(5), pp.1310-1324.

[149] Saha, R.K. and Khan, T.I., 2009. Microstructural developments in TLP bonds using thin interlayers based on Ni–B coatings. Materials characterization, 60(9), pp.1001-1007.

[150] Di Luozzo, N., Boudard, M., Doisneau, B., Fontana, M. and Arcondo, B., 2014. Transient liquid phase bonding of carbon steel tubes using a Cu interlayer: Characterization and comparison with amorphous Fe–B–Si interlayer bonds. Journal of alloys and compounds, 615, pp.S13-S17.

[151] Jalilvand, V., Omidvar, H., Rahimipour, M.R. and Shakeri, H.R., 2013. Influence of bonding variables on transient liquid phase bonding behavior of nickel based superalloy IN-738LC. Materials & Design (1980-2015), 52, pp.36-46.

[152] Lin, T., Li, H., He, P., Wei, H., Li, L. and Feng, J., 2013. Microstructure evolution and mechanical properties of transient liquid phase (TLP) bonded joints of TiAl intermetallics. Intermetallics, 37, pp.59-64.

[153] Jalilian, F., Jahazi, M. and Drew, R.A.L., 2013. Microstructure evolution during transient liquid phase bonding of alloy 617. Metallography, Microstructure, and Analysis, 2(3), pp.170-182.

[154] Sheng, N.C., Liu, J.D., Jin, T., Sun, X.F. and Hu, Z.Q., 2013. Wide gap TLP bonding a single-crystal superalloy: evolution of the L/S interface morphology and formation of the isolated grain boundaries. Metallurgical and Materials Transactions A, 44(4), pp.1793-1804.

[155] Gale, W.F., 2003. Transient liquid phase bonding of intermetallic compounds. In Materials Science Forum (Vol. 426, pp. 1891-1896). Trans Tech Publications Ltd.

[156] Yan, J., Xu, Z., Wu, G. and Yang, S., 2004. Interface structure and mechanical performance of TLP bonded joints of Al2O3p/6061Al composites using Cu/Ni composite interlayers. Scripta Materialia, 51(2), pp.147-150.

[157] Gale, W.F., Butts, D.A., Zhou, T. and Di Ruscio, M., 2002. Microstructure and mechanical properties of titanium aluminide wide-gap, transient liquid-phase bonds prepared using a slurry-deposited composite interlayer. Metallurgical and materials transactions A, 33(10), pp.3205-3214.

[158] Huang, J.H., Wan, Y., Zhao, H.T., Cheng, D.H. and Zhang, H., 2007. Effect of Ti on TLP bonding of SiCp/2618Al composites using interlayers of mixed Al–Ag–Cu system powders. Materials science and technology, 23(1), pp.87-91.

[159] Shao, H., Wu, A., Bao, Y., Zhao, Y. and Zou, G., 2017. Microstructure characterization and mechanical behavior for Ag3Sn joint produced by foil-based TLP bonding in air atmosphere. Materials Science and Engineering: A, 680, pp.221-231.

[160] Lan, L., Ren, Z., Yu, J., Yang, Z. and Zhong, Y., 2014. Microstructure and mechanical properties of partial transient liquid phase bonded Si3N4–DZ483 superalloy joints. Materials Letters, 121, pp.223-226.

[161] Chen, H., Long, C., Wei, T., Gao, W., Xiao, H. and Chen, L., 2014. Effect of Ni interlayer on partial transient liquid phase bonding of Zr–Sn–Nb alloy and 304 stainless steel. Materials & Design, 60, pp.358-362.

[162] Atabaki, M.M. and Idris, J., 2012. Low-temperature partial transient liquid phase diffusion bonding of Al/Mg2Si metal matrix composite to AZ91D using Al-based interlayer. Materials & Design, 34, pp.832-841.

[163] Atabaki, M.M., Bajgholi, M.E. and Dehkordi, E.H., 2012. Partial transient liquid phase diffusion bonding of zirconium alloy (Zr–2.5 Nb) to stainless steel 321. Materials & Design, 42, pp.172-183.

[164] Park, J.W. and Eagar, T.W., 2002, March. Application of the transient liquid phase bonding to microelectronics and MEMS packaging. In 2002 Proceedings. 8th International Advanced Packaging Materials Symposium (Cat. No. 02TH8617) (pp. 30-38). IEEE.

[165] Shirzadi, A.A. and Wallach, E.R., 1997. Temperature gradient transient liquid phase diffusion bonding: a new method for joining advanced materials. Science and Technology of Welding and Joining, 2(3), pp.89-94.

[166] Assadi, H., Shirzadi, A.A. and Wallach, E.R., 2001. Transient liquid phase diffusion bonding under a temperature gradient: modelling of the interface morphology. Acta materialia, 49(1), pp.31-39.

[167] Mahmoudi Ghaznavi, M., Ekrami, A. and Kokabi, A.H., 2011. Effect of solidification mechanism on microstructure and mechanical properties of joint in TLP bonded Al2024-T6 alloy. Science and Technology of Welding and Joining, 16(2), pp.174-180.

[168] Bigvand, A.G., 2013. Numerical simulation of transient liquid phase bonding under temperature gradient. University of Manitoba (Canada).

[169] Wells, R.R., 1976. Microstructural control of thin-film diffusion-brazed titanium. WELD J, 55(1), p.20.

[170] Blanc, A. L. and Mevrel, P., 1990. Proc. Conf. High temperature materials for power engineering. Dordrecht, Netherlands, pp. 1451–1460.

[171] Ohsasa, K., Narita, T. and Shinmura, T., 1999. Numerical modeling of the transient liquid phase bonding process of Ni using Ni-B-Cr ternary filler metal. Journal of phase equilibria, 20(3), pp.199-206.

[172] Sinclair, C.W., 1999. Modeling transient liquid phase bonding in multicomponent systems. Journal of phase equilibria, 20(4), pp.361-369.

[173] Campbell, C.E. and Boettinger, W.J., 2000. Transient liquid-phase bonding in the Ni-Al-B system. Metallurgical and Materials Transactions A, 31(11), pp.2835-2847.

[174] Illingworth, T.C., Golosnoy, I.O., Gergely, V. and Clyne, T.W., 2005. Numerical modelling of transient liquid phase bonding and other diffusion controlled phase changes. Journal of materials science, 40(9), pp.2505-2511.

[175] Li, J.F., Agyakwa, P.A. and Johnson, C.M., 2010. A fixed-grid numerical modelling of transient liquid phase bonding and other diffusion-controlled phase changes. Journal of materials science, 45(9), pp.2340-2350.

Reference

[176] Ghoneim, A. and Ojo, O.A., 2012. Asymmetric diffusional solidification during transient liquid phase bonding of dissimilar materials. Metallurgical and Materials Transactions A, 43(3), pp.900-911.

[177] Abdelfatah, M.M. and Ojo, O.A., 2009. On the extension of processing time with increase in temperature during transient-liquid phase bonding. Metallurgical and Materials Transactions A, 40(2), pp.377-385.

[178] Shirzadi, A.A. and Wallach, E.R., 1999. Analytical modelling of transient liquid phase (TLP) diffusion bonding when a temperature gradient is imposed. Acta materialia, 47(13), pp.3551-3560.

[179] Jabbareh, M.A. and Assadi, H., 2009. Modelling of microstructure evolution in transient-liquid-phase diffusion bonding under temperature gradient. Scripta Materialia, 60(9), pp.780-782.

[180] Ungár, T., Dragomir, I., Révész, Á. and Borbély, A., 1999. The contrast factors of dislocations in cubic crystals: the dislocation model of strain anisotropy in practice. Journal of applied crystallography, 32(5), pp.992-1002.

[181] Corbin, S.F., Winkler, S., Turriff, D.R. and Kozdras, M., 2014. Analysis of fluxless, reactive brazing of Al alloys using differential scanning calorimetry. Metallurgical and Materials Transactions A, 45(9), pp.3907-39153

[182] Ahmed, I.I., Adebisi, J.A., Abdulkareem, S. and Sherry, A.H., 2018. Investigation of surface residual stress profile on martensitic stainless steel weldment with X-ray diffraction. Journal of King Saud University-Engineering Sciences, 30(2), pp.183-187.

[183] Sheng, N., Hu, X., Liu, J., Jin, T., Sun, X. and Hu, Z., 2015. M3B2 and M5B3 Formation in diffusion-affected zone during transient liquid phase bonding single-crystal superalloys. Metallurgical and Materials Transactions A, 46(4), pp.1670-1677.

[184] Kapoor, M., Doğan, Ö.N., Carney, C.S., Saranam, R.V., McNeff, P. and Paul, B.K., 2017. Transient-liquid-phase bonding of H230 Ni-based alloy using Ni-P interlayer: microstructure and mechanical properties. Metallurgical and Materials Transactions A, 48(7), pp.3343-3356.

[185] Zhang, B., Sheng, G., Jiao, Y., Gao, Z., Gong, X., Fan, H. and Zhong, J., 2017. Precipitation and evolution of boride in diffusion affected zone of TLP joint of Mar-M247 superalloy. Journal of Alloys and Compounds, 695, pp.3202-3210.

[186] Ghaderi, S., Karimzadeh, F. and Ashrafi, A., 2020. Evaluation of microstructure and mechanical properties of transient liquid phase bonding of Inconel 718 and nano/ultrafine-grained 304L stainless steel. Journal of Manufacturing Processes, 49, pp.162-174.

[187] Pauzon, C., Markström, A., Dubiez-Le Goff, S. and Hryha, E., 2021. Effect of the Process Atmosphere Composition on Alloy 718 Produced by Laser Powder Bed Fusion. Metals, 11(8), p.1254.

[188] Ruiz-Vargas, J., Siredey-Schwaller, N., Gey, N., Bocher, P. and Hazotte, A., 2013. Microstructure development during isothermal brazing of Ni/BNi-2 couples. Journal of Materials Processing Technology, 213(1), pp.20-29.

[189] Moreau, E.D. and Corbin, S.F., 2019. Application of diffusion path analysis to understand the mechanisms of transient liquid-phase bonding in the Ni-Si-B system. Metallurgical and Materials Transactions A, 50(12), pp.5678-5688.

[190] Tung, S.K., Lim, L.C. and Lai, M.O., 1996. Solidification phenomena in nickel base brazes containing boron and silicon. Scripta materialia, 34(5), pp.763-769.

[191] Sidhu, R.K., Ojo, O.A., Richards, N.L. and Chaturvedi, M.C., 2009. Metallographic and OIM study of weld cracking in GTA weld build-up of polycrystalline, directionally solidified and single crystal Ni based superalloys. Science and Technology of Welding and Joining, 14(2), pp.125-131.

[192] Pouranvari, M., Ekrami, A. and Kokabi, A.H., 2014. Diffusion induced isothermal solidification during transient liquid phase bonding of cast IN718 superalloy. Canadian Metallurgical Quarterly, 53(1), pp.38-46.

[193] Murray, D.C. and Corbin, S.F., 2017. Determining the kinetics of transient liquid phase bonding (TLPB) of inconel 625/BNi-2 couples using differential scanning calorimetry. Journal of Materials Processing Technology, 248, pp.92-102.

[194] Cao, J., Wang, Y.F., Song, X.G., Li, C. and Feng, J.C., 2014. Effects of post-weld heat treatment on microstructure and mechanical properties of TLP bonded Inconel718 superalloy. Materials Science and Engineering: A, 590, pp.1-6.

[195] Gao, Y., Ding, Y., Ma, Y., Chen, J., Wang, X. and Xu, J., 2022. Evolution of annealing twins in Inconel 625 alloy during tensile loading. Materials Science and Engineering: A, 831, p.142188.

[196] You, X., Tan, Y., Cui, H., Zhang, H., Zhuang, X., Zhao, L., Niu, S., Li, Y. and Li, P., 2021. Microstructure evolution of an Inconel 718 alloy prepared by electron beam smelting. Materials Characterization, 173, p.110925.

[197] Chen, Y.T., Yeh, A.C., Li, M.Y. and Kuo, S.M., 2017. Effects of processing routes on room temperature tensile strength and elongation for Inconel 718. Materials & Design, 119, pp.235-243.

[198] Rao, G.A., Kumar, M., Srinivas, M. and Sarma, D.S., 2003. Effect of standard heat treatment on the microstructure and mechanical properties of hot isostatically pressed superalloy inconel 718. Materials Science and Engineering: A, 355(1-2), pp.114-125.

[199] Yan, G., Bhowmik, A., Nagarajan, B., Song, X., Tan, S.C. and Tan, M.J., 2019. Post-bond heat treatment effects on the wide gap transient liquid phase bonding of Inconel 718 with BNi-2 paste filler metal. Materials Science and Engineering: A, 766, p.138267.

[200] Perez, M., 2005. Gibbs–Thomson effects in phase transformations. Scripta materialia, 52(8), pp.709-712.

[201] Zhang, T., Li, H., Gong, H., Wu, Y., Ahmad, A.S. and Chen, X., 2021. Effect of rolling force on tensile properties of additively manufactured Inconel 718 at ambient and elevated temperatures. Journal of Alloys and Compounds, 884, p.161050.

[202] Sang, L., Lu, J., Wang, J., Ullah, R., Sun, X., Zhang, Y. and Zhang, Z., 2021. In-situ SEM study of temperature-dependent tensile behavior of Inconel 718 superalloy. Journal of Materials Science, 56(28), pp.16097-16112.

[203] Gribbin, S., Ghorbanpour, S., Ferreri, N.C., Bicknell, J., Tsukrov, I. and Knezevic, M., 2019. Role of grain structure, grain boundaries, crystallographic texture, precipitates, and porosity on fatigue behavior of Inconel 718 at room and elevated temperatures. Materials Characterization, 149, pp.184-197.

[204] Zhang, W.J., Song, X.Y., Hui, S.X. and Ye, W.J., 2017. In-situ SEM observations of fracture behavior of BT25y alloy during tensile process at different temperature. Materials & Design, 116, pp.638-643.

[205] Wang, J., Zhang, Y., Ma, J., Li, J. and ZHANG, Z., 2017. Microcrack Nucleation and Propagation Investigation ofInconel 740H Alloy Under In SituHigh Temperature Tensile Test. Acta Metall Sin, 53(12), pp.1627-1635.

[206] Zheng, L., Schmitz, G., Meng, Y., Chellali, R. and Schlesiger, R., 2012. Mechanism of intermediate temperature embrittlement of Ni and Ni-based superalloys. Critical Reviews in Solid State and Materials Sciences, 37(3), pp.181-214.

[207] Li, X., Zhang, J., Fu, Q., Akiyama, E., Song, X., Wang, Y., Li, Q. and Zou, N., 2018. Tensile mechanical properties and fracture behaviors of nickel-based superalloy 718 in the presence of hydrogen. International journal of hydrogen energy, 43(43), pp.20118-20132.

[208] Nunes, R.M., Pereira, D., Clarke, T. and Hirsch, T.K., 2015. Delta phase characterization in Inconel 718 alloys through X-ray diffraction. ISIJ International, 55(11), pp.2450-2454.

[209] Di Luozzo, N., Cabeza, S., Boudard, M. and Fontana, M., 2022. Measurement and simulation of residual stresses in transient liquid phase bonded ferritic steels. Journal of Materials Science, pp.1-17.

[210] AL-Nafeay, R.H., AL-Roubaiy, A.O. and Omidvar, H., Finite Element Simulation of Thermal Residual Stress in TLP Bonding of Ni-base Superalloy.

[211] Yan, G., Nagarajan, B., Bhowmik, A., Tan, S.C., Xu, R. and Tan, M.J., 2019. Induction transient liquid phase bonding of Inconel 718 with the nickel-based sintered brazing preform. Applied Surface Science, 473, pp.1024-1037.

[212] Dowling, N.E., 2013. Mechanical Behaviour of Materials. Engineering Methods for Deformation, Fracture, and Fatigue. Fourth.

[213] Xiao, L., Chaturvedi, M.C. and Chen, D.L., 2005. Low-cycle fatigue behavior of INCONEL 718 superalloy with different concentrations of boron at room temperature. Metallurgical and materials Transactions A, 36(10), pp.2671-2684.

[214] Gostariani, R., Ebrahimi, R., Asadabad, M.A. and Paydar, M.H., 2018. Mechanical properties of Al/BN nanocomposites fabricated by planetary ball milling and conventional hot extrusion. Acta Metallurgica Sinica (English Letters), 31(3), pp.245-253.

[215] Ungar, T.J.S.M., 2004. Microstructural parameters from X-ray diffraction peak broadening. Scripta Materialia, 51(8), pp.777-781.

[216] El-Eskandarany, M.S., 2015. Mechanical alloying: nanotechnology, materials science and powder metallurgy. Elsevier.

[217] Ungár, T., Groma, I. and Wilkens, M., 1989. Asymmetric X-ray line broadening of plastically deformed crystals. II. Evaluation procedure and application to [001]-Cu crystals. Journal of applied crystallography, 22(1), pp.26-34.

[218] Ungár, T., Dragomir, I., Révész, Á. and Borbély, A., 1999. The contrast factors of dislocations in cubic crystals: the dislocation model of strain anisotropy in practice. Journal of applied crystallography, 32(5), pp.992-1002.

[219] Neighbours, J.R., Bratten, F.W. and Smith, C.S., 1952. The elastic constants of nickel. Journal of Applied Physics, 23(4), pp.389-393.

[220] Albanese-Kotar, N.F. and Mikkola, D.E., 1987. Dissolution of comminuted magnesium oxide as affected by the density of dislocations introduced by various comminution methods. Materials science and engineering, 91, pp.233-240.

[221] Shyni, P.C. and Alagarsamy, P., 2016. Effect of annealing on structural and magnetic properties of Al substituted nanocrystalline Fe–Si–Co alloy powders. Journal of Magnetism and Magnetic Materials, 417, pp.62-68.

[222] Shyni, P.C. and Perumal, A., 2015. Structural and magnetic properties of nanocrystalline Fe–Co–Si alloy powders produced by mechanical alloying. Journal of Alloys and Compounds, 648, pp.658-666.

[223] Udhayabanu, V., Singh, N. and Murty, B.S., 2010. Mechanical activation of aluminothermic reduction of NiO by high energy ball milling. Journal of alloys and compounds, 497(1-2), pp.142-146.

[224] Kuntz, M.L., Zhou, Y. and Corbin, S.F., 2006. A study of transient liquid-phase bonding of Ag-Cu using differential scanning calorimetry. Metallurgical and Materials Transactions A, 37(8), pp.2493-2504.

[225] Blaine, R.L. and Kissinger, H.E., 2012. Homer Kissinger and the Kissinger equation. Thermochimica acta, 540, pp.1-6.

[226] Shkodich, N.F., Vadchenko, S.G., Nepapushev, A.A., Kovalev, D.Y., Kovalev, I.D., Ruvimov, S., Rogachev, A.S. and Mukasyan, A.S., 2018. Crystallization of amorphous Cu50Ti50 alloy prepared by high-energy ball milling. Journal of Alloys and Compounds, 741, pp.575-579.

[227] Lu, L., Lai, M.O. and Zhang, S., 1997. Diffusion in mechanical alloying. Journal of materials processing technology, 67(1-3), pp.100-104.

[228] Kuntz, M.L., Zhou, Y. and Corbin, S.F., 2006. A study of transient liquid-phase bonding of Ag-Cu using differential scanning calorimetry. Metallurgical and Materials Transactions A, 37(8), pp.2493-2504.

[229] Ghaderi, S., Karimzadeh, F., Ashrafi, A. and Hosseini, S.H., 2020. Effect of pressure, temperature and homogenization on the dissolution behavior and mechanical properties of IN718/AISI 304 during transient liquid phase bonding. Journal of Manufacturing Processes, 60, pp.213-226.

[230] Pouranvari, M., Ekrami, A. and Kokabi, A.H., 2014. Aging response of transient liquid phase bonded wrought IN718 superalloy: influence of post-bond heat treatment. Science and Technology of Welding and Joining, 19(2), pp.105-110.

[231] Gale, W.F. and Wallach, E.R., 1991. Microstructural development in transient liquid-phase bonding. Metallurgical Transactions A, 22(10), pp.2451-2457.

[232] Hynes, N.R.J., Velu, P.S., Kumar, R. and Raja, M.K., 2017. Investigate the influence of bonding temperature in transient liquid phase bonding of SiC and copper. Ceramics International, 43(10), pp.7762-7767.

[233] Zhang, X., Shi, X., Wang, J., Li, H., Li, K. and Ren, Y., 2014. Effect of bonding temperature on the microstructures and strengths of C/C composite/GH3044 alloy joints by partial transient liquid-phase (PTLP) bonding with multiple interlayers. Acta Metallurgica Sinica (English Letters), 27(4), pp.663-669.

[234] Pouranvari, M., Ekrami, A. and Kokabi, A.H., 2008. Microstructure–properties relationship of TLP-bonded GTD-111 nickel-base superalloy. Materials Science and Engineering: A, 490(1-2), pp.229-234.

[235] Bakhtiari, R. and Ekrami, A., 2012. Transient liquid phase bonding of FSX-414 superalloy at the standard heat treatment condition. Materials characterization, 66, pp.38-45.

List of publications:

A. Journals

1. Tarai, U. K., Robi, P. S., & Pal, S. (2020). Synthesis of Ni-Cr-B-Si-Fe-based interlayer alloy for transient liquid phase bonding of Inconel 718 superalloy by mechanical alloying process. The International Journal of Advanced Manufacturing Technology, 111, 2857-2875.
2. Tarai, U. K., Robi, P. S., & Pal, S. (2020). Thermal Properties of Ni–Cr–Si–B–Fe Based Interlayer Material and Its Application in TLP Bonding of IN 718 Superalloy. Acta Metallurgica Sinica (English Letters), 33, 1666-1680.
3. Tarai, U. K., Pal, S., & Robi, P. S. (2023). The effect of post-bond solution treatment and double aging on the microstructural evolution and mechanical properties of TLP-bonded IN718 joint. Archives of Civil and Mechanical Engineering, 23(2), 110.
4. Tarai, U. K., Pal, S., & Robi, P. S. The influence of post-bond heat treatment on the mechanical properties of the TLP bonded IN 718 joint: An approach to produce ASZ free bond (Communicated).
5. Tarai, U. K., Pal, S., & Robi, P. S. Effect of homogenization stage of TLP bonding on microstructure and mechanical properties of TLP bonding of IN 718 (Communicated).
6. Tarai, U. K., Pal, S., & Robi, P. S. Study the kinetics and determination of isothermal solidification time of TLP bonding of IN 718 joint by DSC method (Communicated).
7. Tarai, U. K., Pal, S., & Robi, P. S. Measurement of surface residual stress profile of TLP bonded Inconel 718 joint using X-ray diffraction technique (To be communicated).
8. Tarai, U. K., Pal, S., & Robi, P. S. Investigating high cycle fatigue properties of TLP bonded IN 718 (To be communicated).
9. Tarai, U. K., Pal, S., & Robi, P. S. Study the high-temperature tensile properties of the TLP bonded IN 718(To be communicated).

B. Conferences

1. UK Tarai, PS Robi, S Pal, Development and Characterization of Interlayer Material for Transient Liquid Phase Bonding of IN-718 by Mechanical Alloying, AIMTDR, Pune, 2016

2. UK Tarai, PS Robi, S Pal, Development of a novel Ni-Fe-Cr-B-Si interlayer material for transient liquid phase bonding of Inconel 718. IOP Conference Series: Materials Science and Engineering 346 (1), 012048.